MODELLING GROUNDWATER FLOW AND CONTAMINANT TRANSPORT AT A GOLD MINE SITE IN NORTHERN ONTARIO

BY: ADAM DETTWEILER

THIS THESIS IS SUBMITTED IN PARTIAL FULFILLMENT OF THE REQUIREMENTS FOR THE DEGREE OF:

MASTER OF SCIENCE IN ENGINEERING

IN

ENVIRONMENTAL ENGINEERING

FACULTY OF ENGINEERING

LAKEHEAD UNIVERSITY

THUNDER BAY, ONTARIO

JANUARY 2015

ABSTRACT

The practices of mining and ore processing are used in many countries around the world to extract and concentrate the valuable natural resources found within the rock bodies which make up the earth's crust. However, the solid waste disposal facilities which are used to store the large volumes of waste rock and mine tailings that are produced during these processes can pose a risk to the quality of down-gradient waters due to the slow leaching of various dissolved elements and compounds. Groundwater flow and contaminant transport modelling is an effective way of understanding and investigating a site where dissolved contaminants have been detected in the groundwater.

The Northern Ontario gold mine site, which is the focus of this study, first began ore processing in 1997. Since then, the groundwater and surface water bodies surrounding the site have been continually monitored to detect any changes in water quality. Groundwater samples collected adjacent to the mine's tailings management area (TMA) have consistently detected dissolved cobalt and iron at concentrations above the site's self-appointed trigger level standards. In 2009 seven pumping wells, were installed in the contaminated area to restrict further spread of the plumes by capturing the contaminated groundwater and recycling it back into the TMA.

A numerical groundwater flow (MODFLOW-2005) and contaminant transport (MT3DMS) model has been created which accurately simulates the flow of groundwater through the site both before and after the pumping well system was installed. The validated model was then used to simulate the fate and transport of dissolved cobalt through the subsurface of the site, and to perform a sensitivity analysis on the input parameters. The magnitude of the dispersion

parameters and amount of sorption in the northern portion of the sand aquifer were determined to have the greatest effect on the evolution of the cobalt plume.

An assessment of the pumping well system was performed which indicates the ability of the pumping wells to capture the dissolved cobalt plume within five years of activation. The ability of the pumping wells to continue to restrain the advancement of the cobalt plume was also confirmed for a 15 year simulation period. Additional alternatives such as an intermittent pumping schedule, a 50% reduction in pumping rates, and the decommissioning of four out of the seven pumping wells were also confirmed to successfully restrain the cobalt plume advancement for a 15 year simulation period. A preliminary investigation into the use of a permeable reactive barrier (PRB) as an alternative to the pumping wells was also performed. Two possible PRB locations were proposed, however the large width of the plume indicates that a funnel and gate system should be investigated.

ACKNOWLEDGMENTS

The completion of this thesis project was a major endeavour which I would not have been able to complete without the assistance and support of many friends, family, and professors. First and foremost, I would like to acknowledge my thesis supervisor Dr. Eltayeb Mohamedelhassan, and my thesis co-supervisor Dr. Bruce Kjartanson. Their vast scientific knowledge and analytical skills have provided me with continual guidance throughout this thesis project, and have been paramount to my success. Additionally, their technical and editorial comments were invaluable in increasing the quality of the writing and presentation of this work.

I wish to provide a special recognition to Messrs. Nuri Hmidi and Shane Matson for the valuable time and effort they spent providing information and correspondence to me throughout this project. Without their contributions of literature and data, this project would not have been possible.

I would also like to thank my parents, who I know love and support me through all of my undertakings, and are always available for support or advice when it's needed. I am also grateful for the continual support of Alexis Sharp, whose encouragement and positive attitude have been instrumental for me during the writing of this thesis.

Finally, I want to express thanks to all of my friends and student colleagues who provided me with mutual support and assistance throughout the entire Master's program. I wish to specifically acknowledge my friends and classmates, Jeffry Hoi, Farshad Oveissi, Rimaz Abakar, John Inwood, Shahin Esmaeiliazad, and Tallie MacDonald who created a fun and welcoming atmosphere where I felt comfortable sharing ideas and learning.

TABLE OF CONTENTS

TABLE OF TABLES

TABLE OF FIGURES

1.0 INTRODUCTION

Many of the world's natural resources, such as minerals and metals are found trapped within rock formations deep beneath the earth's surface. In order to make use of these valuable resources, the ores which are rich with the desired minerals must be mined and processed to extract and concentrate the valuable portion. While the minerals that are recovered through ore processing techniques have great economic value, the ore processing also generates a large quantity of waste rock and mine tailings which have little or no value. Not only do these mining wastes have little or no economic value, but they also possess the potential to release large quantities of contaminants, which can pose a long term threat to both human and animal life, and the environment.

1.1 BACKGROUND

Mining activities have been used to recover mineral resources from the earth for hundreds of years. As our demand for mineral resources has grown, so has the global rate of mineral extraction by mining, which reached over 16.6 billion metric tonnes of ore mined globally in 2011 (Reichl et al., 2013). Once this ore is removed from the earth, it is crushed and processed to recover the mineral(s) of value. After processing, the remaining portion of the ore which no longer contains desired elements, or is no longer economically feasible to recover any further elements, is disposed of and referred to as tailings. These tailings often contain high concentrations of leachable heavy metals and sulfide minerals, which, if allowed to oxidize, lead to the production of acid mine drainage (AMD). Preventing the negative environmental impact

of AMD is therefore the most challenging and expensive issue faced by the mining industry today (Price, 2003).

Historically, the negative impacts of AMD were not considered during the development of a mine, and no precautions were taken to prevent its formation. Upon mine closure, the sites were often abandoned and left with no remediation plan to mitigate the environmental effects of AMD. Resultantly, many abandoned mine sites have since allowed massive amounts of contaminated leachate to spread through the surrounding ground and surface water systems, causing extensive ecological and environmental damage. These abandoned sites can continue to produce AMD for hundreds of years after mine closure, and often require millions of dollars worth of work to remediate after the fact (Price, 2003).

Modern mining developments, however, must account for AMD mitigation, prevention, and treatment throughout their entire operating period, as well as post-closure, to ensure the protection of humans and the environment from contaminant releases. AMD mitigation must be well planned out and typically incorporates site management and monitoring strategies, as well as the creation of contingency plans (Price, 2003). Extensive measures are commonly taken to best understand, predict and react to any contaminant releases, and to make sure the most efficient and effective solutions can be employed if required. In order to decide which type of source or plume remediation scheme has the best chance of mitigating the effects of a contaminant release, it is important to quantify the contamination source, understand its location with respect to the groundwater flow patterns on the site, and determine the

reactions and interaction the contaminant will undergo when introduced into the site's groundwater (Kimball et al., 2003).

Computer modelling software is a tool that has been extensively used to aid the study and understanding of both groundwater flow and contaminant transport through the subsurface of a site. A groundwater flow model, created using software such as Visual MODFLOW, can be used to simulate the movement of groundwater through a site's subsurface, and provides insight into the groundwater flow patterns, directions, velocities, and rates of flow. A contaminant transport model code, such as MT3DMS, can be used to simulate the migration and dispersion of contaminants through a site's subsurface, and provides insight into the reactions which the contaminants may experience during their transport. Using these models as investigative tools to simulate real life sites where contamination has been detected is an effective way to develop understanding of the site, and provides a way to investigate the possibility of using various remediation techniques (Kimball et al., 2003). A groundwater flow and transport model can provide extensive insight into the contaminant plume's characteristics, and allows future plume movements and responses to remedial efforts to be simulated. This type of simulation therefore provides a prediction of the plume's behaviour, and can be used to minimize uncertainty and risk when attempting groundwater or soil remediation.

The primary goal of this thesis is to develop a groundwater flow and contaminant transport model for a gold mine site in Northern Ontario. The area of study is located adjacent to an active tailings disposal facility for a currently operating gold mine. The groundwater conditions at the site have been continually monitored since 1995, and samples are consistently tested to

detect the presence of inorganic contaminants which are commonly found in mine tailings. During this monitoring period, elevated concentrations of dissolved cobalt have been detected and flagged as a priority for remediation efforts, while elevated concentrations of dissolved iron have also been detected. In 2009, seven pumping wells were installed on the site in an effort to remove the contaminated groundwater from the underlying aquifer, and to prevent the plume of contamination from spreading any farther. Once a working, calibrated groundwater flow and contaminant transport model of the site has been created, it will be used as a tool to assess the effectiveness of the current pumping well system. Additionally, the model will be used to perform a preliminary investigation regarding the feasibility of a permeable reactive barrier to provide long term mitigation of the contaminant plume migration.

1.2 OBJECTIVES

The six specific objectives of this thesis are as listed below:

- Construct a conceptual site model to represent the site's geology, hydrogeology, contaminant sources, and dissolved cobalt and iron plumes.
- Construct groundwater flow and contaminant transport models of the site using Visual MODFLOW and MT3DMS, and calibrate them to the site's observed groundwater and contamination conditions.
- Simulate the transport of cobalt through the subsurface of the site.
- Assess the effectiveness of the existing pumping wells and determine the optimal pumping rate.

- Perform a preliminary investigation regarding the use of a permeable reactive barrier to prevent further plume migration.
- Assess the design of the current groundwater monitoring network and propose improvements if necessary.

1.3 ORGANIZATION

This thesis begins with a brief introductory chapter, which provides a summary of the project background, outlines the six project objectives, and describes the organization of information contained within. The second chapter provides a detailed literature review and explanation of necessary background information associated with gold mining and the project objectives. Descriptions of gold mining, its regulations, processes, tailings, tailings management, and the associated environmental concerns are all provided. The environmental chemistry of iron and cobalt are briefly explained, followed by a discussion of the major fate and transport processes which typically affect the movement of inorganic species through groundwater. Discussions of mass flux principles and the use of Visual MODFLOW as a tool for modelling groundwater flow and contaminant transport are then presented. An explanation of two remediation strategies that are commonly used to mitigate environmental contamination at mine sites is also provided. The chapter ends with two case studies which provide a summary of relevant groundwater flow and contaminant transport modelling work which was conducted by other researchers.

The third chapter offers a detailed description of the mine site being modelled, including its history, geology, hydrogeology, recharge, and contaminant sources and plumes. Chapter 4

describes the process of creating a groundwater flow model for the Northern Ontario gold mine site, from its boundary conditions and geologic zones, to its calibration and simulation results. Chapter 5 discusses contaminant transport modelling for the mine site, the sensitivity analysis which was performed, and the assumptions and limitations of the model. Chapter 6 then describes the use of the contaminant transport model to simulate remedial activities at the site. This chapter also includes a discussion of the site's current groundwater monitoring network. The final chapter summarizes the results of the simulations and provides conclusions based on the findings. The thesis then concludes by providing recommendations for continued research, model development, and remediation strategies.

2.0 Literature Review and Background Information

2.1 Mining Regulations in Canada

In Canada, the direct involvement of the federal government in mining activities is limited to only a few specific operations. Mining operations that extract uranium, those which are performed by federally owned corporations, and those taking place either on federal lands or offshore areas are the only cases that fall within the extents of federal involvement (Natural Resources Canada, 1996). The majority of mining operations in Canada are therefore left as the responsibility of the respective provincial government whose jurisdiction covers the land in which the mine site lies. Provincial policies are responsible for regulating the exploration, development, mineral extraction, construction, management, reclamation, and close-out plans of all mines within their jurisdiction (Natural Resources Canada, 1996).

In Ontario, The Mining Act regulates various mining activities including mine claim staking, exploration plans and permits, mine closure plans, mine hazards, the rehabilitation of mining lands, and proof of financial assurance (Ontario, 1990). The Mining Act therefore focuses mainly on activities which occur either before or after the mine operation/mineral production stage of the mine, and has limited application to mines during their operation period (Ministry of Northern Development and Mines, 2008).Ontario Regulation 240/00 regulates mine development and closure under part VII of The Mining Act, and specifies that any liquid effluents which are released from a mine site during mine closure may not exceed the concentrations specified in either the existing environmental compliance approvals for the site or those specified in Ontario Regulation 560/94 (Ontario, 2000). Ontario Regulation 560/94 is

the section of the Environmental Protection Act which controls effluent monitoring, effluent quantity, and effluent quality for the metal mining sector. This section of the Environmental Protection Act specifies daily concentration limits and monthly average concentration limits for total cyanide, total suspended solids, copper, lead, nickel, zinc, and arsenic for mine process effluent waters (Ontario, 1994).

Once the mine is closed, The Mining Act requires the continuation of both surface and groundwater monitoring in the area. Surface water monitoring must be conducted for on-site water bodies, downstream water bodies, as well as background reference sites (Ontario, 2000). These surface water quality measurements taken at the closed out mine site are required by Ontario Regulation 240/00 to meet the Ontario Provincial Water Quality Objectives (OPWQOs), as specified by the Ministry of the Environment. The OPWQOs specify maximum values for various physical and chemical characteristics of water to ensure that a minimum acceptable quality of water is being upheld (Ministry of Environment and Energy, 1994). The objective of this monitoring is to ensure that the quality of the surface water at the site is unimpaired, and remains both able to sustain aquatic life and acceptable for human recreational use.

The hydrogeological conditions of a closed mine site must also be addressed through a groundwater characterization study. This study is required to identify the expected uses of the groundwater in the area, the existence of or potential for groundwater contamination, the nature of any contaminants and their potential to migrate, as well as the degree of attenuation which can be expected at the site (Ontario, 2000). Groundwater monitoring at the site is also required, and must include monitoring wells capable of assessing the groundwater quality both

up-gradient and down-gradient of contaminant sources. Although a number of chemical characteristics and contaminants are required to be tested for according to The Mining Act, no specific set of regulatory standards is specified for acceptable contaminant concentrations in the collected groundwater samples. Instead, these values are typically determined on a site by site basis during the creation and approval of the closure plan.

2.2 GOLD MINERALS

At ambient temperatures and pressures elemental gold typically remains inert and does not readily combine with other elements to form stable chemical complexes. For this reason, very few gold minerals are known to exist naturally within the earth's crust. Instead, gold is typically found on Earth as tiny grains of nearly pure elemental gold, known as native gold. However, although native gold can be up to 99.8% pure, it is often found alloyed with different quantities of silver. When the silver content of the grains of gold are above 20%, the alloy is then known as electrum (Stevens, 2010). Gold tellurides are the most common type of gold bearing minerals, and are a group of complex crystals which comprise a combination of gold, silver and tellurium. Other rare gold bearing minerals that are known to exist are compounds of gold with bismuth, antimony, and, extremely rarely, copper (Marsden & House, 1992). Since these minerals are extremely rare, the three most common forms of gold found on Earth are native gold, electrum and gold tellurides.

Gold bearing ore deposits can be classified based on the recovery method which is required in order to extract the gold. Placer ore deposits are alluvial, eluvial, or colluvial in nature and are found in a loosely consolidated form with the gold particles naturally liberated by weathering

and erosion (Marsden & House, 1992). These ores are typically found relatively close to the earth's surface and their gold can simply be recovered through gravity separation. Paleo-placers are older placer ores, which have been lithified by pressure and temperature to form a new rock body deep below the surface. These ores require crushing and milling to liberate the gold prior to extraction, and are found at depths of up to 3 km below the earth's surface. Hydrothermal ores are gold deposits which have leached from their parent rock and become concentrated in a hydrothermal fluid. The dissolved gold is then naturally precipitated once the hydrothermal fluid reaches a highly reductive environment, forming a hydrothermal ore (Marsden & House, 1992).

2.3 Gold Mining Processes

When gold bearing ore is mined, it is often found in the form of native gold which is finely dispersed in large amounts of unwanted gangue minerals. Further processing of the ore is therefore required to concentrate the gold, however the grade of the mined ore is rarely sufficiently high enough to justify shipping it very large distances for processing. Processing of the ore, known as ore dressing is therefore usually performed on, or very close to the mine site. Figure 2.1 displays a schematic of the basic processes used in a typical ore dressing plant at a gold mine. Basic ore dressing can be broken down into two main steps; first is size reduction, and second is mineral separation to concentrate the elements of value.

Size reduction is done to physically free the valuable mineral crystals or gold particles which are trapped inside the gangue minerals, and is accomplished by milling and grinding. Size reduction is an extremely energy intensive process, and typically requires multiple stages for the ore to

reach the desired size. The large ore particles are crushed using ball mills or rod mills until fine sand to silt sized particles are obtained (Spitz & Trudinger, 2009). Once the ore is crushed to adequately sized particles, one of a number of available separation techniques is used to concentrate the targeted mineral.

Oxidative pre-treatment is sometimes required prior to mineral separation, when the ore contains a large quantity of refractory minerals such as sulphides or carbonates. Refractory minerals are minerals that interfere with mineral separation processes, and lead to low gold recovery rates. Sulphide minerals readily react with, and consume unacceptable quantities of chemical reagents, while carbonates are known to adsorb gold during a leaching process (Marsden & House, 1992).

Mineral separation techniques that can be used in mineral processing include magnetic separation, flotation, gravity settling, and leaching. The method of separation which is used by an ore processing plant depends both on the ore's composition and the mineral which is being separated. In gold mining, the most commonly used mineral separation process is a leaching technique known as cyanidation.

2.3.1 CYANIDATION

Cyanidation is the process of dissolving gold from the crushed ores by leaching with an oxidative cyanide solution. The chemical stability of gold allows it to remain non-reactive in most aqueous solutions, including strong acids. To reduce the gold's stability, both an oxidant and at least one of a few specific complexing ligands must be present in solution. Only cyanide (CN^-), thiourea ($SC(NH_2)_2$), thiocyanate (SCN^-), thiosulfate (${S_2O_3}^{2-}$), and a few halides are

known to form stable complexes with gold. This selective nature allows gold to be targeted for dissolution, even from very low grade ores. Due to its high effectiveness, and its relatively low cost, cyanide is almost exclusively used as a leachate in gold mining.

In water, cyanide ions will hydrolyse to form hydrogen cyanide, a weak acid which incompletely dissociates at low pH values. This incomplete dissociation reduces the amount of free cyanide in solution, which is needed to dissolve the gold. Additionally, hydrogen cyanide has a high vapour pressure, and evaporates relatively quickly into the atmosphere, causing a continual loss of cyanide. To prevent the aforementioned issues caused by the use of cyanide at low pH values, the pH control step in Figure 2.1 is used to raise the pH value of the tailings slurry prior to the addition of cyanide. Cyanidation is then performed at a high pH value which limits the formation of hydrogen cyanide. When introduced to an aerated cyanide solution, the gold is oxidized, while dissolved oxygen is reduced according to the following chemical reaction known as Elsner's equation (Marsden & House, 1992).

ELSNER'S EQUATION:

$$4Au_{(s)} + 8CN^-_{(aq)} + O_{2(aq)} + 2H_2O_{(l)} \rightarrow 4Au(CN)_2^-{}_{(aq)} + 4OH^-_{(aq)}$$

After leaching, the gold is removed from the pregnant solution either by the carbon adsorption step shown in Figure 2.1, or by zinc precipitation, followed by various refining techniques.

2.4 GOLD MINE TAILINGS

Mine tailings is the term given to the waste materials that are remaining after the majority of the valuable minerals are extracted from the ore in the mine's processing plant. The mine

tailings consist of finely crushed ore particles as well as residual chemical compounds that are added during the extraction processes. Additionally, because the extraction processes are not 100% efficient, small amounts of gold also remain in the tailings.

Tailings are typically discharged from the ore processing plant along with the effluent process water as a slurry mixture containing less than 50% solids (Marsden & House, 1992). The tailings slurry is pumped through a pipe network to its final disposal location, known as a tailings management area (TMA). The TMA is usually a low lying area with abundant storage capacity, typically contained behind a dam (Stevens, 2010).

Once deposited in the TMA, the solid and liquid portion of the tailings separate by gravity settling. The surface water from the tailings management area is then commonly pumped back to the ore processing plant as a water source. This reduces both the amount of fresh water being consumed by the mine, and the amount of effluent which is being discharged to the environment.

2.4.1 Properties of Gold Mine Tailings

The physical and chemical properties of mine tailings vary greatly depending on the type of ore, the extraction processes being used, the efficiency of the processes, and the age of the tailings (Marsden & House, 1992).

2.4.1.1 Physical Properties

When discharged from the processing plant, mine tailings are released as a slurry solution of finely crushed ore particles and process water that is approximately 50-80% liquid (Marsden &

House, 1992). At some mines, a dewatering step is included prior to final discharge in the tailings management area, to recover process water for reuse, and to reduce the total volume of slurry being disposed. A thickened tailings stacking disposal method is also an effective way of expanding the storage capacity of a TMA (Kam et al., 2014). The solid portion of the mine tailings is made up mainly of fine sand to silt sized particles of unwanted gangue minerals (Spitz & Trudinger, 2009). Investigation of the physical characteristics of mine tailings solids at Ontario mines indicates a porosity range of 0.4-0.55 with a large variation in hydraulic conductivities between 10^{-6} and 10^{-2} cm/s (Blowes et al., 2003).

While the quantity of tailings produced by a mine will depend on the quantity and grade of the ore body being mined, the solid portion of typical gold mine tailings makes up more than 95% of the total mass of ore mined (Blowes et al., 2003).

2.4.1.2 CHEMICAL PROPERTIES

Mine tailings not only contain minerals, but also residual chemicals from the processing plant. In the case of gold mines which use a cyanidation process for gold recovery, alkalinity and cyanide are commonly found to have high residual values. The presence of potentially high concentrations of toxic cyanide species is the greatest immediate threat presented by gold mine tailings. High cyanide concentrations present a threat to wildlife that may come into contact with the tailings, as well as a threat of contamination to the environment via a potential spill or accidental release. At modern mines, the tailings slurry will typically undergo a cyanide removal process (Figure 2.1) prior to being deposited in the tailings management area. A

cyanide removal process is used to reduce the residual cyanide concentration by either breaking the cyanide down or removing it for re-use (Stevens, 2010).

The mineral composition of mine tailings solids depend on the mineralogy of the ore, however, it typically consist mainly of silicates, but can also include varying quantities of sulphates and carbonates. Due to the high pH range used during the cyanidation process, the tailings slurry is often discharged at an alkaline pH value.

2.4.2 Tailings Leachate Formation

Before being mined, the metals and mineral ores found below the earth's surface as well as their surrounding host rocks exist under anaerobic conditions, and are typically found in their most reduced form (Kortatsi & Akabzaa, 2009). Once mined, rocks and minerals are exposed to the atmosphere where they are subject to meteorological processes such as precipitation, wind, evaporation, and solar radiation, which causes them to weather and disperse throughout the environment (Santos Jallath, 2009).

The oxidation and weathering of minerals causes them to break down or decompose, which can produce harmful by-products. Some minerals, such as iron sulphides, readily react with water and oxygen to form acidic compounds, which leads to the production of acid mine drainage. Acid mine drainage (AMD), also known as acid rock drainage (ARD) is the term given to the acidic leachate that is produced during the oxidation of the sulphide minerals found in mine tailings and waste rock (Kortatsi & Akabzaa, 2009). Although iron sulphides are not the only minerals that contribute to AMD formation, they are the greatest contributor for numerous reasons, which are explained below (Kortatsi & Akabzaa, 2009).

The two most abundant sulphide minerals found in most mine tailings are pyrite (FeS_2) and pyrrhotite ($Fe_{(1-x)}S$), both of which are iron sulfides. While pyrite has a fixed composition, pyrrhotite encompasses a wide range of compositions, where x can vary from 0.125 (Fe_7S_8) to 0 (FeS) (Blowes, Ptacek, & Jurjovec, 2003). When removed from the ground and exposed to oxidizing atmospheric conditions, these minerals combine with water and oxygen to decompose according to the reactions below (Blowes et al., 2003).

REACTION 1: PYRITE (FeS_2) OXIDATION

$$2FeS_{2(s)} + 7O_{2(aq)} + 2H_2O_{(l)} \rightarrow 2Fe^{2+}{}_{(aq)} + 4SO_4{}^{2-}{}_{(aq)} + 4H^{+}{}_{(aq)}$$

REACTION 2: PYRRHOTITE ($Fe_{(1-x)}S$) OXIDATION

$$Fe_{(1-x)}S_{(s)} + \left(2 - \frac{x}{2}\right) O_{2(aq)} + xH_2O_{(l)} \rightarrow (1-x)Fe^{2+}{}_{(aq)} + SO_4{}^{2-}{}_{(aq)} + 2xH^{+}{}_{(aq)}$$

Pyrite and pyrrhotite are oxidized to form ferrous iron (Fe^{2+}), sulphate ($SO_4{}^{2-}$), and hydrogen (H^+) ions, which lower the pH of the surrounding solution. In the presence of additional oxygen, the ferrous iron which is released can be further oxidized to ferric iron (Fe^{3+}).

REACTION 3: FERROUS IRON (Fe^{2+}) OXIDATION

$$4Fe^{2+}{}_{(aq)} + O_{2\,(aq)} + 4H^{+}{}_{(aq)} \rightarrow 4Fe^{3+}{}_{(aq)} + 2H_2O_{(l)}$$

This ferric iron product is an important oxidant, which can then cause additional pyrite oxidation and acid production (Lottermoser, 2007).

REACTION 4: PYRITE (FeS_2) OXIDATION BY FERRIC IRON (Fe^{3+})

$$FeS_{2(s)} + 14Fe^{3+}{}_{(aq)} + 8H_2O_{(l)} \rightarrow 15Fe^{2+}{}_{(aq)} + 2SO_4{}^{2-}{}_{(aq)} + 16H^{+}{}_{(aq)}$$

Both dissolved oxygen and ferric iron could therefore act simultaneously to oxidize sulphide minerals in mine tailings. However, the relative rates at which these oxidants work depends on the pH condition of the surrounding solution (Iribar et al., 2000). Studies of pyrite oxidation in the presence of both oxidants have been investigated to determine their relationships. Bonnissel-Gissinger et al. (1998) oxidized pyrite under low pH conditions and in the presence of both oxidants, and discovered that ferric iron ions instead of dissolved oxygen were found on the surfaces of the oxidizing pyrite minerals. This suggests that ferric iron is the primary oxidant of pyrite rather than dissolved oxygen.

However, under neutral or moderate pH conditions, aqueous ferric iron has extremely low solubility, and will be readily hydrolyzed, and precipitate out of solution.

REACTION 5: FERRIC IRON (Fe^{3+}) PRECIPITATION

$$Fe^{3+}_{(aq)} + 3H_2O_{(l)} \leftrightarrow Fe(OH)_{3\,(s)} + 3H^{+}_{(aq)}$$

This reaction will remove free ferric iron ions from solution under neutral pH conditions. If the ferric iron ions are precipitated through reaction 5, they are no longer available to oxidize sulphide minerals, and reaction 4 will be restricted. For this reason, at neutral pH values, dissolved oxygen becomes the main oxidant of sulfide minerals (Seal & Hammarstrom, 2003). It is important to note that, although this precipitation reaction removes ferric iron ions from solution, which reduces the amount of oxidant present, it also causes the release of hydrogen ions and contributes to acid production and the lowering of the pH conditions. This is important because ferric iron precipitation (reaction 5) is a reversible reaction which can proceed forwards or backwards depending on the chemical conditions. If the pH of solution were to

lower sufficiently, large quantities of once precipitated iron would dissolve and release ferric iron ions back into solution, which would then increase sulphate oxidation.

At low pH values, when ferric iron is soluble, if not catalyzed by bacteria, the oxidation of ferrous iron to ferric iron (reaction 3) proceeds very slowly. The ferric iron ions would oxidize the sulfate minerals faster than they could be produced by reaction 3, and this reaction would become the rate limiting step to sulfide oxidation by ferric iron (Blowes et al., 2003). However, some acidophilic bacterial species which thrive at very low pH values, such as *Acidithiobacillus ferrooxidants,* catalyze the oxidation of ferrous iron to ferric iron (Gould & Kapoor, 2003) increasing the rate of reaction 3 by a factor of 100,000 (Seal & Hammarstrom, 2003).

Other non-iron sulphides, such as galena (PbS) and covellite (CuS), do not contribute significantly to AMD formation due to several reasons. Their crystal structures are much more stable than an iron sulphide mineral's structure, which slows the oxidation rate of their sulphur molecules, and therefore reduces their acid production rate. Additionally, when they do break down they do not release iron ions which cause the formation of additional oxidants. They are also more likely to form low solubility by-product minerals during their dissolution, which can encapsulate the sulphides and prevent their further oxidation (Lottermoser, 2007).

Acid production from the AMD formation processes above work together to collectively lower the pH of the pore water in the TMA. A decrease in pH will not only increase the rate of sulfide oxidation, but also increase the solubility of many other metals and compounds that are also found in the tailings minerals (Price, 2003). With an increase in solubility, many elements will dissolve from the tailings minerals into the aqueous phase allowing them to be transported

with the leachate water. While, in general, a decreased pH will increase the solubility of many contaminants, especially metals such as iron, copper and aluminum, it is not the sole cause of contaminant mobility. It is important to note that many elements typically found in AMD leachates, such as antimony, arsenic, cadmium, molybdenum, selenium, and zinc remain relatively soluble even at neutral pH values (Price & Errington, 1998).

2.4.3 Leachate Prevention and Treatment

The prevention of leachate formation by the AMD process is critical to reducing the risk of contamination to the soil and groundwater in the region surrounding the tailings management area. It is important to note that acid mine drainage is a natural phenomenon that occurs when any rock containing sulfide minerals is exposed to the atmosphere, and is not solely due to mining activity. Mining simply accelerates this weathering process by exposing large quantities of sulfide minerals to oxidizing conditions.

Mitigation of the effects of AMD at mine sites is done in two ways, by containment of the mine tailings to a single area, and by reducing sulfide oxidation. A TMA is designed to retain the unwanted mine tailings in one specific area. This minimizes the impacted land area as well as the number of possible receptors that could be affected by a contaminant leak. The TMA is also typically retained behind a low permeability barrier which is designed to contain any leachates formed in the tailings and minimize the possible contamination of downstream surface or ground water (Marsden & House, 1992). The kind of optimal site conditions which are necessary for creating a single, impermeable TMA can sometimes be very difficult to find close to the mine location. This has to be taken into consideration during the early stages of a mining

investigation and feasibility study, as it can sometimes be a deciding factor in determining the feasibility of a mine development (Spitz & Trudinger, 2009).

The acidic, heavy metal contaminated leachate that is produced by mine tailings in a TMA is primarily due to the AMD process. To prevent this acid formation would require the prevention of the AMD reactions described previously. The removal, or restriction of any one of the three necessary reactants in reaction 1 and 2 would effectively slow, or halt AMD formation. The necessary reactants for AMD formation are water, oxygen, and sulfide minerals (Santos Jallath, 2009).

Restricting oxygen from contacting the surfaces of the sulfide minerals in mine tailings is the most common method of reducing AMD and leachate formation. Various methods of varying costs and efficiencies have been developed, most of which involve the placing of a cover material over the tailings which restricts the diffusion of oxygen. Natural materials such as native soils, clays, or organic matter, and synthetic materials such as geo-membranes are most commonly used to create a lining on top of the tailings (Santos Jallath, 2009). Water covers are also an effective method of preventing sulfide oxidation, where the entire TMA is flooded to allow all of the tailings to be submerged in water.

2.5 Mine Tailings Dams

Mine tailings dams are constructed on the down gradient side of the TMA in order to effectively contain the discarded tailings slurry and prevent their migration. Historically, tailings dams were simply constructed using borrow materials, waste rock, or coarse tailings and often included a drainage layer to allow the leachate to drain to a nearby surface water body, or into an aquifer

below (Blowes et al., 2003). This was done to prevent a buildup of hydrostatic pressure behind the dam, and to maintain dam stability.

Modern tailings dams no longer facilitate drainage, and are intended to both contain the tailings solids and prevent the release of contaminated leachate to surface or groundwater systems (Blowes et al., 2003). These dams are commonly constructed of low permeability materials, and are designed to withstand the hydrostatic pressure of the tailings' pore water. The cross section of a typical TMA and tailings dam are shown in Figure 2.2 (Spitz & Trudinger, 2009).

2.5.1 Design and Construction

Tailings dam construction is often done in phases; with dam lifts being required to increase the capacity of the TMA once a certain quantity of tailings have been disposed. Three methods of dam rising can be employed, upstream, downstream, and centreline, which are displayed in Figure 2.3 (Spitz & Trudinger, 2009). In downstream dam construction, subsequent lifts are built outward from the tailings, with the entire base of the dam extending away from the TMA. This method allows the upstream toe of the dam to maintain a constant location as it rises. In centerline dam construction, the dam is extended directly upwards, with part of the base being built on top of previously deposited tailings (Blowes et al., 2003). In upstream dam construction, the subsequent lifts are built inward, with a large portion of the base being built on top of previously deposited tailings. This method allows the downstream toe of the dam to maintain a constant location as it rises. It is important to assess the strength and stability of the previously deposited mine tailings before determining a construction method for the

subsequent tailings dam lifts. Constructing part of the dam's foundation on previously deposited tailings will typically reduce the overall strength of the dam; as a result, upstream construction typically has the highest risk of failure and downstream construction typically has the lowest risk (Spitz & Trudinger, 2009).

For cost effectiveness, it is often desired to use as much native site material as possible during the construction of a tailings dam. If native material is to be used to construct the low permeability dam core, a minimum of 40% silt and clay sized particles is recommended, and sufficient testing should be conducted to ensure adequately low permeability and high strength are attainable (Bedell et al., 2002). Grain size distribution, water content, standard proctor, triaxial shear, hydraulic conductivity, consolidation, and Atterberg limit testing are recommended for determining the soil properties and characteristics. A quality assurance and an in-situ testing program should also be carried out during construction of the dam core to ensure adequate compaction and strength is being obtained by the construction techniques being employed.

Prior to dam construction, any high permeability, unconsolidated material found below the dam location should be removed until a stable material of sufficiently high strength and low permeability is reached. Grouting of a fractured bedrock base or the incorporation of impermeable synthetic materials may also be necessary to provide a stable, low permeability foundation for the dam (Blowes et al., 2003).

2.5.2 Seepage From Mine Tailings Dams

Seepage from mine tailings dams is an environmental concern due to the nature of the leachate and the affect it can have on downstream surface and groundwater. Although it is not as catastrophic as an accidental spill or dam failure, the slow seepage of leachate through the mine tailings dams can create an extremely pervasive and long lasting environmental problem that is an even greater threat in the long term (Blowes et al, 2003).

The seepage from a mine tailings dam occurs extremely slowly through the materials of low permeability which are used to confine the tailings. Seepage can occur through the dam core, between the dam's lifts, or under the dam foundation. Imperfections in the material, or the development of cracks, can allow seepage to occur through a material that would typically have a low permeability.

2.5.3 Contaminants of Concern

The low pH value of mine tailings leachate facilitates the dissolution of the heavy metal components of soil minerals, and allows them to be transported away from the mine site through a ground or surface water system. Almas & Manoko (2012), tested soil and water samples taken from around a gold mine site to determine if elevated concentrations of trace contaminants may be present. Arsenic, cadmium, chromium, nickel, selenium, uranium and zinc were all discovered in concentrations which were noted to greatly exceed the World Health Organization's (WHO's) recommendations. Other metals which are not mentioned in the WHO's standards, but were found in high concentrations were aluminum and cobalt (Almas & Manoko, 2012).

Heavy metal contaminants in groundwater are sometimes considered even more dangerous than organic compounds because they are not biodegradable and can have a cumulative toxic effect on living organisms (Stoica et al., 2009). Although some metals are much more harmful than others, cadmium, copper, lead, manganese and zinc are the most toxic metal elements (Stoica et al., 2009).

2.5.4 Characterization and Groundwater Monitoring

Due to evolving environmental regulations which have been established to protect groundwater quality, the development of groundwater monitoring programs has become necessary to detect the introduction of any contaminants downstream of potentially hazardous sites. In general, the groundwater monitoring program in place must be capable of measuring background water quality up-gradient of the potential source, and be able to detect quantifiably significant changes in groundwater quality down-gradient of the potential source (Sara, 2006). The number of monitoring wells that are required to ensure these capabilities are met is site-specific, and depends on the type and complexity of the site as well as the regulatory agency.

The ability of a groundwater monitoring system to effectively detect down-gradient changes in groundwater quality is largely dependent on the quality of design of the well network, and the individual wells themselves. Figure 2.4 shows the cross sectional view of a typical groundwater monitoring well. The location, depth to screen, design, and installation method of a monitoring well are extremely important factors that contribute to the quality of information that can be derived from the samples that are collected from it (Nielsen & Schalla, 2006). For this reason, a

large amount of knowledge about the subsurface characteristics of a site should be obtained prior to well installation.

Site characterization is the first step to designing an effective groundwater monitoring system, where various investigative techniques are used to gain a thorough understanding of the site's geologic, hydrogeologic, geochemical, and biological conditions (Nielsen & Schalla, 2006). Site characterization is performed by the collection and review of all previously measured historical site data, followed by a detailed field investigation to examine the subsurface conditions. Field investigation techniques are intended to confirm historical data accuracy, settle any discovered discrepancies, and fill in existing knowledge gaps. Numerous site investigation techniques exist that may be used to characterize a site, including soil boring, direct push probing, cone penetration tests, piezometers, hydraulic conductivity tests, and groundwater sampling (Nielsen & Schalla, 2006).

Sufficient site characterization is crucial to understanding preferential flow paths, predicting future contaminant movement, assessing risk, and assisting in groundwater monitoring efforts. An insufficient quantity or quality of site data can lead to inaccurate conclusions being drawn, ineffective monitoring and remedial efforts being employed, increased costs, and increased risk to humans and the environment (Nielsen et al., 2006).

2.6 Environmental Chemistry of Cobalt and Iron

Cobalt and iron are both classified as transition metals and are situated next to each other on the periodic table of elements, with atomic numbers of 26 and 27, respectively. Although their

atomic weights of 55.845 g/mol and 58.933 g/mol make them similar in mass, they are quite different in both their abundance on earth, and behaviour in the environment.

Cobalt is a rare element on Earth, comprising only approximately 0.0025% of the mass of the earth's crust. Cobalt occurs naturally as a component of various sulfides and arsenides such as smeltite ($CoAs_{2-3}$), cobaltine ($CoAsS$), and linneite (Co_3S_4). Although several isotopes of cobalt are known to exist, natural cobalt (cobalt-59), which has 27 protons and 32 neutrons, and is stable and non-radioactive, is the only cobalt isotope which is naturally found on earth (Johanson, 2008). Cobalt can exist at oxidation states of 0, +2, and +3, although the oxidation state of +2 is most common due to its stability. Cobalt (+3) is rare because it will readily accept an electron to reduce to cobalt (+2); cobalt (+3) is a very strong oxidant which even has the capability to oxidize water (Sciences International, Inc., 2006). As seen in Figure 2.5, the solubility of cobalt (+2) in water is lower than that of ferrous Iron, but much higher than that of ferric iron.

Iron is one of the most abundant elements on Earth, and comprises approximately 5% of the mass of the earth's crust. As a result, iron is one of the main components of many soil and rock minerals such as pyrite, magnetite, goethite, hematite, biotite, ferrihydrite and olivine (Prietzel et al., 2007). Although iron can exist at oxidation states between -2 and +6, the most common naturally occurring oxidation states are +2 (ferrous iron) and +3 (ferric iron). The iron atoms in most iron minerals are typically found at their more reduced ferrous state, however, in the presence of oxygen, ferrous iron will oxidize to ferric iron as discussed in section 2.4.2.

In the pH range of most groundwater (5-8), the low dissolution rates of iron minerals will cause only a small amount of ferrous iron to be released into solution. As displayed in the solubility diagram in Figure 2.5 (Dyer & Scrivner, 1998), ferrous iron will remains soluble in water over a much larger range of pH values than ferric iron (Dyer & Scrivner, 1998). In anoxic groundwater, the ferrous iron that is released will remain soluble and be transported with the groundwater movement. In oxic groundwater, the aqueous ferrous iron will be oxidized into ferric iron, which will then typically precipitate as iron oxides or oxyhydroxides on the surfaces of soil minerals, predominantly as crystalline goethite (Mettler, et al., 2001). Due to the insolubility of ferric iron at moderate pH values, ferrous iron is the main form of dissolved iron typically found in groundwater (Appelo & Postma, 2005).

2.7 Fate and Transport Parameters

When a contaminant such as dissolved cobalt or iron enters a groundwater system, it tends to move and spread from the initial source location along with the surrounding groundwater. The resulting zone of contaminated groundwater is known as a plume. The size and shape of the plume that forms is dependent on the fate and transport processes which are acting on the contaminant in the aquifer. Transport processes are those that affect the physical movement of the contaminant, while fate processes include the reactions and transformations that the contaminant will undergo (Alvarez & Illman, 2006). Non-reactive contaminant species are those which are not influenced by chemical or biological processes. For such non-reactive species, only transport processes need to be considered (Sharma & Reddy, 2004).

2.7.1 HYDROGEOLOGICAL PARAMETERS

Since the fate and transport processes, which govern the movement of contaminants, occur in the subsurface groundwater, it is important to have a detailed understanding of the hydrogeological parameters of the subsurface soils. Extensive site investigation is often performed to sufficiently characterize the hydrogeological parameters of a site's subsurface layers to first understand the groundwater movements prior to investigating contaminant transport. Hydrogeological parameters such as hydraulic conductivity, hydraulic gradient, hydraulic head, porosity, specific storage, and specific yield are important inputs which are required for any groundwater flow model. It is assumed that these hydrogeological parameters are adequately understood by the reader and are therefore only briefly discussed in this section. Table 2.1 presents values for some of these parameters, which are considered approximately representative of the subsurface materials, based on their soil type (Mays, 2012).

2.7.1.1 HYDRAULIC CONDUCTIVITY

Hydraulic conductivity (K) is a property of a porous medium which, in hydrogeology, describes the ease with which water can flow through a soil (Schwartz & Zhang, 2003). The hydraulic conductivity of an aquifer material is dependent on many physical characteristics of the soil particles such as size, shape, distribution, orientation, and the interconnected porosity of the material as well as the properties of the fluid (Mays, 2012). Since it describes the rate at which fluid can move through a porous material, hydraulic conductivity is expressed in the same units as velocity (distance/time). The anisotropic properties of a porous medium can also cause the hydraulic conductivity of a soil to vary depending on the direction of groundwater flow. This is

accounted for in Visual MODFLOW by allowing the input of different hydraulic conductivity values for the X, Y, and Z directions of the model (Schlumberger Water Services, 2011).

Hydraulic conductivity values can vary over many orders of magnitude for different types of porous media (as seen in Table 2.1), making it a difficult parameter to predict with a great degree of accuracy. Clay soil usually has a hydraulic conductivity value much lower than most other soil types, with a value of $2x10^{-7}$ cm/s being considered representative of typical clay soil (Mays, 2012). However, a layer of clay soil found at the ground surface is exposed to weathering, which can cause the formation of cracks and fractures that significantly increase the hydraulic conductivity of the clay layer. McKay, Cherry, and Gillham (1993) performed field experiments to determine a representative horizontal hydraulic conductivity value for the upper portion of a site covered in clay till. Due to weathering and fracturing, hydraulic conductivity measurements in the upper 1.5-5.5m of the clay can be up to three orders of magnitude greater than the average hydraulic conductivity value for the unfractured clay (McKay et al., 1993). Based on large scale, in situ experiments, the hydraulic conductivity of weathered surface clay was determined to be in the range of $1x10^{-5}$ to $3x10^{-5}$ cm/s (McKay et al., 1993).

2.7.1.2 HYDRAULIC HEAD

Hydraulic head (h) is a measure of the total energy available to drive the flow, expressed as a height of water above a datum elevation. Field measurements of hydraulic head are taken using piezometers or monitoring wells, where the water level is allowed to naturally rise in a vertical tube which is exposed to atmospheric pressure at the top end. Sea level is typically used as the

reference datum elevation, and head measurements are expressed in meters above sea level (Schwartz & Zhang, 2003).

2.7.1.3 HYDRAULIC GRADIENT

Hydraulic gradient (i) is a measure of the change in potential energy between two points along a groundwater flow path. Hydraulic gradient is expressed as the difference between the total hydraulic head measurements taken at two points, divided by the distance along the flow path between the points (Alvarez & Illman, 2006). If the vertical hydraulic gradient is not significant, the distance along the flow path can be taken as the horizontal distance between the two points.

2.7.1.4 POROSITY

Porosity (n) is an expression of the proportion of voids present in a porous medium. Total porosity (n_T) is expressed as the total volume of voids in a porous material divided by its total volume (Schwartz & Zhang, 2003). However, in a soil matrix, not all voids are sufficiently interconnected to allow groundwater to flow through them. In hydrogeology, effective porosity (n_e) is often used, and represents the ratio of interconnected voids to total volume (Mays, 2012). This ratio includes only the portion of voids in the soil which are interconnected and available for groundwater flow, and excludes the non-interconnected and dead-end pores (Sharma & Reddy, 2004). For the creation of groundwater flow and contaminant transport models using Visual MODFLOW, an input value for both total and effective porosity are required (Schlumberger Water Services, 2011).

2.7.1.5 SPECIFIC YIELD

Specific yield (S_y) is a property of a porous medium which quantifies the amount of water that can be released or stored in the medium due to a change in hydraulic head, and is known as the storage term for an unconfined aquifer (Schlumberger Water Services, 2011). The specific yield of a porous medium is defined as the amount of water which is released from a saturated medium when it is allowed to drain by the force of gravity, and is used when the aquifer material under consideration is unconfined (Schwartz & Zhang, 2003). Specific yield is expressed as a ratio between the volume of water expelled from a soil sample due to gravitational drainage and the total volume of the sample, as described in equation 2.1 below.

$$S_y = \frac{V_d}{V_T} \tag{2.1}$$

Where: $S_y = Specific\ Yield\ [Length^3/Length^3]$

$V_d = Volume\ of\ Water\ Drained\ [L^3]$

$V_T = Total\ Volume\ of\ Porous\ Medium\ [L^3]$

2.7.1.6 SPECIFIC STORAGE

Specific storage (S_s) is also a property of a porous medium which quantifies the amount of water that can be released or stored in the medium due to a change in hydraulic head, but is used for aquifers under confined conditions (Schlumberger Water Services, 2011). Confined conditions typically occur when a high permeability aquifer material is located beneath a layer of low permeability material, and its pore water is experiencing a confining pressure. Specific storage is defined as the volume of water that a unit volume of porous material will release due to the aquifer compression and water expansion that is caused by a unit decrease in hydraulic

head (Schlumberger Water Services, 2011). Specific storage therefore takes into account the compressibility of both the granular matrix and the water contained within it, and is expressed per unit change in hydraulic head as shown in equation 2.2 (Schwartz & Zhang, 2003).

$$S_s = \gamma_w(\beta_p + n\beta_w) \tag{2.2}$$

Where: $S_s = Specific\ Storage\ \left[\frac{1}{L}\right]$

$\gamma_w = Unit\ Weight\ of\ Water\ \left[\frac{Force}{L^3}\right]$

$\beta_p = Vertical\ Compressibility\ of\ Porous\ Medium\ \left[\frac{L^2}{F}\right]$

$n = Porosity\ of\ Porous\ Medium\ \left[\frac{L^3}{L^3}\right]$

$\beta_w = Compressibility\ of\ Water\ \left[\frac{L^2}{F}\right]$

For groundwater flow modelling using Visual MODFLOW, the layers of the model can be defined by the user as being confined, unconfined, or both confined and unconfined. The parameter which is used to calculate the storage volume of a cell depends on whether the cell is considered confined or unconfined. Input specific yield values are used to determine the storage volume of the cells in layers which are defined as being unconfined. For layers which are specified as confined, Visual MODFLOW calculates a storage coefficient by multiplying the specific storage value by the thickness of the layer. When a layer is defined as being both confined and unconfined, Visual MODFLOW will use the head value which it calculates for the cell to determine if it should be treated as being confined or unconfined (Schlumberger Water Services, 2011).

2.7.2 TRANSPORT PARAMETERS

A contaminant moving through an aquifer will experience three transport processes; advection, dispersion, and diffusion (Sharma & Reddy, 2004). These three processes work simultaneously in a flowing aquifer to spread the contaminant from its source location and create a plume of contaminated water.

2.7.2.1 ADVECTION

Advection is the movement of a contaminant down-gradient of its source location by being carried by flowing groundwater, and is typically the most dominant transport process. Advection assumes that the contaminant will flow at the same velocity as the groundwater as if it were a particle of water itself (Alvarez & Illman, 2006). Advective transport can therefore be simulated in the same way as groundwater flow, using Darcy's law. The average velocity of pore water flowing through a porous medium, known as the seepage velocity, or advective velocity, can be calculated by equation 2.3 below.

$$v_x = -\frac{Ki}{n_e} \tag{2.3}$$

Where: $v_x = Seepage\ Velocity\ \left[\frac{L}{Time}\right]$

$K = Hydraulic\ Conductivity\ \left[\frac{L}{T}\right]$

$i = Hydraulic\ Gradient\ \left[\frac{L}{L}\right]$

$n_e = Effective\ Porosity\ \left[\frac{L^3}{L^3}\right]$

2.7.2.2 DISPERSION

Dispersion is a spreading effect that is caused by the variations in flow velocities throughout the network of interconnected pores in the porous medium (Alvarez & Illman, 2006). The random distribution of soil particles creates variations in both pore size and connectivity, which affect flow velocity through the soil matrix. As a contaminant navigates through the soil matrix, these variations will cause the plume to diverge and spread over a larger area than it would due to advection alone (Schwartz & Zhang, 2003). Dispersion will occur to different extents in three different directions; longitudinal, transverse horizontal and transverse vertical. The amount of dispersion that will occur in each direction is represented by a numerical coefficient, which is the product of the groundwater's seepage velocity and the soil's dispersivity value for the direction in question (Schlumberger Water Services, 2011). Dispersivity is a property of the porous medium which is also scale dependant. It will have a different value depending on the type of soil, the scale of the contaminant plume, and the direction in question. Equation 2.4 shows the expression for dispersion in the x-direction.

$$D'_x = \alpha_x v_x \tag{2.4}$$

Where: $D'_x = Coefficient\ of\ Dispersion\ \left[\frac{L^2}{T}\right]$

$\alpha_x = Dispersivity\ in\ the\ X - Direction\ [L]$

$v_x = Seepage\ Velocity\ \left[\frac{L}{T}\right]$

Contaminant transport modelling in Visual MODFLOW is able to account for dispersion in all three directions; longitudinal (α_L), transverse horizontal (α_h), and transverse vertical (α_v). The

three inputs which are required for each model layer are a longitudinal dispersivity value, a ratio of horizontal to longitudinal dispersivity (α_h/α_L), and the ratio of vertical to longitudinal dispersivity (α_v/α_L) (Schlumberger Water Services, 2011). Dispersivity in the longitudinal direction is typically 10-20 times greater than dispersivity in the transverse horizontal direction, which is an additional 2 times greater than transverse vertical dispersivity (Alvarez & Illman, 2006). When longitudinal dispersivity is increasingly large relative to transverse dispersivity, the plume would become increasingly elongated.

Estimating a representative value for the coefficient of dispersivity to be used in modelling applications can be difficult due to the variability of site measured dispersivity values when investigated at increasing distances from the contaminant source. Dispersivity measurements display the general trend of increasing with distance from a contaminant source, but the relationship is not predictable (Dunnivant & Anders, 2006). This variability of collected data is attributed to different degrees of heterogeneity that exist in the aquifers where the measurements are recorded (Gelhar et al., 1992). When performing contaminant transport modelling, conservative estimates from data previously measured during site investigations can be used for initial dispersivity values, but detailed sensitivity analysis should be performed on the model. Dispersivity is typically estimated using a correlation with the observed plume length, which is estimated from historical contaminant source and groundwater monitoring data (Dunnivant & Anders, 2006).

For the purpose of predicting dispersivity values, Gelhar et al. (1992) compiled dispersivity values measured at 59 different field sites, and classified the data based on its reliability. The

collection of data indicates that dispersivity values can vary between 2-3 orders of magnitude for any given plume length, however the data with the highest reliability indicated that the lower end of this range is likely the most accurate (Gelhar et al., 1992).

Several researchers have attempted to create regression formulas which can relate measured dispersivity values to the overall scale or length of a contaminant plume. Figure 2.6 (Xu & Eckstein, 1995) compares some equations proposed by Neuman (1990) to those determined by Xu and Eckstein (1995). Neuman (1990) proposed that the relationship between longitudinal dispersivity and plume length could be described by two straight lines fit on a log-log plot of the parameters. One line is considered representative for plume lengths less than 100m (Equation 2.5, labelled at Eq.22 on Figure 2.6) (Neuman & Zhang, 1990), and the other is considered representative of plume lengths 100m or greater (Equation 2.6, labelled as Eq.32 on Figure 2.6) (Neuman & Zhang, 1990).

$$\alpha_L = 0.0175\, L^{1.46} \qquad For\ L < 100m \tag{2.5}$$

$$\alpha_L = 0.32\, L^{0.83} \qquad For\ L \geq 100m \tag{2.6}$$

Where: $\alpha_L = Longitudinal\ Dispersivity\ [meters]$

$L = Plume\ Length\ [meters]$

In order to include for the fact that data points were considered to have varying levels of reliability, Xu and Eckstein (1995) used a weighted least-squares statistical analysis technique. Using this technique allowed Xu and Eckstein (1995) to developed several regression formulas which applied various weights to the data points depending on whether they were of low,

medium, or high reliability. Two of the regression formulas produced by Xu and Eckstein (1995) are plotted on Figure 2.6. Equation 2.7 (Xu & Eckstein, 1995) (labelled as Eq. 12b on Figure 2.6) describes the regression curve determined using a weighting scheme of 1:1:1 (equal weight for all data points). Equation 2.8 (Xu & Eckstein, 1995) (labelled as Eq. 14b on Figure 2.6) describes the regression curve determined using a weighting scheme of 1:2:3 for low, medium, and high reliability data points.

$$\alpha_L = 1.20\ [\log(L)]^{2.958} \tag{2.7}$$

$$\alpha_L = 0.83\ [\log(L)]^{2.414} \tag{2.8}$$

Where: $\alpha_L = Longitudinal\ Dispersivity\ [meters]$

$L = Plume\ Length\ [meters]$

As seen in Figure 2.6, the weighted regression curve of Equation 2.8 also indicates that the lower range of dispersivity values is most representative of field conditions. Additionally, because this curve is asymptotic, it is believed that the changes in the dispersivity value will not cause significant error once the plume has exceeded 1000m in length (Xu & Eckstein, 1995).

2.7.2.3 DIFFUSION

Diffusion is the movement of a contaminant through a solution due to a chemical concentration gradient (Sharma & Reddy, 2004). Diffusion occurs in any system where a concentration difference exists between two points, and will only stop once the concentration throughout the entire solution is constant. The random movements of dissolved or suspended particles cause the contaminant to transport from an area of high concentration to an area of low

concentration even without any fluid movement (Alvarez & Illman, 2006). Values for molecular diffusion coefficients (D_0), which represent the diffusion of various ions and molecules into a still, homogeneous liquid at specific temperatures, have been published in the literature.

For contaminant movement in groundwater, diffusion occurs along the tortuous pathways of interconnected pores through the soil matrix, and is therefore slower than diffusion in pure water (Batu, 2006). For diffusive transport through soil, the effective diffusion coefficient (D_e) is commonly used, which is also represented by a numerical coefficient, and is a product of the diffusion coefficient of the species at a given temperature and the soil's dimensionless tortuosity coefficient (τ). Equation 2.9 below shows the expression for the effective diffusion coefficient (Batu, 2006).

$$D_e = \tau D_0 \tag{2.9}$$

Where: $D_e = Effective\ Diffusion\ Coefficient\ \left[\frac{L^2}{T}\right]$

$\tau = Tortuosity\ Coefficient\ [Unitless]$

$D_0 = Molecular\ Diffusion\ Coefficient\ \left[\frac{L^2}{T}\right]$

The tortuosity coefficient is a property of the porous medium which accounts for the roundabout nature of the diffusion pathways through the soil matrix (Alvarez & Illman, 2006). Values of tortuosity coefficients must be between 0 and 1, and typically range between approximately 0.3-0.7 for most types of soil, however 0.67 is believed to be most appropriate value for sandy aquifers (Batu, 2006). A soil with highly indirect and circuitous diffusion pathways will have a low tortuosity coefficient, whereas a soil with very direct flow paths will

have a relatively high tortuosity coefficient. For diffusion through pure liquids, the tortuosity coefficient is equal to 1, and the effective diffusion coefficient is equal to the molecular diffusion coefficient (Batu, 2006).

It is important to note that diffusion happens in all directions as long as there is a concentration gradient. However, the process of diffusion happens extremely slowly, and its effect on contaminant transport is often negligible in comparison to the effects of advection when there is movement of the groundwater (Alvarez & Illman, 2006). The effect of diffusion becomes an increasingly important factor in a porous medium with a very low hydraulic conductivity such as a clay liner, or when an extremely small hydraulic gradient is present and the groundwater flow velocity is very small. To account for diffusion in contaminant transport simulations, Visual MODFLOW accepts a single effective diffusion value for each contaminant being simulated (Schlumberger Water Services, 2011).

2.7.2.4 HYDRODYNAMIC DISPERSION

Hydrodynamic dispersion is simply a combination of mechanical dispersion and effective diffusion. Since they have mathematical similarly in contaminant transport modelling, mechanical dispersion and bulk diffusion are commonly expressed together as hydrodynamic dispersion, which is also represented by a numerical coefficient (Alvarez & Illman, 2006). The hydrodynamic dispersion coefficient is the sum of the coefficient of dispersion and the coefficient of bulk diffusion as demonstrated in equation 2.10.

$$D_x = D'_x + D_e \tag{2.10}$$

Where: $D_x = Coefficient\ of\ Hydrodynamic\ Dispersion \left[\frac{L^2}{T}\right]$

$D'_x = Coefficient\ of\ Dispersion \left[\frac{L^2}{T}\right]$

$D_B = Effective\ Diffusion\ Coefficient \left[\frac{L^2}{T}\right]$

When compared to pure advection, the two main effects that hydrodynamic dispersion has on contaminant transport are the dilution of the contaminant concentrations inside the plume, and an increase in the total volume of contaminated water (Alvarez & Illman, 2006).

2.7.3 Fate Parameters

As contaminants flow through groundwater, they come into contact with various species, both chemical and biological, with which they can react. The main fate process that affects inorganic contaminants is sorption. Fate processes reduce, or slow down the transport of the contaminant species, causing aqueous concentrations to be lower at a certain location than would be expected due to transport parameters alone (Alvarez & Illman, 2006). The degree to which the contaminant migration is slowed relative to the velocity of the groundwater is known as the retardation factor (R_f), and is shown in equation 2.11.

$$R_f = \frac{v_x}{v_c} \tag{2.11}$$

Where: $R_f = Retardation\ Factor\ [Unitless]$

$v_x = Seepage\ Velocity \left[\frac{L}{T}\right]$

$v_c = Contaminant\ Migration\ Velocity \left[\frac{L}{T}\right]$

2.7.3.1 SORPTION

Sorption refers to the attachment of contaminant particles onto the minerals and organic matter encountered in the soil matrix. The term sorption combines the effects of the adsorption, chemisorption, and absorption processes, since knowledge of their collective influence on the contaminant movement is often desired (Sharma & Reddy, 2004). The sorption term therefore describes the overall distribution of the contaminant between the solid phase and the dissolved phase in an aquifer material, which is also known as partitioning. The amount of sorption that occurs in an aquifer will vary greatly, depending on the physical and chemical characteristics of the contaminant, the aquifer material, and the groundwater (Todd & Mays, 2005).

To describe sorption of a particular contaminant onto a porous medium, the relationship between the equilibrium concentration of the contaminant in solution (C) and the concentration of contaminant sorbed onto the porous medium (S) is investigated. The relationship that develops between these two factors under conditions of constant temperature can be plotted, and is known as an isotherm (Sharma & Reddy, 2004). Three different types of isotherms can be used to describe sorption relationships: the linear isotherm, the Freundlich isotherm, and the Langmuir isotherm. The linear isotherm is the most commonly used isotherm in fate and transport modelling because of its simplicity and validity at low concentration ranges (Alvarez & Illman, 2006). The linear isotherm is shown in equation 2.12 below.

$$S = K_d C \tag{2.12}$$

Where: $S = Mass\ of\ Contaminant\ Sorbed\ Per\ Unit\ Dry\ Mass\ of\ Soil\ \left[\frac{M}{M}\right]$

$K_d = Distribution\ Coefficient\ \left[\frac{L^3}{Mass}\right]$

$C = Aqueous\ Concentration\ of\ Contaminant\ at\ Equilibrium\ \left[\frac{M}{L^3}\right]$

The contaminant transport modelling engine MT3DMS used by Visual MODFLOW can account for the sorption of a contaminant onto the soil particles using the relationship described by any one of the three isotherms (Schlumberger Water Services, 2011). The input parameters which are required by the model are dependent on the type of sorption chosen. When linear sorption is chosen, Visual MODFLOW requires the input of a distribution coefficient value for each contaminant being simulated.

Sorption parameters are often determined through laboratory testing where most conditions can be held as constants during testing (Alvarez & Illman, 2006). However, parameter determination using field methods or empirical methods is also possible (Sharma & Reddy, 2004). The use of the surface area of the soil solids is one method that can be used to estimate the sorption parameters of inorganic contaminants when the surface areas of the soil minerals are high. This method assumes linear sorption, and relates the distribution coefficient to the soil minerals' surface area, using the metric units specified, through equation 2.13 (Sharma & Reddy, 2004).

$$\log K_d = 0.061(SA) + 2.89 \tag{2.13}$$

Where: $K_d = Distribution\ Coefficient\ \left[\frac{mL}{g}\right]$

$$SA = Average\ Surface\ Area\ of\ Soil\ Particles\ \left[\frac{m^2}{g}\right]$$

Once the relationship of a contaminant's sorption onto a material is known, it becomes convenient to express the retardation factor of the contaminant in terms of the properties of the aquifer material. When the sorption isotherm is linear, the retardation factor can be expressed by equation 2.14 below.

$$R_f = 1 + \frac{\rho_b K_d}{n} \tag{2.14}$$

Where: $R_f = Retardation\ Factor\ [Unitless]$

$\rho_b = Bulk\ Dry\ Density\ of\ Soil\ \left[\frac{M}{L^3}\right]$

$K_d = Partitioning\ Coefficient\ \left[\frac{L^3}{M}\right]$

$n = Porosity\ \left[\frac{L^3}{L^3}\right]$

This equation allows us to determine the relative movement of groundwater and contaminants through an aquifer based on two soil parameters and the partitioning coefficient of the contaminant (Dunnivant & Anders, 2006). Alternatively, if the relative velocities of the contaminant and groundwater movement are known, equation 2.14 can be used to estimate the partitioning coefficient for the contaminant.

Sorption of inorganic ions mainly occurs through cation exchange onto the surfaces of the clay minerals, zeolites, or metallic oxides and hydroxides (Alvarez & Illman, 2006). Clay mineral surfaces have a net negative charge, which is typically neutralized by native cations in the

groundwater such as hydrogen, sodium, and potassium adhering to the surface. When polyvalent metallic cations are introduced into solution, their higher charge density makes them more strongly attracted to the negative mineral surfaces, and causes them to displace the native ions of weaker attraction (Dunnivant & Anders, 2006). The quantity of exchangeable cations that a mineral particle can retain on its surface is known as its cation exchange capacity (CEC) and is expressed as a number of exchangeable charges per unit mass of dry soil. Since the sorption of metal cations onto an aquifer material depends of the availability of exchange sites, the sorption capacity of an aquifer is finite for most inorganic, non-biodegradable contaminants (Todd & Mays, 2005).

When multiple metal cations of the same valence are found in solution, the ions compete for adsorption sites. Sorption of a metal will be greater for those which have a higher affinity for the soil surface. The affinity of a soil surface for a specific metal cation is directly and inversely related to it the ion's atomic radius (Dunnivant & Anders, 2006). Of two metal ions with the same valence, the one with a smaller atomic radius will have a higher affinity for the soil. Overall, sorption of any aqueous cation will increase with an increase in pH of the solution (Dunnivant & Anders, 2006). This is because a reduction in the number of aqueous hydrogen ions will reduce the competition for adsorption sites with the metal cations. At high pH values, the mineral surfaces are deprotonated, and more adsorption sites are free for the metal ions to attach without having to exchange with another ion. In addition, as seen in Figure 2.5, many metal ions tend to be least soluble in solutions at high pH values (10-12). The decrease in solubility of the metal ions tends to increase precipitation of the metals onto the surface of the soil particles.

2.8 Flux Based Site Management Principles

When evaluating contaminated sites, the goal is to first determine the risk that the contaminant poses to downstream receptors, and then to initiate a remedial strategy in an effort to reduce that risk. It is important to investigate the contaminant source and groundwater concentrations as well as the speed and direction in which the plume is advancing. Typical site management strategies look to compare the measured contaminant concentrations in collected groundwater samples to a set of water quality standards in order to determine if the site poses a risk to potential receptors. Although this method can be used to identify if the site is a risk or not, it cannot be used to quantify the risk that the site poses in order to compare it to other sites (Verreydt et al., 2012). A flux based management strategy is a more relevant way to manage contaminated sites than the typical site management strategy described above. Instead of simply comparing collected samples to a set of standards, a flux based management strategy provides an alternative method of characterizing contaminated sites based on their contaminant mass flux measurements or estimates (Einarson & Mackay, 2001).

Mass flux is the measure of a substance's mass transport rate, which is expressed as the mass of a contaminant being transported through a cross sectional area of an aquifer over a given time (Goltz, et al., 2009). Mass flux measurements indicate the strength and mobility of a contaminant plume in a quantifiable way, which improves the evaluation of the risk that the plume poses to downstream receptors. Quantifying a plume's strength based on mass flux measurements has many advantages including the ability to prioritize contaminated sites or

multiple contaminant sources on one site in the order of their overall risk to humans and the environment (Goltz et al., 2007).

In addition to being able to prioritize contaminated sites for employing remedial efforts, determining mass flux values at a site also provides valuable information required to choose the most appropriate remedial process to employ, and to optimize the design of such a process (Annable, et al., 2005). Mass flux data are also useful for determining the source terms to be used in a contaminant transport model of the site, predicting the site's natural attenuation rates, and confirming or assessing the performance of a previously employed remediation effort (Goltz, et al., 2009).

2.8.1 Monitoring Well Control Planes

A monitoring well control plane is a group of groundwater monitoring wells that are installed across a contaminant plume, perpendicular to the direction of groundwater flow. Multiple planes can be installed in numerous locations along the plume length. The first plane is typically located slightly down-gradient of the contaminant source, and the others are located further down-gradient at consistent intervals in order to cover the entire length of the plume. Control planes are used to quantify the mass flux of contaminants that cross them, and identify any changes in mass flux along the length of the plume. Either single or multiple level monitoring wells can be installed, but it is important to have sampling points across the entire width and depth of the plume's cross section in order to ensure that accurate flux values can be calculated (Goltz et al., 2007). Sampling points should be spread wide enough across the plume to yield non-detect samples at the plume edges and ensure that the entire plume cross section is

passing through the plane. A control plane with a sparse number of sampling points can be extremely unreliable, and can yield mass flux estimates that can be misleading. It is therefore desired to have as many sampling points as possible; however, the number of points typically installed on a site is usually limited by the geologic conditions of the site and/or by the cost of monitoring well installation (Bockelmann et al., 2003).

2.8.2 Mass Flux Calculations

The accuracy of a mass flux calculation for a control plane is dependent on both the number and location of the sampling points in the plane, as well as their ability to accurately represent the actual distribution of contaminant concentrations across the plane. In order to calculate mass flux across a control plane, groundwater samples must first be collected from each monitoring point, and the contaminant concentrations of each sample determined. The concentration measured at each sampling point is then designated to a portion of the control planes cross sectional area which is assumed to be represented by that concentration. This representative area typically extends half way to the adjacent sampling points in all directions of the plane (Bockelmann et al., 2003). The mass discharge rate for each sample location can then be calculated and summed to obtain a total mass discharge across the control plane, as expressed in equation 2.15 below.

$$M_d = \sum_{i=1}^{i=n} C_i q_i A_i \tag{2.15}$$

Where: $n = Total\ Number\ of\ Sample\ Locations\ in\ the\ Plane$

$M_d = Total\ Mass\ Discharge\ Across\ the\ Plane\ \left[\frac{M}{T}\right]$

$$C_i = Concentration\ at\ Sample\ Location\ i\ \left[\frac{M}{L^3}\right]$$

$$q_i = Specific\ Discharge\ at\ Sample\ Location\ i\ \left[\frac{L}{T}\right]$$

$$A_i = Cross\ Sectional\ Area\ Associated\ with\ Sample\ Location\ i\ [L^2]$$

2.8.3 Assessment of Attenuation Rates From Mass Flux Measurements

Mass flux measurements estimate the mass of a contaminant moving through a cross section of the aquifer over a given time. Examining the differences in mass flux measurements between two adjacent transects can therefore give an insight into how the contaminant is reacting or interacting with the aquifer material in that area. A quantifiable decrease in measured mass flux values between two adjacent transects can therefore be used to determine a site's natural attenuation rates for the contaminant being measured (Einarson & Mackay, 2001). Additionally, examination of how the mass flux value of a contaminant at a given transect changes from one sampling period to the next can provide useful information about the effectiveness of a remediation effort.

Bockelmann et al. (2003) demonstrated the application of mass flux measurements in determining attenuation rate constants for sites with a limited monitoring network. The attenuation rate constants determined using the plume centerline point data were in general agreement with the rates determined using more detailed calculations. Attenuation rates can therefore be fairly accurately determined from scarce point data, provided that tracer test data or a groundwater flow model can reliably outline the plume centerline (Bockelmann et al., 2003). The attenuation rate constants that are determined by the use of mass flux measurements cannot distinguish the specific processes which are causing the attenuation of

the contaminant. Rather, the estimated attenuation rates are an expression of the collaborative effect of all processes which reduce the contaminant concentration measured in solution except dispersion and reversible sorption, (Stenback et al., 2004).

2.9 VISUAL MODFLOW

Visual MODFLOW is a computer modelling software marketed by Schlumberger Water Services, which can be used to perform three dimensional groundwater flow and contaminant transport simulations. Visual MODFLOW integrates multiple numerical engines including a three dimensional finite difference groundwater flow engine, a particle tracking engine, a contaminant transport engine, and statistical analysis software that can assist in model calibration by parameter estimation (Schlumberger Water Services, 2011). Visual MODFLOW provides a graphical user interface where the user can build a three dimensional site model and input all necessary hydrogeologic, transport, and fate parameters. The various parameters which are specified by the user in the model are then automatically translated into the input files which are required to run the computational engines (Alvarez & Illman, 2006).

The software's graphical user interface allows users to build three dimensional models of their site, and then simulate the flow of groundwater and the transport of contaminants through the site based on their specified parameters and boundary conditions. This interface provides simplicity, flexibility and realism to the simulations that are being performed. The model as well as the simulation results can then be viewed in both two dimensional cross section and plan view sections, or generated in a three dimensional display (Schlumberger Water Services, 2011).

2.9.1 Constructing a Model

To construct a three dimensional conceptual site model, the user is first required to input a base map image, define the model's extents and subsurface thickness, then divide the model into a grid of elements by defining a mesh size and a number of layers. This is done because the finite difference engine that calculates groundwater flow requires the model to be divided into a number of discrete rectangular elements, called cells (Mays, 2012). Once the dimensions of the model and cells are defined, the site's geologic information can be input into the individual cells themselves. Differences in the hydrogeological parameters of the various soil layers and strata that exist across the site are accounted for in the model through the creation of zones (Schlumberger Water Services, 2011). Each zone can be assigned a different value for various geotechnical parameters, and therefore the cells within a zone represent an area of the subsurface which has a relatively consistent soil type. Many different soil types can therefore be represented, with no limit to the number of zones which can be created (Schlumberger Water Services, 2011). By assigning each cell in the model to a zone, any spatial changes in the site's subsurface properties can be accurately represented. Subsurface information can come from any number or combination of various geophysical exploration techniques. The hydrogeological parameters that can be input into each individual cell are hydraulic conductivity, storage, initial head, density, initial concentration, and dispersion (Schlumberger Water Services, 2011).

2.9.2 GROUNDWATER FLOW MODELLING

Visual MODFLOW contains a number of different three dimensional finite difference engines that can be chosen to simulate the flow of groundwater through the model. These engines use numerical methods to find solutions to the partial differential equation that governs three dimensional groundwater flow, shown as Equation 2.16 below (Harbraugh, 2005). This equation is valid for three dimensional transient flow through a three dimensional anisotropic and heterogeneous medium that could be confined, unconfined, or a combination of both (Mays, 2012).

$$\frac{\partial}{\partial x}\left(K_{xx}\frac{\partial h}{\partial x}\right)+\frac{\partial}{\partial y}\left(K_{yy}\frac{\partial h}{\partial y}\right)+\frac{\partial}{\partial z}\left(K_{zz}\frac{\partial h}{\partial z}\right)-W=S_s\frac{\partial h}{\partial t} \qquad (2.16)$$

Where: $K = Hydraulic\ Conductivity\ \left[\frac{L}{T}\right]$

$h = Hydraulic\ Head\ [L]$

$W = Volumetric\ Flux\ Per\ Unit\ Volume\ (Sources\ and\ Sinks)\ \left[\frac{1}{T}\right]$

$S_s = Specific\ Storage\ \left[\frac{1}{L}\right]$

$t = Time\ [T]$

Combined with user specified flow and/or head boundary conditions at the model's edges, this equation can represent a complete groundwater flow system. The boundary conditions which provide the source of water movement that can be defined in Visual MODFLOW are lines of constant head or constant flux. Head dependant flux conditions can also be specified, which provide a varying flux into the model dependant on the head values found in the model's

boundary cells (Mays, 2012). If no boundary conditions are specified at a model's edge, the edge is defaulted as a no-flow boundary. No-flow boundaries do not allow the movement of water across the boundary, and act as if the edge is impermeable (Schlumberger Water Services, 2011). No-flow boundaries are therefore most appropriate for areas where the groundwater flow direction is parallel to the model's edge, and will not contribute groundwater flow into the model domain. External stresses that affect groundwater flow, such as initial head values, site recharge, evapotranspiration, pumping wells, drains, rivers, and lakes can also all be defined by the user (Schlumberger Water Services, 2011). The results produced by the flow engine are always in equilibrium with all boundary conditions provided by the user. Outputs from the groundwater simulation include hydraulic head values as well as groundwater flow rates and directions for all cells across the site.

2.9.3 Contaminant Transport Modelling

Visual MODFLOW also provides a selection of different numerical engines to choose from when simulating contaminant transport. Contaminant transport engines are separate from groundwater flow engines, and must be run after the groundwater flow simulation is complete. This is because the transport engine takes the distribution of head values produced by the MODFLOW engine, calculates the velocity distribution across the model cells, and uses it as an input file. In order to determine the transport of contaminants, the transport engine then uses numerical methods to find solutions to the governing differential equation that describes fate and transport of aqueous species in a three-dimensional transient groundwater flow system (Zheng & Wang, 1998).

$$\frac{\partial C_k}{\partial t} = \frac{\partial}{\partial x_i}\left(D_{ij}\frac{\partial C_k}{\partial x_j}\right) - \frac{\partial}{\partial x_i}(v_i C_k) + \frac{q_s}{n}C_k' + r_k \qquad (2.17)$$

Where: $k = 1,2,3 \ldots m$

$m = Total\ Number\ of\ Aqueous\ Species$

$C_k = Aqueous\ Phase\ Concentration\ of\ the\ k^{th}\ Species\ \left[\frac{M}{L^3}\right]$

$C_k' = Solid\ Phase\ Concentration\ of\ the\ k^{th}\ Species\ \left[\frac{M}{L^3}\right]$

$D_{ij} = Coefficient\ of\ hydrodynamic\ dispersion\ \left[\frac{L^2}{T}\right]$

$v_i = Seepage\ velocity\ \left[\frac{L}{T}\right]$

$q_s = Volumetric\ Flux\ of\ Water\ Per\ Unit\ Volume\ of\ Aquifer\ \left[\frac{1}{T}\right]$
$(Representing\ Sources\ and\ Sinks)$

$r_k = Reaction\ Rate\ \left[\frac{M}{L^3T}\right]$

$n = Porosity\ \left[\frac{L^3}{L^3}\right]$

Using different numerical engines to conduct groundwater and contaminant simulations means that Visual MODFLOW must solve the flow equation and transport equation independently. However, solving these equations separately and consecutively implies that the results of the transport engine have no effect on the results of the MODFLOW engine. Visual MODFLOW must therefore assume that the changes in the contaminant concentrations in the aquifer which are calculated by the transport engine have a negligible effect on the input parameters used by the MODFLOW engine such as the density of water, or the hydraulic conductivity and porosity of the soil (Alvarez & Illman, 2006).

2.9.4 Calibration and Sensitivity Analysis

Model calibration is done to ensure that the model being used for the simulations accurately represents the actual site conditions, and provides reasonable results. Calibration of the model is done by comparing calculated output values to the field measured data, and minimizing residuals for each data point. A residual is the numerical difference between the field measured value (observed value) and the model simulated value (calculated value).

Before contaminant transport is simulated, the site must first be properly modelled, and groundwater flow simulations must be adequately calibrated to ensure that the model accurately represents the actual flow of groundwater across the site. The accuracy of the model is determined by comparing the field measured groundwater elevation values collected from the groundwater monitoring wells to the total head values calculated by the model for the cell in the well's location. In order to determine the quality of fit, the residual value for each monitoring well is calculated. Calibration of the model is done by adjusting the model's inputs until the residuals are minimized, and the closest fit between the observed and calculated data sets is achieved. A trial and error approach is typically taken to systematically vary the model parameters until a good fit between the calculated and observed head values is obtained (Alvarez & Illman, 2006). In order to quantify the degree of calibration, Visual MODFLOW provides a calibration plot displaying a graph of the calculated versus observed values. Additionally, Visual MODFLOW also automatically calculates and displays maximum, minimum, mean, and absolute mean residual values, as well as standard error, root mean squared (RMS), normalized RMS, and correlation coefficient values for the data. These values are useful in order to quantitatively measure and compare the quality of fit of various simulations.

In order to aid with the calibration of a model, Visual MODFLOW also contains a parameter estimation code known as WINPEST. WINPEST can be used to further improve the calibration of the model after adjusting parameters by a trial and error approach is exhausted. WINPEST allows the user to indicate which of the input parameters they would like to make variable, and at which observation points they would like to minimize the residuals. The software will then minimize the root mean square error estimate value of the specified observation points by varying the input parameters specified as variables. This is done by running the simulation in multiple iterations, varying the inputs each time until the residuals of the specified observation points are minimized.

Sensitivity analysis is performed by running multiple simulations while varying a single model input parameter within an acceptable range, and comparing the model output results to known conditions (Mays, 2012). Performing sensitivity analysis on different model inputs will demonstrate the model's sensitivity to changes or uncertainty in the various input parameters. Sensitivity analysis should be performed on inputs such as dispersion and partitioning coefficients as well as chemical, biological, or nuclear degradation rates. Special care should be taken while performing a sensitivity analysis on dispersion coefficients, which should be varied over a much more broad range than most parameters (up to 2-4 orders of magnitude) due to their high difficulty of estimation (Dunnivant & Anders, 2006).

2.9.5 Particle Tracking

Particle tracking is used to determine the flow path that an imaginary particle would take, from a specified starting location, through the model over a given time. The particle tracking engine

used by Visual MODFLOW is called MODPATH, which is a post-processor to the MODFLOW engine. MODPATH takes the head distribution output from the MODFLOW engine and uses it to calculate the velocity distribution and determine the path that a particle would take from the user specified start location and trace it down gradient (Todd & Mays, 2005). Tracking a particle's path from a specific contaminant source location can help to determine expected plume centerlines, or determine if the contaminants can be expected to be captured by a pumping well, or come in contact with an alternative remedial strategy. It can also be a useful tool to examine the effects of boundary conditions, or simply to better visualize the flow paths that take place and detect any errors in the flow model (Todd & Mays, 2005).

2.10 Remedial Activities for Releases From Mine Tailings

Contaminant releases from mine tailings are typically characterized by low pH values and high concentrations of dissolved heavy metals. Remedial activities for mine sites therefore focus on both removing heavy metals and moderating the pH of the downstream groundwater. Slow leakage from mine tailings into nearby groundwater systems can be extremely pervasive, and continue to cause an environmental issue for an extended period of time, well after the mine has been shut down (Blowes et al., 2003). The longevity as well as the effectiveness of a remedial process should therefore both be taken into consideration when treating releases from mine wastes.

The most commonly used techniques for the remediation of contaminated groundwater are pump and treat, in-situ flushing, permeable reactive barriers, in-situ air sparging, monitored natural attenuation, and bioremediation (Sharma & Reddy, 2004).

2.10.1 PUMPING WELLS

Pump and treat remediation is the most commonly used technique to treat contaminated groundwater. As shown in Figure 2.7 (Sharma & Reddy, 2004), a pump and treat system utilizes pumping wells to remove the contaminated groundwater from the aquifer and pump it into a reactor or treatment process which can remove the contaminants of concern. After treatment, the cleaned water is then pumped back into the aquifer through recharge wells, discharged to a surface water body, or sent to a sewage treatment plant (Sharma & Reddy, 2004). At a mine site, pumping wells may also be used to simply remove the contaminated groundwater from the aquifer and pump it back into the TMA without treatment. This would act as a waste containment strategy rather than a treatment strategy. Depending on the rate of contaminant transport, the size of the contaminant plume, and the pumping rate of the wells, a pump and treat system can be used to either prevent the spread of the contaminant, or even reduce the size of existing plume (Sharma & Reddy, 2004). Pumping wells can be used at mine sites as an interim method to prevent further contaminant transport down gradient of the tailings management area, but are likely not a long term treatment solution for a site where the contaminant source is very large or pervasive.

Caution should be taken when determining the number and location of pumping wells to be installed, as well as the pumping rate to be used. The overall goal of a pumping well system is to capture all contaminated water in the plume while simultaneously not capturing excessive amounts of uncontaminated water (Sharma & Reddy, 2004). Installing too few wells, or using too low of a pumping rate will provide the opportunity for the contaminant to escape capture by the pumping wells, and allow the contaminant to continue to spread. Installing too many

wells, or using too high of a pumping rate will raise installation and operating costs above what is necessary to capture the contaminant.

Using a pumping rate which is too high will not only consume additional energy to run the pump, but also result in a large quantity of uncontaminated water being captured and sent through the treatment system. Additionally, a higher pumping rate will create a larger cone of depression in the groundwater table, which could increase the hydraulic gradient away from the TMA and potentially increase future contaminant movement.

The drawdown of the groundwater table and cone of depression that are formed due to the installation of a pumping well are show in Figure 2.8 (HDR Engineering Inc., 2001). The size of the influence zone of a pumping well is dependent on a number of factors including the hydraulic conductivity and thickness of the aquifer material, the pumping rate of the well, and the depth and size of the well screen (Powers et al., 2007). Empirical equations which are used to predict the radius of the influence zone of a pumping well have been published in literature. One equation estimates the radius of the influence zone using the drawdown in the pumping well and the hydraulic conductivity of the surrounding soil, and is shown in equation 2.18 below (Coduto, 1999).

$$r_0 = 300\ (h_0 - h_w)\ \sqrt{k} \tag{2.18}$$

Where: $r_0 = Radius\ of\ the\ Influence\ Zone\ [L]$

$h_0 = Total\ Head\ in\ AquiferBefore\ Pumping\ [L]$

$h_w = Total\ Head\ Inside\ Well\ During\ Pumping\ [L]$

$$k = Hydraulic\ Conductivity\ of\ Aquifer\ \left[\frac{cm}{s}\right]$$

$r_0,\ h_0,$ and h_w must be in the same units, and k must me in cm/s.

One major disadvantage of a pump and treat system is the large operating and maintenance costs that are associated with treating a large amount of contaminated water over a long period of time (Sharma & Reddy, 2004). Additionally, a pump and treat system can experience ineffectiveness to complete treatment due to contaminant rebound.

2.10.2 Permeable Reactive Barrier

A permeable reactive barrier (PRB) is a site remediation technique that aims to reduce the concentrations of a mobile groundwater plume by degrading or immobilizing the contaminants. As their name suggests, permeable reactive barriers are flow through barrier systems composed of a porous reactive medium, which causes the removal or destruction of specific contaminants by initiating reduction, precipitation, or adsorption reactions (Pichtel, 2007). The reactions that are initiated in a PRB are very similar to those utilized in the porous bed reactors which are used to remove the dissolved contaminants during a pump and treat remediation process; however a PRB has significant advantages (Suthersan, 1997).

Figure 2.9 shows a typical layout of a PRB on a contaminated site. As shown in this figure, PRBs are installed by excavating a trench perpendicular to the direction of groundwater flow, and slightly down gradient of the contaminant plume or contaminant source location and then inserting a reactive medium (Sharma & Reddy, 2004). The barrier is situated in such a manner that as the contaminant plume advances through the aquifer, it is forced to flow through the

PRB as well. As the contaminant comes into contact with the reactive media in the PRB, reactions that either decompose or prevent the movement of the contaminant are initiated. If the contaminant plume is very wide or deep, it may not be economical to install a PRB across the entire plume width. In this case impermeable barriers such as slurry walls, grout curtains or sheet piling can be installed to funnel the contaminated water toward one or more downstream PRBs, known as reactive gates (Pichtel, 2007). Funneling walls can also be used when an aquifer material is very heterogeneous, or when contaminant distributions are non-uniform, in order to direct the contaminant towards locations which are optimal for PRB installation (Sharma & Reddy, 2004).

Since large variations in contaminant types and physical site configurations can be encountered at contaminated sites, a large amount of site characterization must be done to select the most efficient PRB layout and reactive medium for the site in question. The most important characteristics to be evaluated prior to PRB design include site hydrogeology and geochemistry, contaminant types and concentrations, and microbiological properties of the site (Pichtel, 2007). Evaluating these parameters is important to better predict the behaviour of the barrier and the reactions that can be facilitated, as well as aid in the selection of the porous barrier medium to be installed. Depending on the reactive medium which is chosen, PRBs can be used to remediate a large number of both organic and inorganic contaminants, or be tailored to target a specific contaminant of concern (Sharma & Reddy, 2004).

The reactive medium which is chosen is mainly dependant on the contaminant which is being removed, and the reaction which is used to remove it. Inorganic contaminants which are

usually found at metal mine sites will typically take part in redox reactions, which can be used to precipitate many of the contaminants as carbonates, sulfides or hydroxides (Sharma & Reddy, 2004). These precipitation reactions can be exploited by a PRB to easily remove dissolved metals from the groundwater. For mine sites where tailings leachate has contaminated the groundwater with elevated concentrations of heavy metals, limestone is the most commonly used reactive medium for remedial PRBs (Morrison et al., 2002). However, not all contaminants will precipitate, or can be treated with a single reactive medium. Multiple reactive media are sometimes required, and can also be placed sequentially in a PRB one behind another in order to remove multiple types of contaminants via individual reactions (Sharma & Reddy, 2004).

One major advantage of a PRB is that there is no pumping or operational cost required to maintain flow through the treatment system. The PRB can be buried and left to passively treat the groundwater with only minimal monitoring efforts being required. Provided that the reactive medium in the barrier is depleted sufficiently slowly during the treatment reactions, the barrier can be left to work effectively and unimpeded for decades (Sharma & Reddy, 2004). A drawback to the PRB system is the potential for a decrease in the reactivity or hydraulic conductivity of the barrier's reactive medium over time. Additionally, digging a trench down-gradient of a known contaminant source poses the risk of the large cost that would arise if contaminated soil is accidently excavated during the installation of the barrier (Suthersan, 1997). These drawbacks, however, can be mitigated with thorough site investigation and experimentation which can reduce the risk and uncertainty during the design process.

2.11 SUMMARIES OF RELEVANT CASE STUDIES

The following case studies provide insight into cases which are similar to the Northern Ontario Mine site, where computer modelling was used to investigate the groundwater flow and contaminant transport at a site where inorganic contaminants have been detected in the groundwater aquifer. A summary of the work that has been done by the researchers to construct the groundwater flow and contaminant transport models, as well as the conclusions that were drawn from the model simulations are outlined.

2.11.1 CASE STUDY 1 (ARTIIMO ET AL., 2004)

Hitura nickel mine in Finland is located adjacent to a classified groundwater aquifer, which is protected because it provides potable drinking water to a local community. Once elevated concentrations of sulphate, chloride, and nickel began being detected in the aquifer as a result of tailings derived water, it became necessary to find and seal the site of the leak. This was accomplished through thorough site investigation, and groundwater flow modelling.

Although historical soil maps and descriptions were used to obtain some knowledge of the subsurface, in order to properly characterize the aquifer in the area of interest, extensive field investigations were also conducted. Field investigations included the use of gravimetric measurements, seismic soundings, and ground penetrating radar soundings as well as the collection of soil samples from 20 rotary drill holes, and 44 test pits on all sides of the TMA to observe any changes in the subsurface stratigraphy. The investigations were able to determine the variations and extent of various geological units located beneath the site.

The geological information obtained from the various site characterizations were input into a three dimensional geological modelling software named EarthVision. A three dimensional model of the site's subsurface geology was created, and the soil was divided into five geological units. The five units were bedrock, till, silt/clay, interlobate esker, and littoral sand. The geological model extents were 3km wide and 3km long, the domain of the model was divided into a grid of 20m x 20m cells, and the depth was divided into 5m thick layers. Figure 2.10 displays a view of the ground surface from the three dimensional geologic model. Due to the geological complexity of the subsurface, it was determined that the site could not be adequately represented by a two dimensional, or single layered groundwater flow model.

The information provided by the geological model was then used to create a three dimensional numerical groundwater flow model, which used a MODFLOW code. The groundwater model originally had the same extents as the geological model, but was later extended to 4km wide and 4km long. The groundwater flow model maintained the 20m x 20m grid size, and was given two layers. The vertical and the horizontal changes in the site's geological units were represented through the creation of zones which allowed the soil properties to be varied in different areas of the model. The boundaries of the zones coincide with the boundaries of the geological units, which were obtained from the geological model. The input parameters required for the zones of the groundwater flow model, such as hydraulic conductivity, recharge, and effective porosity were determined through a combination of field investigations and collected literature values. Effective porosity values were determined to range between 0.08 and 0.25 for different soil types on the site. Recharge rates in most areas of the site were

estimated to vary between 100-253mm/yr, however, rates as low as 16mm/yr were estimated to be representative of low permeability regions.

The site groundwater flow pattern was determined by measuring the water levels at 176 observation points across the site, which included wells and surface waters. Seasonal changes in hydraulic head values observed across the site were reported to be insignificant, and resulted in the use of a steady state condition for the groundwater flow simulations. The steady state flow model's boundary conditions were then determined from the site's hydraulic head distribution which was observed from the collected data. In the north and northeastern portion of the model, the dewatering of the mine site caused drawdown of the water table below the top of the relatively impermeable bedrock layer. To represent this drawdown, specified head boundaries with a total head value equivalent to the bedrock surface elevation were assigned to the region where the groundwater table and bedrock surfaces intersected. Inactive cells were then placed in the region where the observed groundwater table was below the bedrock surface. A specified head boundary was also assigned in the southwestern portion of the site, as determined from the observed head values. It is noted that the region where the cells of specified head are located is far enough from the main aquifer that the simulated boundary did not have a major impact on the area of concern in the model.

The groundwater flow model was calibrated using the calibration assistance code MODFLOWP, which adjusted the hydraulic conductivity values of the various zones in order to minimize the residual values. Figure 2.11 displays the simulated potentiometric surface of the Hitura mine calibrated groundwater flow model. A data set containing 110 observed values across the site

was used to calibrate the model, and the observed total head drop across the modelled area was approximately 30m. After final calibration of the groundwater flow model, the average residual value was -0.11m. This means that, on average, the simulated total head values in the model were 0.11m lower than the measured groundwater elevations collected from the 110 observation points at the site.

Contaminant transport modelling of the mine site was not attempted due to insufficient historical data pertaining to both the background contaminant concentrations as well as the evolution of the plume. Instead of contaminant transport modelling, the groundwater flow model was used to simulate the movement of imaginary particles through the aquifer using MODPATH. The groundwater flow and particle tracking simulations were used in an attempt to confirm the area where a flow connection between the TMA and the aquifer existed. This flow connection would allow the contaminated tailings derived waters to enter the protected aquifer, and be detected downstream.

As a result of this modelling project, the tailings embankment was exposed and reconstructed in the identified area of the flow connection, and the leak of tailings derived water was sealed. The groundwater flow model was also used to determine a new intake location to be used to draw potable water from the aquifer. The groundwater simulations also indicated that the new intake location could provide substantially higher intake rates than the previous location. Additionally, the groundwater flow model will be used to determine the effects that various mine closure procedures will have on the aquifer in the area.

Some complications in modelling the TMA were noted during the modelling process. The low permeability of the tailings embankments created a barrier to flow, and caused a steep hydraulic gradient to form along the edges of the TMA. Large variations in hydraulic conductivity values over relatively short distances in the TMA were the cause of model instability during the simulations. This instability was corrected by simplifying the model in the area of the TMA without significantly decreasing the quality of the simulation.

2.11.2 CASE STUDY 2 (MOLDOVAN ET AL., 2008)

Rabbit Lake In-pit Tailings Management Facility (RLITMF) is located in the Athabasca Basin of northern Saskatchewan, the source of a large portion of the earth's annual uranium production. Since the tailings from uranium mines often contain transuranic elements, the facilities that manage these tailings must be designed for a 10 000 year (10 ka) contaminant containment period. Another contaminant of concern in uranium mine tailings is arsenic, which typically comprises 2-3% by weight of the uranium ores. The objective of the study by Moldovan et al. (2008) was to assess the ability of the RLITMF to achieve the 10 ka containment period for arsenic contamination.

The RLITMF is formed inside a previously exhausted open-pit mine, which measured approximately 300m wide and 425m long at the surface. As the tailings were deposited in the pit, the pit walls and bottom were lined with a layer (5.6m to 6.7m thick) of high permeability coarse-grained rock followed by a sand filter layer (1m to 3m thick). This liner was placed between the pit walls and the tailings on all sides of the facility. The high hydraulic conductivity of the outer layer acts as a hydraulic trap, and allows the groundwater to easily flow around the

outside of the RLITMF, without having to pass through the tailings. This minimizes the hydraulic gradient and advective transport through the tailings, and allows the movement of contaminants in the tailings pore water to be controlled mainly by diffusion.

Characterization of the previously deposited tailings was done by coring using a sonic drill. Core samples, as well as Eh and pH measurements were collected at approximately 0.5m depth intervals. Pore fluid samples were obtained from the core samples using squeezing and centrifugation methods, and were analyzed to determine the concentrations of dissolved arsenic and other contaminants. Dried core samples were also analyzed to determine the elemental composition of the tailings solids at various depths.

The groundwater flow model was created in three dimensions using Visual MODFLOW. The edges of the modelled area were extended at least 50m on all sides of the RLITMF, and the overall extent of the model is approximately 530m wide by 570m long, and is divided into a 5m x 5m grid. Figure 2.12 displays a plan view of the RLITMF groundwater flow and contaminant transport model at the layer which corresponds to the surface of the tailings. The total depth of the model is 120m, and is divided into layers from 1.8m to 6.8m in thickness. Figure 2.13 displays a cross sectional view of the model. The thickness of the various model layers was determined based on the actual observed stratigraphy of the previously deposited tailings, as recorded during the core sampling. The sand and coarse rock layers which surround the tailings were simplified, and were each assigned a single cell thickness (5m) on all sides of the tailings in the model.

Specified head boundary conditions were applied to all cells along the upstream (west) and downstream (east) edges of the model, with a total head difference of 10m between them. It is noted that this head difference is inferred from the surface topography in the area, and is not based on any observed data collected from groundwater monitoring wells. Since the north and south boundaries of the model are parallel to the flow of groundwater, they were assigned no-flow conditions. These groundwater conditions were assumed to be constant, and steady state groundwater flow was simulated. The input parameters for the soil characteristics of the sand, coarse rock, and surrounding aquifer material for groundwater flow simulations were obtained from previously conducted site investigations.

Contaminant transport modelling was conducted using Visual MODFLOW's multi-species transport simulation code MT3D99, and the contaminant being modelled was total dissolved arsenic. Diffusion and sorption input parameters to be used in the model were determined by performing single-reservoir diffusion-cell tests on a sample of the tailings which was collected during coring. The measured results of the diffusion tests were analyzed using the numerical model POLLUTEv6 which provided estimates for bulk diffusion coefficient, effective porosity, and distribution coefficient. The results indicated that the coefficient of bulk diffusion for arsenic through the tailings is 4.5×10^{-10} m^2/s, the effective porosity of the tailings is 0.36, and the distribution coefficient for arsenic in the tailings is between 2-4 cm^3/g. For the tailings layers of the model, a distribution coefficient value of $2 cm^3/g$ was used to be conservative. Although a previous study had reported that a distribution coefficient of $2 cm^3/g$ was representative for arsenic adsorption onto the surrounding sand filter material, it was assumed

in the model that the arsenic didn't sorb on any material except the tailings (all other zones were assigned a distribution coefficient of 0 cm^3/g.

The source of the dissolved arsenic contamination was assigned to the zones which represented the various tailings layers. Each layer of tailings was assigned a source concentration equivalent to the dissolved arsenic concentration measured in the pore water of the coring sample. The initial concentrations input into the tailings cells were not held constant with time, but rather were allowed to decrease due to sorption and diffusion throughout the simulation time. Similarly, all other cells in the model were assigned an initial arsenic concentration of 0.001 mg/L, which was based on historical groundwater monitoring data in the surrounding aquifer material.

Each tailings layer of the model also needed to be assigned a value for the number of available sorption sites that remained on ferrihydrite crystals in the tailings. This value was estimated through a correlation of the amount of iron found in each tailings layer to the amount of cobalt in the same layer. The correlation is based on the assumption that dissolved arsenic adsorbs primarily onto the surfaces of ferrihydrite present in the mine tailings. Evidence for this assumption was provided when the analysis of cored samples indicated a strong negative correlation between the iron/arsenic ratio of the tailings solids, and the concentration of dissolved arsenic in the tailings pore water. It was also assumed that the maximum adsorption capacity for arsenic on ferrihydrite is 0.5 moles arsenic per mole of ferrihydrite. If the elemental composition of the tailings solids indicated a ratio of arsenic to ferrihydrite of less than 0.5, it was assumed that the ferrihydrite in the tailings had not yet reached its maximum a sorption

capacity, and further sorption of arsenic would occur on the tailings over time. The quantity of available sorption sites for each layer was taken as the difference between the maximum sorption capacity and the mass of arsenic which is currently sorbed. This was calculated three different times using a maximum sorption capacity of 0.5, 0.25, and 0 moles arsenic per mole ferrihydrite to create three simulation situations, named scenarios 1, 2, and 3, respectively. Scenario 1 represented the anticipated adsorption, scenario 2 represented a case where adsorption was reduced, and scenario 3 represented a case where no further adsorption of arsenic occurred on the tailings material.

The total simulation time for the contaminant transport model was 10 ka, with time steps of 100 years for the first 1000 years, followed by time steps of 1 ka afterwards. The three scenarios were simulated using the three different maximum sorption capacities for the tailings solids. Results of the simulations showed a steady reduction of the average arsenic concentration in the tailings due to the diffusion and sorption mechanisms. Zone budget analysis in Visual MODFLOW was used to calculate mass fluxes of arsenic from the source toward various parts of the model, and used to perform mass balance checks. At the beginning of each simulation, the overall mass of dissolved arsenic in the tailings pore fluid was 24,300 kg. After the 10 ka simulation time for scenarios 1 and 2, the total mass of dissolved arsenic remaining in the tailings fluid was only 10,100 kg and 10,200 kg respectively. At the same time, the mass of dissolved arsenic in the sand layer increased from 0 kg to only 102 kg for both scenarios, and the dissolved arsenic concentrations in the aquifer material did not rise above its initial condition of 0.001 mg/L. These two scenarios produced very similar results, and suggest

that approximately 99% of the dissolved arsenic in the tailings pore fluid is either adsorbed onto ferrihydrite, or remains dissolved within the tailings pore fluid after 10 ka.

In scenario 3, the total mass of dissolved arsenic in the tailings pore fluid was reduced from 24,300 kg at time zero, to 18,700 kg after 10 ka. Since there was no sorption being simulated in this case, the mass of arsenic must have been transported throughout the model. The mass of dissolved arsenic in the sand layer increased from 0 kg to 4,500 kg, and the dissolved arsenic concentrations in the aquifer material reached 1.05 mg/L. This simulation indicates that if no attenuation mechanism were to take place, approximately 23% of the total mass of dissolved arsenic will diffuse from the tailings within 10 ka. Approximately 80% of the diffused arsenic would remain in the sand filter, and the remaining 20% would reach the aquifer.

As a result of the project, the contaminant transport model of the RLITMF was also able to demonstrate the effect that adsorption will have on the transport of arsenic. If no attenuation were taking place, concentrations of dissolved arsenic should be expected to increase in the surrounding aquifer. However, even with very conservative estimates for sorption capacity of the tailings, the simulations indicate that the RLITMF should continue to be very effective as a long term containment solution for dissolved arsenic in the mine tailings.

Porous Material	Particle Size (mm)	Porosity (%)	Specific Yield (%)	Hydraulic Conductivity (cm/s)
Gravel, coarse	16.0-32.0	28	23	1.7E-01
Gravel, medium	8.0-16.0	32	24	3.1E-01
Gravel, fine	4.0-8.0	34	25	5.2E-01
Sand, coarse	0.5-1.0	39	27	5.2E-02
Sand, medium	0.25-0.5	39	28	1.4E-02
Sand, fine	0.125-0.25	43	23	2.9E-03
Silt	0.004-0.062	46	8	9.3E-05
Clay	<0.004	42	3	2.3E-07
Till, predominantly silt	Various	34	6	-
Till, predominantly sand	Various	31	16	5.7E-04
Till, predominantly gravel	Various	-	16	3.5E-02

- No Data Available

Table 2.1 Representative Hydrogeologic Parameters for Various Soil Types (Mays, 2012)

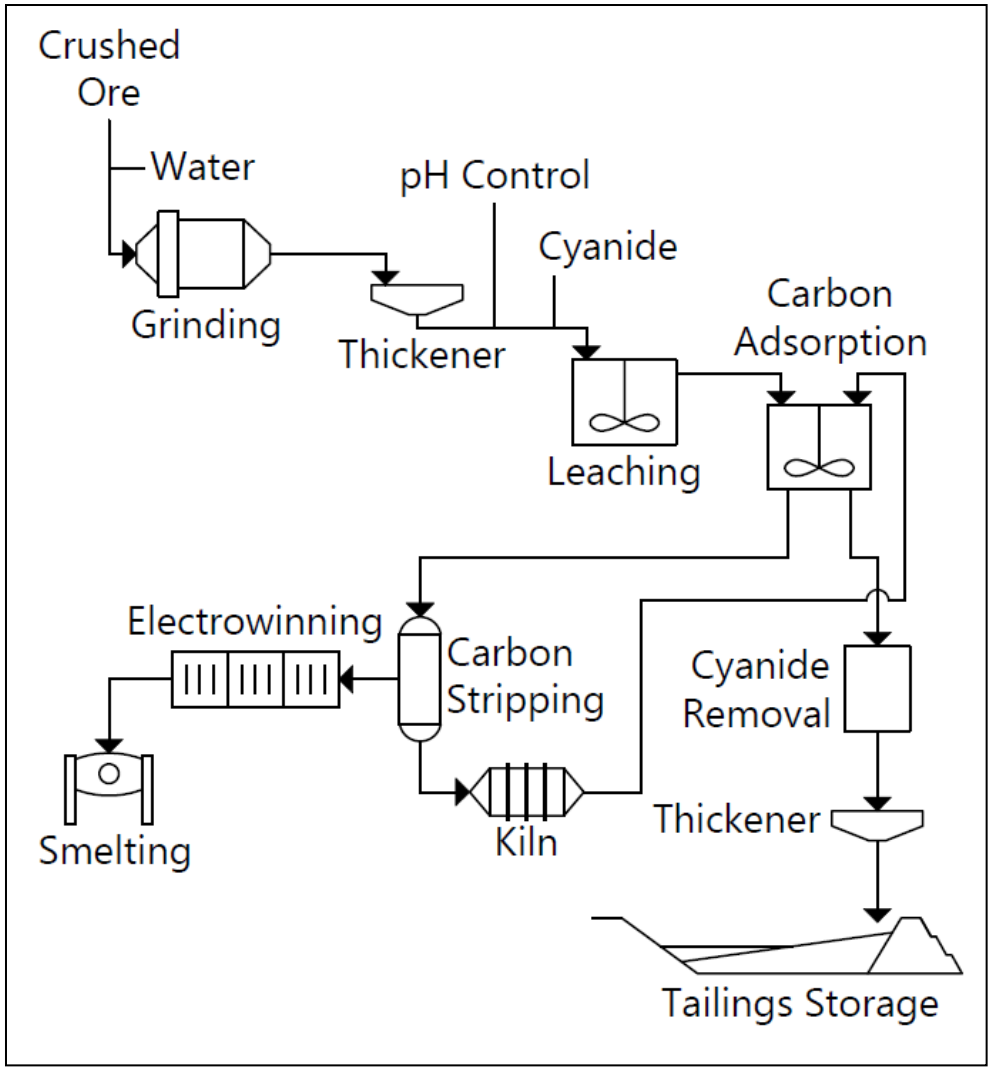

Figure 2.1 Gold Extraction Process, after (Spitz & Trudinger, 2009)

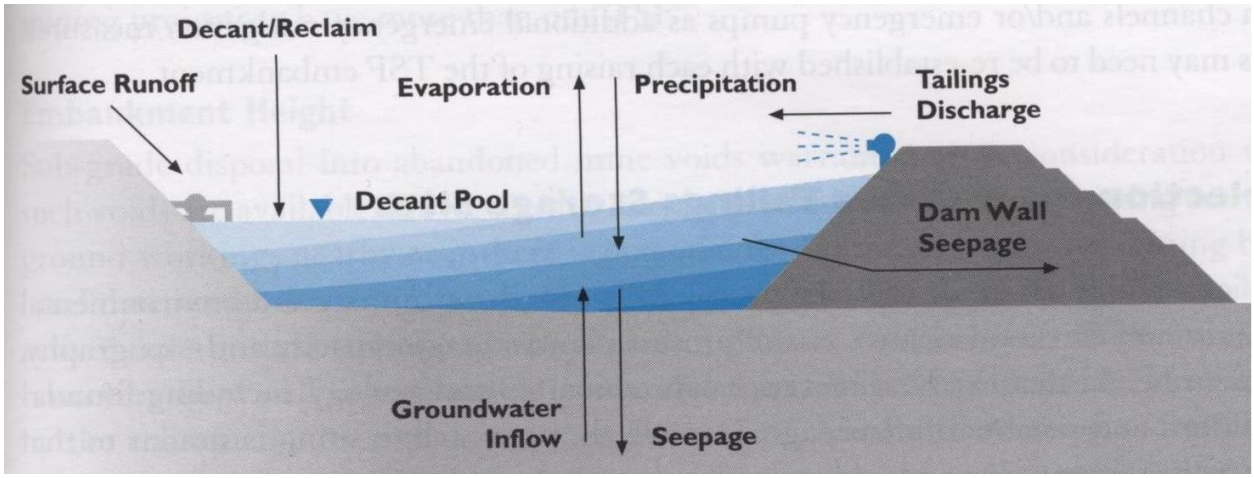

Figure 2.2 Typical Cross Section of a Tailings Management Area (Spitz & Trudinger, 2009)

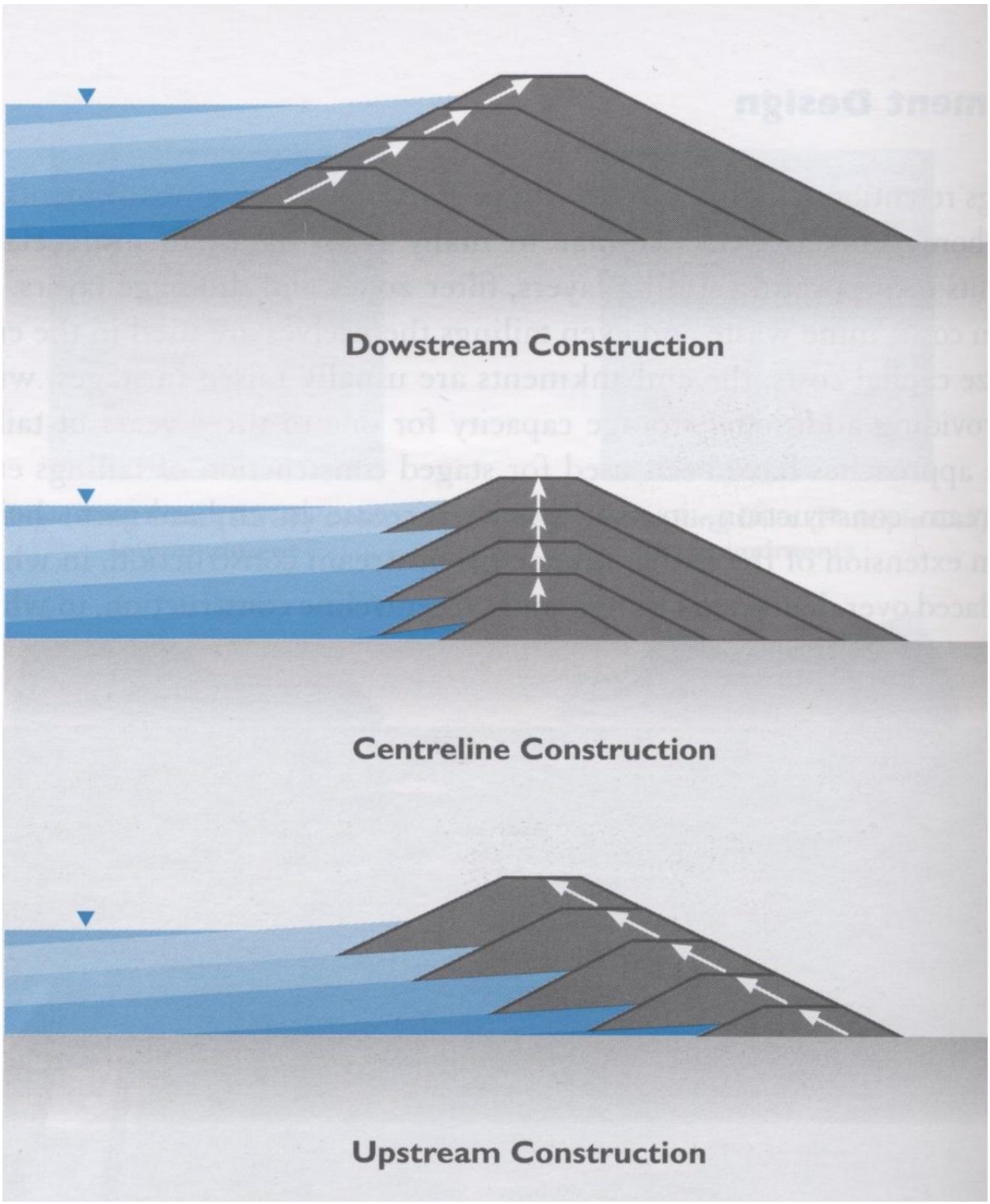

Figure 2.3 Tailings Dam Construction Methods (Spitz & Trudinger, 2009)

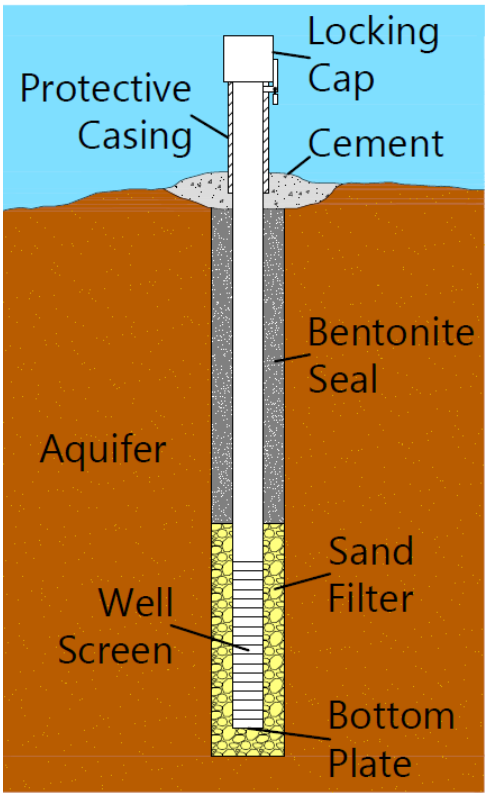

Figure 2.4 Typical Groundwater Monitoring Well, after (Todd & Mays, 2005)

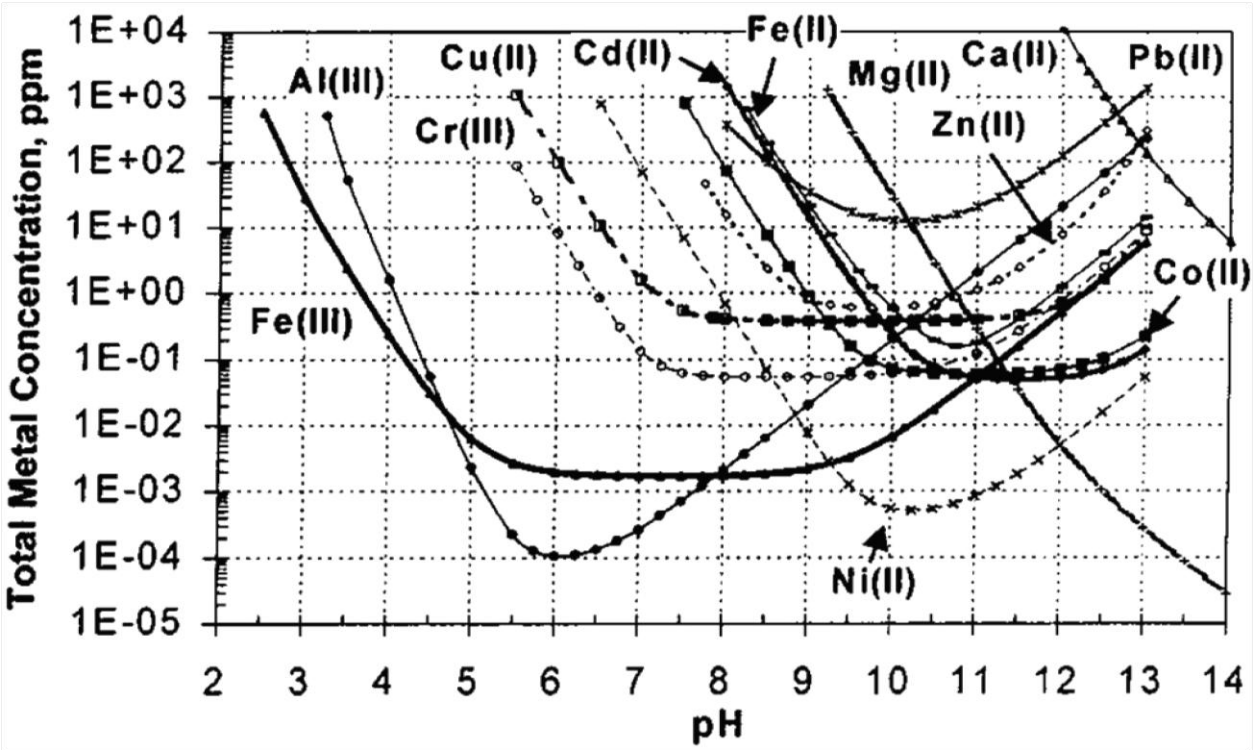

Figure 2.5 Solubility of Various Metal Hydroxides vs. pH (Dyer & Scrivner, 1998)

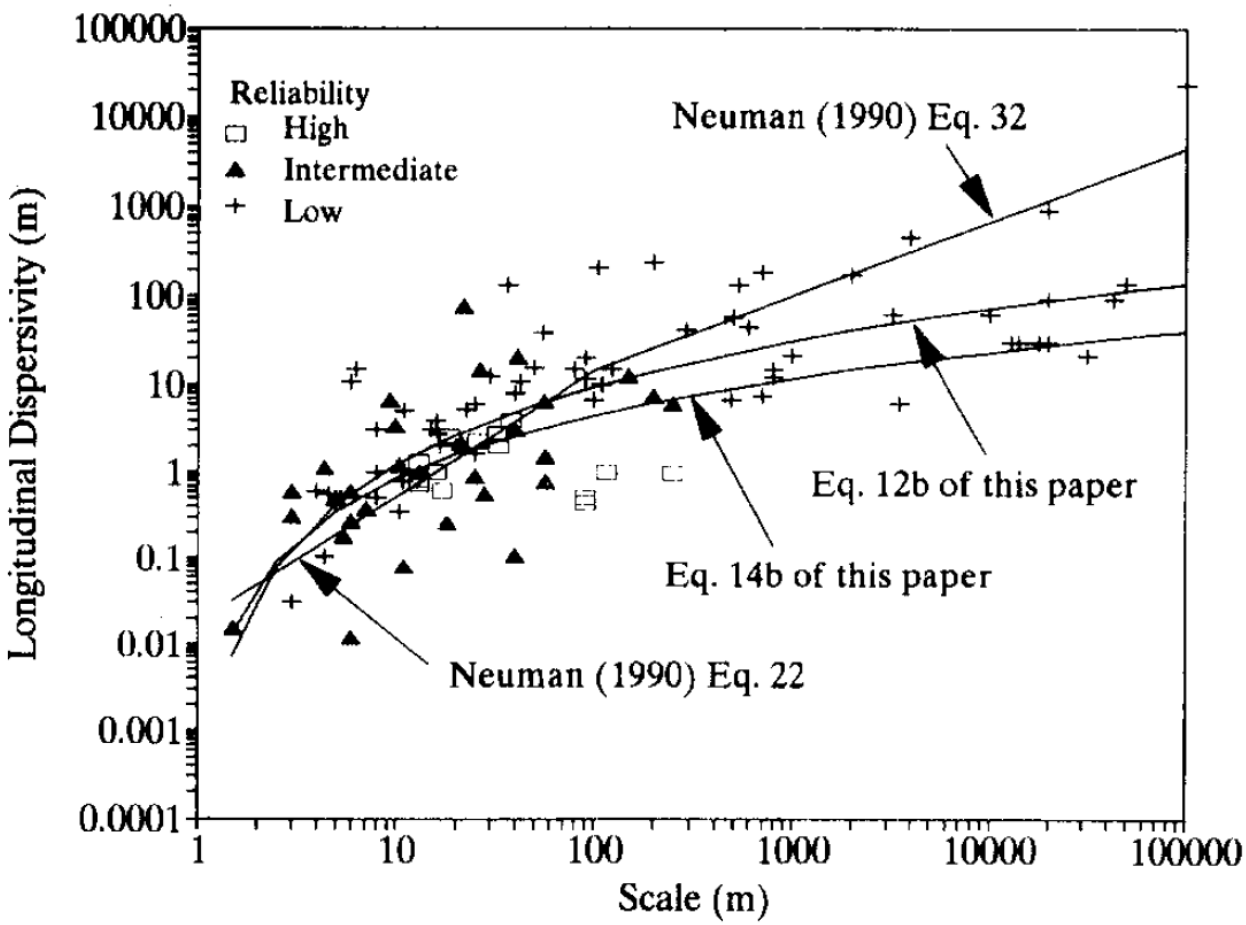

Figure 2.6 Longitudinal Dispersivity Versus Plume Length Plot (Xu & Eckstein, 1995)

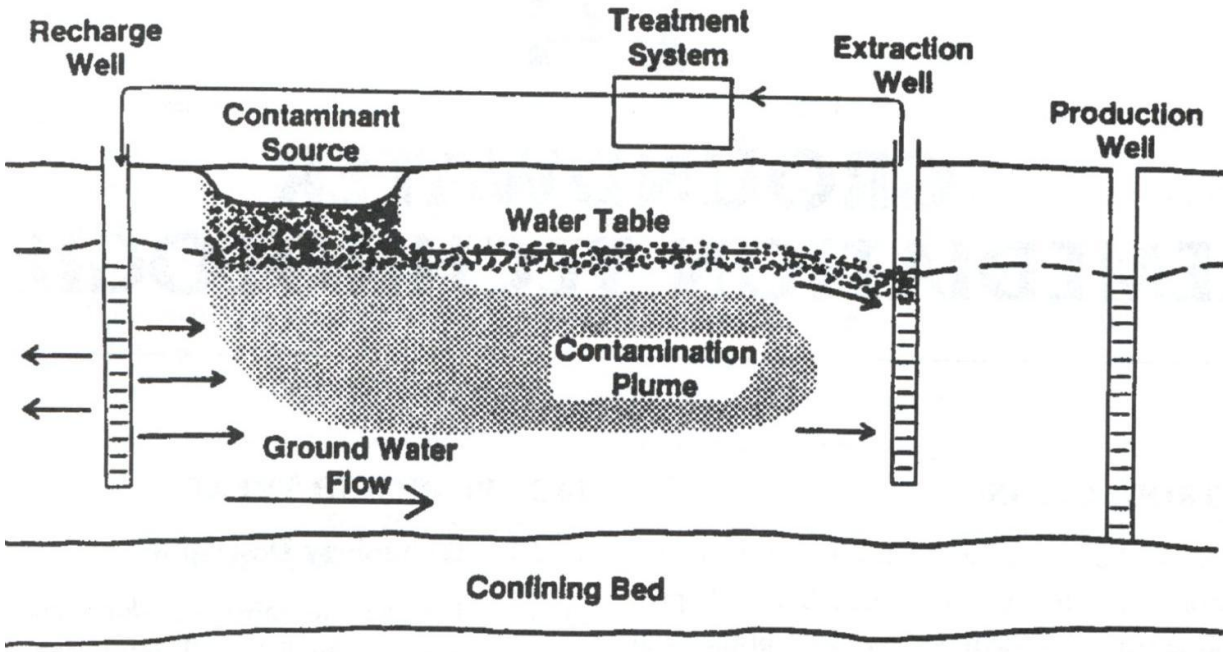

Figure 2.7 Typical Pump and Treat System (Sharma & Reddy, 2004)

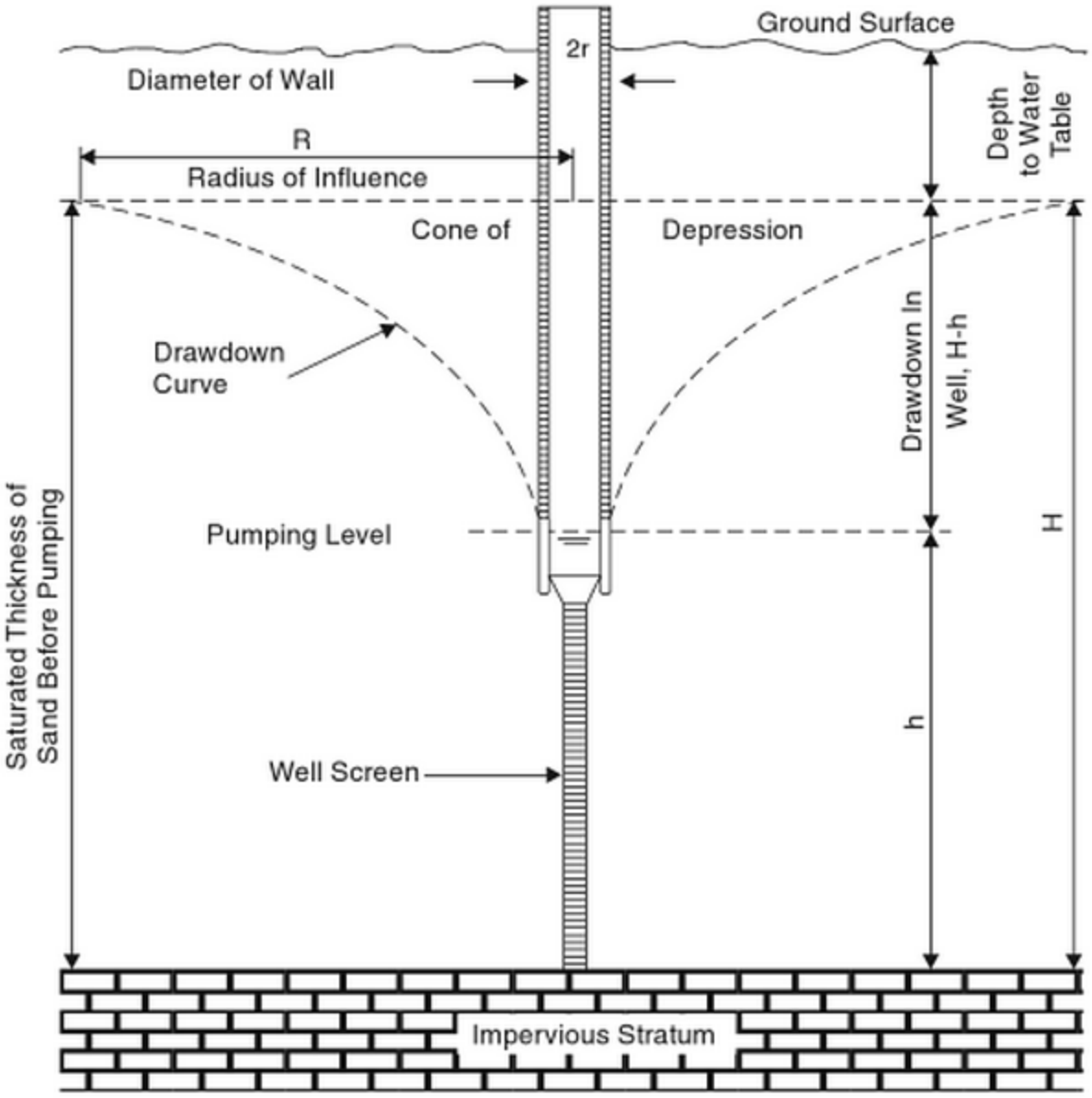

Figure 2.8 Pumping Well Influence Zone (HDR Engineering Inc., 2001)

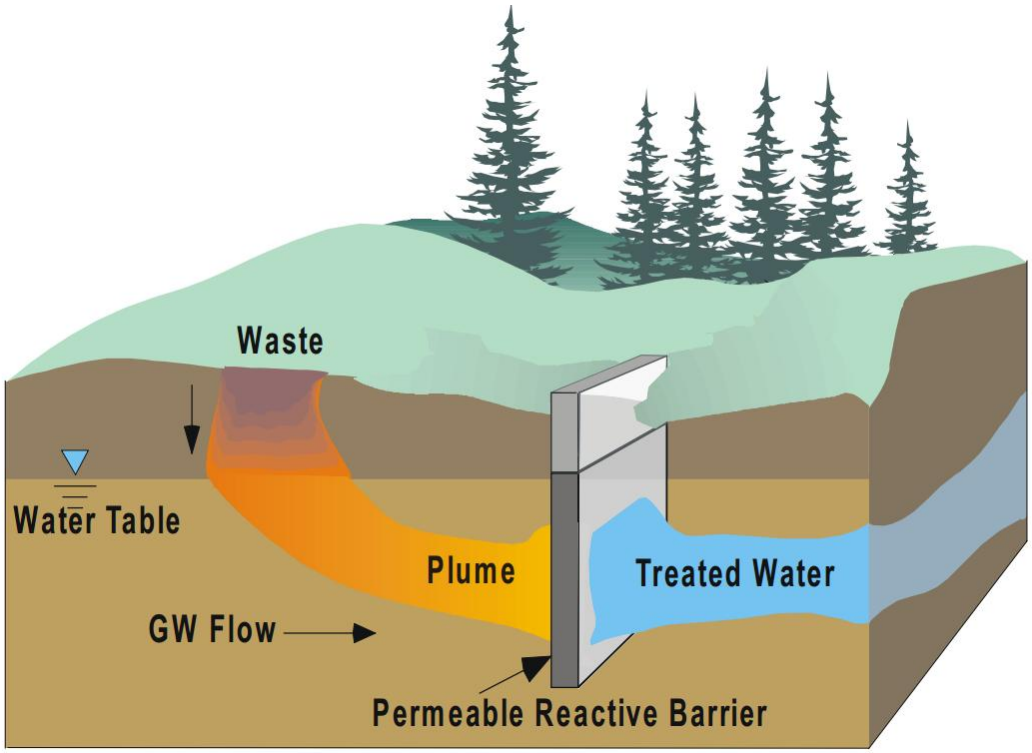

Figure 2.9 Typical Permeable Reactive Barrier (USEPA, 1998)

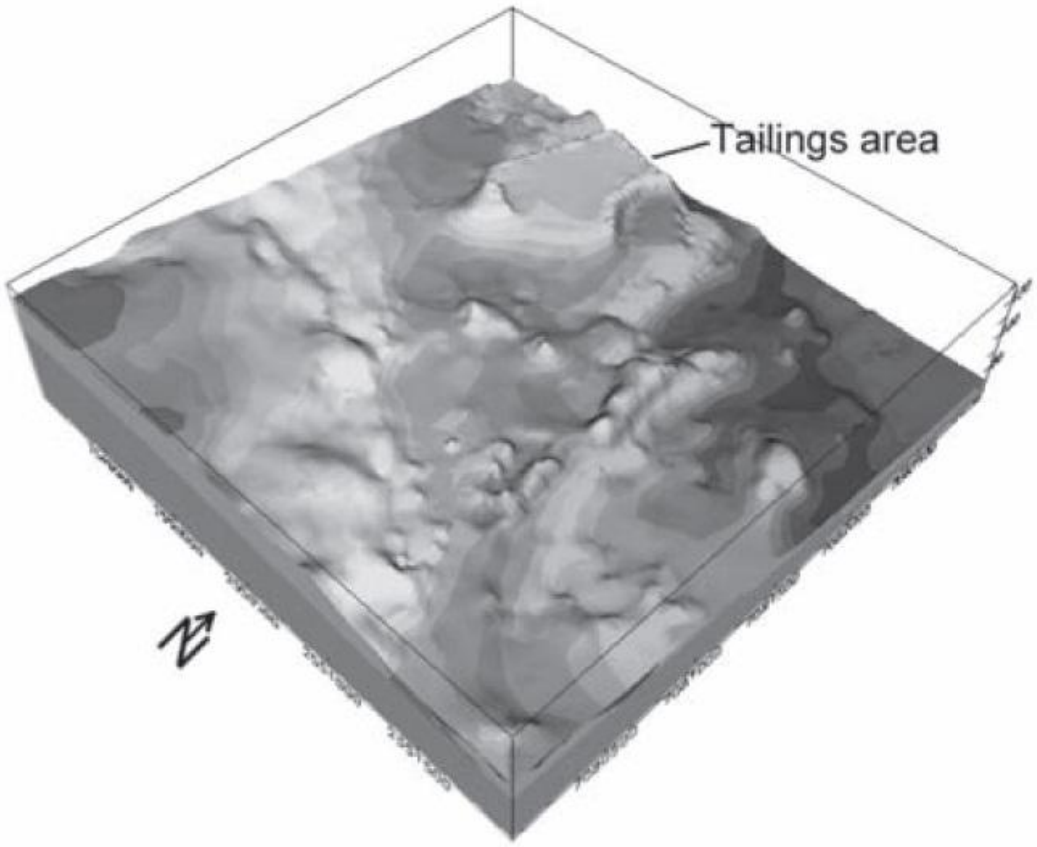

Figure 2.10 Ground Surface of Hitura Mine 3-D Geologic Model (Artimo et al., 2004)

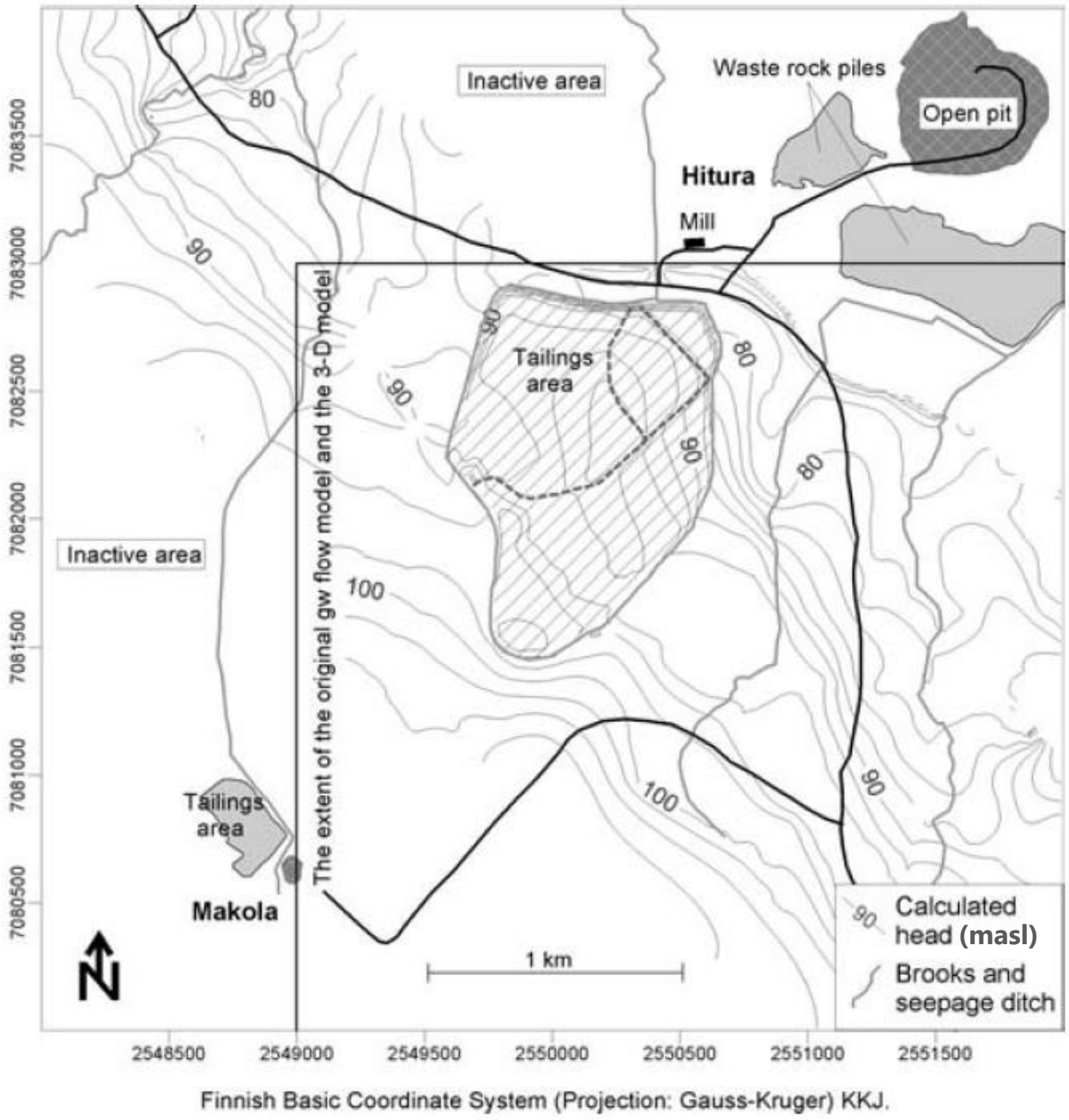

Figure 2.11 Hitura Mine Groundwater Flow Model Simulated Potentiometric Surface (Artimo et al., 2004)

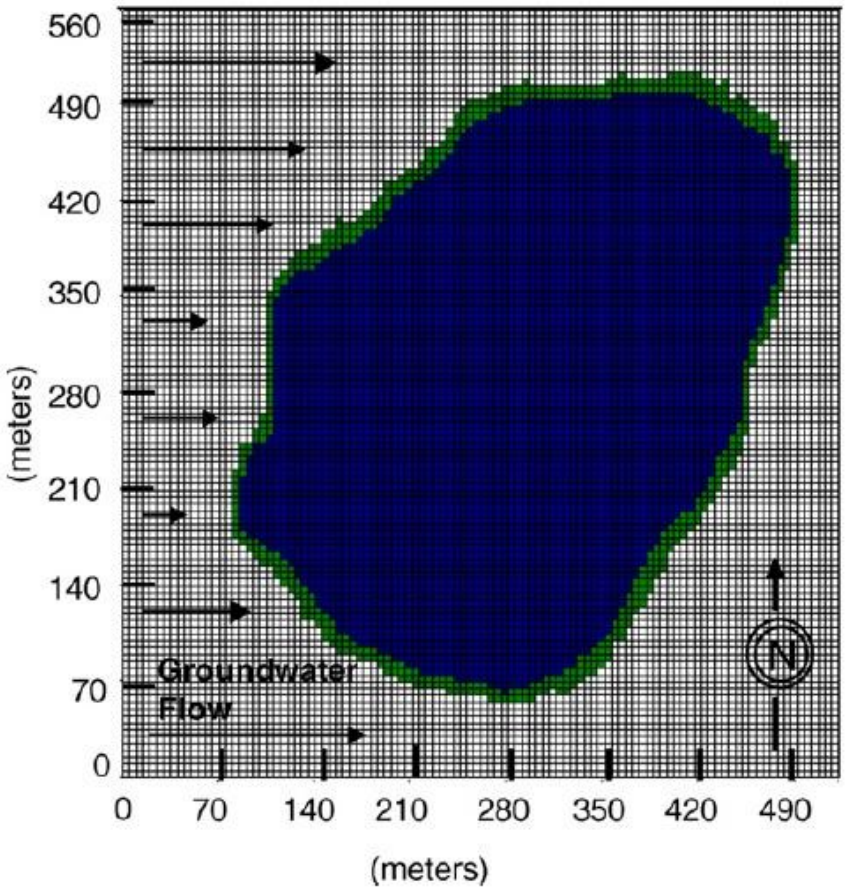

Figure 2.12 RLITMF Model Plan View (Moldovan et al., 2008)

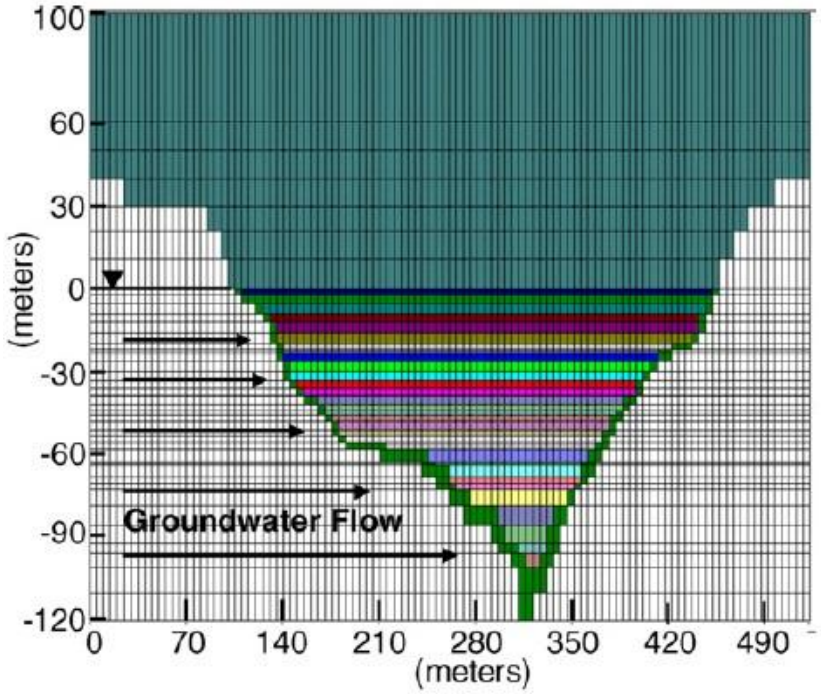

Figure 2.13 RLITMF Model Cross Section (Moldovan et al., 2008)

3.0 Northern Ontario Gold Mine Site Characteristics

The following section provides a detailed description of the Northern Ontario gold mine site with respect to its geographical location, history, geology, hydrogeology, and extent of the presently detected groundwater contamination.

3.1 Site Description

The Northern Ontario gold mine site is located in Northwestern Ontario, approximately 1.5 km southwest of a currently operational gold mine and ore processing plant. The ore processing plant utilizes the cyanidation process, as described in section 2.3.1 and displayed in Figure 2.1, to extract the finely dispersed native gold from the surrounding gangue minerals. The resulting tailings are then put through a cyanide recovery process followed by a cyanide destruction process to significantly lower their residual cyanide concentration. The tailings are then pumped to a dewatering process, which utilizes settling tanks to reduce their water content before they are disposed of in a tailings management area (TMA).

The study site is located adjacent to the mine's only TMA, and extends approximately 2000m long and 1200m wide, and encompasses an area of land located between the TMA and an adjacent lake. This area is the sole focus of this project, and is illustrated in plan view in Figure 3.1. The site contains notable surface features such as a gravel access road, an overburden storage area, a constructed fish habitat, and a seepage collection pond (SCP). Figure 3.1 also demonstrates the original ground surface topography in the area, as well as the name and location of each groundwater monitoring well, and each pumping well.

The name of each well displayed in Figure 3.1 consists of three main parts, which provide information about the well in that location (for example, 96-GW-11). The first two numbers in the name represent the year in which the well was installed (96 indicates that the well was installed in 1996). The second part consists of two letters, either GW, or PW. GW indicates that the well is a groundwater monitoring well, and PW indicates that the well is a pumping well. The third part of the name indicates the well number (11 indicates well number 11). The well numbers that are succeeded by the letter S, M, or D, are nested wells. The letter S indicates a shallow depth screen, the letter M indicates the medium depth screen, and the letter D indicates a deep screen. The label 95-GW-4S,M,D therefore indicates the location of groundwater monitoring well number 4, which was installed in 1995, and consists of three nested wells which have a shallow, a medium, and a deep screen. Screen length and midpoint elevations for each well are displayed in Table 3.1.

3.2 SITE HISTORY

Prior to 1995, initial site investigations were conducted to determine the location of the TMA, and determine the general direction of groundwater flow in the area of the site. In 1995, the first groundwater monitoring wells were installed downstream of the proposed TMA location, to collect samples and establish a baseline of the site's groundwater quality prior to any mining activity or tailings deposition. Additionally, a groundwater monitoring well (96-GW-LF1) was installed upstream of the proposed TMA, to act as a continual indicator of background water quality throughout the mine's operational period.

The TMA was located in a natural topographical low, which was contained on the southeast by the north-northwest trending moraine ridge shown by the contours in Figure 3.1. Before the TMA was constructed, a small pond existed in this location, which drained to the SCP through the lowest of the saddles that occurred along the ridge (Piteau Associates Engineering Ltd., 2011). The TMA was formed by constructing three tailings dams across these saddles to form a containment basin. The dams were constructed of sand and gravel, with a low permeability compacted till core, as well as slurry cut-off walls which were keyed into the native till material at depth. It is noted, however that the west end of Dam B did not have native clay or till material present at the maximum possible excavation depth, and was therefore not able to be keyed into low permeability material (Piteau Associates Engineering Ltd., 2011). The likely result of this situation is seepage occurring below the western end of Dam B. Construction of the TMA, mine shaft, and ore processing plant were all completed in 1996, followed by full mine operation and deposition of mine tailings into the TMA beginning in the spring of 1997 (Piteau Associates Engineering Ltd., 2011).

Throughout the following years of regular mine operation, the monitoring wells were continually maintained and sampled approximately two to four times annually, to detect any changes in groundwater quality. During this time, numerous field investigations were also conducted in the monitored area between the TMA and the lake. These investigations were conducted to develop a better understanding of the subsurface characteristics, and to gain further knowledge of groundwater flow in the area. The findings from many of these investigations led to the installation of new groundwater monitoring wells, which would improve the quality of both the groundwater monitoring network, and the collected data.

In 2009, a groundwater interception system was installed approximately half way between the TMA and the lake. The system consisted of seven pumping wells installed in a row along the gravel access road (see Figure 3.1) and perpendicular to the groundwater flow in the area. The intent of these pumping wells was to intercept contaminated water released from the TMA as it was migrating toward the lake. In the spring of 2010, the interception system was commissioned and began removing water from the ground, and pumping it back into the TMA behind the tailings dams.

Since this time, continual groundwater monitoring has been conducted on the forty-one groundwater monitoring wells which are currently in operation. The groundwater monitoring program includes both groundwater level measurements and groundwater sample collection from each of the monitoring wells. Groundwater level measurements are collected monthly and reported as elevations, in units of meters above sea level (masl). Groundwater sampling frequency varies from two to four times per year, depending on the location of the monitoring well (Water Management Consultants, 2007). In addition to the monitoring wells, seven pumping wells continue to recycle water from the ground back into the TMA.

3.3 SITE GEOLOGY

The geologic conditions of the site were classified through the examination of borehole log reports, which were recorded during the installation of the monitoring wells. From these reports, the subsurface of the site can be classified into six main units; bedrock, till, sand, silty-clay, peat, and fill. The stratigraphy of these geologic units is illustrated through three geologic

cross sections of the site, shown in Figure 3.2. The areal location of these cross sectional cuts can be seen in Figure 3.1.

The bedrock underling the site has been encountered at depths varying between 7.29m and 23.41m, with an average depth of approximately 12m. This bedrock is described as a "medium to dark green, fine grained, actinolite-plagioclase-rich assemblage of ultramafic volcanics" (Piteau Associates Engineering Ltd., 2011). This means that the bedrock is hard, very dense, and rich in iron and magnesium. The surface of the bedrock, however, is assumed to be partially fractured, and the reported range of hydraulic conductivity values measured near the surface of the bedrock is from $2x10^{-6}$ to $2x10^{-4}$ cm/s (Piteau Associates Engineering Ltd., 2011). The till layer, which overlies the bedrock across the majority of the site, is composed of very dense gray silty-sand with clay, gravel, cobble, and boulder size particles. Measured hydraulic conductivity values for this dense till material have been reported as being higher than the bedrock, but still relatively low, from $1x10^{-5}$ to $2x10^{-4}$ cm/s (Piteau Associates Engineering Ltd., 2011).

The sand layer is the most consistent stratigraphic unit, as it is the only unit to be noted in every reported borehole log. This sand layer has been confirmed to be up to 11.58m thick, but averages approximately 6m in thickness across the site. Although the sand texture is slightly variable across the site, ranging in description from medium sand to sand with bands of gravel, it is assumed to behave as a single unit. The thickest portion of the sand layer is estimated to run from northeast to southwest, parallel to the alignment of the existing moraine ridge and tailings dams (as shown in Section A-A', Figure 3.2), then turns southward toward the lake just to the east of the fish habitat (Piteau Associates Engineering Ltd., 2011). In some areas where

the bedrock surface rises, the sand layer thickness decreases and is nearly pinched out. This creates a preferential flow path which follows the thickest portion of the sand layer.

Measured hydraulic conductivity values for the sand layer from slug testing performed in 1995 have been reported from as low as $2x10^{-5}$ cm/s to higher than $2x10^{-3}$ cm/s. However, it is noted that a total of seven slug tests were performed on the aquifer in 1995, and five of the tests presented results greater than $2x10^{-3}$ cm/s (Piteau Associates Engineering Ltd., 2011). In 2007, the first pumping tests were performed on the aquifer in the area of the future pumping wells. The reported hydraulic conductivity values from these tests ranged from $1x10^{-1}$ to 1 cm/s, with a median value of $4x10^{-1}$ cm/s (Water Management Consultants, 2008). Further pumping tests performed at well 09-PW-5 during 2009 provided very similar hydraulic conductivity measurements, which ranged between $1.5x10^{-1}$ to $1.7x10^{-1}$ cm/s (Water Management Consultants, 2010). Additionally, slug tests were performed on the monitoring wells installed in 2009. The reported hydraulic conductivity values at these wells range from $9x10^{-4}$ to $9x10^{-2}$ cm/s, with 19 out of the 20 measurements having a value greater than $3.6x10^{-2}$ cm/s (Table 3.2). Although there is significant variation in these hydraulic conductivity values, the majority of these measurements are several orders of magnitude higher than those reported for either the till or bedrock. This indicates that the sand layer is in fact the predominant material through which groundwater flow occurs at this site.

The silty-clay layer overlies the sand layer across the entire site, except for one area just northeast of the seepage collection pond, as shown in cross section A-A' (Figure 3.2). In the locations where the silty-clay was detected, its thickness ranged from 0.4m to 5.24m, with an

average of approximately 2.3m. This layer is important because it has a relatively low hydraulic conductivity, and effectively creates a confined aquifer condition for the sand below. The silty-clay layer impedes both surface water from entering the aquifer and groundwater from leaving the aquifer.

Above the silty-clay layer there are areas of fill, which was introduced during the construction of the gravel access roads and tailings dams, as well as peat, which naturally covers the clay in low lying areas. The peat layer ranges in thickness from 0.3m to 6.7m, with an average thickness of 1.5m. Since these layers are above the confining clay layer, they are not considered to have much hydrogeological significance.

3.4 SITE HYDROGEOLOGY

The regularly collected groundwater level (elevation) data measured in the monitoring wells provide valuable insight into the hydrogeologic conditions and groundwater flow patterns of the site. By examining and comparing these measurements taken at various times, seasonal or time dependant changes in the groundwater flow conditions can be identified. Figure 3.3 highlights the locations of various wells which are more closely examined in the following analysis of the hydrogeologic conditions of the Northern Ontario gold mine site.

At the Northern Ontario gold mine site, fairly consistent seasonal changes in the groundwater elevations are observed across the site each year. Figure 3.4 shows the measured groundwater elevations collected from various wells between the TMA and the lake throughout 2009. These wells (wells 95-GW-2S, 95-GW-3S, 95-GW-6S, 95-GW-10D, 96-GW-14S, 96-GW-15D, 00-GW-19, 06-GW-24, and 06-GW27; highlighted in Figure 3.3) were selected because they are well

distributed across the site to the west of the seepage collection pond, in the area of greatest interest. From Figure 3.4 it is observed that the groundwater elevations lower steadily throughout the winter months, coming to a yearly low at the end of the winter season. This yearly low is followed by a sudden increase in groundwater elevations which corresponds to the period of spring thaw. The groundwater elevations then continue to rise throughout the summer months, and reach a yearly maximum at the end of the summer season, before beginning to lower throughout the remainder of the year. Figure 3.5 displays groundwater elevation data collected monthly (between January 2006 and January 2010) from wells 96-GW-14S, 95-GW-6S, 06-GW-24, and 06-GW27, which lie approximately along what is predicted to be the main flow path between the TMA and the lake. By examining the trend of this longer term data, it can be concluded that this general pattern of seasonal groundwater elevation change displayed during 2009 is approximately representative of a typical year at the site. Although the yearly maximum seems to vary between July and November depending on the year, the yearly minimum consistently occurs in either March or April, and is followed by a sudden increase in groundwater elevation during the spring months.

Although the seasonal changes displayed in Figure 3.4 occur very similarly in all the plotted wells which are distributed well across the western portion of the site, a few locations in the east of the site have notable variations from this pattern. From Figure 3.6 it can be seen that, although they follow the same general seasonal pattern, the wells in the northeastern portion of the site (wells 96-GW-13, 96-GW-17, 96-GW-12, 96-GW-11, and 95-GW-4; highlighted in Figure 3.3) have a much less drastic and sudden increase in groundwater elevation during the

spring thaw period. This is likely due to the fact that these five wells are the farthest wells from the edge of the lake; all located more than 840m from the lake at the closest point.

Although the elevation of the lake surface is not measured and recorded, it is assumed that, during the spring thaw event, the lake will experience a sudden and significant increase in water surface elevation due to the large volume of runoff water that it likely receives. Comparison of Figures 3.4 and 3.6 shows that this sudden increase in groundwater elevation during the spring thaw period is experienced the most significantly in wells located closest to the lake. This seems to be indicative of the effect that the lake water surface elevation has on the surrounding groundwater table. It is assumed that the effect of a change in lake elevation is experienced greatly by those wells in close proximity, but does not have nearly as significant of an effect on the wells farther upstream, which are closer to the TMA. This shows that the groundwater elevations in wells located adjacent to the TMA are likely affected primarily by factors such as infiltration and runoff in an area upstream of the TMA, or by seepage of the tailings pore water through or beneath the dams, rather than by the lake elevation. Similarly, the two easternmost of the five northeastern wells (wells 95-GW-4 and 96-GW-11) are located relatively close to the east pond, as shown in Figure 3.1. The east pond has a nominal elevation of approximately 300m (Piteau Associates Engineering Ltd., 2011), and is likely to have a greater effect on the groundwater in this area than the lake, or even the TMA.

In order to determine the general groundwater flow patterns of the site, the collected monitoring well groundwater elevation data were contoured to estimate the potentiometric surface of the site at different points in time. Table 3.1 presents the observed groundwater

elevation data collected from the monitoring wells during April 2009, August 2009, and April 2011. These data sets were used to construct three potentiometric surfaces in order to analyze the groundwater flow patterns of the site. The interpolation of values between two observed data points was assumed to follow a linear distribution during the creation of contour lines. The April 2009 and August 2009 data sets were chosen because they represent the seasonal low, and seasonal high groundwater conditions during 2009, respectively (as seen in Figure 3.4). These data sets also contain a relatively large amount of data points, and were collected in the most recent year prior to the installation of the pumping wells. Comparing the seasonal low data to the seasonal high data allows any seasonal changes in the groundwater condition to be determined. The April 2011 data set was chosen because it represents the seasonal low groundwater condition one year after the commencement of the pumping wells. Comparing the seasonal low groundwater data before and after the activation of the pumping wells allows the effect of the pumping wells on the groundwater condition to be determined.

The presence of a vertical hydraulic gradient of the Northern Ontario Gold Mine site was investigated by examining the data collected from various sets of nested wells. Eight multi-level wells have been installed on the site which can be used to determine if any vertical hydraulic gradient is present in the subsurface. As shown in Figure 3.7, the shallow and deep screened intervals of various multi-level wells at the site produce very similar groundwater elevation data, indicating that no significant vertical gradient is present. Most of the wells fluctuated between a slight upward and a slight downward gradient from one month to the next, likely indicating that the difference in measured groundwater elevations was due to slight error in the measurements rather than the presence of any actual vertical groundwater hydraulic gradient.

Well 96-GW-15S,D did produce groundwater elevations which were consistently measured higher in the deep screened well than they were in the shallow screened well, indicating that an upward hydraulic gradient may be present in this location. However, as shown in Figure 3.8, the groundwater elevation data collected from well 96-GW-15S was also consistently lower than that collected from well 96-GW-6S, which is located closer to the lake along the preferential flow path. Noting the location of these wells from Figure 3.3, it is not probable that groundwater elevations in well 96-GW-15S are actually lower than those in well 95-GW-6S, and instead are likely erroneous. For this reason, the measurements collected from well 96-GW-15S were regarded as being anomalous, and the measurements from 96-GW-15D were used in constructing the observed potentiometric surfaces instead. Other than well 96-GW-15, the groundwater elevations collected from the shallow screened wells were used to construct the April 2009, August 2009, and April 2011 potentiometric surfaces.

Figure 3.9 displays the interpreted potentiometric surface of the site during April 2009, which represents the yearly low in the groundwater elevations, as seen in Figures 3.4 and 3.6. The general directions of groundwater flow are perpendicular to the potentiometric surface contours, and are demonstrated in Figure 3.9 with arrows. In the easternmost portion of the site, the groundwater tends to flow southward from the TMA towards the lake. In the central area on the site, the groundwater flow trends westward, almost parallel to the edge of the TMA. In the western portion of the site, this western flow then turns southward and flows toward the lake just east of the fish habitat. It is noted that the flow directions for the central and western portions of the site observed here match that of the preferential flow path created by the alignment of the thickest portion of the sand layer, as described in section 3.3.

The potentiometric surface contours and implied direction of groundwater flow, however, can be directly influenced by the seasonal changes in the measured groundwater elevations described above. For this reason, potentiometric surfaces must be created from multiple collected data sets, and compared to one another, to determine any seasonal changes in groundwater flow directions. Comparing the potentiometric surface created by the yearly low groundwater elevations to that created by the yearly high elevations provides the largest contrast in the hydrogeological condition of the site which can be reasonably expected to occur in a year.

Figure 3.10 displays the interpreted potentiometric surface of the site during August 2009, when the groundwater was at its maximum yearly elevation. Although the potentiometric surface displayed in Figure 3.10 is approximately 0.7m higher than that of Figure 3.9, the general shape, and relative horizontal distance between the contours (hydraulic gradient) remains the same. In fact, the arrows displaying groundwater flow direction are in the exact same location in both Figures 3.9 and 3.10. Comparison of these two figures therefore leads to the conclusion that, although the potentiometric surface raises and lowers seasonally, it has little effect on the direction of groundwater flow. Further to this point, Figure 3.11 shows the groundwater elevations observed in various monitoring wells along the preferential flow path during both April, and August of 2009. The fairly consistent relative difference in groundwater elevations between these two plots indicates that the change in groundwater elevation in each well between the spring low and the fall high is approximately the same. This means that the total head difference along this flow path remains approximately the same as well.

For simplicity, since these graphs demonstrate that the flow conditions at the site remain essentially unchanged seasonally, it has been assumed that the groundwater flow condition of the site prior to the activation of the pumping wells can be effectively represented by a single potentiometric surface. For the purpose of this project, the April 2009 potentiometric surface contours are assumed to represent the groundwater condition of the site between 1997 and 2009.

Besides seasonal groundwater fluctuations, human intervention can also affect the hydrogeologic conditions of the site. In the case of the Northern Ontario gold mine site, a pumping well system was installed with the objective of altering the hydrogeologic conditions of the site. In order to determine the extent of the pumping wells' effect on the flow patterns of the site, groundwater elevation data collected after the commencement of pumping were also used to create potentiometric surfaces. Figure 3.12 displays the interpreted potentiometric surface of the site for April 2011, approximately one year after the commencement of pumping. This figure clearly shows the cone of depression in the potentiometric surface, which is created by the pumping. By comparing Figure 3.9 and Figure 3.12, which both represent the spring low time period, the changes in the hydrogeological conditions of the site due to the pumping can be analyzed. The most notable difference is the change of direction of groundwater flow between the pumping wells and the lake. In this area, the potentiometric surface has been sufficiently lowered to cause reverse flow in nearly the exact opposite direction of the original flow pattern. This shows that the pumping wells are not only effective in reducing flow from the TMA to the lake, but are actually drawing groundwater away from the edge of the lake. In all

other areas of the site, the direction of groundwater flow has not changed from the original flow pattern described above, and the flow direction arrows remain in the same locations.

Further examination of Figure 3.11 shows the distribution of the total head drop with distance along the preferential flow path between the TMA and the lake. It is apparent that the flow path has two zones, with a distinctly different hydraulic gradient in each. The beginning portion of the flow path has a steep hydraulic gradient (0.0028 m/m), as a drop in total head of approximately 2m occurs within the first 715m of flow. However, the second portion of the flow path has a much flatter hydraulic gradient (0.00097 m/m), as a total head drop of only 0.5m occurs across 517m of flow distance. This sudden change in hydraulic gradient indicates that a sudden change in one or more of the hydrogeologic parameters exists in this area. As noted in section 3.3 above, slug tests performed in 1995, in the area adjacent to the TMA, yielded hydraulic conductivity values for the aquifer which were several orders of magnitude lower than those performed farther downstream near the pumping wells and adjacent to the lake. This difference in the hydraulic conductivity of the aquifer material could be the cause of the sudden change in hydraulic gradient along the flow path. If the flow rate and aquifer thickness are assumed to be constant along the flow path, then a lower hydraulic conductivity near the TMA would cause a steeper hydraulic gradient in the upstream portion of the flow path. Similarly, a higher hydraulic conductivity in the area of the pumping wells would cause the hydraulic gradient to flatten near the end of the flow path.

3.5 SITE RECHARGE

Temperature and precipitation data collected from the mine site show the meteorological conditions of the area, and can be helpful in determining the expected surface recharge. Table 3.3 lists the averages of monthly collected temperature and precipitation measurements taken between years 2000 and 2010 at the Northern Ontario gold mine site. According to these data, the average annual precipitation for the site is 569mm. As explained in section 2, all but two borehole logs show that a layer of silty-clay overlies the sandy aquifer layer. This silty-clay layer has a relatively low hydraulic conductivity, effectively confining the aquifer, and will impede the infiltration of any surface water into the aquifer below. This will cause the majority of the precipitation which falls on the site to discharge to the lake as surface runoff.

As mentioned in various groundwater reports, several areas of standing water and small ponds of trapped water have been noted to exist in the low lying areas of the site, and areas where surface runoff is impeded by the gravel access road (Water Management Consultants, 2005, 2007, 2008, Piteau Associates Engineering Ltd., 2011). This provides further evidence that rainfall, and surface runoff do not easily infiltrate into the underlying aquifer. It is therefore reasonable to assume that only a small portion of the 569mm of average annual precipitation is able to penetrate the silty-clay layer, and act as recharge for the aquifer. The majority of water entering the aquifer is believed to occur in an unknown location upstream of the TMA where the surface soil is likely more permeable. Additionally, a source of water entering the aquifer is likely due to seepage from the TMA. The high elevation of the decanting pool at the tailings

beach could create a downward hydraulic gradient from the tailings' pore water to the underlying aquifer, causing infiltration into the aquifer to occur beneath the TMA.

3.6 GROUNDWATER CONTAMINATION

As discussed in section 2.5.3, the main contaminants of concern, which typically result from mining activities, are heavy metals and other inorganic contaminants. For this reason, the detection of inorganic contaminants in the groundwater down-gradient of the TMA has been the main focus of the sampling and testing at the Northern Ontario gold mine site. Although the Ontario Provincial Water Quality Objectives (OPWQOs) are only meant to quantify surface water quality, they are used at the Northern Ontario gold mine site as comparisons for the groundwater samples as well. These comparisons are used to determine when the groundwater contaminants have reached levels which could be deemed as a potential concern for the surrounding surface waters. Table 3.4 lists all the chemical characteristics for which the groundwater samples taken from the Northern Ontario gold mine site are tested, as well as the corresponding OPWQO's when specified. From examination of the historical groundwater sample testing results at the Northern Ontario gold mine site, dissolved cobalt has been consistently detected above its respective OPWQO, and is the primary focus of this project. Dissolved Iron has also been consistently detected above its OPWQO, and the nature and extent of the dissolved iron plume forms a basis of comparison with the dissolved cobalt plume.

Examination of the groundwater contamination data was approached by first investigating the original, pre-mining geochemical conditions of the groundwater in the area. Groundwater samples collected prior to 1997 (pre-mining results) and samples collected upstream of the

TMA in well 96-GW-LF1 (background results) were used for this purpose. Once background concentrations were determined, they were used as a baseline for the samples collected after tailings deposition had commenced, in order to determine changes in the groundwater quality due to the TMA. Yearly average concentrations for selected monitoring wells were also plotted versus time to describe the general trend of the plume advancement. The general shape of the contaminant plume was estimated by using the collected data to create concentration contours in plan view of the site. Additionally, successive time snapshots of the plumes' contours were used to assess the contaminants' spread and movement over time.

3.6.1 Pre-Mining and Background Concentrations

Examining the movement of dissolved cobalt and iron at the Northern Ontario gold mine site starts with examining the natural groundwater quality of the site before the influence of the mine tailings was introduced. As mentioned in section 3.2 above, groundwater sample collection at the Northern Ontario gold mine site began as early as 1995, which is prior to any mining activity. This was done to determine the pre-mining, background concentrations of any dissolved chemical species which may have existed naturally in the area, or may have been coming from an already existing contaminant source. Additionally, a background monitoring well (96-GW-LF1) was installed upstream of the TMA to continue to monitor the background water quality for comparison throughout the operation of the mine.

Unfortunately, although all samples taken from the site prior to 1997 were reported as non-detects for dissolved cobalt (as shown in Figure 3.13), the high detection limits for these tests limits the usefulness of the data. The detection limits used when testing the pre-mining

samples for dissolved cobalt were 15mg/L and 10mg/L for tests performed in 1995 and 1996 respectively. These detection limits are much greater than the OPWQO of 0. 9µg/L (listed in Table 3.4) for dissolved cobalt, and do not provide an accurate basis for detection. Instead, more recently collected data from background well 96-GW-LF1 is used to quantify the pre-mining cobalt concentrations at the site. As shown in Figure 3.14, recently collected groundwater samples taken upstream of the TMA indicate that the background water contains only trace amounts of dissolved cobalt. In fact, 9 of the 11 tests were reported as non-detect samples, with a detection limit of 0.5µg/L. This indicates that the aquifer upgradient of the TMA contains dissolved cobalt concentrations which are consistently below the OPWQO of 0.9µg/L.

Fortunately, the pre-mining detection limit for the samples for dissolved iron (0.03mg/L) was much lower than the OPWQO of 0.3mg/L; however, the test results are quite varied. The pre-mining data include all test results obtained from samples collected during 1995 and 1996. These pre-mining data were averaged for each well in order to determine its pre-mining dissolved iron concentration. As seen in Figure 3.15, the pre-mining concentrations of dissolved iron were spatially variable, and ranged from 0.03mg/L to 0.98mg/L at different wells across the site. Although some of the wells had iron concentrations above the OPWQO, no discernible pattern or existing plume shape was determined to exist at the site from the pre-mining data. Additionally, Figure 3.14 displays more recently collected dissolved iron data from background well 96-GW-LF1, which shows temporal variability in the detected concentrations as well. Dissolved iron concentrations in the background well ranged between 0.166mg/L and 1.27mg/L depending on the sampling date. These measurements indicate that the pre-mining condition

of dissolved iron in the subsurface of the site contains a high degree of inconsistency, and were at times naturally exceeding the OPWQOs.

3.6.2 GROUNDWATER PLUMES

Examining the results of historical groundwater sample analyses provides evidence of the presence of dissolved contaminants in the subsurface of the site. By comparing the results of analyses performed at different times, the movement, expansion, or contraction of contaminant plumes can be observed.

Figures 3.16 and 3.17 show the yearly average concentrations for dissolved cobalt and iron, respectively, measured at select monitoring wells. Monitoring wells 96-GW-14S, 95-GW-6S, and 06-GW-28 were selected because they lie approximately along the main flow path between the TMA and the lake (see Figure 3.3), which is also expected to be the centerline of the contaminant plumes. Well 95-GW-10D is included to provide an indication of the concentrations adjacent to the lake over a longer period of time. The error bars presented in Figures 3.16 and 3.17 were determined by calculating the standard error of the reported concentrations measured during each calendar year. Standard error was calculated by dividing the standard deviation of the sample by the square root of the sample size. This standard error represents the degree to which the plotted sample mean represents the actual mean concentration present in the well for that time period. Large error bars are caused by a large degree of scatter or amount of variability in the data, and therefore indicate uncertainty in the measured concentrations. However, these figures are only meant to demonstrate the general trend of dissolved cobalt and iron concentrations over time at various locations along the flow

path. More detail of the measurements in these wells is displayed through time series scatter plots in Appendix A. For the purpose of calculating the yearly averages and standard error, as well as displaying the data in the time series scatter plots, non-detect measurements were assumed to be equivalent to the detection limit for the contaminants at the time the sample was tested.

The overall trend of the dissolved cobalt concentrations, as shown in Figure 3.16, seems to be steadily increasing over time. At well 96-GW-14S, located close to the TMA, concentrations appear to steadily increase at a fairly consistent rate between 1998 and 2009, where they seem to stabilize temporarily around 22µg/L. This short stability period is followed by a sharp increase in 2011 to 35µg/L where it remains through 2013. Data collected from well 95-GW-6S seems to mimic that of well 96-GW-14S, but at a delay of approximately two years, and nearly reaches the 35µg/L concentration observed in 96-GW-14 by 2013. Well 06-GW-28 was not sampled until 2006; however, cobalt concentrations were consistently measured around 4µg/L from 2006 until 2008. In 2009 the concentration in well 06-GW-28 jumped to values greater than 6µg/L, but immediately started to fall upon commencement of pumping in 2010, and was measured below the detection limits (0.5µg/L) by 2013. In well 95-GW-10D, cobalt concentrations were not confirmed to exceed the OPWQO of 0.9µg/L until 2007. They then experienced a small increase to a maximum of approximately 3µg/L in 2011 before falling back below 1µg/L by 2013. Overall, the amount of scatter observed in the dissolved cobalt concentrations in the groundwater was relatively low and did not affect the overall trend of the data. Of the examined wells, the amount of variability displayed by the cobalt concentrations was greatest in well 96-GW-14S. In this well, groundwater samples taken during the same

calendar contained concentrations of dissolved cobalt which varied by more than 10µg/L. This high degree of variability in the cobalt concentrations was observed during multiple years for well 96-GW-14S, and exceeded 13µg/L in 2011. In the other examined wells, the amount of variability of the samples exceeded 5µg/L only once.

The overall trend of the dissolved iron concentrations, as shown in Figure 3.17, are more variable and erratic than the dissolved cobalt concentrations, but also show a general increase from the pre-mining concentrations. Iron concentrations in well 96-GW-14S increased fairly sharply from 1997 until they reached approximately 3.5mg/L in 2001. These concentrations remained between 3-4mg/L until 2011. In 2012 and 2013, the concentrations then dropped to approximately 2.5mg/L. Well 95-GW-6S demonstrates erratic behaviour, reaching maximums of around 2.5mg/L in 2001 and 2007, while also dropping to nearly 1mg/L in 2004. More recently, well 95-GW-6S has hovered around 1.5mg/L between 2008 and 2013. Well 06-GW-28 showed the most distinct trend, which was similar to that of cobalt in the same well. Concentrations increased from below 3mg/L in 2006 to a maximum above 4.5mg/L in 2009. Upon commencement of pumping in 2010, the concentrations fell quickly to less than 0.5mg/L by 2013. In well 95-GW-10D, concentrations were very low until a sudden breakthrough in 2002 when they jumped to approximately 1mg/L. They then slowly increased to a maximum of slightly less than 2mg/L in 2010 before steadily dropping back down to 1mg/L by 2013. The amount of scatter displayed by the observed dissolved Iron concentrations in the groundwater was generally much larger than that which was observed in the cobalt measurements. This is indicated by the size of the error bars presented in Figure 3.17. Of the examined wells, the amount of variability observed in the dissolved iron concentrations was greatest in well 96-GW-

14S. In this well, samples collected in 2001 varied by more than 5.8mg/L. In each of the other examined wells the variability of the observed concentrations exceeded 1.2mg/L, typically during multiple years.

As demonstrated by Figures 3.16 and 3.17, and described above, the concentrations of dissolved cobalt and iron have shown an overall rising trend in various monitoring wells. In order to develop a spatial understanding of the extent of the contamination, and to determine the shape and extent of the contamination plumes which have formed, the measured concentration data are used to construct concentration contours of the contaminants. The plume evolution can be tracked by constructing multiple sets of contours from data collected at different times. Comparison of these figures can determine the speed at which the contaminant plume is expanding, contracting, or moving. Figures 3.18 and 3.19 show multiple snapshots of the dissolved cobalt plume at different points in time to demonstrate its movement. Although background concentrations of cobalt are rarely greater than the detection limits of 0.5µg/L (described in section 3.6.1), by 2000, a distinct plume with concentrations nearing 10µg/L was detected adjacent to the TMA (Figure 3.18). By 2006, concentrations of 4µg/L were detected adjacent to the lake, with concentrations above 14µg/L being detected next to the TMA (Figure 3.18). In 2009, before the pumping wells were installed and activated, the plume reaches its maximum extent, where concentrations exceeded 22µg/L and 6µg/L beside the TMA and lake respectively (Figure 3.19). By 2010, after the pumping wells are started, the concentrations detected adjacent to the lake immediately start to drop, and by 2012 were below 0.7µg/L. Conversely, as concentrations dropped between the lake and the pumping wells, they increased

substantially between the pumping wells and the TMA. Concentrations detected adjacent to the TMA rose sharply to 35µg/L by 2012 (Figures 3.19 and 3.16).

Movement of the dissolved iron is demonstrated by Figures 3.20 and 3.21, which show an evolution similar to that of the cobalt plume. By 2000 a distinct plume shape is formed, with concentrations above 2mg/L adjacent to the TMA (Figure 3.20). By 2006, concentrations of nearly 3mg/L were detected adjacent to the lake, with concentrations above 4.8mg/L being detected next to the TMA (Figure 3.20). In 2009, before the pumping wells were installed and activated, the plume reached its maximum extent, where concentrations of 4.6mg/L were detected beside the lake in well 06-GW-28. These concentrations actually exceeded those measured next to the TMA (3.7mg/L in well 96-GW-14D), as shown in Figure 3.21. Similarly to cobalt, once the pumping wells were activated in 2010, the concentrations detected adjacent to the lake immediately started to drop, and by 2012 were only 2.3mg/L (Figure 3.21). However, at the same time, the concentrations detected in well 09-GW-34, located close to the pumping wells, increased to almost 5.4mg/L in 2012. Concentrations detected adjacent to the TMA in 2012 only measured around 3.5mg/L (Figure 3.21). Unlike the dissolved cobalt concentrations, the maximum iron concentrations were not always detected in the wells closest to the TMA at any given point in time. Therefore, either the flow path carrying the maximum dissolved iron concentrations from the TMA to the lake must flow in a path that is missed by the upstream wells, or the source, or fate and transport parameters of dissolved iron varies with time.

It is clear from observing Figures 3.18-3.21 that distinct contamination plumes of increasing cobalt and iron concentrations have been migrating downstream from the TMA toward the

lake. This contaminant migration was likely due mainly to the natural flow of groundwater in this area, since the observed centerlines of the contamination plumes are approximately along the preferential flow path through the aquifer material, as described in sections 3.3 and 3.4. Additionally, it is clear that pumping has had a large impact on both the natural hydrogeologic condition of the site and the cobalt and iron plumes. The overall goal of the pumping wells, which was to intercept the contamination plumes and reduce the contaminant concentrations adjacent to the lake, has therefore been largely successful. However, the pumping wells have apparently caused an increase in contaminant concentrations in the region between their location and the TMA. The averaged observed contaminant concentrations which were used to construct Figures 3.18-3.21 can be found in Appendix B.

Well Name	Lithology at Screen Elevation	Screen Midpoint Elevation (m)	Screen Length (m)	Groundwater Elevation (m)		
				Apr-09	Aug-09	Apr-11
95-GW-1S	Till	290.65	0.3	293.05	293.80	292.77
95-GW-1D	Bedrock	285.10	0.3	293.01	293.80	292.73
95-GW-2S	Sand	286.65	0.3	292.61	293.45	-
95-GW-2D	Bedrock	281.65	0.3	292.60	293.44	-
95-GW-3S	Sand	283.15	0.3	292.67	293.43	-
95-GW-3D	Bedrock	277.70	0.3	292.68	293.44	-
95-GW-4S	Sand	290.80	0.3	293.35	293.98	293.32
95-GW-4M	Till	283.50	0.3	293.38	294.00	293.17
95-GW-4D	Bedrock	272.80	0.3	293.70	294.36	293.74
95-GW-6S	Sand	284.05	0.3	292.71	293.59	292.16
95-GW-6D	Bedrock	279.10	0.3	293.74	294.55	293.21
95-GW-10S	Sand	286.50	0.3	293.47	292.28	-
95-GW-10D	Sand	278.80	0.3	292.47	292.30	292.41
96-GW-11	Sand	291.62	3	293.53	294.13	293.36
96-GW-12	Sand	288.74	3	-	294.62	-
96-GW-13	Sand	290.22	3	294.77	295.35	295.00
96-GW-14S	Sand	288.85	1.5	293.96	294.62	294.11
96-GW-14D	Sand	280.41	1.5	294.03	294.70	294.15
96-GW-15S	Sand	288.29	1.5	292.66	293.53	292.26
96-GW-15D	Till	281.88	1.5	292.78	293.59	292.34
96-GW-17	Sand	287.85	1.5	294.53	295.00	294.65
00-GW-19	Sand	286.61	1.5	292.61	293.46	292.15
04-GW-20	Sand	287.66	1	-	293.49	294.06
04-GW-21	Sand	285.81	1	-	293.31	292.03
06-GW-24	Sand	287.18	3	292.57	293.41	292.18
06-GW-25	Silt/Sand	287.75	1.5	293.04	293.79	292.78
06-GW-26	Sand	288.21	-	293.57	293.21	292.28
06-GW-27	Sand	287.92	-	292.33	293.12	292.25
06-GW-28	Sand	287.66	-	293.77	293.12	292.31
07-GW-29	Sand	289.55	6	292.58	293.45	292.04
07-GW-30	Sand	289.60	2.5	292.63	293.48	291.92
09-GW-31	Sand	282.19	3	-	293.48	292.08
09-GW-32	Sand	285.25	3	-	293.51	292.13
09-GW-33	Sand	285.80	3	-	292.07	292.01
09-GW-34	Sand	287.17	3	-	293.52	291.91
09-GW-35	Sand	288.00	3	-	293.50	291.87
09-GW-36	Sand	287.61	3	-	293.53	291.90
09-GW-37	Sand	286.63	3	-	-	292.22
09-GW-38	Sand	287.32	3	-	-	292.15
09-GW-39	Sand	287.36	3	-	-	292.16
10-GW-40	Sand	286.17	3	-	-	292.29

- No Data Available

Table 3.1 Observed Groundwater Elevations

Well	Hydraulic Conductivity (cm/s)	Interpretation Method
09-GW-31	5.91E-02	McElwee et al. Method
09-GW-31	5.08E-02	McElwee et al. Method
09-GW-32	4.16E-02	McElwee et al. Method
09-GW-32	4.43E-02	McElwee et al. Method
09-GW-33	4.16E-02	McElwee et al. Method
09-GW-33	9.04E-02	McElwee et al. Method
09-GW-34	3.6E-02	Hvorslev Method
09-GW-34	3.6E-02	Hvorslev Method
09-GW-35	5.4E-02	Hvorslev Method
09-GW-35	3.6E-02	Hvorslev Method
09-GW-36	8.9E-04	Bouwer-Rice Method
09-GW-36	5.4E-02	Bouwer-Rice Method
10-GW-37	7.3E-02	McElwee et al. Method
10-GW-37	7.9E-02	McElwee et al. Method
10-GW-38	6.8E-02	McElwee et al. Method
10-GW-38	7.3E-02	McElwee et al. Method
10-GW-39	6.0E-02	McElwee et al. Method
10-GW-39	6.5E-02	McElwee et al. Method
10-GW-40	7.3E-02	McElwee et al. Method
10-GW-40	6.0E-02	McElwee et al. Method

Table 3.2 Slug Test Results (2009 & 2010) (Water Management Consultants, 2010)

Month	Temperature (°C)	Precipitation (mm)
January	-18.5	25
February	-16.1	18
March	-8.4	17
April	0.7	26
May	7.4	58
June	13.9	81
July	17.3	97
August	16.0	81
September	9.9	79
October	2.2	49
November	-6.2	18
December	-17.2	20
Total		569

Table 3.3 Average Monthly Temperature and Precipitation (Years 2000-2010) (Piteau Associates Engineering Ltd., 2011)

Characteristic	OPWQO	Units
Anion Sum	-	me/L
Cation Sum	-	me/L
Ion Balance	-	%
BiCarbonate	-	mg/L
Carbonate	-	mg/L
Chemical Oxygen Demand	-	mg/L
Colour	-	Color
Dissolved Aluminum	0.075	mg/L
Dissolved Antimony	0.02	mg/L
Dissolved Arsenic	0.005	mg/L
Dissolved Barium	-	mg/L
Dissolved Beryllium	1.1	mg/L
Dissolved Bismuth	-	mg/L
Dissolved Boron	0.2	mg/L
Dissolved Cadmium	0.0005	mg/L
Dissolved Calcium	-	mg/L
Dissolved Chloride	-	mg/L
Dissolved Chromium	0.001	mg/L
Dissolved Cobalt	0.0009	mg/L
Dissolved Copper	0.005	mg/L
Dissolved Iron	0.3	mg/L
Dissolved Lead	0.005	mg/L
Dissolved Lithium	-	mg/L
Dissolved Magnesium	-	mg/L
Dissolved Manganese	-	mg/L
Dissolved Mercury	0.0002	mg/L
Dissolved Molybdenum	0.04	mg/L
Dissolved Nickel	0.025	mg/L
Dissolved Oxygen	>5	mg/L
Dissolved Phosphate	-	mg/L
Dissolved Phosphorus	0.03	mg/L
Dissolved Potassium	-	mg/L

Characteristic	OPWQO	Units
Dissolved Selenium	0.1	mg/L
Dissolved Silicon	-	mg/L
Dissolved Silver	0.0001	mg/L
Dissolved Sodium	-	mg/L
Dissolved Strontium	-	mg/L
Dissolved Sulphate	-	mg/L
Dissolved Tellurium	-	mg/L
Dissolved Tin	-	mg/L
Dissolved Thallium	0.0003	mg/L
Dissolved Titanium	-	mg/L
Dissolved Tungsten	-	mg/L
Dissolved Uranium	0.005	mg/L
Dissolved Vanadium	0.006	mg/L
Dissolved Zinc	0.02	mg/L
Dissolved Zirconium	-	mg/L
Dissolved Solids	-	mg/L
Suspended Solids	-	mg/L
Lab Turbidity	-	NTU
Hydroxide	-	mg/L
Specific Conductivity	-	uS/cm
Total Ammonia	-	mg/L
Un-ionized Ammonia	0.02	mg/L
Nitrate	-	mg/L
Nitrite	-	mg/L
Total Kjeldahl Nitrogen	-	mg/L
Total Alkalinity	-	mg/L
Total Hardness	-	mg/L
Total Cyanide	0.005	mg/L
WAD Cyanide	0.005	mg/L
Temperature	-	°C
Field pH	6.5-8.5	pH unit
Lab pH	-	pH unit

- No Standard Specified

Table 3.4 Tested Groundwater Characteristics and OPWQOs (Ministry of Environment and Energy, 1994)

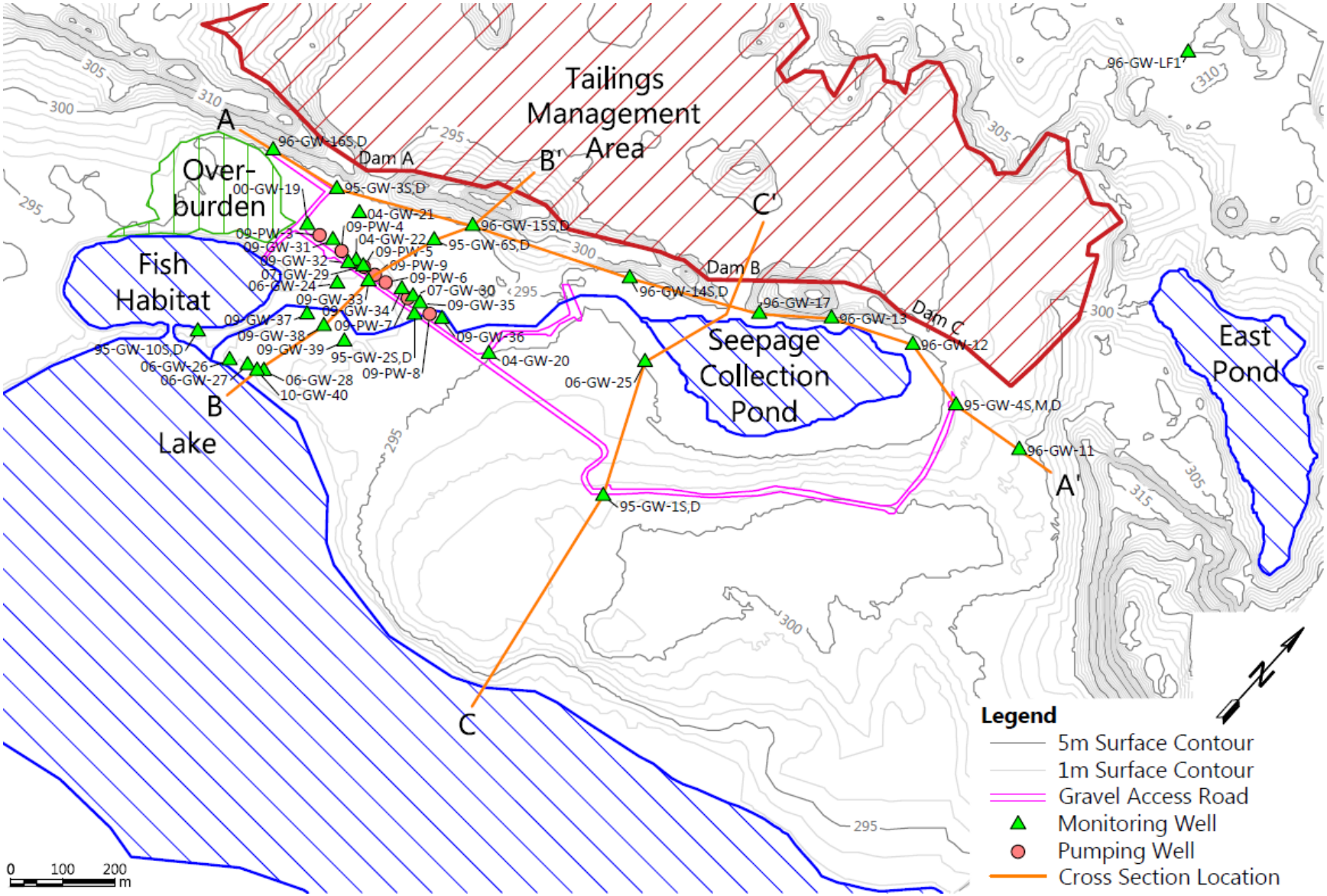

Figure 3.1 Site Layout

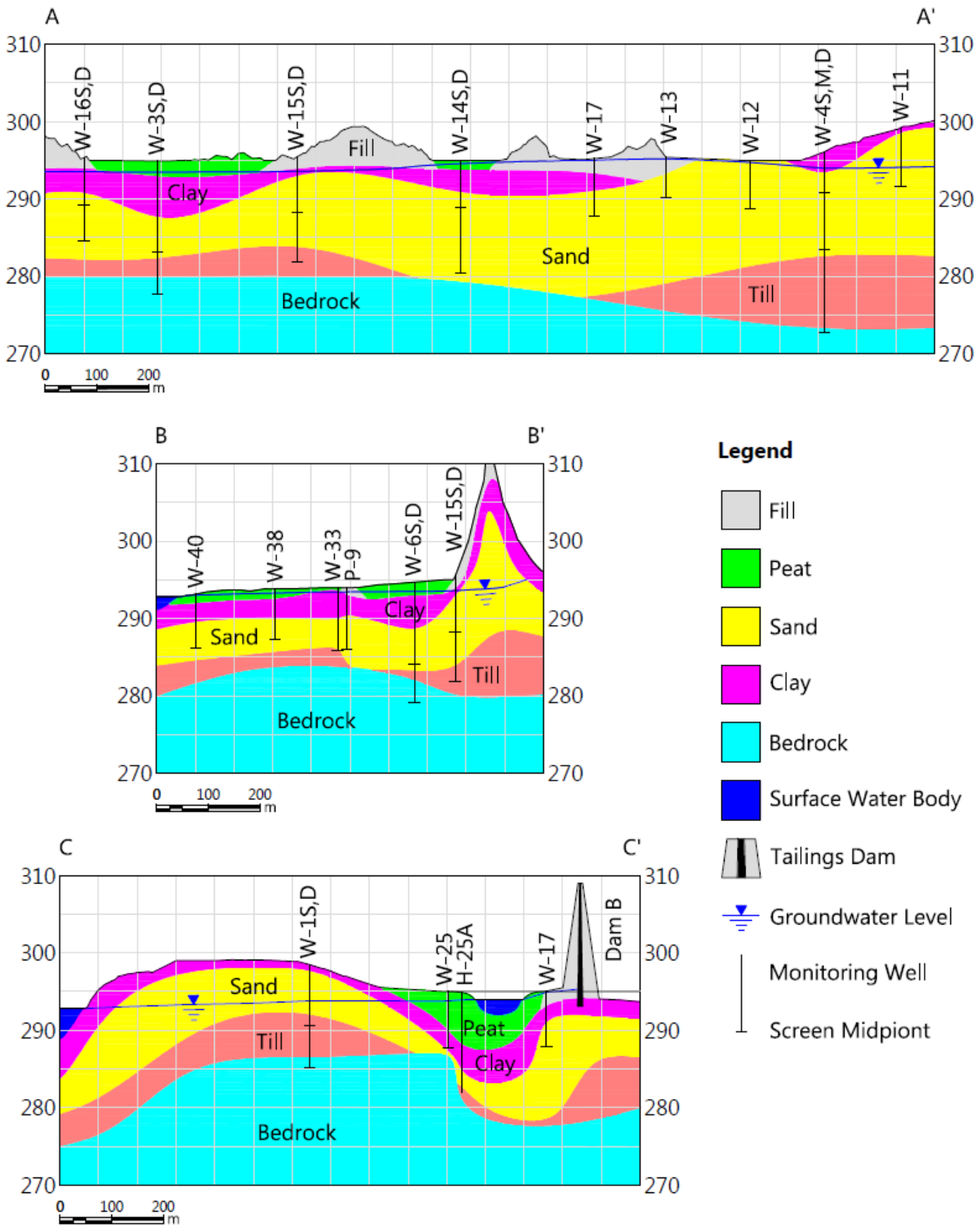

Figure 3.2 Geological Cross Sections

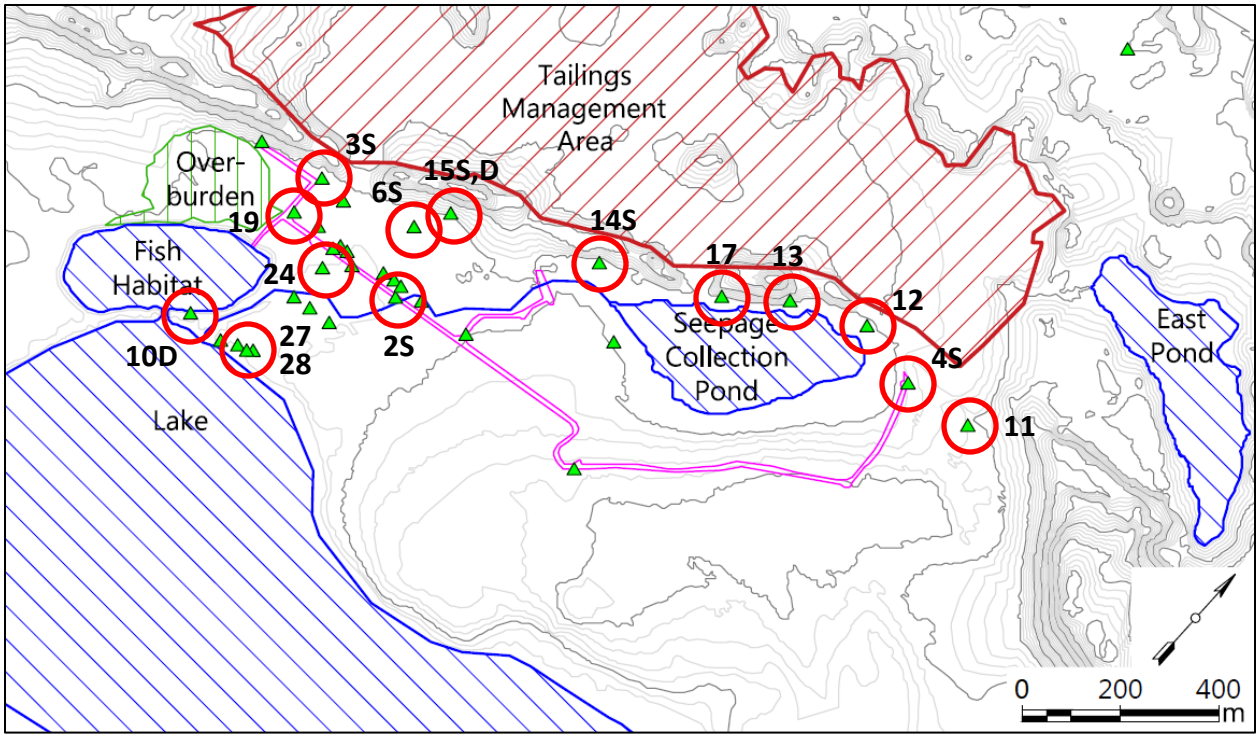

Figure 3.3 Locations of Highlighted Wells

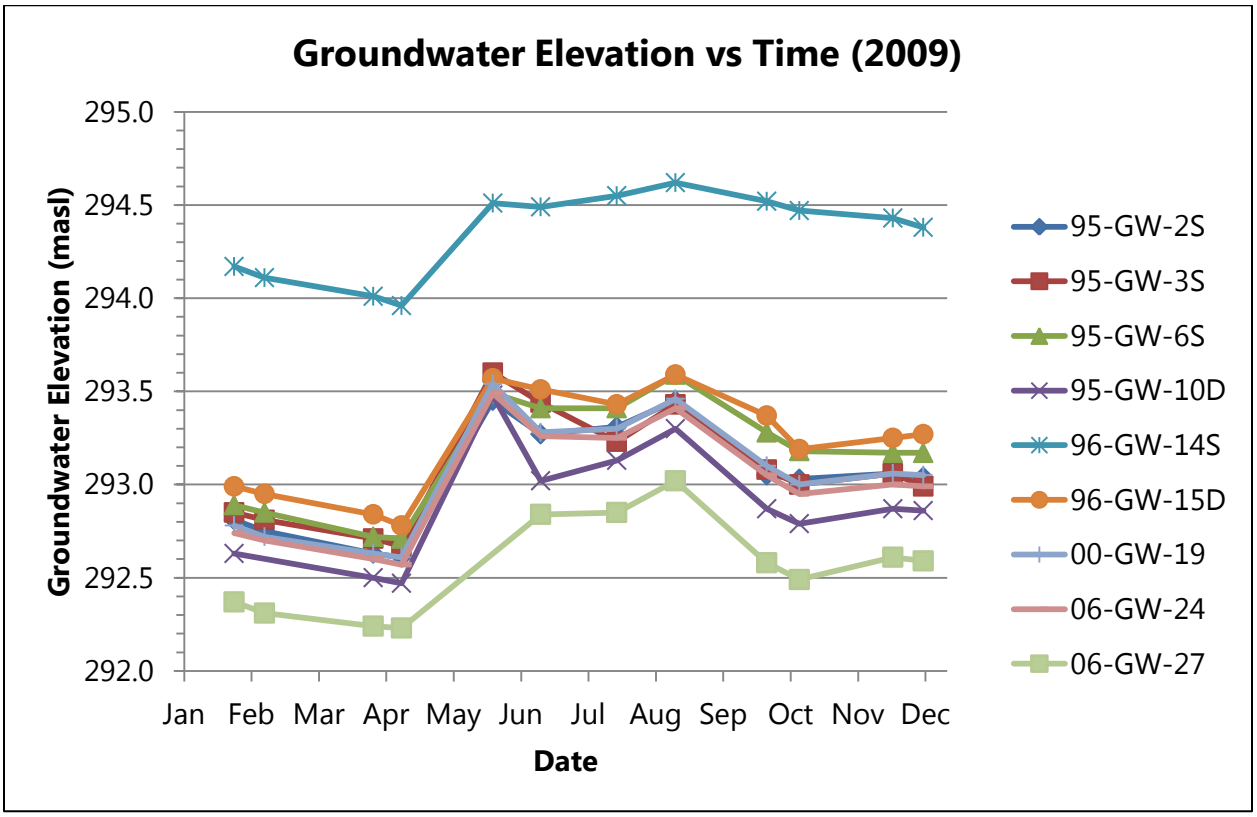

Figure 3.4 Groundwater Elevation Time Series (2009)

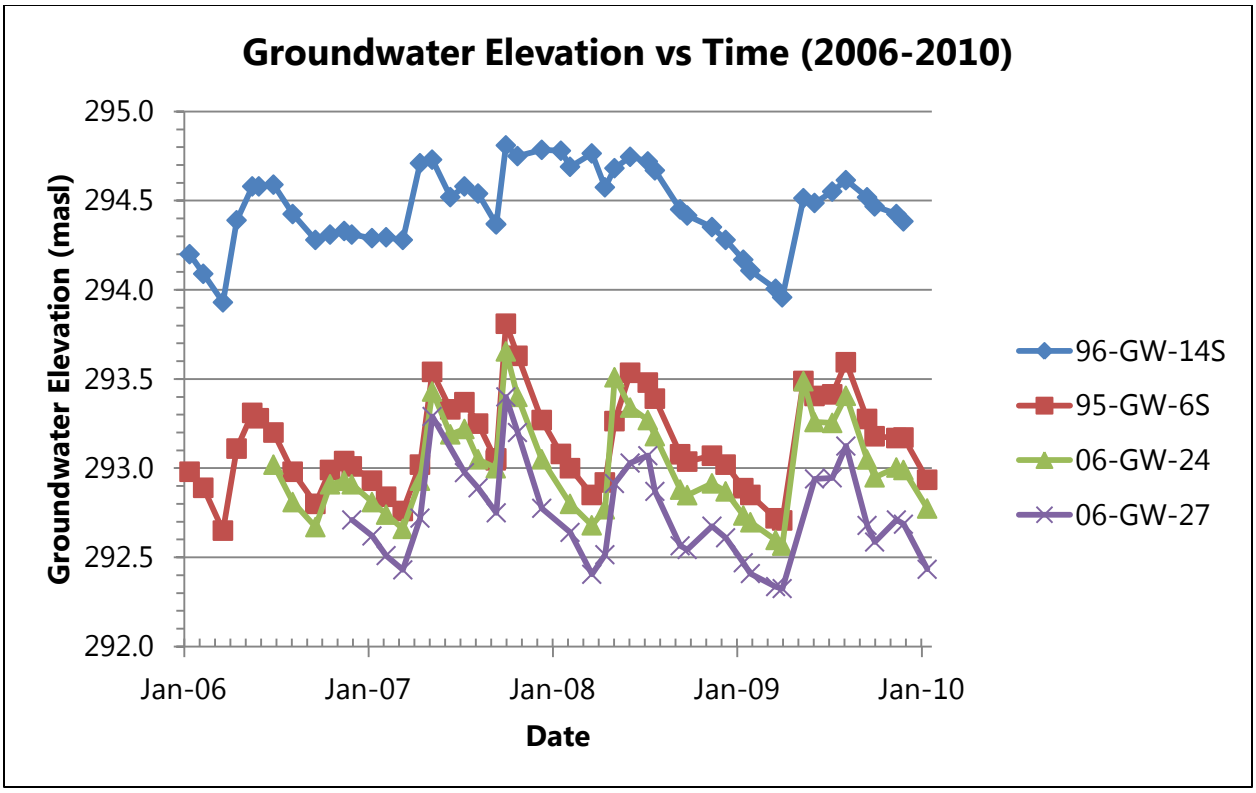

Figure 3.5 Long Term Goundwater Elevation Trend (2006-2010)

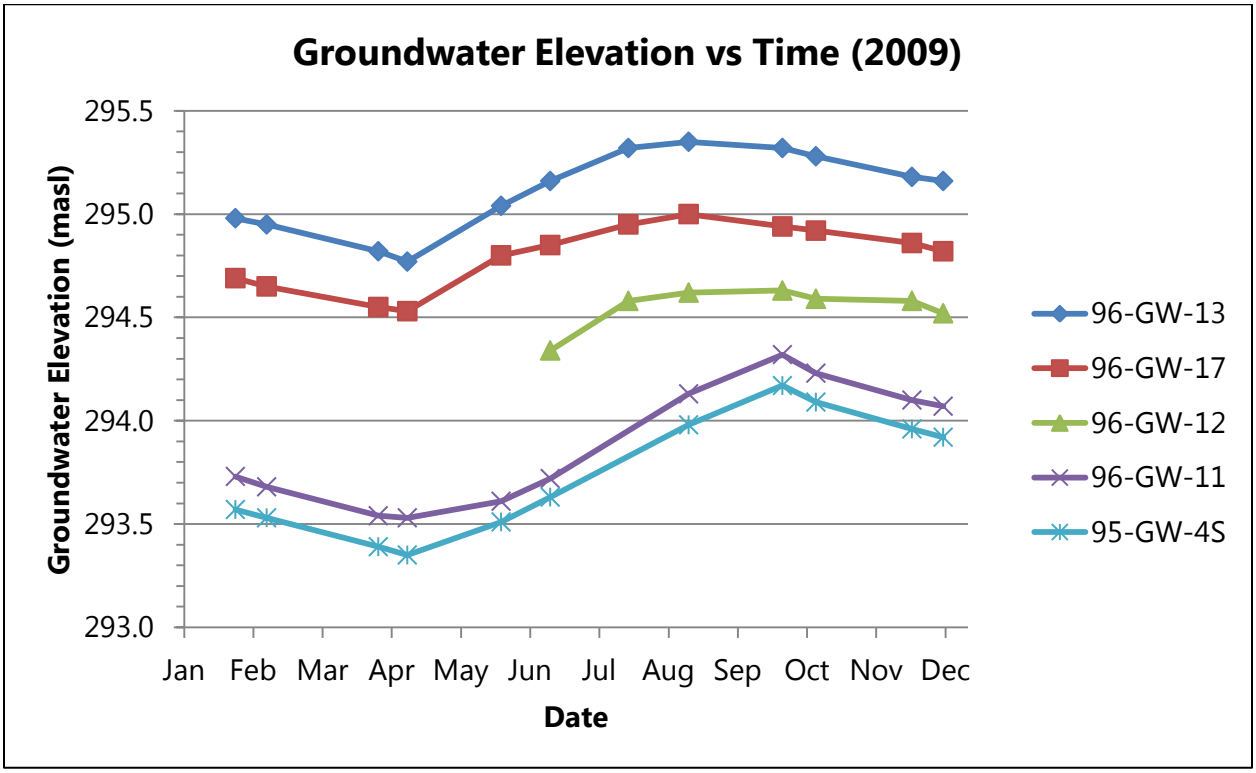

Figure 3.6 Northeastern Wells Groundwater Elevation Time Series (2009)

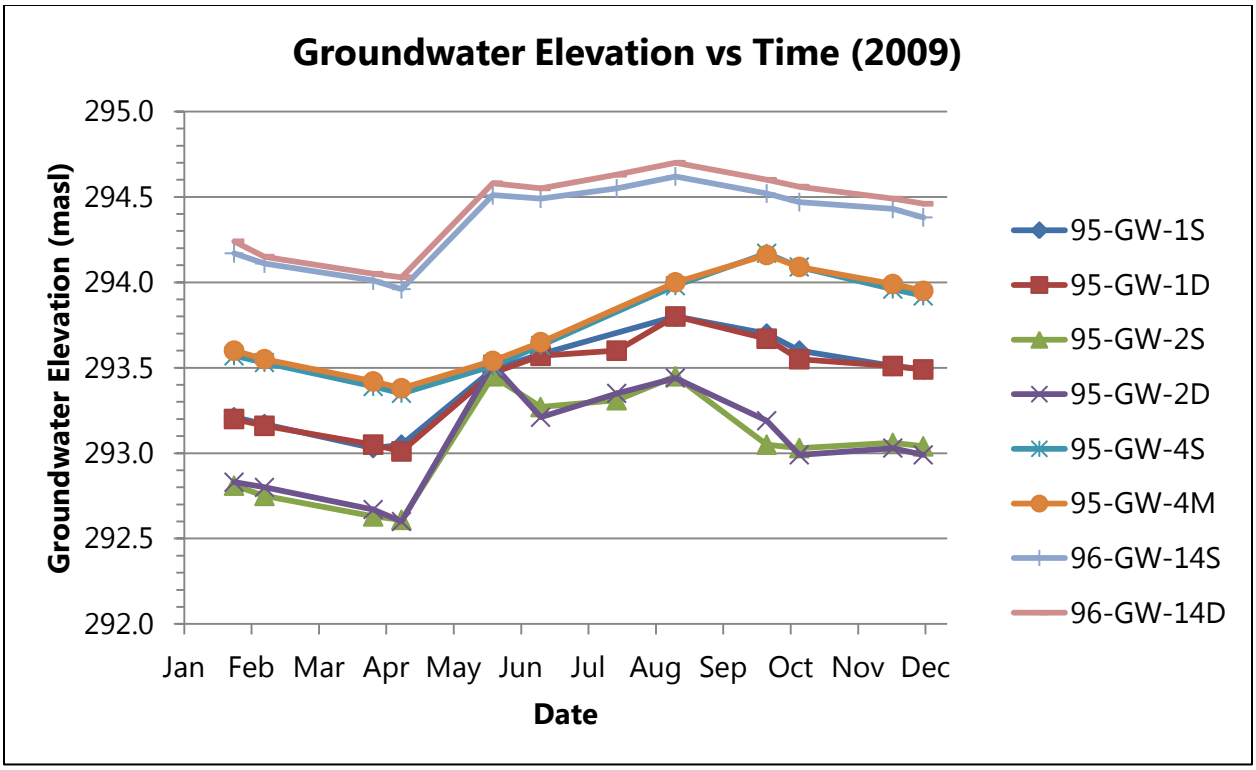

Figure 3.7 Nested Well Groundwater Elevation Time Series (2009)

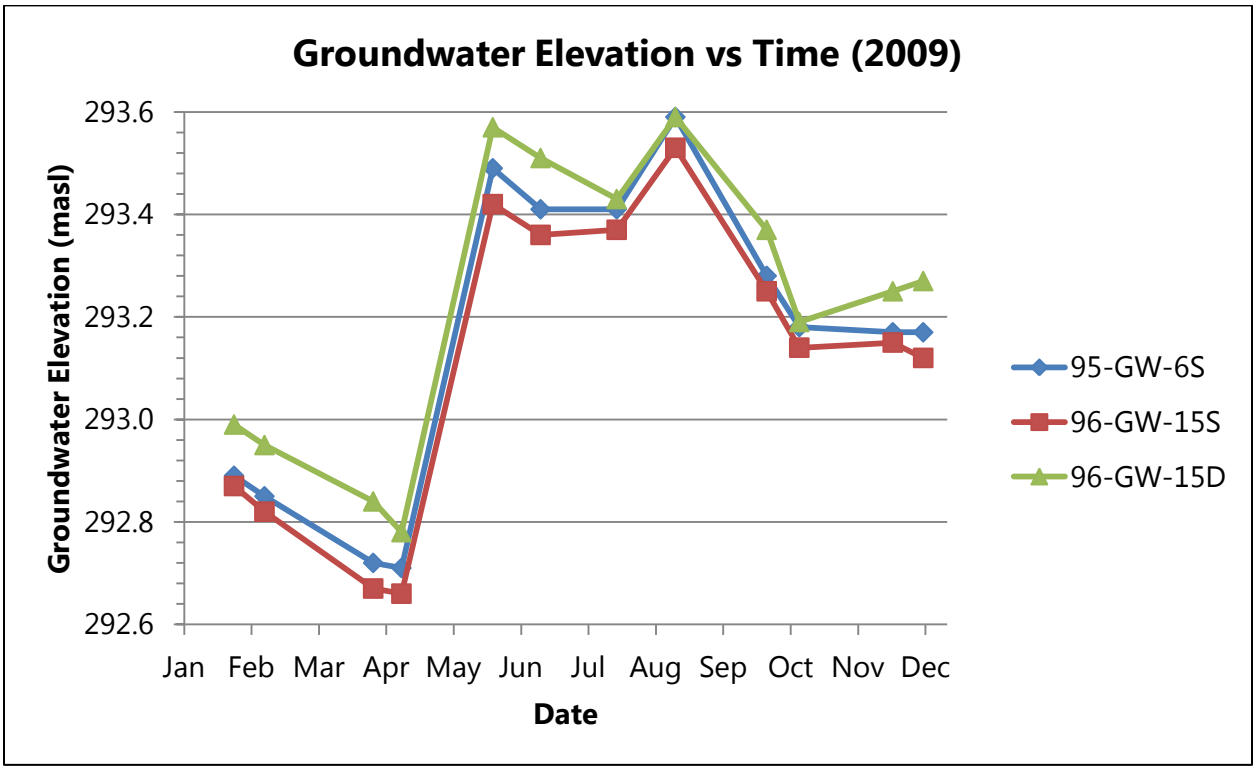

Figure 3.8 Well 96-GW-15S,D Groundwater Elevation Time Series (2009)

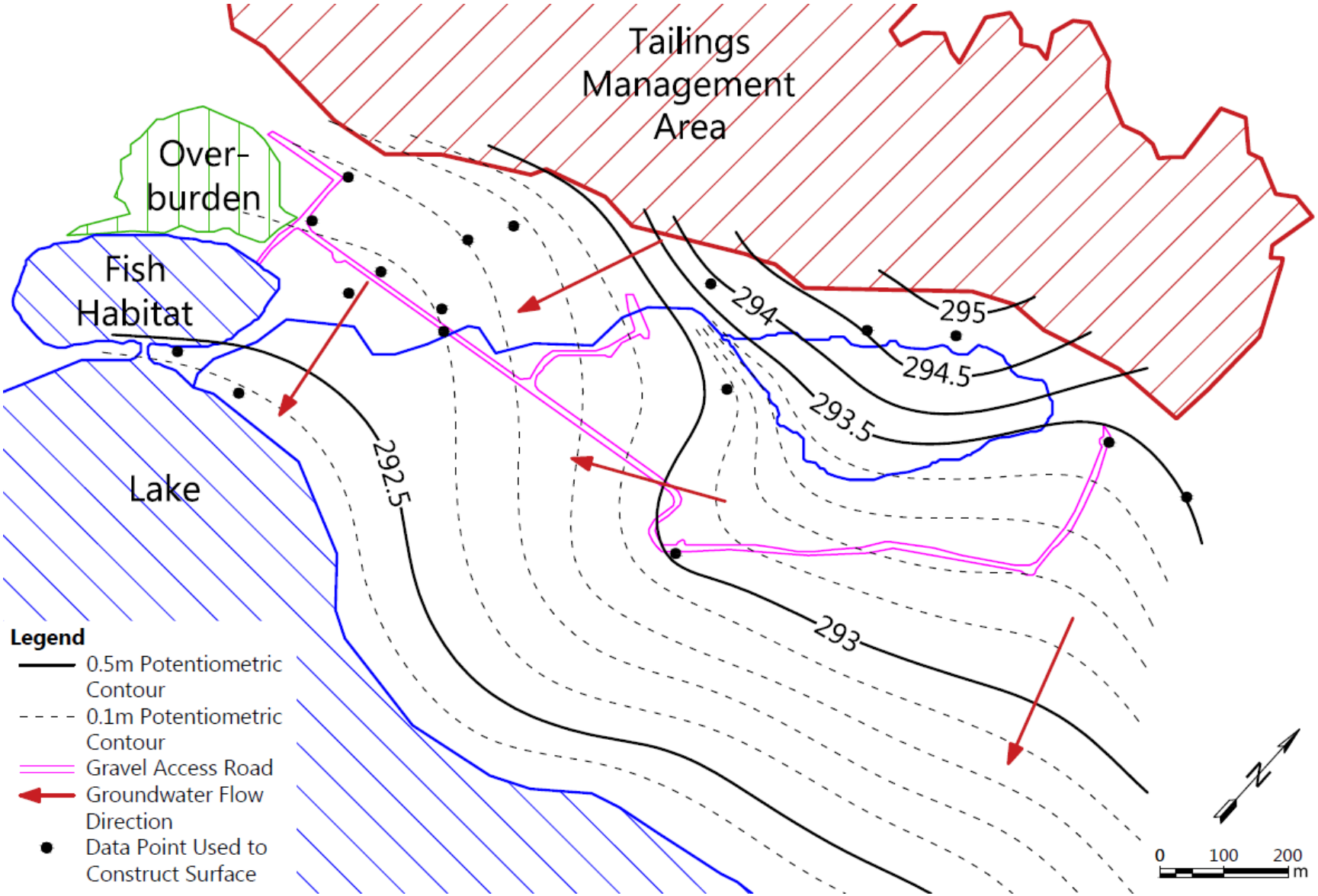

Figure 3.9 April 2009 Potentiometric Surface

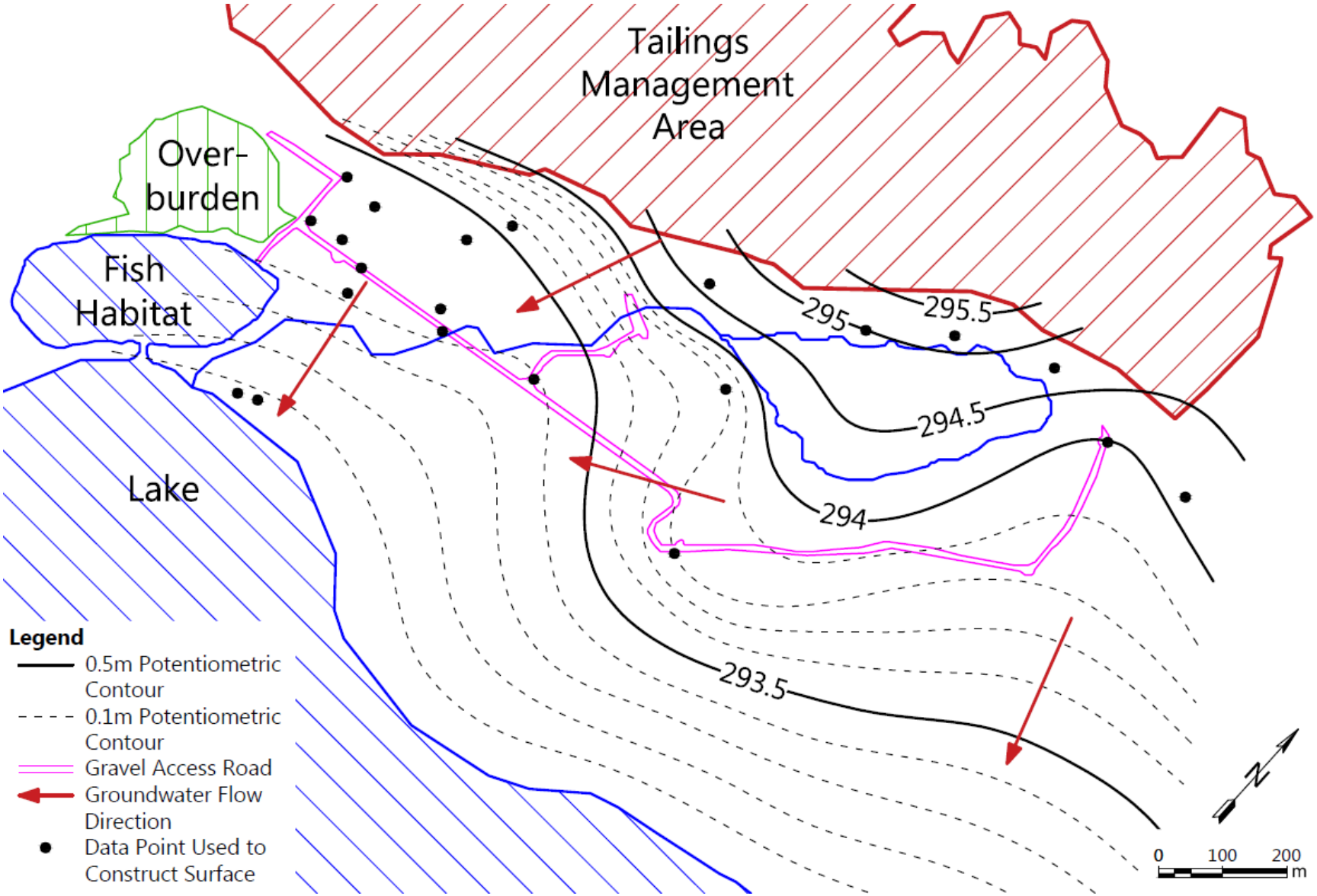

Figure 3.10 August 2009 Poteniometric Surface

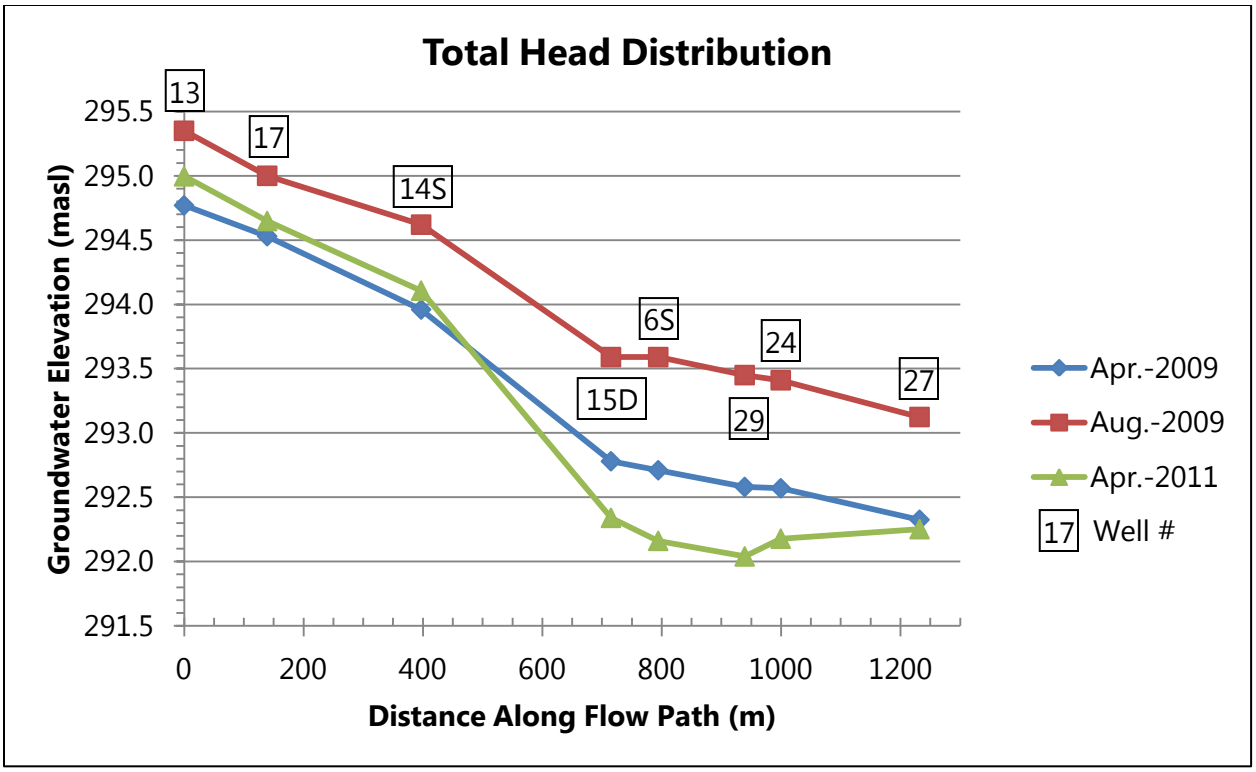

Figure 3.11 Hydraulic Gradient Along Preferential Flow Path

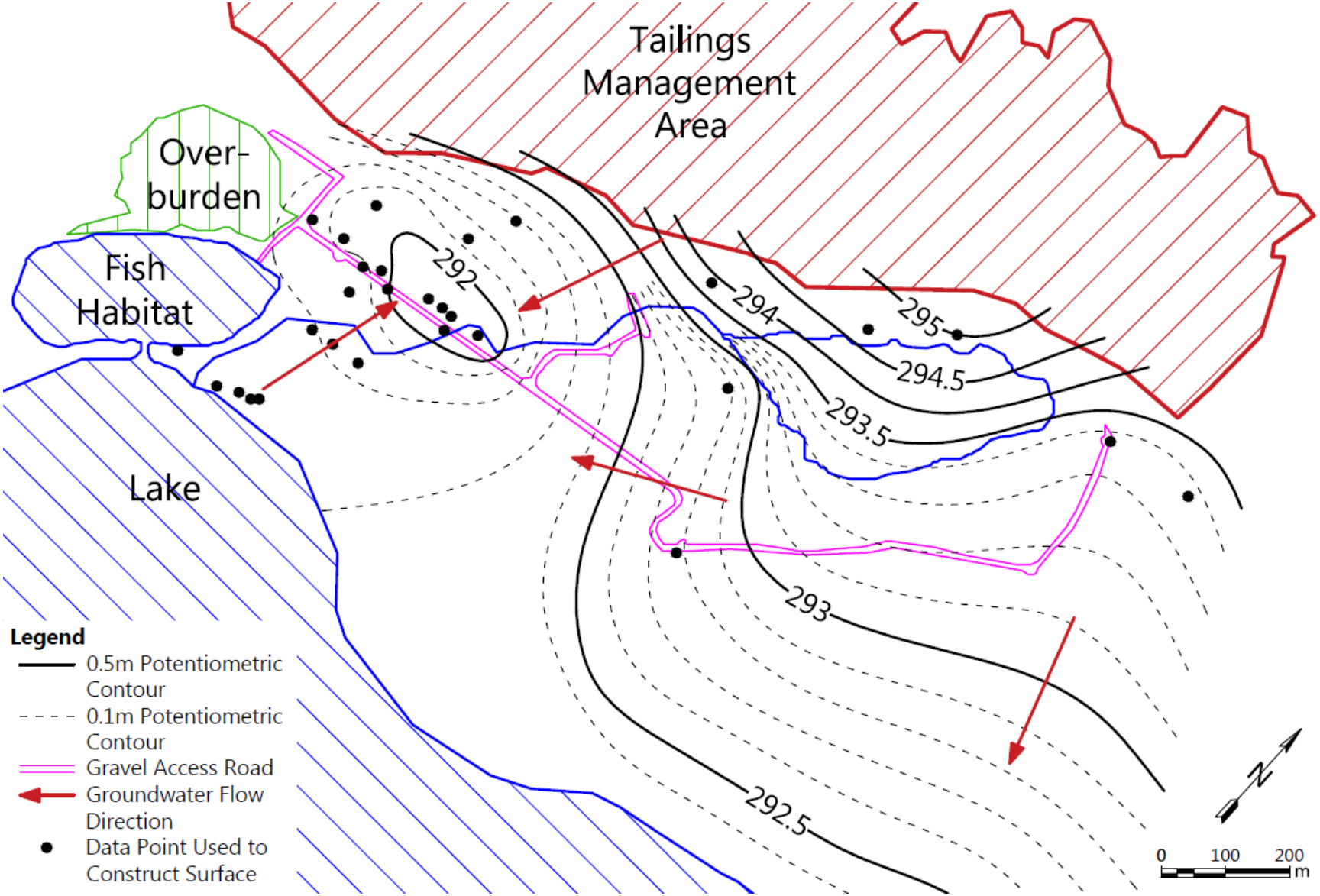

Figure 3.12 April 2011 Potentiometric Surface

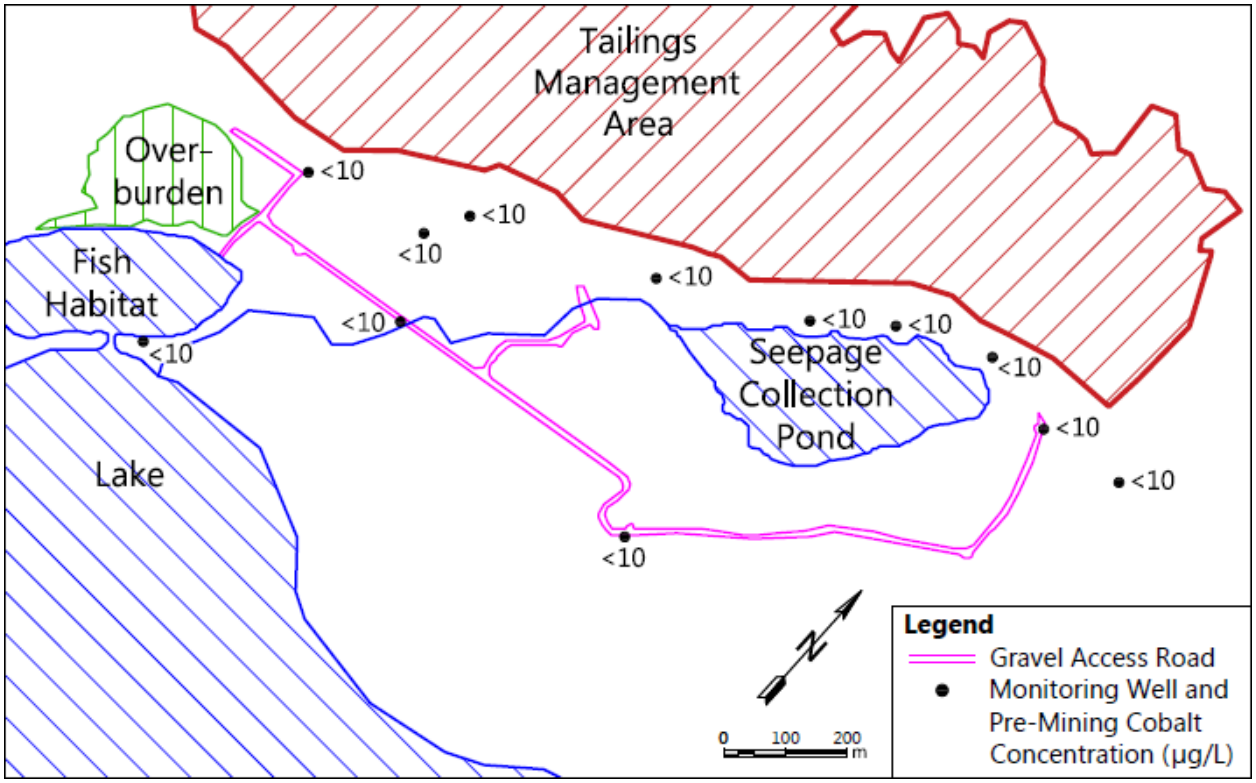

Figure 3.13 Pre-Mining Dissolved Cobalt Concentrations (1996)

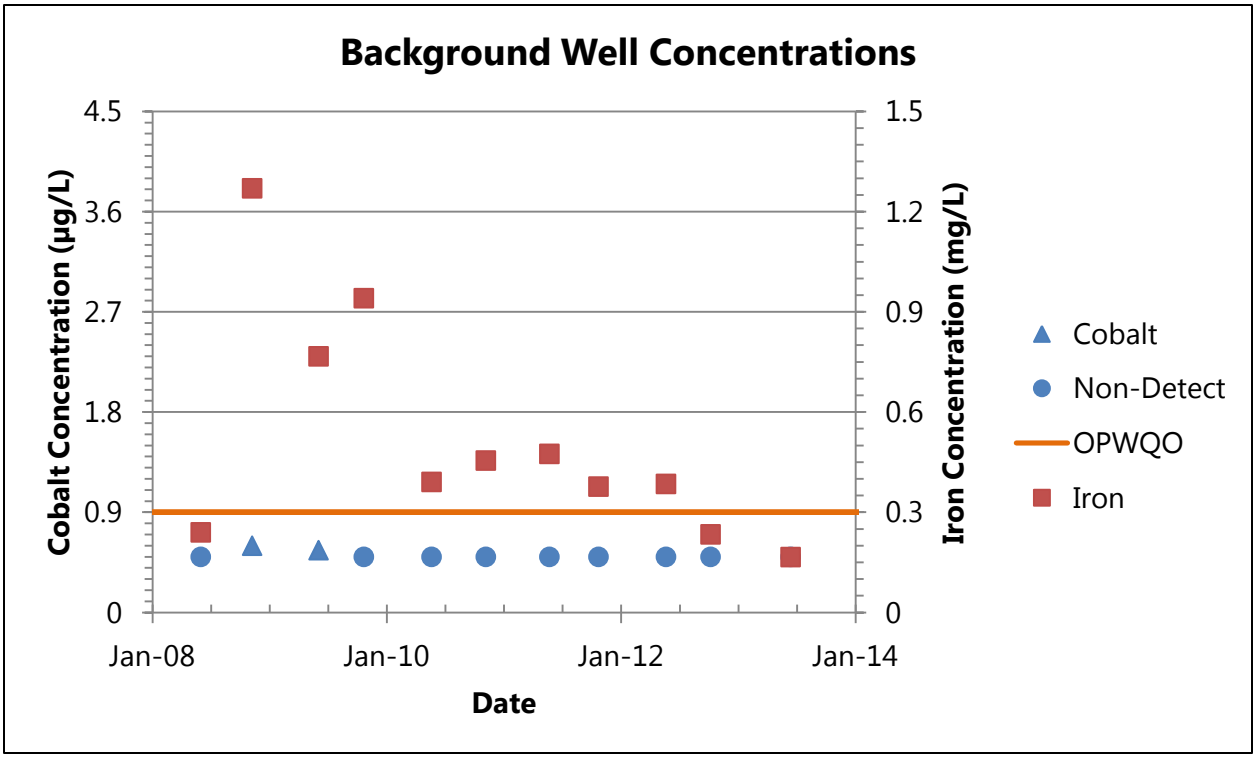

Figure 3.14 Dissolved Cobalt and Iron Concentrations in Background Well 96-GW-LF1

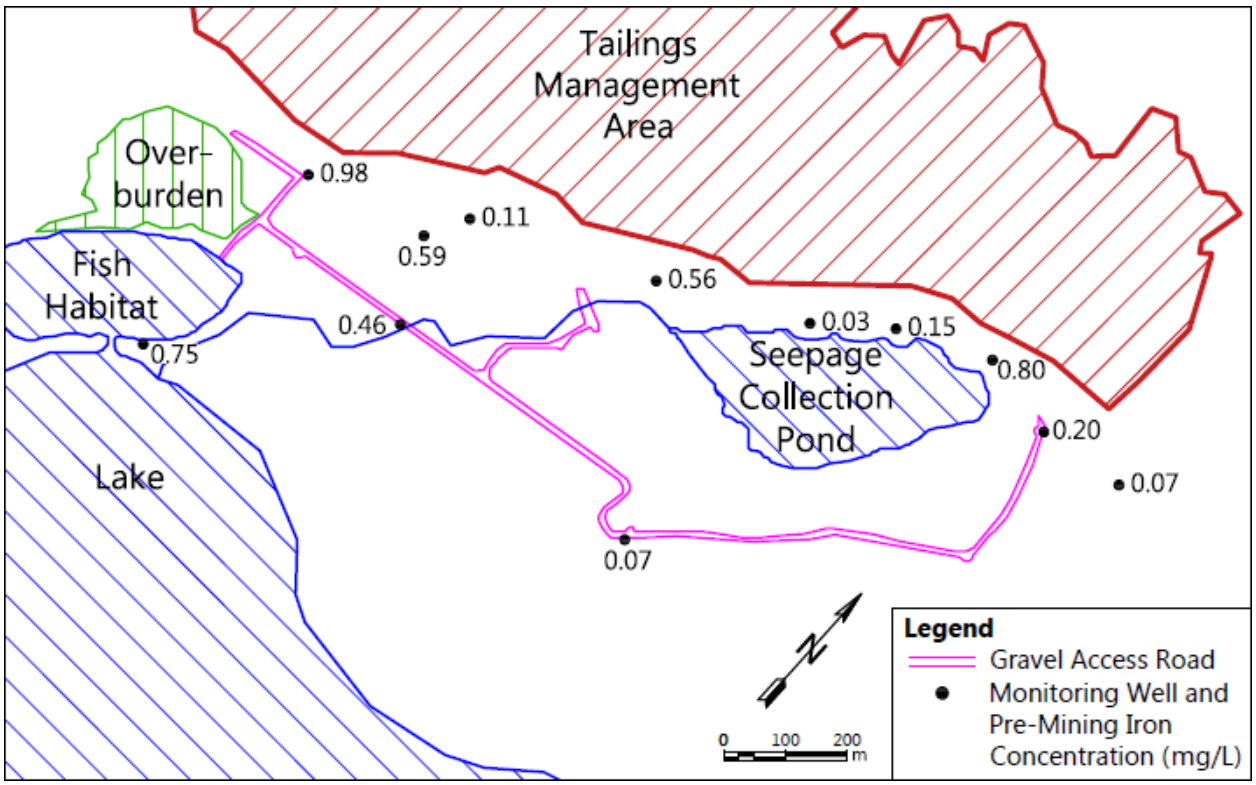

Figure 3.15 Pre-Mining Dissolved Iron Concentrations (1995 & 1996 Average)

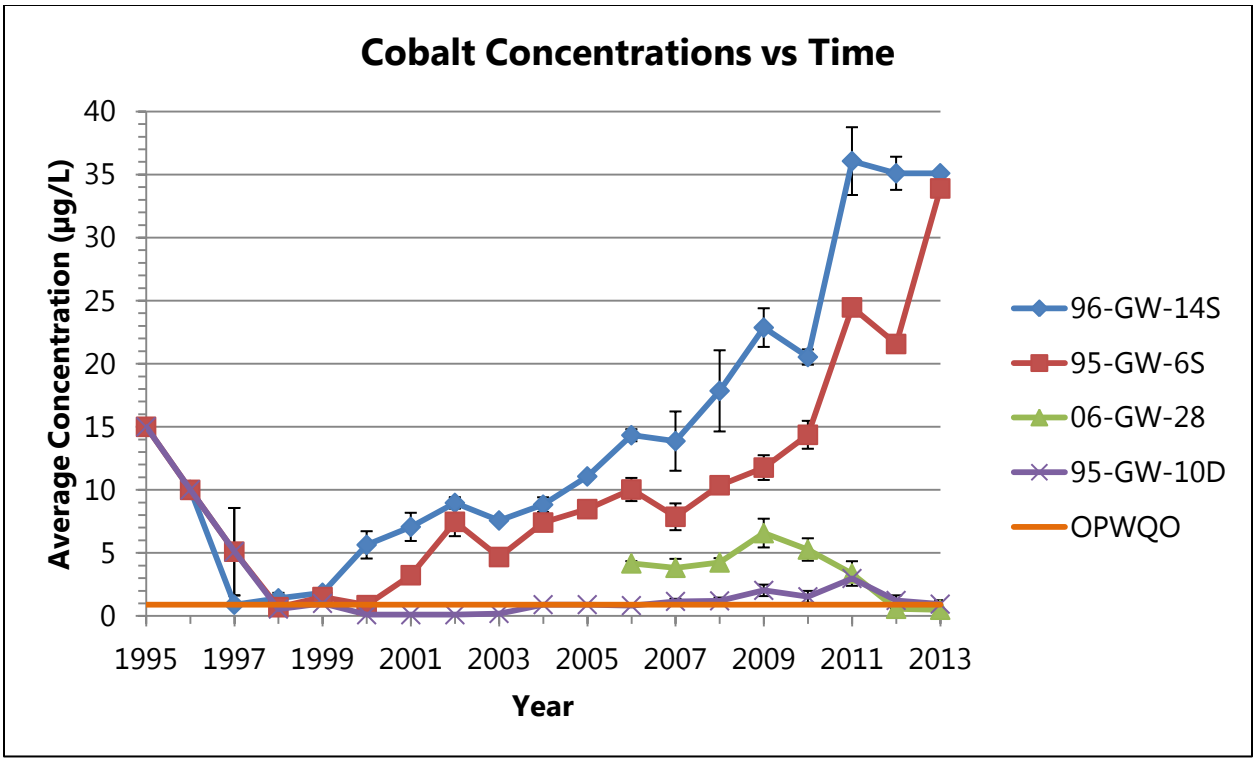

Figure 3.16 Yearly Average Dissolved Cobalt Concentrations

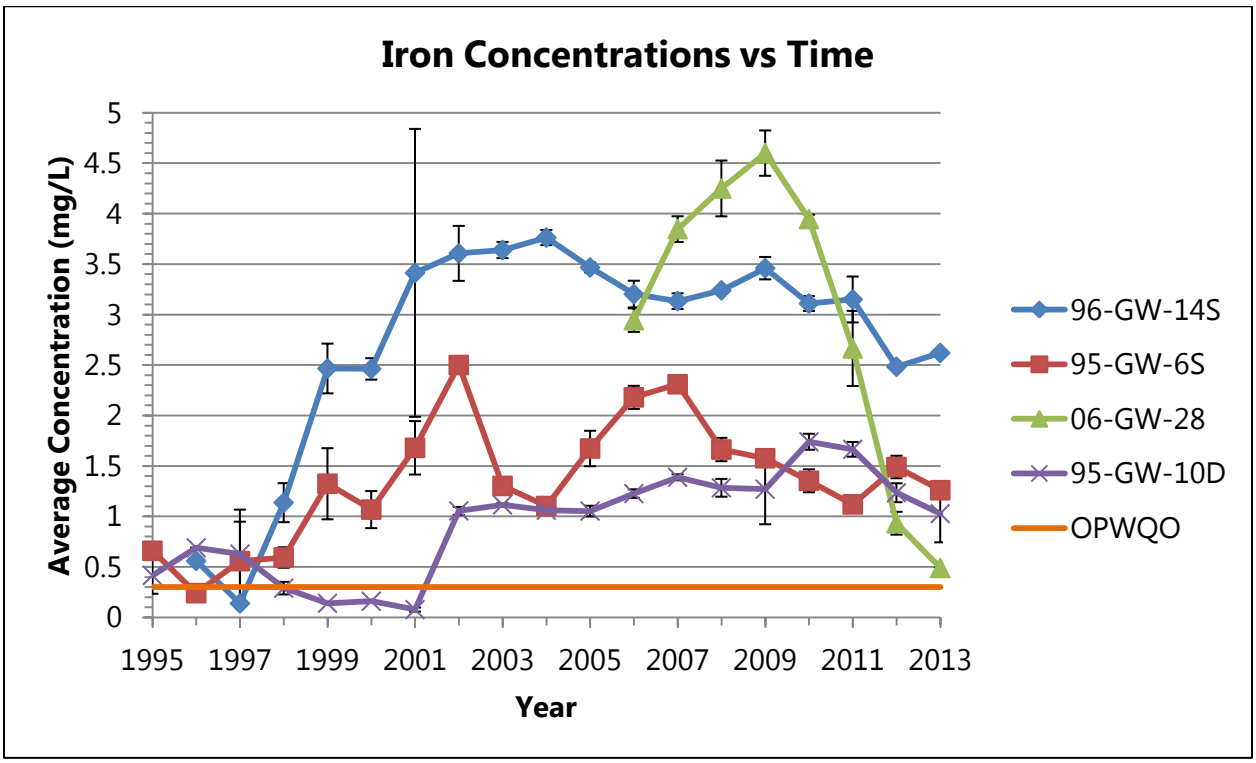

Figure 3.17 Yearly Average Dissolved Iron Concentrations

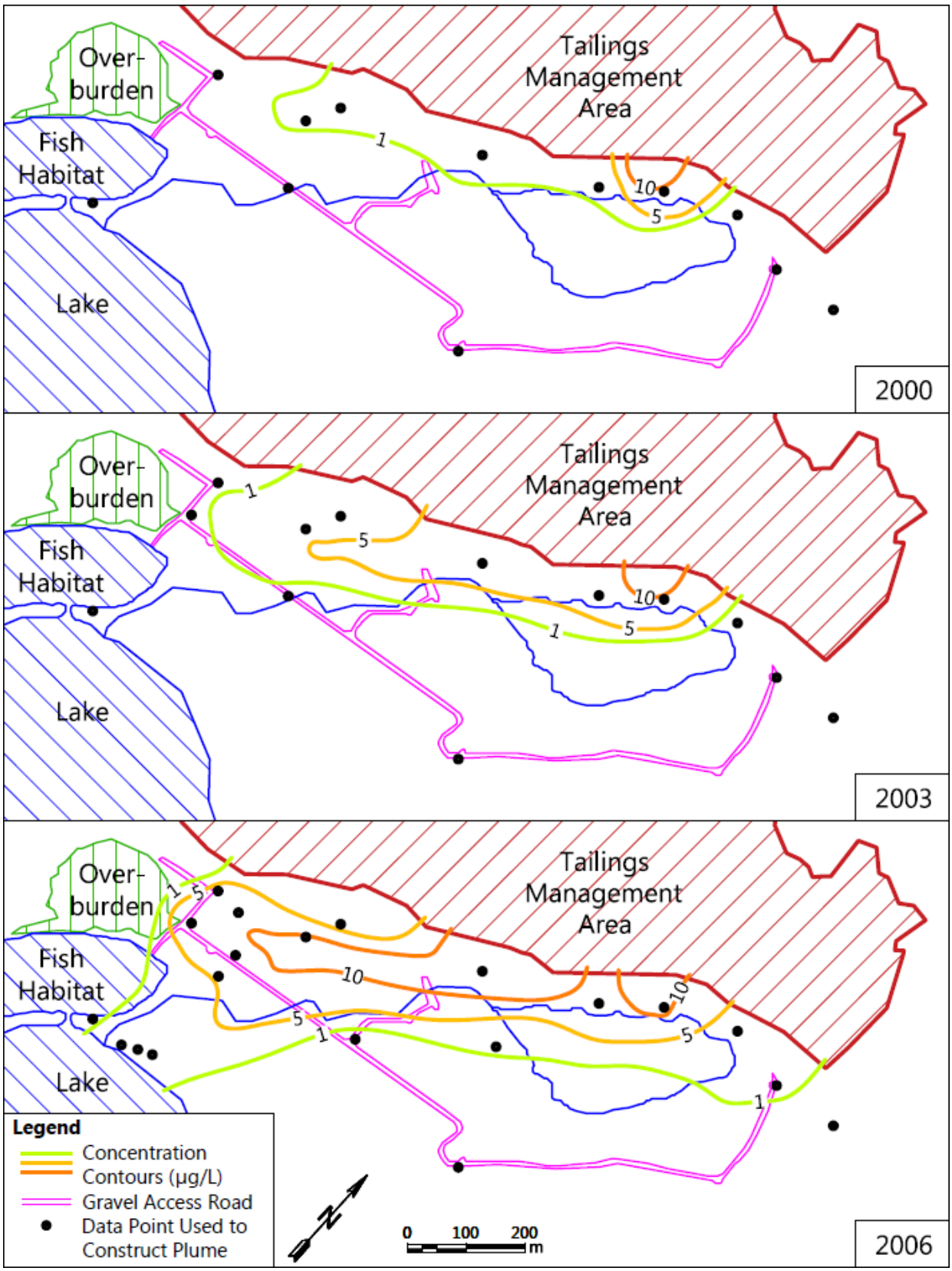

Figure 3.18 Cobalt Concentration Contours (2000, 2003, 2006)

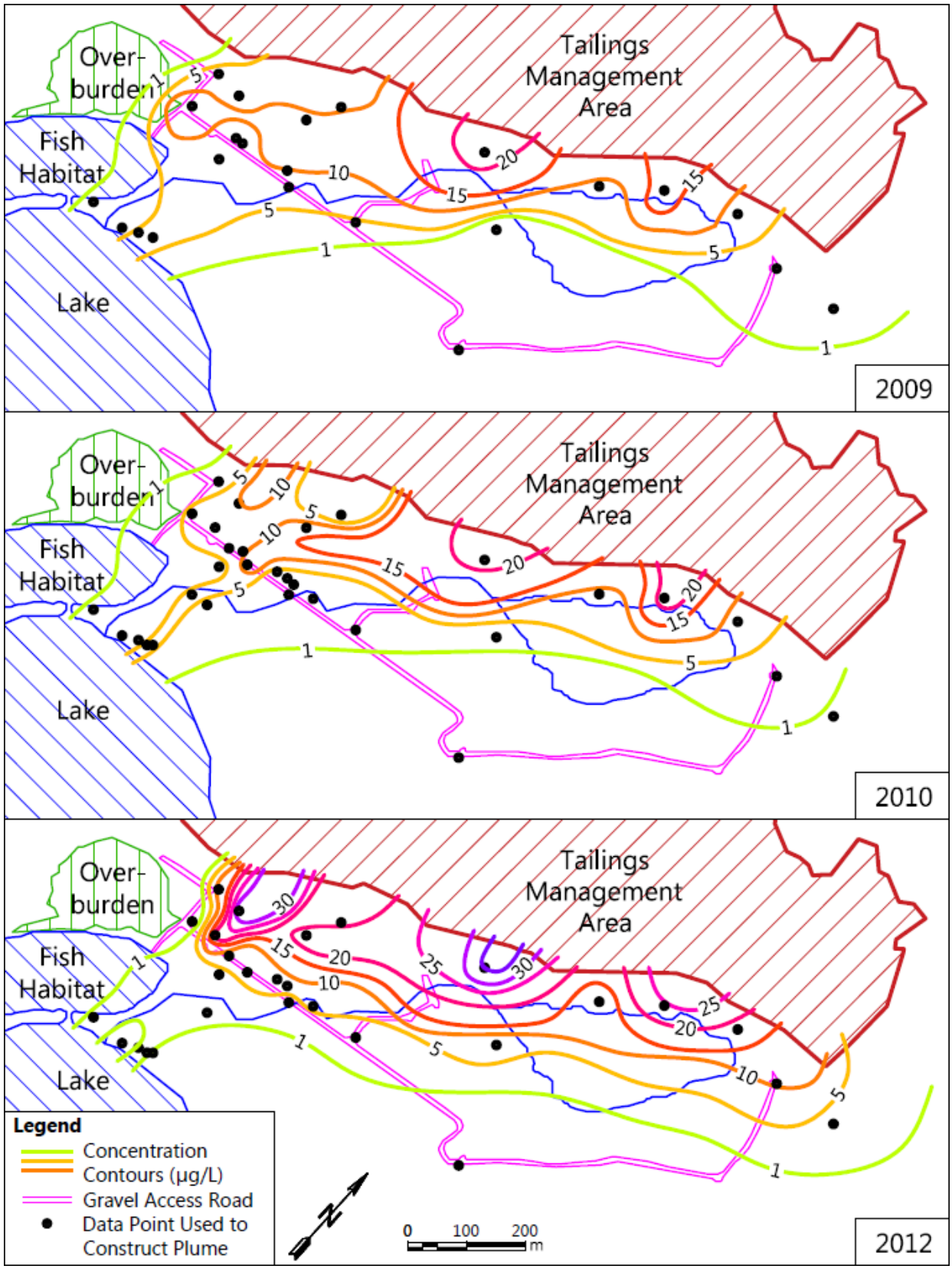

Figure 3.19 Cobalt Concentration Contours (2009, 2010, 2012)

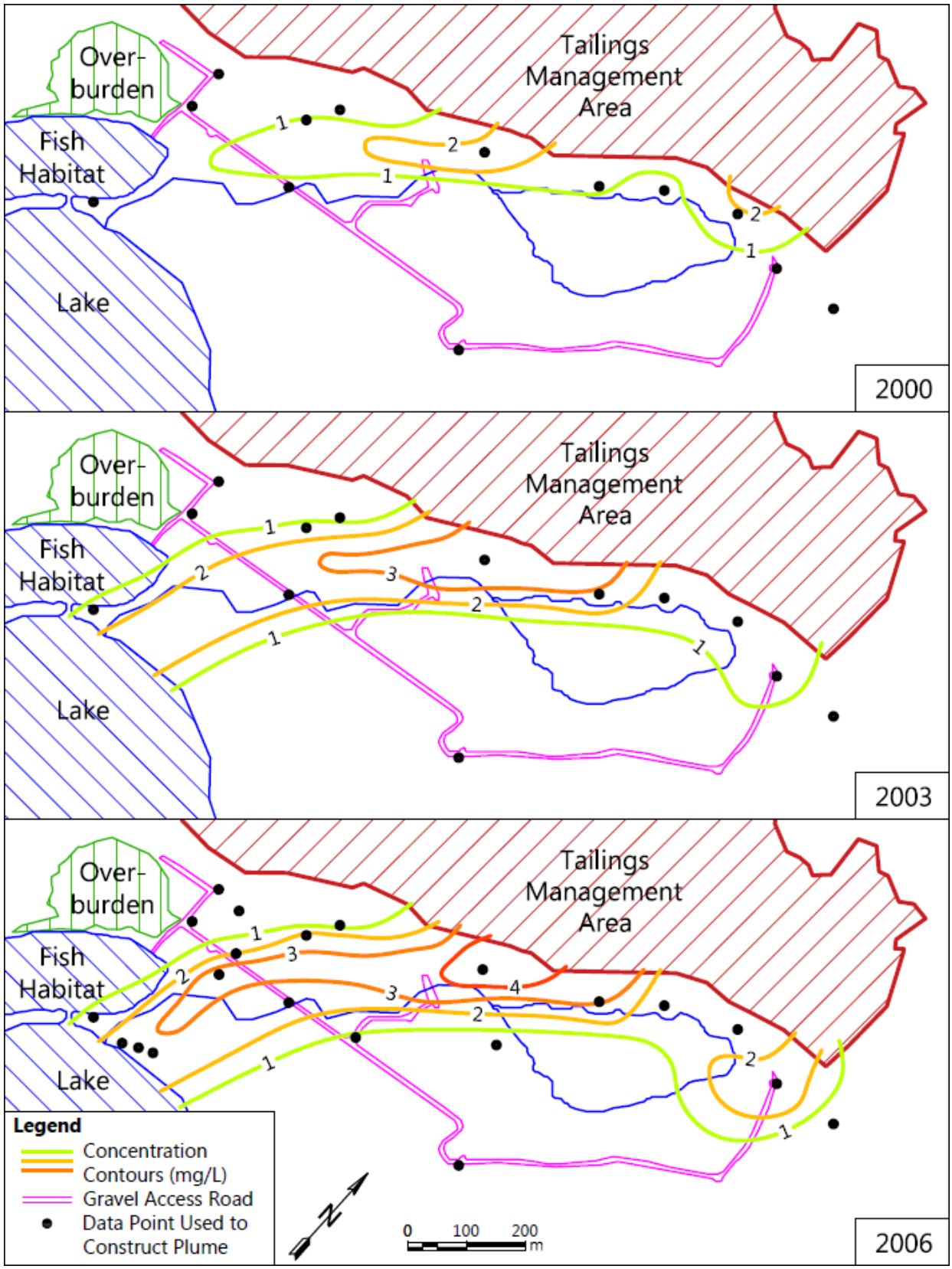

Figure 3.20 Iron Concentration Contours (2000, 2003, 2006)

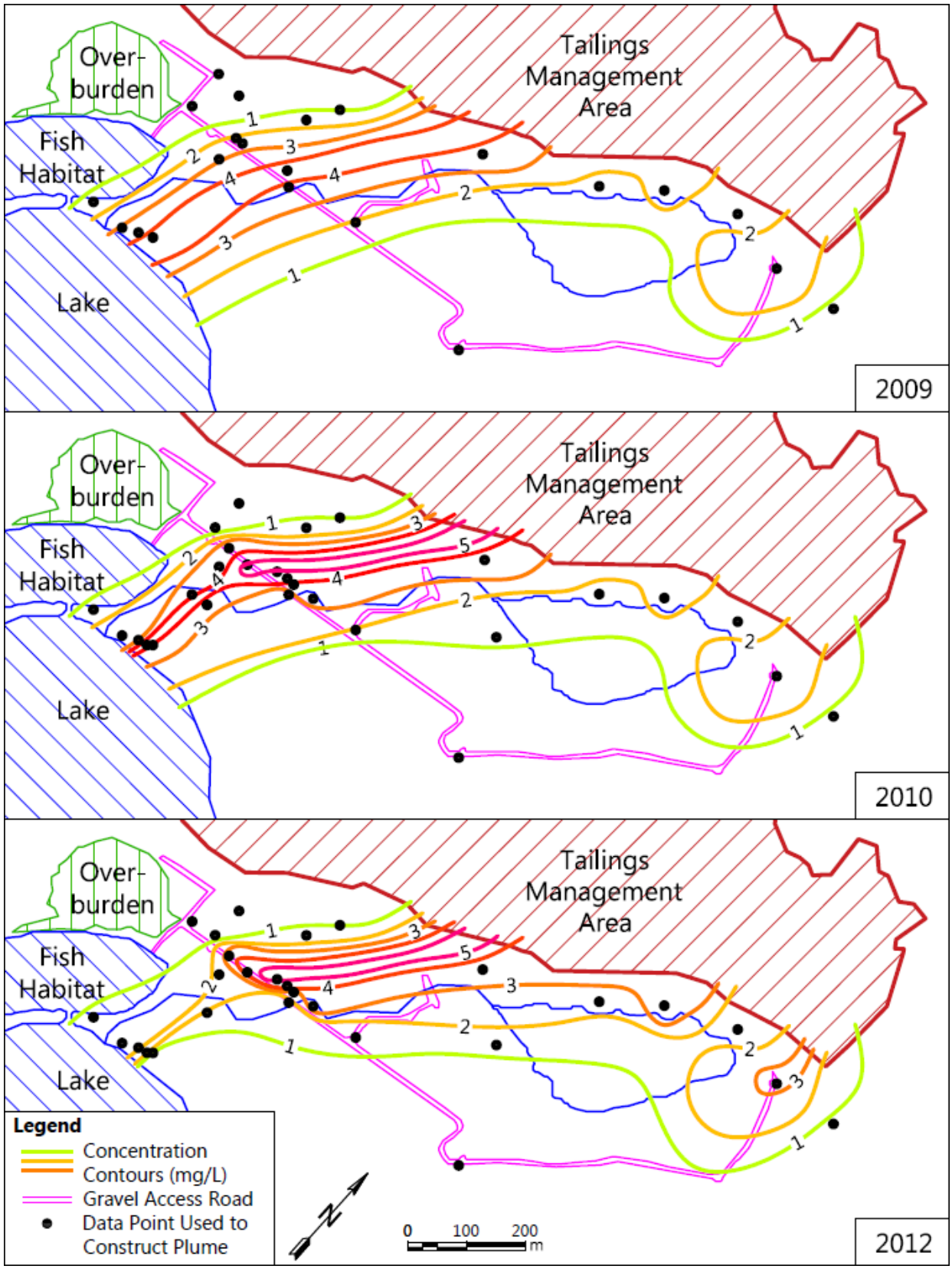

Figure 3.21 Iron Concentration Contours (2009, 2010, 2012)

4.0 GROUNDWATER FLOW MODELLING

Computer-based models, which are commonly used for simulating groundwater flow and contaminant transport, can be divided into two main categories. These two categories are based on the method which the software uses to solve the partial differential equations described in section 2.9. The two common methods of solution for these differential equations are numerical, and analytical. For the purpose of this project, only Visual MODFLOW engines, which calculate numerical solutions, have been used to simulate groundwater flow and contaminant transport.

4.1 MODELLING METHODOLOGY

The overall process of creating a numerical model to simulate groundwater flow and contaminant transport at a contaminated site is outlined in Figure 4.1. This methodology was followed throughout the modelling process for the Northern Ontario gold mine site as described below.

The first step in developing a groundwater flow and contaminant transport model is to determine the purpose of the modelling efforts, and to outline exactly what goals the model is intended to achieve. The purpose of modelling the Northern Ontario gold mine site was defined through the creation of six modelling objectives, which are described in section 1.2, and clearly outline the goals of this thesis project. The next two steps of site data collection and assessment, as well as the construction of a conceptual site model, have been completed, and are described in detail in chapter 3.0. A conceptual site model is a construction or

representation of the site's properties, and characteristics through the incorporation of descriptions, pictures, diagrams, tables, and any other medium which may aid in the understanding of the site, and the processes which are occurring within it (Alvarez & Illman, 2006).

Following these steps is the selection of the computational code which is to be used to perform the simulations. For this project, a well-known and commonly used groundwater flow and contaminant transport software known as Visual MODFLOW has been chosen. Visual MODFLOW, as described in section 2.9, is a well-recognised software package that contains a wide variety of numerical engines which can be utilized to perform tasks such as simulating the flow of groundwater, the transport of contaminants, and the movement of particles, as well as providing calibration assistance.

Once the above steps are completed, the construction of the numerical model may commence. The process of constructing the numerical model and selecting the simulation settings for the Northern Ontario gold mine site are described in section 4.2 below. This process involves defining the model extents, grid size, input parameters, and boundary conditions. Once the model is constructed, the specified input conditions can be simulated and the model can be calibrated.

Calibration of the model takes place in two steps; first calibration of the groundwater flow model, then calibration of the contaminant transport model separately. The calibration of the groundwater flow model is performed by first analyzing the results of the initial simulation, then systematically adjusting various input parameters in order to produce a more accurate fit

between the observed and calculated data. As noted in section 3.4, the potentiometric surface created from the April 2009 collected data is used to represent the hydrogeologic conditions of the site before the installation and activation of the pumping wells (1997-2009). For this reason, the April 2009 set of observed data are used for the calibration of the groundwater flow model. A detailed description of this process is provided in section 4.3 below.

Once the groundwater flow model is calibrated, it will then be put through a validation step. This is done by simulating an alternative set of data which has not been previously used for model calibration. This alternative data is usually a set of observations which were collected during a previously performed aquifer test, such as a pumping test or tracer test. If the calibrated model can accurately simulate an alternative data set without requiring further calibration, it is then considered to be validated. A validated model provides additional confidence in the simulation results, and is the best tool to be used for the prediction step. Validation of the groundwater flow model for the Northern Ontario gold mine site is attempted by simulating a parallel set of collected data without changing any input parameters. Since the data collected before the installation of the pumping wells are used for model calibration, an alternative set of data collected after the installation of the pumping wells are used for validation. In this case, the calibrated model will be used to simulate the effect of the pumping well installation without a change in input parameters, and its accuracy assessed.

Completion of the model validation process is followed by contaminant transport modelling. The process of constructing and calibrating a contaminant transport model is similar to the process used for a groundwater flow model, and is described in chapter 5.0. Following the

contaminant transport model calibration is a sensitivity analysis step, before prediction can commence. For the prediction stage, described in chapter 6.0, the model is used to simulate future scenarios, the results of which are typically used to accomplish the objectives of the modelling.

4.2 Model Construction, Inputs, and Boundary Conditions

Upon commencing the construction of the model, general simulation parameters such as numerical engine choice, flow type, and units must be specified. The general simulation parameters specified for the use of this project have been summarized in Table 4.1. Once the general parameters are input, model construction can commence.

4.2.1 Model Construction

The areal extent of the Northern Ontario gold mine site model was chosen to encompass the entire area between the tailings management area (TMA) and the lake, which is the area of the greatest interest for this project. The orientation of the model boundaries were chosen such that the lake encompasses the entire southern boundary and the TMA encompasses the majority of the northern boundary. The eastern and western boundaries of the model were chosen to extend slightly beyond the edge of the TMA in either direction. The overall dimensions of the model are 2040m wide and 1200m long. The model was then divided into 80 rows and 136 columns, creating a 15m x 15m grid. Figure 4.2 shows a plan view of the model's domain, range, and finite difference grid.

To simplify the site's geology, the model was divided into three layers, one to represent each of the main stratigraphic units found on the site as described in section 3.3, and shown by the geological cross sections of Figure 3.2. The top layer (layer 1) represents the silty-clay which covers the majority of the site and confines the aquifer. The second layer (layer 2) represents the sandy aquifer material, and the bottom layer (layer 3) represents the underlying glacial till and fractured bedrock surface which has relatively low permeability. The bottom of the model represents the dense, non-fractured bedrock which lies below the till and fractured rock layer. For the purpose of this model, the non-fractured bedrock is assumed to be impermeable, and creates the lower boundary of the simulated area.

The elevation of the top of layer 1 was estimated from the ground surface contours shown in Figure 3.1, and was input into the model as an array of points. The thicknesses of each layer, as well as the depth of contact between the layers, were interpolated from borehole logs. These stratigraphic data were input into the model as a series of points which provided the elevations of the layer contacts at each monitoring well location. Additional points were also created to assist Visual MODFLOW with extrapolation of the layer surfaces to areas of the model where no borehole log data were present. The elevations for the layer contacts at the created points were estimated based on the nearby subsurface characteristics and the surface topography. A summary of the input data which were used in the construction of the model layers is displayed in Table 4.2. Figure 4.3 shows cross section D-D' (column 78 of the model) which demonstrates the layout of the three modelled layers. The location of cross section D-D' can be seen in Figure 4.2. The location of cross section D-D' is very similar to geologic cross section C-C', displayed in Figure 3.2. Comparing cross sections of the model layers to previously constructed geological

cross sections created from site characterization data, provides a good method for determining the accuracy of the model construction. This method can help to determine if the thickness of the model layers is adequate to represent the geological conditions of the site.

4.2.2 INPUT PARAMETERS

The input parameters required for a groundwater flow model include hydraulic conductivity, specific storage, specific yield, and porosity. For the Northern Ontario gold mine site, initial estimates for the input value of these parameters were obtained through a combination of historical data, previous field investigation results, and values from literature.

Initial hydraulic conductivity estimates used for the Northern Ontario gold mine site model were obtained through a combination of historical in situ slug test and pumping test results, and published literature values. The top layer of the model, which represents the site's overlying silty-clay confining layer, was assigned a nearly uniform hydraulic conductivity value of $2x10^{-5}$ cm/s. This value was obtained from McKay et al. (1993), who proposed that it could be approximately representative of surface clay till which has been exposed to weathering, as discussed in section 2.7.1.1. Since the clay layer at the Northern Ontario gold mine site is found at the ground surface, it is also likely weathered and fractured, and was assumed to have a hydraulic conductivity value similar to that reported by McKay et al. (1993). However, a small portion of the top layer, north of the seepage collection pond, around well 96-GW-12, was instead assigned a hydraulic conductivity value which matched that of the sand layer below. This was done because site investigations showed that there was no overlying clay present in this location, as discussed in section 3.3. The portion of the top layer, which was assumed to

not have an overlying silty-clay layer and was assigned the same properties as the sand layer below, is outlined in Figure 4.4.

The initial hydraulic conductivity distribution of the sand layer was determined through examination of the reported slug test and pumping test results. As described in section 3.3, the slug tests performed in 1995, in the area adjacent to the TMA, yielded hydraulic conductivity values for the aquifer which were several orders of magnitude lower than those performed farther downstream near the pumping wells and adjacent to the lake. Additionally, as described in section 3.4, an abrupt change in hydraulic gradient is also observed between the northern and southern portions of the main flow path. For these reasons, the sand layer was divided into two main hydraulic conductivity zones. Figure 4.5 shows the initial distribution of the two conductivity zones within the second layer of the model. A hydraulic conductivity value of approximately $2x10^{-3}$ cm/s was determined from the slug tests performed in 1995, and was chosen to represent the sand layer in the northern portion of the site. The area of this zone covered the entire width of the model, and extended southward from the northern boundary, past the southern edge of the TMA, where the majority of the wells that were installed in 1995 are located, as well as beneath the SCP as shown in Figure 4.5. The sand layer in the central and southern portion of the site was assigned a hydraulic conductivity value of $1.5x10^{-1}$ cm/s, which is representative of the hydraulic conductivity values which were measured by slug tests and pumping tests performed around the pumping well locations.

The glacial till and fractured bedrock, which underlay the sand layer, are represented in the model by layer 3, and have been assigned a uniform hydraulic conductivity value of $2x10^{-5}$ cm/s.

This value is approximately representative of the hydraulic conductivity values reported in historical groundwater reports for both the till and the fractured bedrock surface, as discussed in section 3.3.

Specific yield and porosity values were determined from Table 2.1, as reported by Mays (2012). For layer 1, values between those reported for silt and those reported for clay were chosen to represent the silty-clay confining layer. Since the sandy aquifer was often noted as medium to coarse sand in the borehole logs, the values reported for medium-grained sand were used in layer 2. Layer 3 represents the underlying till, which is described in the borehole logs as hard, silty, and grey, and was therefore assigned values representative of a predominantly silty till.

A specific storage value for the sand layer of $2x10^{-4}$ 1/m was determined for the Northern Ontario gold mine site based on values reported from the pumping tests which were performed on the aquifer material. However, because the groundwater flow model is run under steady state conditions, a specific storage value is not required. When the simulation is calculated by the MODFLOW-2005 engine under steady state conditions, the time dependant head term on the right hand side of equation 2.16 becomes zero, and the specific storage term becomes unnecessary. Specific storage values are therefore not used in steady state simulations (Schlumberger Water Services, 2011). The value determined for the aquifer sand, however, was input into all layers of the model for the sake of completeness, in case a transient groundwater flow simulation was later desired. A summary of the initial input parameters used in the model is shown in Table 4.3.

4.2.3 BOUNDARY CONDITIONS

The elevations of the groundwater in the monitoring wells vary from season to season, however the general flow direction is very consistent. Since the groundwater flow direction does not change, and hydraulic gradients across the site do not change significantly, a steady state model has been chosen to represent the hydrogeologic condition of the site. The potentiometric surface created using groundwater elevation data collected on April 11th 2009 was chosen to represent the steady state flow condition prior to the installation of the pumping wells. This date was chosen because it represents the spring low groundwater condition, was collected in the most recent year prior to the installation of the pumping wells, and contains a relatively complete number of data points.

Four different boundary conditions were used in the groundwater flow model for the Northern Ontario gold mine site; constant head, no flow, river, and recharge boundaries. All of these boundary conditions were kept both spatially and temporally constant throughout the simulation time, since a steady state simulation was desired. Figure 4.6 shows the location of each of these boundary conditions within the model's domain and range.

A constant head boundary condition was assigned in the northern portion of the site along the edge of the TMA. The values which were assigned to this boundary were determined by extrapolating the April 2009 potentiometric surface, which was chosen to represent the steady state flow condition, as shown in Figure 3.9. The cells located between this line of constant head and the northern boundary of the model are outside the area of interest of the simulation, and were therefore assigned as inactive cells, as shown in Figure 4.6.

Two additional lines of constant head were also assigned in the northern portion of model, one along the eastern boundary, and one along the western boundary. These two constant head boundaries were assigned to correspond to the location of steep topographical inclines, as indicated by the ground surface contours in these areas (shown in Figure 3.1). The eastern and western constant head boundaries were assigned values of 295.5m and 294m, respectively. The remaining portions of the eastern and western boundaries were assigned as no flow boundaries because they are assumed to be approximately perpendicular to the flow of groundwater.

In the southern portion of the site, a constant head boundary was used to represent the influence of the lake on the surrounding groundwater. The constant head boundary was assigned along the edge of the lake, and given a value equivalent to the lake's water surface elevation. However, since the water surface elevation of the lake has never been measured and recorded, the value had to be estimated from the groundwater elevations measured in the wells located closest to the edge of the lake. For the groundwater flow condition being modelled, the surface of the lake was determined to be approximately 292.3m during April 2009. Similar to the northern boundary, the cells which are located between the line of constant head at the edge of the lake and the southern edge of the model were assigned an inactive condition.

The influence of the seepage collection pond and the fish habitat were approximated by assigning river boundaries to the top layer of the model, in the cells which corresponded to their locations. A river boundary allows the user to input values for the stage and bottom elevations of the water, as well as the conductance of the riverbed. For the seepage collection

pond, although the stage would be expected to vary with time, a nominal elevation of 293.5m was assigned to the model. This value was reported by Water Management Consultants (2005, 2007, 2008), and corresponds well with the existing ground surface contours in the surrounding area. The bottom elevation of the SCP was determined by assuming a constant depth of 1.05m. The maximum storage capacity and surface area of the SCP are reported to be approximately 80,000m^3 and 75,000m^2, respectively (Water Management Consultants, 2005). For this reason, the SCP was assigned a constant bottom elevation of 292.45m. The fish habitat was assigned a stage elevation of 292.3m, the same as that specified for the lake. A constant depth of 1m was assumed for the entire fish habitat by assigning a constant bottom elevation of 291.3m. Due to the quiescent nature of the SCP and fish habitats, as well as the silty-clay overlying the surrounding ground surface, the riverbed properties were input as 0.3m of silty-clay, with a hydraulic conductivity value of $2x10^{-5}$ cm/s for both locations. The river boundary condition allows the assigned cells to either gain or lose water depending on the calculated total head in the surrounding cells.

The recharge rate for the Northern Ontario gold mine site is expected to be low due to a number of factors, as discussed in section 3.5. Due to the reasons presented, a recharge rate of 30 mm/year (approximately 5% of the average yearly precipitation) was assigned across the majority of the model domain. In groundwater flow modelling, typical recharge rates range from 5% to 20% of the yearly precipitation collected on the site (Schlumberger Water Services, 2011). The small portion of the top layer which was assumed not to have an overlying silty-clay layer was assigned a recharge rate double that of the rest of the site (60mm/yr). In Visual MODFLOW, recharge rates are assigned, by default, to the top layer of the model. Additionally,

inactive or dry cells (cells which are located entirely above the top of the simulated groundwater table) in the top layer will cause the recharge value to be carried down to the layer below until an active cell is reached (Schlumberger Water Services, 2011). However, due to steep topographical rises in the northeast and northwest corners of the Northern Ontario gold mine site model, a large number of dry cells existed in all three layers of the model. This caused problems with the recharge parameter, and the model could not converge on a solution. To solve this issue, the recharge options were changed to have the recharge rate applied directly to the top of the sand layer (layer 2) only. The recharge is then only applied to the active wet cells in layer 2 of the model and represents surface water which was able to permeate the top silty-clay layer and enter the aquifer.

4.3 Modelling Results

Output results from the groundwater flow simulation include both potentiometric surface contours and groundwater velocity vectors. Determining the quality of the simulation results can sometimes be difficult to quantify, but is typically done in two ways. The first is by comparing the output of potentiometric surface contours to a potentiometric surface which was created from the measured groundwater elevations. Comparing the shape and distance between various contours can identify whether the simulated groundwater flow directions and gradients are similar to those which were observed. Secondly, in order to quantifiably measure the quality of fit of the simulated data, a calibration plot can be created. A calibration plot compares the actual collected groundwater elevation data (observed values) to the total head values simulated by the model for the cells in the same location as the monitoring wells

(calculated values). By directly comparing these two sets of values, the amount of error (residual) at each data point can be determined. A residual is the numerical difference between the observed value and the calculated value at each monitoring well location. By minimizing the maximum and average residuals in the model, a better fit between the observed and simulated data sets can be obtained.

The output model results in this section are therefore presented as both simulated potentiometric contours output from the sand layer and as calibration plots which compare the calculated and observed values from the well screen locations. In the figures which present the simulated potentiometric contours, inactive cells are highlighted in blue and dry cells are highlighted in olive green. The simulated potentiometric surface contours are shown in 0.1m intervals, are displayed as navy blue lines, and are labelled with elevations in meters above sea level.

4.3.1 INITIAL SIMULATIONS

Initial Visual MODFLOW simulations were performed using the input parameters and boundary conditions described above. In the initial simulation a very simple hydraulic conductivity distribution was assumed, where the sand layer (layer #2) was divided into just two hydraulic conductivity zones, as described in section 4.2.2, and shown in Figure 4.5. The simulation using these initial values gave the potentiometric contour distribution within the sand layer shown in Figure 4.7. Comparing these simulated contours to the estimated potentiometric contours from April 2009 displayed in Figure 3.9 shows a fairly good match in the contour shape, with the groundwater flow direction bending westward in the central portion of the site.

To quantifiably measure the fit of the simulated data, the actual collected groundwater elevation data from April 11th 2009 (observed values) is compared to the total head values simulated by the model for the cells in the same locations as the monitoring wells (calculated values). Figure 4.8 shows the calibration plot for the 19 observed data points versus the calculated value for their corresponding location in the model. This plot shows that a maximum residual of -0.472m was calculated at well 95-GW-1S, which represents 19.3% of the total observed head drop across the site (2.44m between wells 96-GW-13 and 06-GW-27). Ideally, a groundwater flow simulation should produce residuals which are less than 10% of the site's total head drop. Additionally, it can be seen that the residual mean of -0.181m and the absolute residual mean of 0.181m have the same magnitude. This indicates that the value of the residual at every calibration point is negative (the calculated value is lower than the observed value). This can also be seen by the fact that all of the data points lie below the solid blue 45° line on the plot. Ideally, a calibrated simulation would produce a balance of residuals which were both positive and negative, and would therefore produce a residual mean which was much lower than the absolute residual mean. Since the initial simulation produced relatively large residuals, and the calculated data did not accurately represent the observed data, the model must not be accurately representing the actual conditions of the site, and therefore needs to be improved through the calibration process.

4.3.2 CALIBRATION

Calibration of a groundwater flow model is accomplished by adjusting the value of input parameters and boundary conditions in order to improve the quality of fit between the

calculated and observed data points. The goal of calibration is to achieve the best possible correlation between the observed and calculated values, in order to ensure that the simulated groundwater flow pattern closely matches the actual flow at the site. Consequently, many of the initially estimated input parameters are often changed before the best calibration is achieved.

For the Northern Ontario Gold Mine Site model, the calibration process was approached by considering the main sources of error due to the estimation of the input parameters or boundary conditions. One possible source of error was in the estimation of the constant head values used for the northern boundary condition applied along the edge of the TMA. These values were estimated from Figure 3.9, the potentiometric surface which was approximated from the April 11th 2009 observed groundwater elevations. Since these values were approximations of extrapolated data, they may not accurately represent the actual conditions of the site. For this reason, the distribution of the constant head values along this northern boundary was manually edited. The values were adjusted in a systematic manner to achieve a better fit between the observed and calculated data from the initial simulation. Although this method was effective in improving some of the residual values, it only had a noticeable effect on the wells located immediately adjacent to the TMA.

Another possible reason for the initial simulation not accurately representing the actual site conditions was due to the oversimplification of the hydraulic conductivities in the sand layer. As discussed in section 4.2.2, and shown in Figure 4.5, the sand layer was divided into just two hydraulic conductivity zones in the initial simulation. However, the actual condition of the sand

layer beneath the site is likely much more complicated than can be accurately modelled by just two hydraulic conductivity zones. It is therefore likely that the distribution of hydraulic conductivity values in the initial simulation does not accurately represent the actual condition of the sand layer beneath the site. For this reason, an intermediate groundwater flow model containing additional hydraulic conductivity zones was created. A trial-and-error approach was taken to create the zones, with the goal of reducing the residuals of the wells in the central portion of the site. The size, shape, and value of the different hydraulic conductivity zones were edited one by one, while monitoring the effect that the changes had on the quality of fit.

The numerical value and spatial distribution of the hydraulic conductivity zones within the sand layer are shown in Figure 4.9. The variation in the hydraulic conductivity values assigned to these zones was generally limited to one order of magnitude from the originally estimated value; however this was not possible in one location. Due to the large degree of westerly flow in the central portion of the site, as determined through the observed groundwater elevations and shown by the groundwater flow direction arrows in Figures 3.9, 3.10, and 3.12, the southerly groundwater flow in this area of the model needed to be limited. This was accomplished by creating a zone adjacent to the lake (zone 12) which had a notably lower hydraulic conductivity value compared to the zones up-gradient. The creation of zone 12 was necessary to sufficiently cause the bending of the potentiometric surface contours in this area, and to improve the calibration of the simulated values to the observed groundwater elevations. The result of adding the new hydraulic conductivity zones to the model was a simulated potentiometric surface which more closely matches the April 2009 observed groundwater data. Figure 4.10 shows the output potentiometric surface contours from the sand layer simulated by

the manually calibrated intermediate groundwater flow model. The calibration plot for these results is shown in Figure 4.11, which indicates a maximum residual of 0.11m at well 06-GW-25, and an absolute mean residual of 0.053m. This maximum residual corresponds to only 4.5% of the total head drop across the model, which is well below the targeted 10%. Additionally, a better balance between positive and negative residuals was obtained, however the calibration plot indicates that a large majority of the residuals are positive. The results of the manually calibrated groundwater flow model were regarded as being very promising, and this case was used to continue to automatic calibration.

The last step in the calibration process was the use of the PEST software package to further minimize the residual values by varying the hydraulic conductivity values in various zones. Figure 4.12 shows the final distribution of the hydraulic conductivity values used in the calibrated groundwater flow model. This calibrated model produces an output potentiometric surface, shown in Figure 4.13, which very closely matches the observed conditions demonstrated by the April 2009 data. The calibration plot for the final calibrated model reveals the quality of fit between the data sets, and is shown in Figure 4.14. The calibrated model has a maximum residual head value of -0.091m at well 95-GW-10D, and an absolute mean residual of 0.033m. When compared to the total head drop across the site of 2.44m between wells 95-GW-13 and 07-GW-28, these errors represent a maximum and average of 3.7% and 1.4%, respectively. Table 4.4 summarizes the observed head, calculated head, and residual values of each calibration point for the final calibration of the April 2009 groundwater flow model. It is important to note that the maximum residual was experienced in well 95-GW-10D, which, even though it is located adjacent to the lake, consistently had measured water level values

approximately 0.1-0.15m higher than the other wells also located adjacent to the lake (wells 09-GW-26, 06-GW-27, 06-GW-28, and 10-GW-40). For this reason, well 95-GW-10D was considered anomalous, and regarded with lesser importance during the calibration process.

It is important to note that, except for zone 12, as discussed earlier, the final hydraulic conductivity values used in both the manually calibrated and PEST calibrated model agree with the initial estimated conductivity values within one order of magnitude. For comparison, Table 4.5 presents the initial, intermediate, and final conductivity values for each of the 15 zones.

4.4 VALIDATION

Once a calibrated groundwater flow model is established, which produces acceptable residual values using reasonable input conditions, the model is typically put through a validation step. Model validation is typically accomplished by using the calibrated groundwater flow model to simulate the observed results of a tracer test or pumping test. In order for this simulation to confirm the validity of the model, the alternative observed data set which is used as a comparison must not have been used during the model calibration. The objective is to assess if the model's response to the simulated test is the same as the response which was actually observed on the site when the test was performed. If the model is able to accurately simulate the change of conditions, it is considered validated, and can more confidently be used to simulate future scenarios.

For the Northern Ontario gold mine site, the commencement of the seven pumping wells in 2009 creates a change in the groundwater flow pattern in the central area of the site, very similar to a pumping test. The aquifer's response to the commencement of these pumping wells

was described in section 3.4, and the altered groundwater flow pattern is shown by the April 2011 potentiometric surface in Figure 3.12. Since only the April 2009 data were used to calibrate the groundwater flow model, the April 2011 observed groundwater elevations represent an alternative data set which can therefore be used for model validation. The methodology for model validation in this project is to introduce the input conditions of the seven pumping wells into the April 2009 calibrated model, and simulate the model's response to the change in conditions. The output of the validation simulation will then be compared to the actual response of the Northern Ontario Gold Mine site as observed through the April 2011 collected data.

The seven pumping wells which were installed on the Northern Ontario Gold Mine site are situated in a line along the gravel access road approximately half way between the TMA and the lake. The pumping rates at which these pumping wells have been run since they started operation in the spring of 2009 have remained seasonally variable, and independent of one another. Therefore, since the flow rates from the pumping wells vary with time, and the groundwater flow model is a steady state simulation, a single value which is approximately representative of the pumping condition needed to be determined for each well. In order to determine a pumping rate which could be input into a steady state model, a seasonal average was used. The pumping rates which were input into the model were determined by averaging the daily pumping rates collected over a year long period for each well. Table 4.6 summarizes pumping rate and screen elevation data which was input into the April 2009 calibrated groundwater flow model during model validation.

The response of the April 2009 calibrated groundwater flow model to the addition of the seven pumping wells running at average pumping rates is shown by the simulated potentiometric surface in Figure 4.15. This figure displays a groundwater flow pattern that is very similar to that presented by the April 2011 potentiometric surface, as shown in Figure 3.12. The quality of fit between the output potentiometric surface of the validation simulation, and the April 2011 observed data is shown through the calibration plot in Figure 4.16. From this figure we can see that this simulation produces a maximum residual value of -0.286m at well 96-GW-14D, and an absolute mean residual of 0.080m. Although most of the data points seem to fit relatively well, this calibration plot has a much higher margin of error than that of the April 2009 final calibrated model (presented in Figure 4.14). The observed data, calculated data, and residual values for each data point are also displayed in Table 4.7. By examining Figure 4.16 and Table 4.7, we can see that the majority of the error is due to discrepancy in the wells with high total head values (wells 95-GW-4, 96-GW-11, 96-GW-13, 96-GW-14, and 96-GW-17), which are located far from the location of the pumping wells. It should be noted that these are also the Northeastern wells which demonstrated a slightly different hydrogeologic pattern that the majority of the site's wells, as described in section 3.4. If these wells were to be removed from the plot, and only the wells within the influence zone of the pumping wells were to be considered, the maximum residual would be 0.113m in well 04-GW-21 and the absolute mean residual would be 0.047m, as seen in Figure 4.17. This indicates that the error for the remaining 23 data points within the area of greatest importance of the model is actually relatively small. It is also important to note that the maximum residual was experienced in well 04-GW-21, which, even though it is located approximately half way between the pumping wells and the TMA,

consistently had measured water level values approximately 0.05-0.12m lower than the wells located directly adjacent to the pumping wells (wells 00-GW-19, 09-GW-31, and 09-GW-32). For this reason, well 04-GW-21 was considered anomalous, and regarded with lesser importance during the model validation process.

In order to further explain the error in the initial validation step, it is also important to note that the boundary conditions of the April 2009 final calibrated groundwater flow model were not changed during the initial validation step, even though a completely new set of observed data was compared to the simulated data. This kind of comparison would require the unreasonable assumption that all of the boundary conditions for the entire site were exactly the same during the April 2009 and April 2011 data collection periods. To further examine the inaccuracy in the calibrated model's response to the pumping well insertion, and the importance of the boundary conditions, we can more closely examine the collected data from these two time periods. If we compare these two data sets, as tabulated in Table 3.1, there is an important similarity, and two important differences that can be observed.

The most important similarity is seen in the wells located closest to the lake. We can see that at each of these time periods, the observed groundwater elevation values adjacent to the lake are approximately the same. If it is assumed that these wells provide a good indication of the actual water level in the lake at the time of data collection, then we can conclude that the lake level was at approximately the same elevation when each of these data sets was collected. This is an important consideration because it ensures that we are comparing two data sets which could use the same lake boundary condition.

On the contrary, there are also two important differences between the two data sets, which contribute to the inaccuracy of the model's response to pumping wells. The first of these differences is seen in well 96-GW-13, which also has the highest observed head value of any well on the site. This well is located approximately 772m from the nearest pumping well, and would not be expected to be influenced by the pumping. The empirical relationship of equation 2.18 in section 2.10.1 was used to estimate the radius of influence of the pumping wells at the Northern Ontario gold mine site. Using conservative estimates for both the conductivity of the aquifer material (0.3 cm/s) and the amount of drawdown created by the pumping (1.0m), a radius of 164m was calculated from equation 2.18. This conservative estimate for the pumping well radius of influence is less than 25% of the distance from the closest pumping well to monitoring well 96-GW-13. Although well 96-GW-13 is estimated to be outside the influence zone of the pumping wells, the observed value reported for this well in 2011 is 0.23m higher than it was reported in 2009. This is not necessarily surprising considering the fact that the upstream head values at this site are likely controlled by variables outside the domain of this model, such as rainfall and snow melt, which vary yearly. The second difference is seen in well 96-GW-11. This well is located in the easternmost portion of the site, approximately 1163m from the nearest pumping well, and also not expected to be affected by the pumping. However, the observed value reported for this well in 2011 is 0.17m lower than it was reported in 2009. Similar to the last case, this well is also very likely to be controlled by factors outside the model domain. It is important to note that there is a pond located approximately 360m to the northeast of well 96-GW-11 which stands at a much higher elevation. The water level of this

pond likely has a large influence on the eastern site boundary and the water levels observed in this well.

In order to provide a more realistic comparison to the April 2011 data, the boundary conditions of the groundwater flow model must be adjusted to accurately represent the actual boundary conditions that the site was experiencing at the time of measurement. In order to accomplish this, the constant head boundary condition in the northern portion of the site needed to be slightly raised, and the eastern constant head boundary condition slightly lowered. However, it is important to note that the western and southern constant head boundary conditions as well as the river boundaries, no flow boundaries, recharge rates, and all other input parameters were held constant.

The new response of the groundwater flow model with adjusted boundary conditions to the input of the pumping wells can be seen through the simulated potentiometric surface displayed in Figure 4.18. This figure is very similar to the direct response of the April 2009 calibrated model shown by the potentiometric surface in Figure 4.15, with the groundwater flow directions being nearly identical. However, as seen in Figure 4.19, the calibration plot of the model with adjusted boundaries shows a much better quality of fit between the observed and calculated values. This simulation produces a maximum residual of -0.124m in well 96-GW-13, and an absolute average residual of just 0.055m, which is only 0.022m greater than that produced by the April 2009 final calibrated model. Table 4.7 summarizes the observed head, calculated head, and residual values of each calibration point for the final validation simulation of the April 2011 groundwater flow model. For its ability to accurately simulate the effect of the

pumping wells on the groundwater flow conditions, this groundwater flow model should be considered validated.

4.5 PARTICLE TRACKING

Particle tracking is a useful tool in groundwater flow simulations to trace the movement of imaginary particles through the site's subsurface. Particles can be traced either forwards, to determine the destination of a particle from a given source, or backwards, to determine the source of a particle that is detected at a given destination. This can also be a great tool for identifying preferential flow paths through the aquifer.

To test the simulated flow patterns on the Northern Ontario gold mine site, a line of particles was assigned to the sand layer (layer 2) along the edge of the TMA. These imaginary particles would represent particles of a dissolved contaminant which made their way from the TMA through the low permeability clay and into the sand aquifer in this location. The starting location of the particles, as well as their resulting flow path lines are shown in Figure 4.20. The particles were tracked for a simulation period of 12 years, which would represent the distance that any dissolved contaminant would have been able to travel between the beginning of tailings deposition in the TMA and the installation of the pumping wells (1997 to 2009). The path lines of each particle are also marked with an arrow which represents their location at 1 year intervals. As we can see from this figure, only particles from a few certain regions of the TMA were able to reach the edge of the lake within a 12 year time frame. It is also important to note that the particle tracking engine allows the particles to move by advective flow only, and does not consider any retardation that the actual dissolved contaminants may encounter.

These particles therefore represent the absolute maximum extent that any contaminant which originated in the TMA would have been able to travel by year 2009. Examination of the simulated path lines shows that the speed and route that the particles travel are directly affected by the distribution and magnitude of the hydraulic conductivity zones and hydraulic gradients in the calibrated model.

Parameter	Input
Flow Type	Saturated Constant Density
Flow Engine	MODFLOW 2005
Transport Engine	MT3DMS
Units:	
Length	m
Time	Days
Conductivity	cm/s
Pumping Rate	m^3/d
Recharge	mm/yr
Mass	kg
Concentration	µg/L

Table 4.1 General Simulation Parameters

Well Name	Model Co-ordinate (m)		Elevation (masl)			
	X	Y	Surface	Top of Sand	Top of Till	Top of Bedrock
95-GW-1S,D	1169.44	579.04	298.35	297.74	292.11	286.57
95-GW-2S,D	713.67	790.21	294.15	291.41	286.23	284.40
95-GW-3S,D	494.22	970.15	294.15	287.75	282.42	280.01
95-GW-4S,M,D	1754.57	963.25	296.75	293.40	286.08	273.34
95-GW-6S,D	703.04	937.83	293.95	288.77	283.19	282.12
95-GW-10S,D	330.09	625.38	293.05	287.87	278.58	268.37
96-GW-11	1897.28	921.48	299.22	298.46	-	-
96-GW-12	1638.30	1046.20	296.44	296.44	-	-
96-GW-13	1474.21	1043.35	296.32	293.22	-	-
96-GW-14S,D	1082.49	990.72	294.61	290.95	-	279.37
96-GW-15S,D	763.77	981.56	294.88	293.05	283.86	280.76
96-GW-16S,D	353.56	999.42	294.81	290.85	-	283.68
96-GW-17	1339.91	1006.37	296.30	291.12	-	-
00-GW-19	462.82	887.02	294.51	289.32	-	-
06-GW-24	553.91	798.59	293.98	289.78	286.08	-
06-GW-25	1162.28	848.06	295.00	287.40	-	286.80
06-GW-25A	1153.46	874.20	295.00	284.90	282.70	-
07-GW-29	590.54	846.63	297.00	294.60	-	284.80
07-GW-30	699.51	822.51	295.00	292.00	-	286.20
07-PW-01	593.33	843.13	294.00	289.70	-	283.00
07-PW-02	696.66	828.25	298.00	295.00	-	289.50

- No Data Available

Table 4.2 Layer Input Data

Well Name	Model Co-ordinate (m)		Elevation (masl)			
	X	Y	Surface	Top of Sand	Top of Till	Top of Bedrock
09-PW-3	491.78	876.00	295.26	287.10	-	279.80
09-PW-4	541.45	860.82	295.16	287.00	-	280.70
09-PW-5	591.59	846.04	295.76	291.50	-	284.80
09-PW-6	641.23	831.15	296.04	291.30	-	284.60
09-PW-7	691.01	816.31	295.29	291.00	-	288.00
09-PW-8	740.80	801.25	295.18	291.50	286.90	286.40
09-PW-9	617.00	838.32	295.28	290.40	284.20	-
09-GW-31	518.80	875.08	294.39	289.20	281.60	-
09-GW-32	561.39	842.96	295.05	290.20	284.40	-
09-GW-33	609.19	822.43	294.10	290.10	285.90	-
09-GW-34	674.54	828.81	294.47	290.80	-	286.00
09-GW-35	716.88	814.56	295.20	291.50	287.70	-
09-GW-36	766.04	799.57	294.86	289.40	286.70	-
09-GW-37	518.14	724.13	293.43	289.60	284.30	-
09-GW-38	555.87	713.35	293.82	290.20	285.60	-
09-GW-39	602.87	698.21	294.06	290.60	285.60	-
10-GW-40	462.37	590.84	293.67	289.60	284.50	-
Created-1	1812.00	1042.00		292.65	285.33	273.5
Created-2	1642.00	704.00		299	292.47	287.13
Created-3	1507.00	129.00		288.93	283.83	278.29
Created-4	967.00	275.00		297	290.47	285.13
Created-5	686.00	382.00		288.93	283.83	278.29
Created-6	1282.00	330.00		299.7	293.17	287.83
Created-7	1282.00	173.00		288.93	283.83	278.29
Created-8	1642.00	455.00		299	292.47	287.13
Created-9	445.00	1192.00		293	283.6	280.3
Created-10	84.00	1162.00		306	300.37	294.83
Created-11	1835.00	1192.00		293.7	284.3	281
Created-12	2006.00	1162.00		302	296.37	290.83
Created-13	1972.00	547.00		298.7	292.47	286.83
Created-14	1957.00	67.00		288.93	283.83	278.29
Created-15	68.00	460.00		287.82	278.53	268.32

- No Data Available

Table 4.2 Layer Input Data (continued)

Parameter	Input
Extent of Model in X-Direction	2040m
Extent of Model in Y-Direction	1200m
Number of Rows	80
Number of Columns	136
Cell Dimensions (ΔX x ΔY)	15m x 15m
Number of Layers	3
Specific Storage (S_s)	$2x10^{-4}$ 1/m
Specific Yield (S_y):	
Layer 1 - Silty Clay	5%
Layer 2 - Sand Aquifer	28%
Layer 3 - Till	6%
Porosity:	
Layer 1 - Silty Clay	44%
Layer 2 - Sand Aquifer	39%
Layer 3 - Till	34%
Recharge Rate	30 mm/yr
Hydraulic Conductivity:	
Layer 1 - Silty Clay	$2x10^{-5}$ cm/s
Layer 2 - Sand Aquifer	Varied
Layer 3 - Till	$2x10^{-5}$ cm/s

Table 4.3 Initial Input Parameters

Well/Point Name	Model Co-ordinate		April 2009 Observed Head (m)	Initial Simulation		Intermediate Model		Final Model	
	X (m)	Y (m)		Calculated Head (m)	Residual (m)	Calculated Head (m)	Residual (m)	Calculated Head (m)	Residual (m)
00-GW-19/S	462.82	887.02	292.61	292.523	-0.087	292.673	0.063	292.626	0.016
06-GW-24/S	553.91	798.59	292.57	292.483	-0.087	292.631	0.061	292.600	0.030
06-GW-25/S	1162.28	848.06	293.04	292.685	-0.355	293.150	0.110	293.114	0.074
06-GW-27/S	441.72	594.88	292.33	292.330	0.000	292.356	0.026	292.353	0.023
07-GW-29/S	590.54	846.63	292.58	292.504	-0.076	292.657	0.077	292.623	0.042
07-GW-30/S	699.51	822.51	292.63	292.504	-0.126	292.670	0.040	292.646	0.016
95-GW1/S	1169.44	579.04	293.05	292.578	-0.472	293.096	0.046	293.072	0.022
95-GW10/D	330.09	625.38	292.47	292.352	-0.118	292.387	-0.083	292.379	-0.091
95-GW2/S	713.67	790.21	292.61	292.494	-0.116	292.653	0.043	292.632	0.022
95-GW3/S	494.22	970.15	292.67	292.553	-0.117	292.702	0.032	292.656	-0.014
95-GW4/S	1754.57	963.25	293.35	293.238	-0.112	293.398	0.048	293.334	-0.016
95-GW4/M	1754.57	963.25	293.38	293.254	-0.126	293.409	0.029	293.348	-0.032
95-GW6/S	703.04	937.83	292.71	292.532	-0.178	292.718	0.008	292.693	-0.017
96-GW-11/S	1897.28	921.48	293.53	293.493	-0.037	293.635	0.105	293.572	0.042
96-GW-13/S	1474.21	1043.35	294.77	294.522	-0.248	294.693	-0.077	294.728	-0.042
96-GW-14/S	1082.49	990.72	293.96	293.594	-0.366	294.015	0.055	294.013	0.053
96-GW-14/D	1082.49	990.72	294.03	293.594	-0.436	294.015	-0.015	294.013	-0.017
96-GW-15/D	764.48	987.83	292.78	292.621	-0.159	292.797	0.017	292.781	0.001
96-GW-17/S	1339.91	1006.37	294.53	294.309	-0.221	294.460	-0.070	294.481	-0.049

Table 4.4 Groundwater Flow Model Calibration Simulation Residuals

Zone	Hydraulic Conductivity K_x (cm/s)		
	Initial	Intermediate	Final
1	2.0E-05	2.0E-05	2.0E-05
2	2.0E-05	2.0E-05	2.0E-05
3	0.150	0.090	0.131
4	0.002	0.003	0.003
5	-	0.200	0.250
6	-	0.002	0.0018
7	-	0.150	0.256
8	-	0.250	0.323
9	-	0.090	0.086
10	-	0.100	0.091
11	-	0.200	0.322
12	-	0.008	0.004
13	-	0.300	0.307
14	-	0.025	0.029
15	-	0.080	0.060

- Zone Did Not Exist

Table 4.5 Values Assigned to Hydraulic Conductivity Zones

Well Name	Model Co-ordinates		Screen (masl)		Pumping Rate (m^3/day)
	X (m)	Y (m)	Top	Bottom	
09-PW-3	491.78	876.00	282.80	279.80	191.05
09-PW-4	541.45	860.82	283.40	280.70	1.52
09-PW-5	591.59	846.04	288.80	285.80	176.63
09-PW-6	641.23	831.15	287.80	284.80	159.01
09-PW-7	691.01	816.31	290.30	287.30	148.57
09-PW-8	740.80	801.25	289.90	286.90	115.05
09-PW-9	617.00	838.32	287.50	284.50	113.39

Table 4.6 Pumping Well Input Properties

Well/Point Name	Model Co-ordinate		April 2011 Observed Head (m)	Initial Validation		Final Validation	
	X (m)	Y (m)		Calculated Head (m)	Residual (m)	Calculated Head (m)	Residual (m)
00-GW-19/S	462.82	887.02	292.15	292.231	0.081	292.232	0.082
04-GW-21/S	550.2	940.34	292.03	292.143	0.113	292.145	0.115
06-GW-24/S	553.91	798.59	292.18	292.114	-0.066	292.116	-0.064
06-GW-25/S	1162.28	848.06	292.78	292.840	0.060	292.863	0.083
06-GW-26/S	405.54	592.94	292.28	292.307	0.027	292.307	0.027
06-GW-27/S	441.72	594.88	292.25	292.302	0.052	292.302	0.052
06-GW-28/S	474.83	594.95	292.31	292.292	-0.018	292.293	-0.017
07-GW-29/S	590.54	846.63	292.04	291.981	-0.059	291.983	-0.057
07-GW-30/S	699.51	822.51	291.92	291.830	-0.090	291.835	-0.085
09-GW-31/S	518.8	875.08	292.08	292.147	0.067	292.149	0.069
09-GW-32/S	561.39	842.96	292.13	292.076	-0.054	292.078	-0.052
09-GW-33/S	609.19	822.43	292.01	291.965	-0.045	291.967	-0.043
09-GW-34/S	674.54	828.81	291.91	291.898	-0.012	291.902	-0.008
09-GW-35/S	716.88	814.56	291.87	291.871	0.001	291.875	0.005
09-GW-36/S	766.04	799.57	291.90	291.959	0.059	291.965	0.065
09-GW-37/S	518.14	724.13	292.22	292.222	0.002	292.223	0.003
09-GW-38/S	555.87	713.35	292.15	292.187	0.037	292.189	0.039
09-GW-39/S	602.87	698.21	292.16	292.158	-0.002	292.160	0.000
10-GW-40/S	462.37	590.84	292.29	292.296	0.006	292.297	0.007
95-GW1/S	1169.44	579.04	292.77	292.803	0.033	292.822	0.052
95-GW10/D	330.09	625.38	292.41	292.332	-0.078	292.332	-0.078
95-GW4/M	1754.57	963.25	293.17	293.309	0.139	293.283	0.113
95-GW4/S	1754.57	963.25	293.32	293.293	-0.027	293.268	-0.052
95-GW6/S	703.04	937.83	292.16	292.092	-0.068	292.097	-0.063
96-GW-11/S	1897.28	921.48	293.36	293.535	0.175	293.355	-0.005
96-GW-13/S	1474.21	1043.35	295.00	294.727	-0.273	294.876	-0.124
96-GW-14/S	1082.49	990.72	294.11	293.864	-0.246	294.028	-0.082
96-GW-14/D	1082.49	990.72	294.15	293.864	-0.286	294.028	-0.122
96-GW-15/S	764.48	987.83	292.26	292.287	0.026	292.293	0.033
96-GW-15/D	764.48	987.83	292.34	292.294	-0.046	292.300	-0.040
96-GW-17/S	1339.91	1006.37	294.65	294.471	-0.179	294.619	-0.031

Table 4.7 Groundwater Flow Model Validation Simulation Residuals

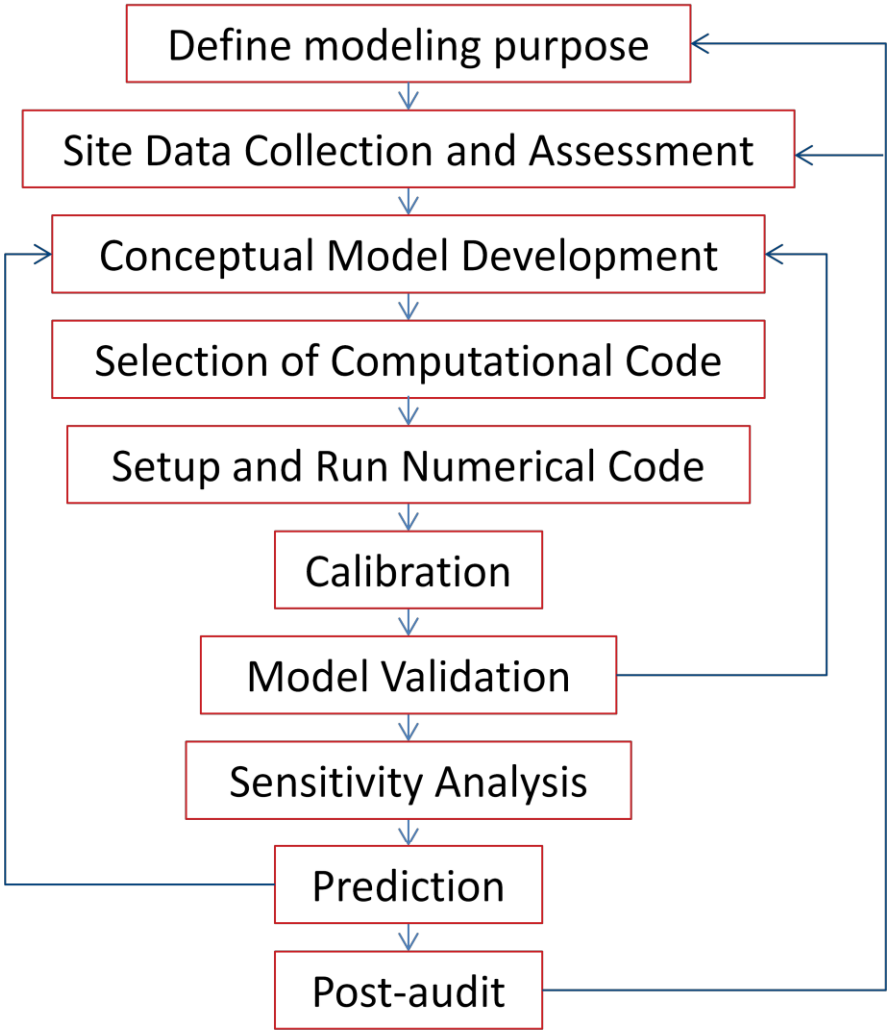

Figure 4.1 Numerical Model Creation Process, after (Alvarez & Illman, 2006)

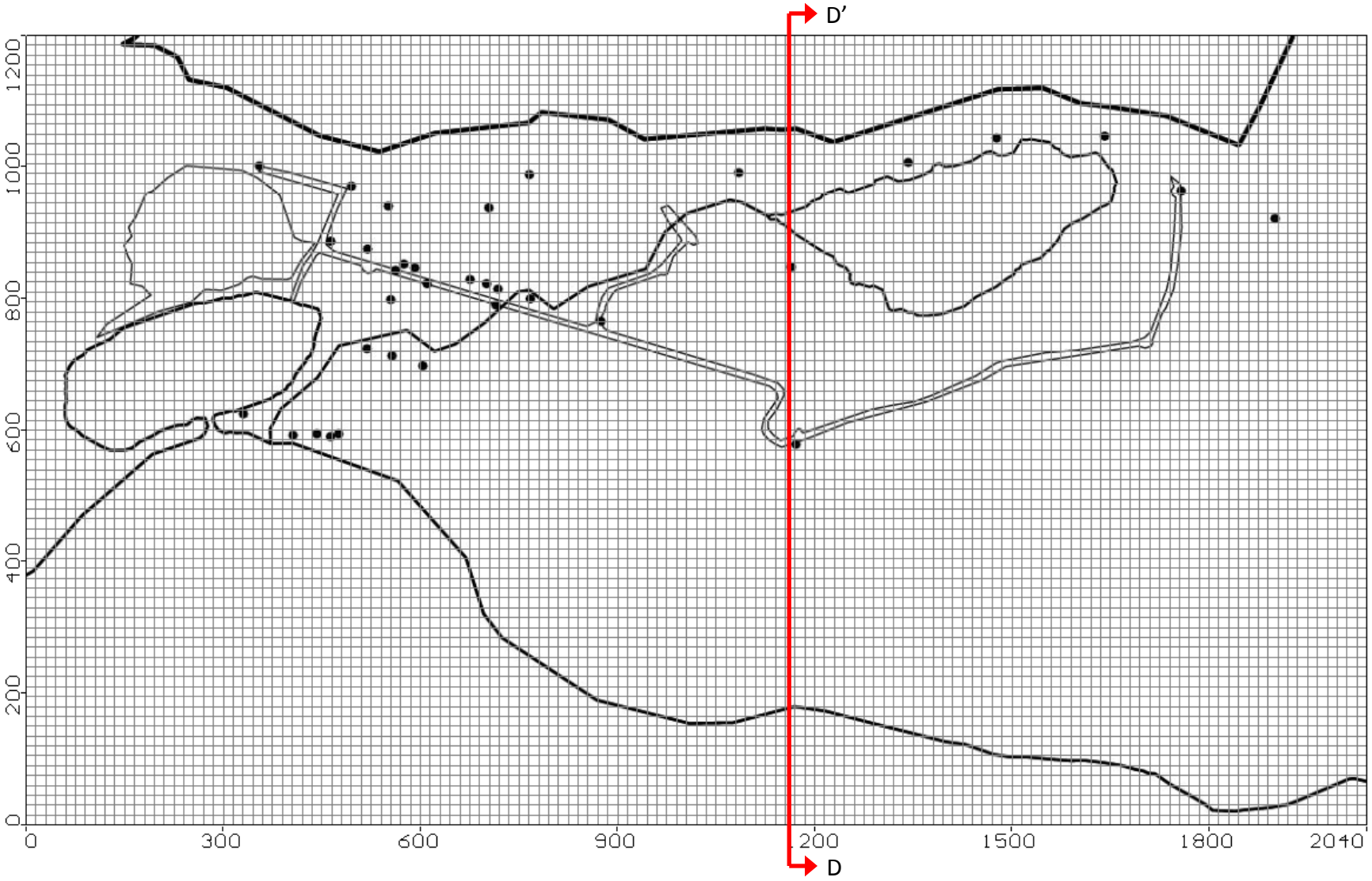

Figure 4.2 Model Extents and Grid Layout

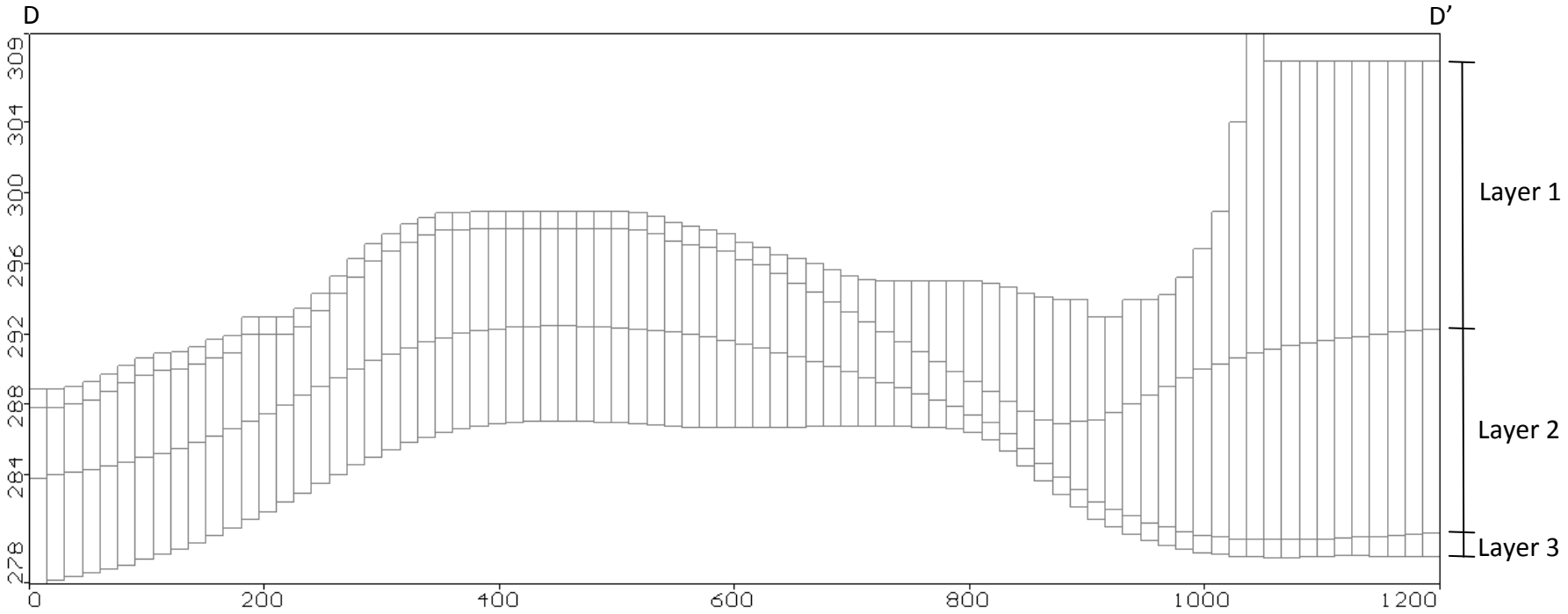

Figure 4.3 Model Cross Section D-D'

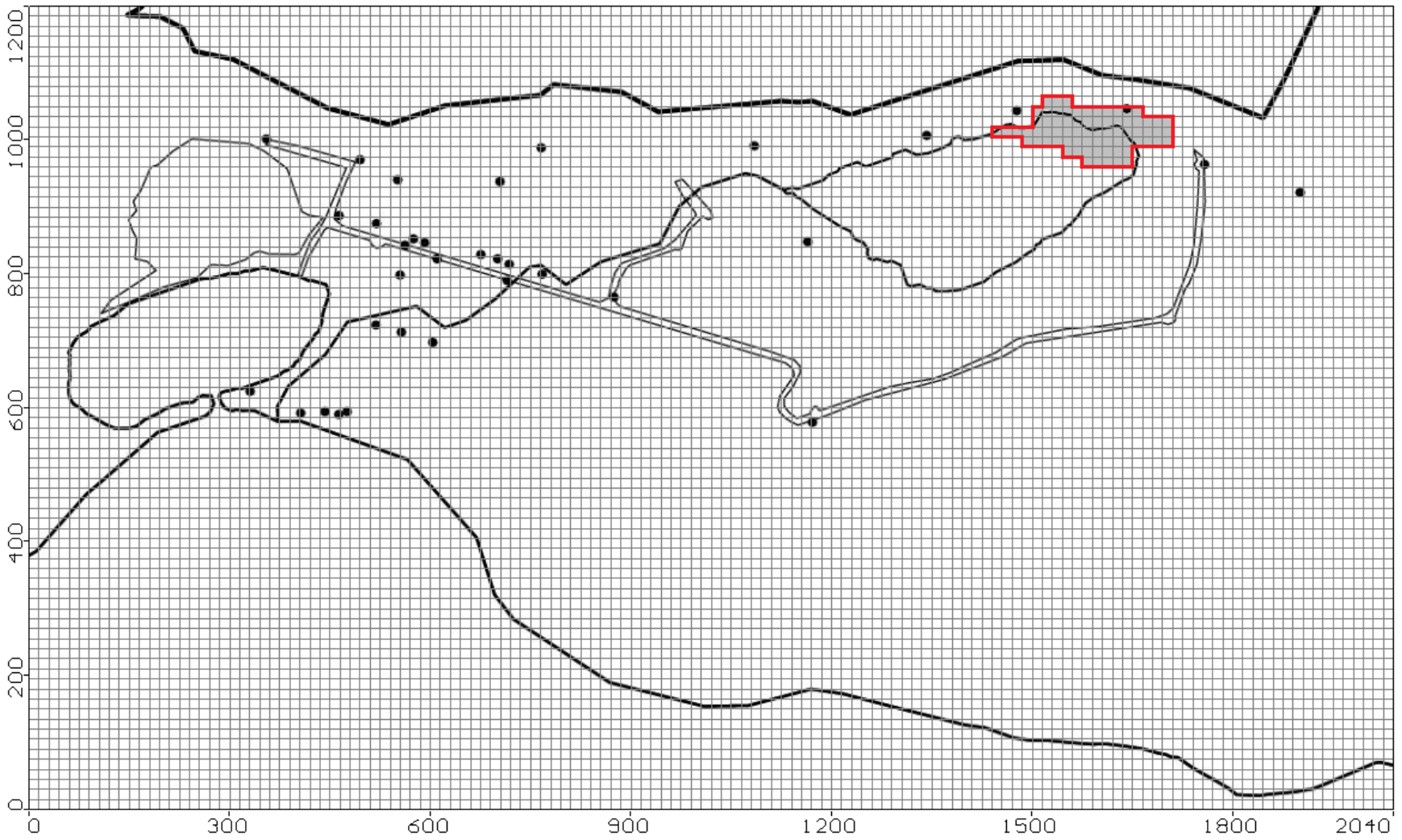

Figure 4.4 Discontinuity of Silty-Clay in Layer 1

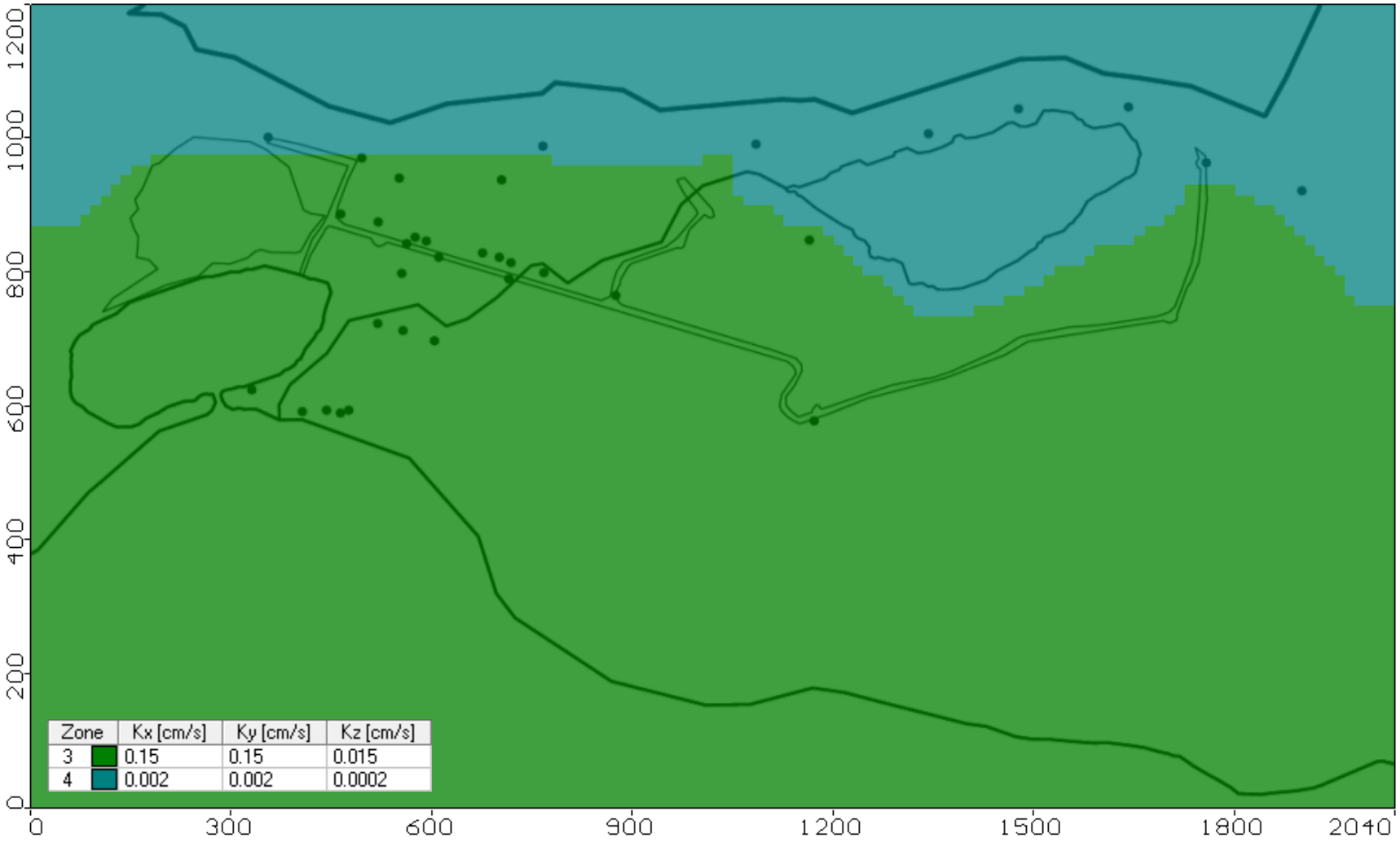

Figure 4.5 Initial Hydraulic Conductivity Distribution in Sand Layer

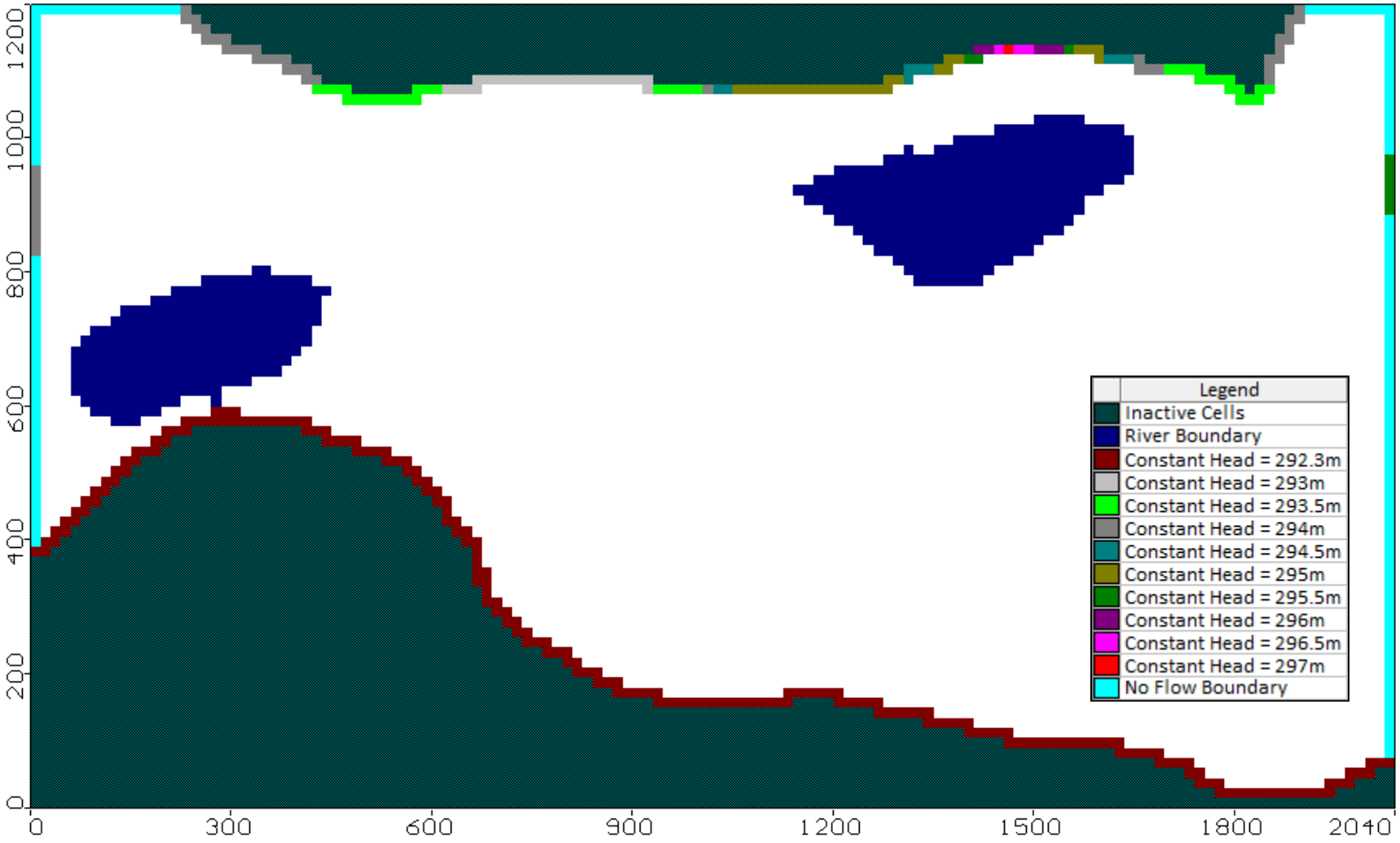

Figure 4.6 Groundwater Flow Model Boundary Conditions

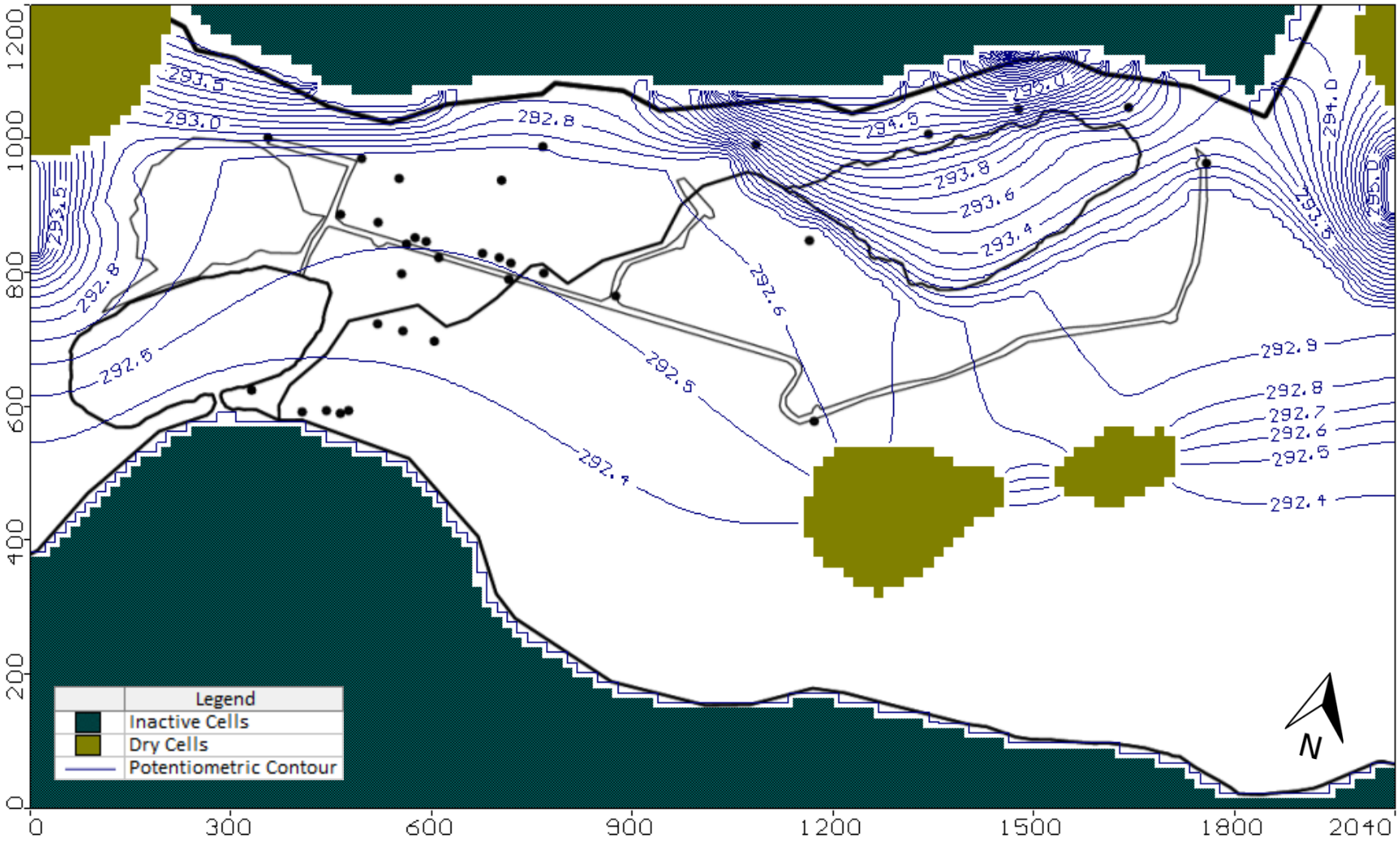

Figure 4.7 Initial Simulation Potentiometric Surface

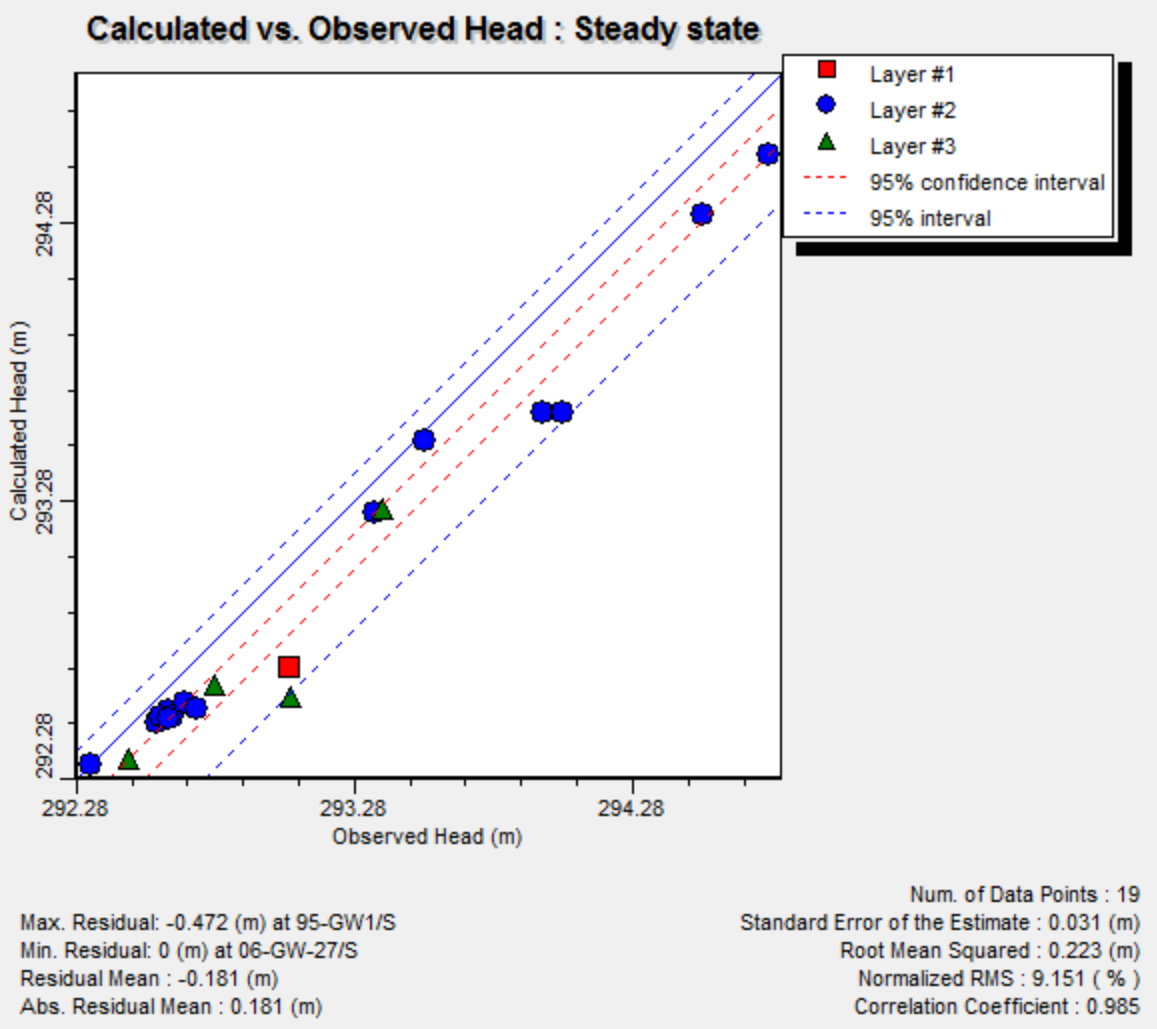

Figure 4.8 Initial Simulation Calibration Plot

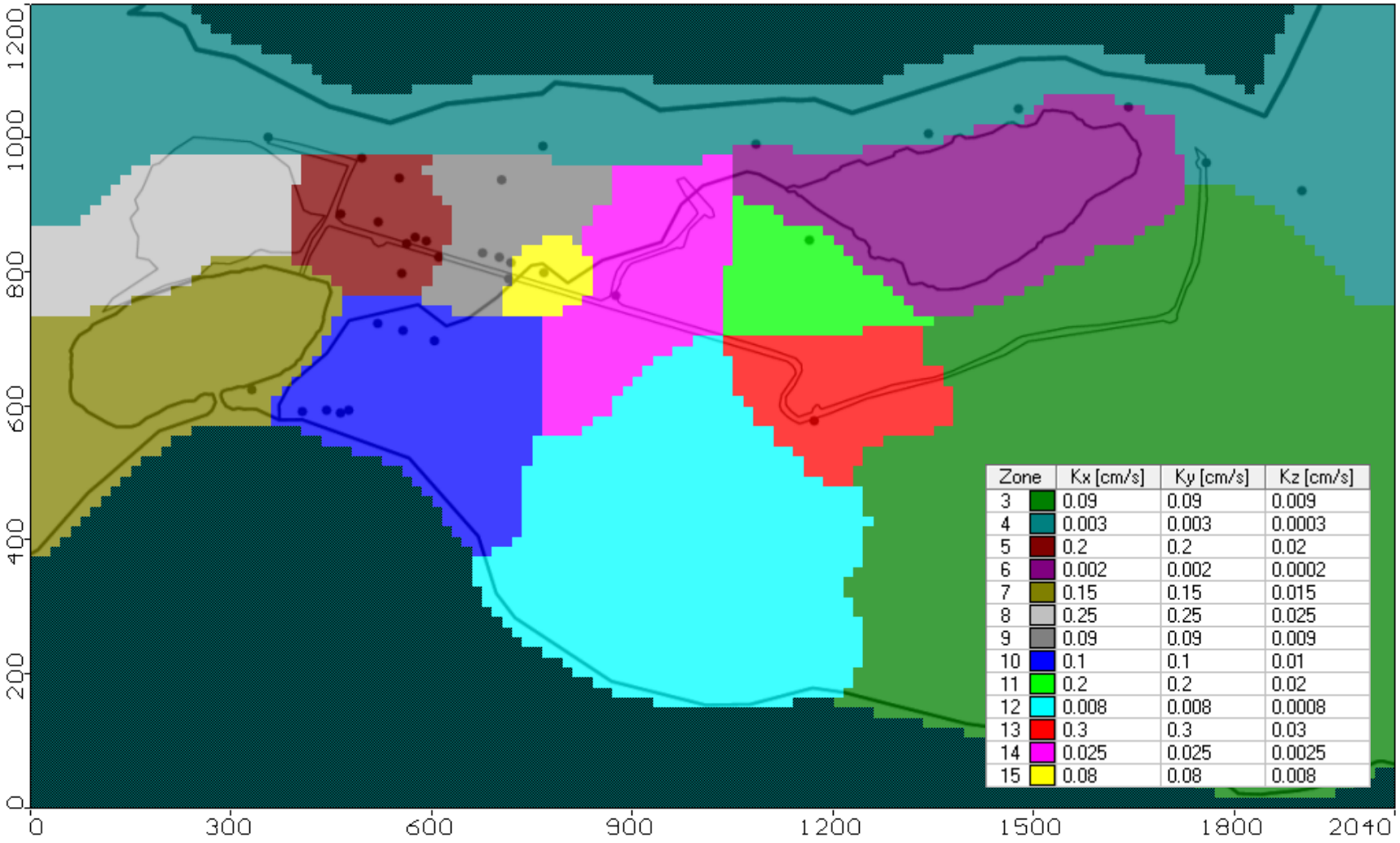

Figure 4.9 Intermediate Model Hydraulic Conductivity Distribution in Sand Layer

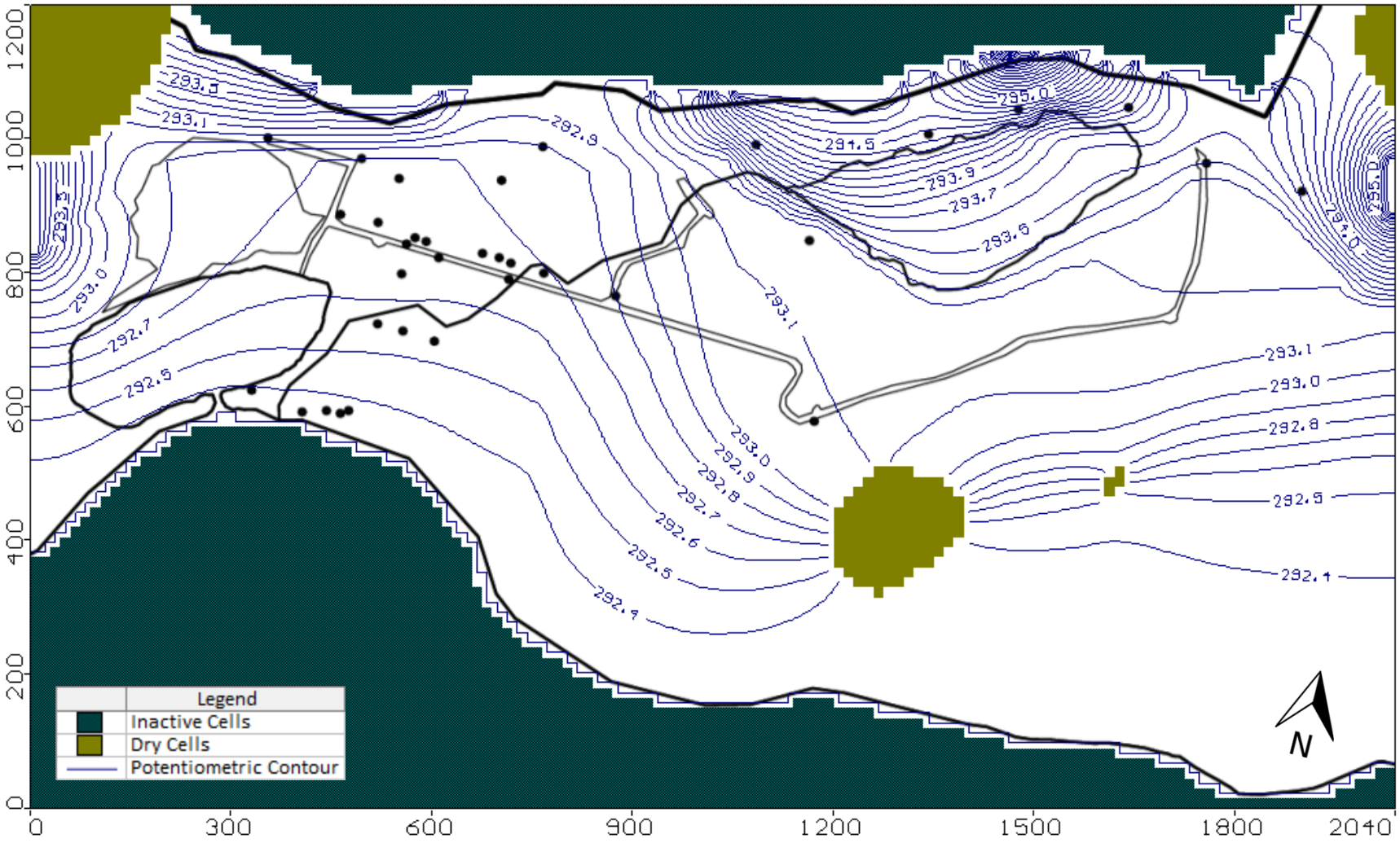

Figure 4.10 Intermediate Model Potentiometric Surface

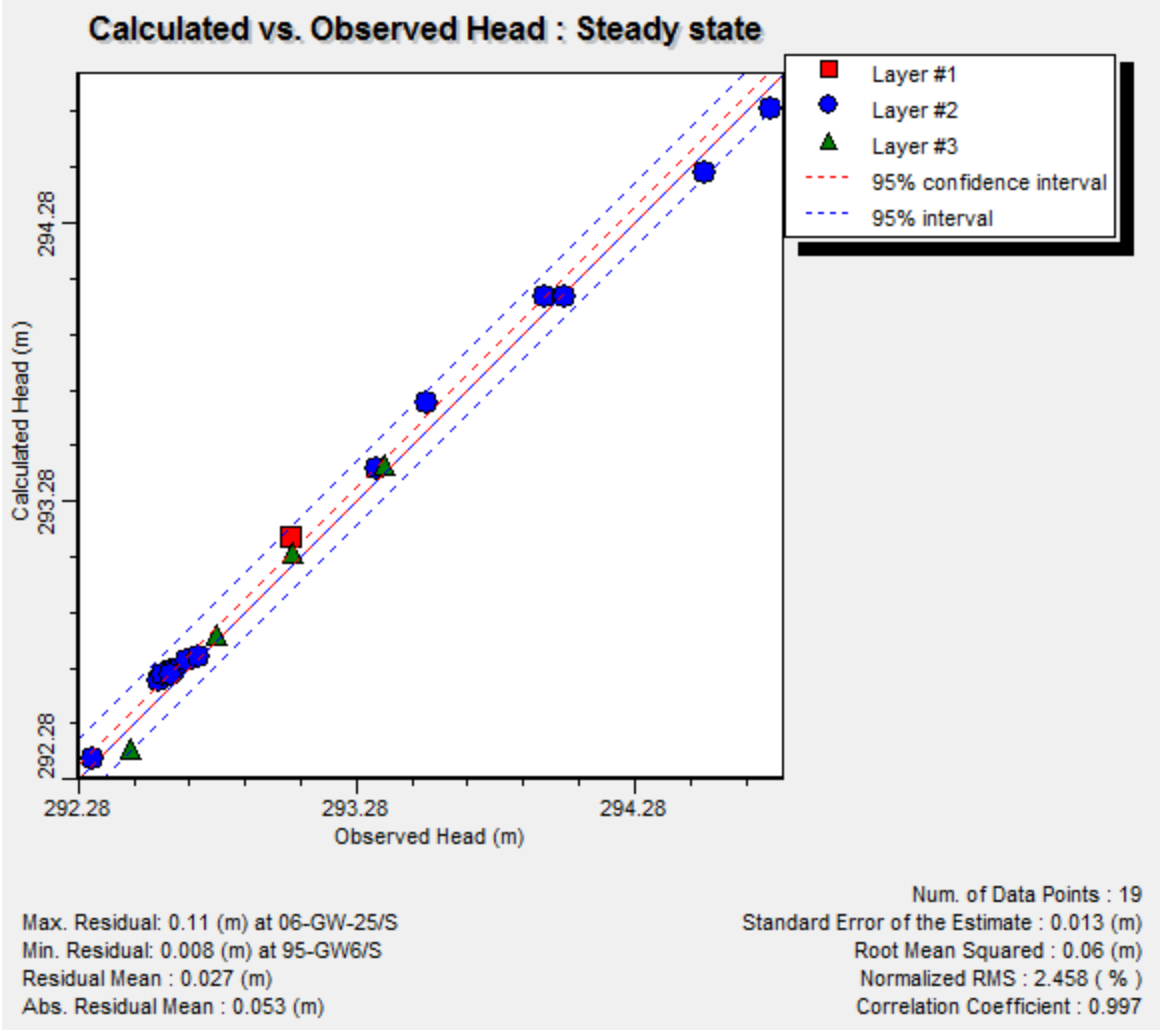

Figure 4.11 Intermediate Model Calibration Plot

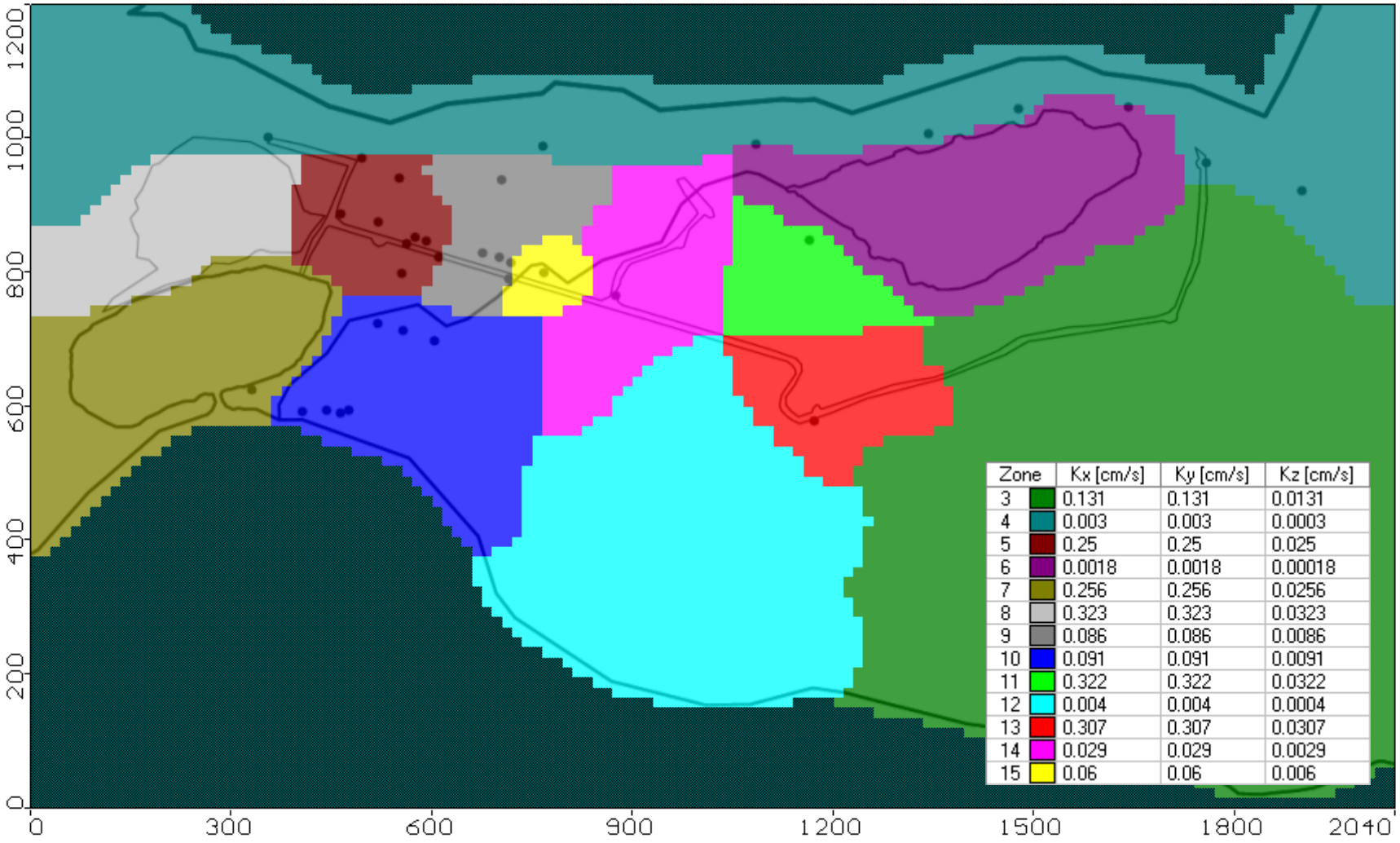

Figure 4.12 Final Model Hydraulic Conductivity Distribution in Sand Layer

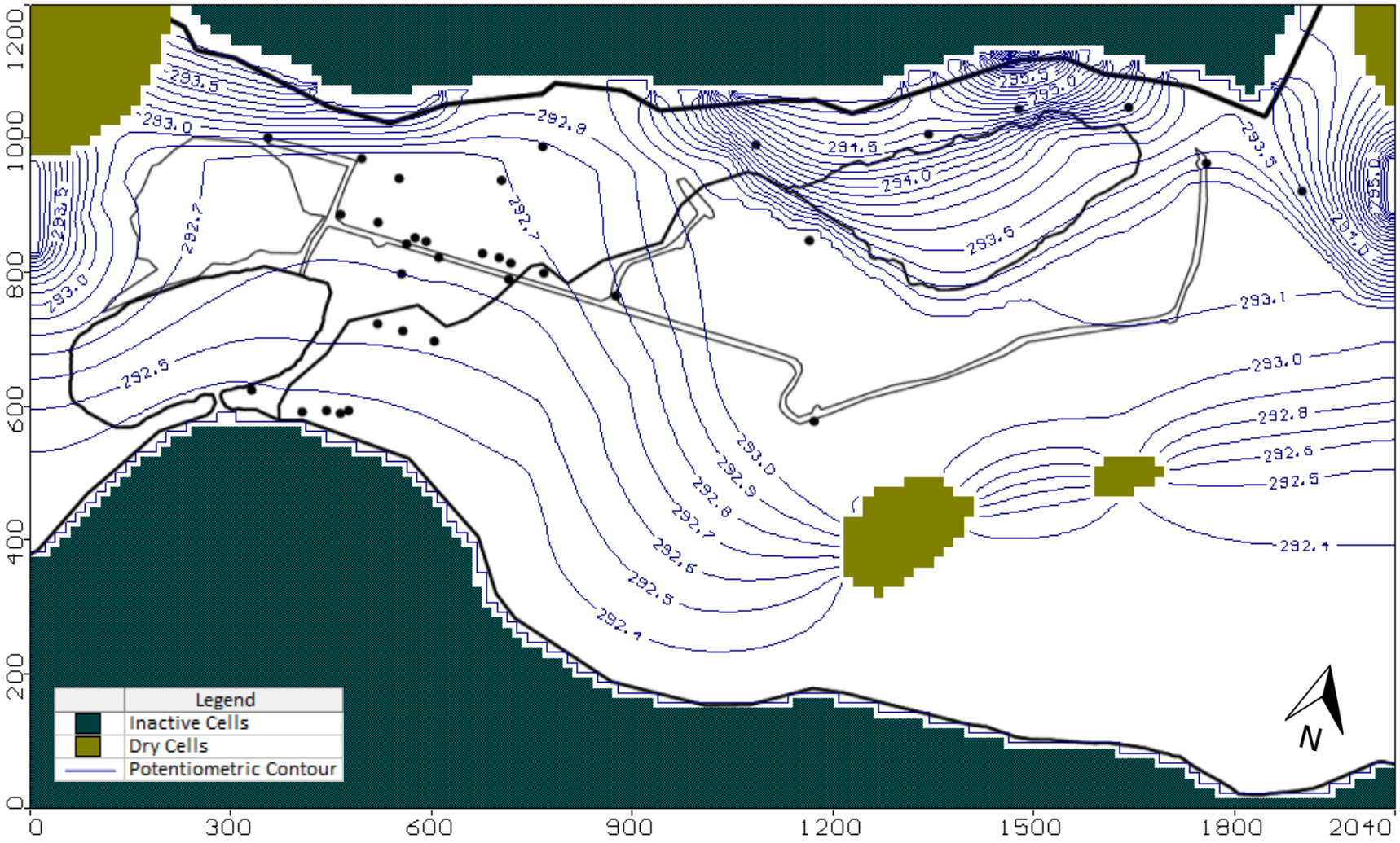

Figure 4.13 Final Model Simulated Potentiometric Surface

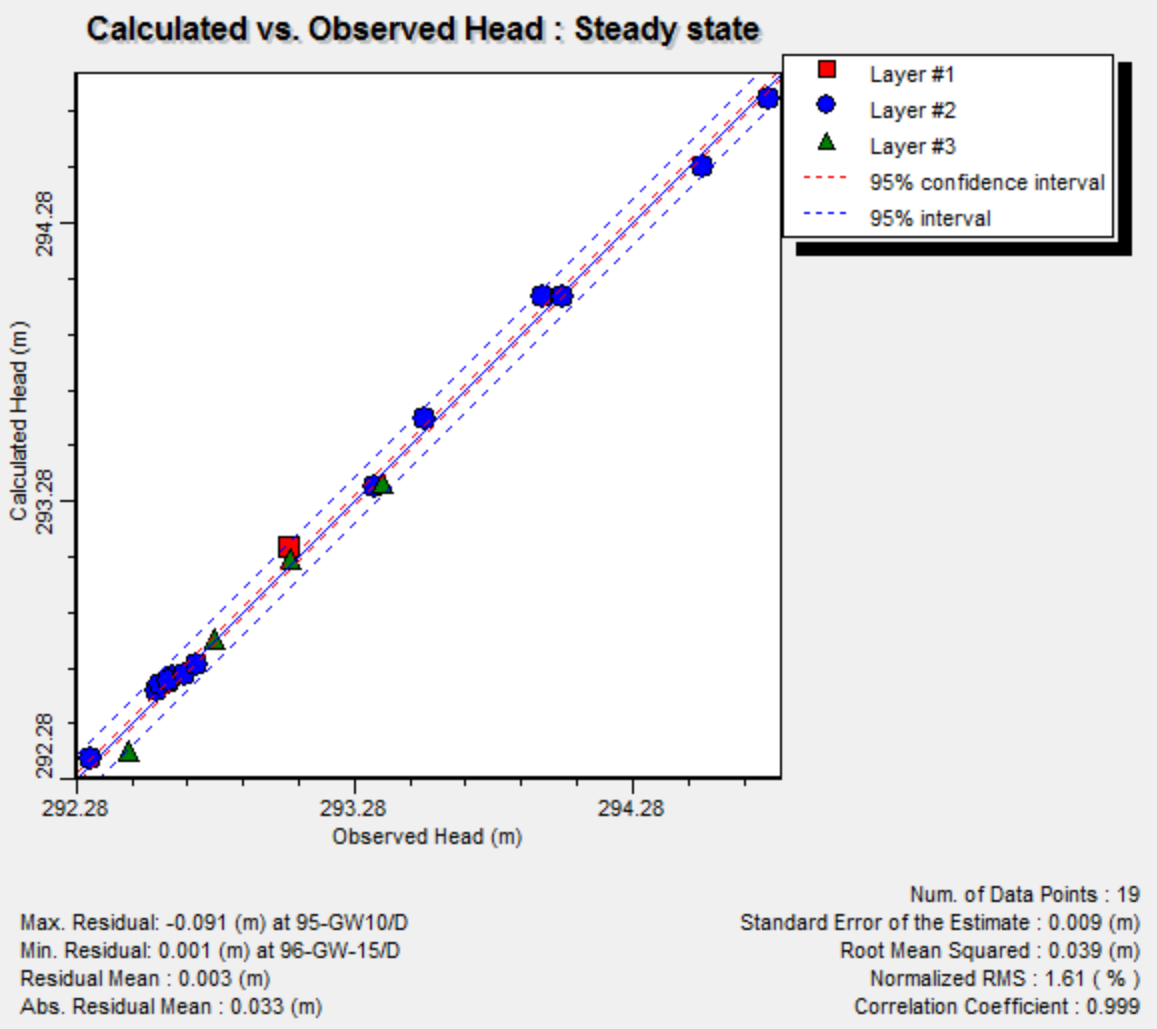

Figure 4.14 Final Model Calibration Plot

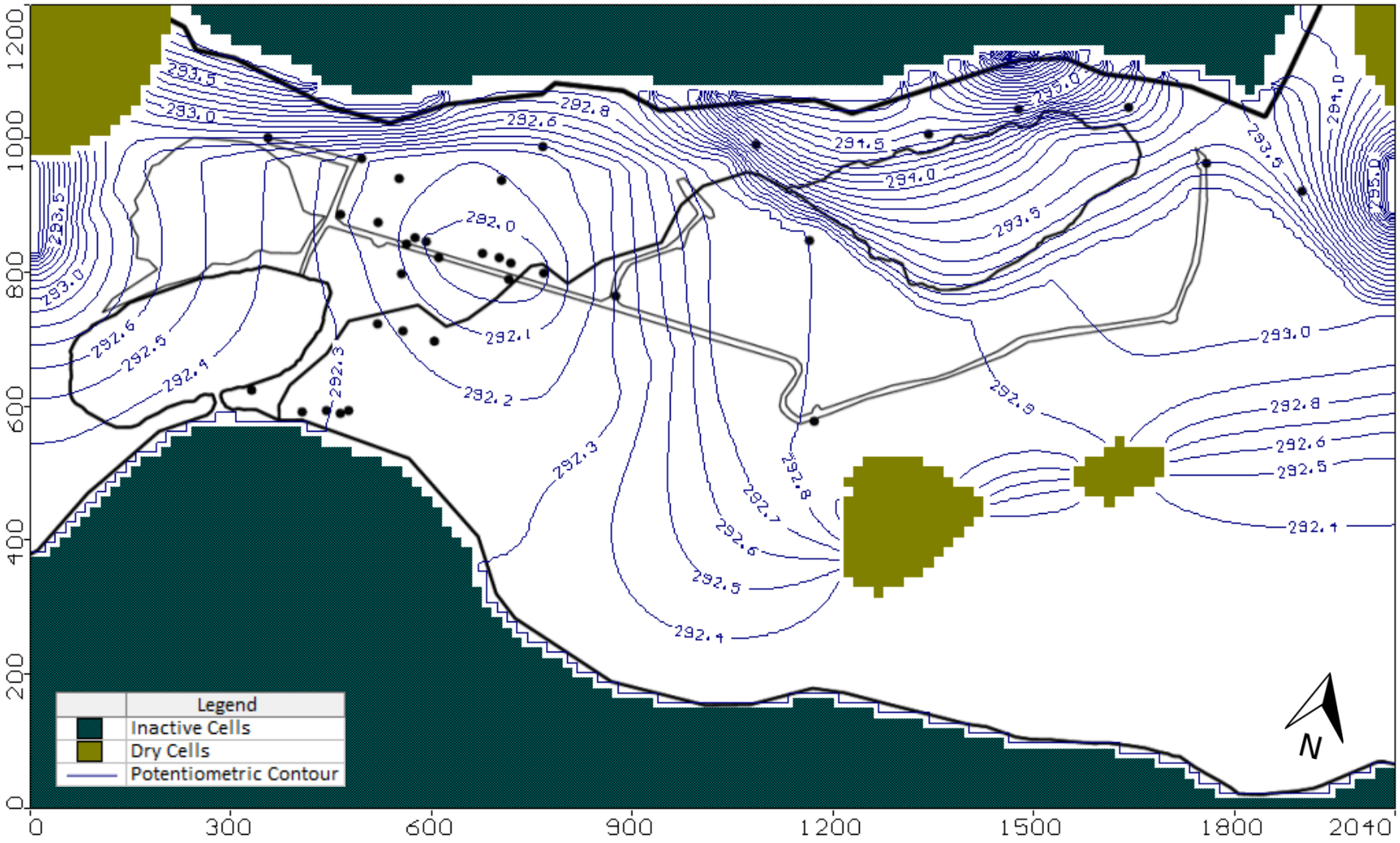

Figure 4.15 Final Model Simulated Potentiometric Surface With Pumping Wells

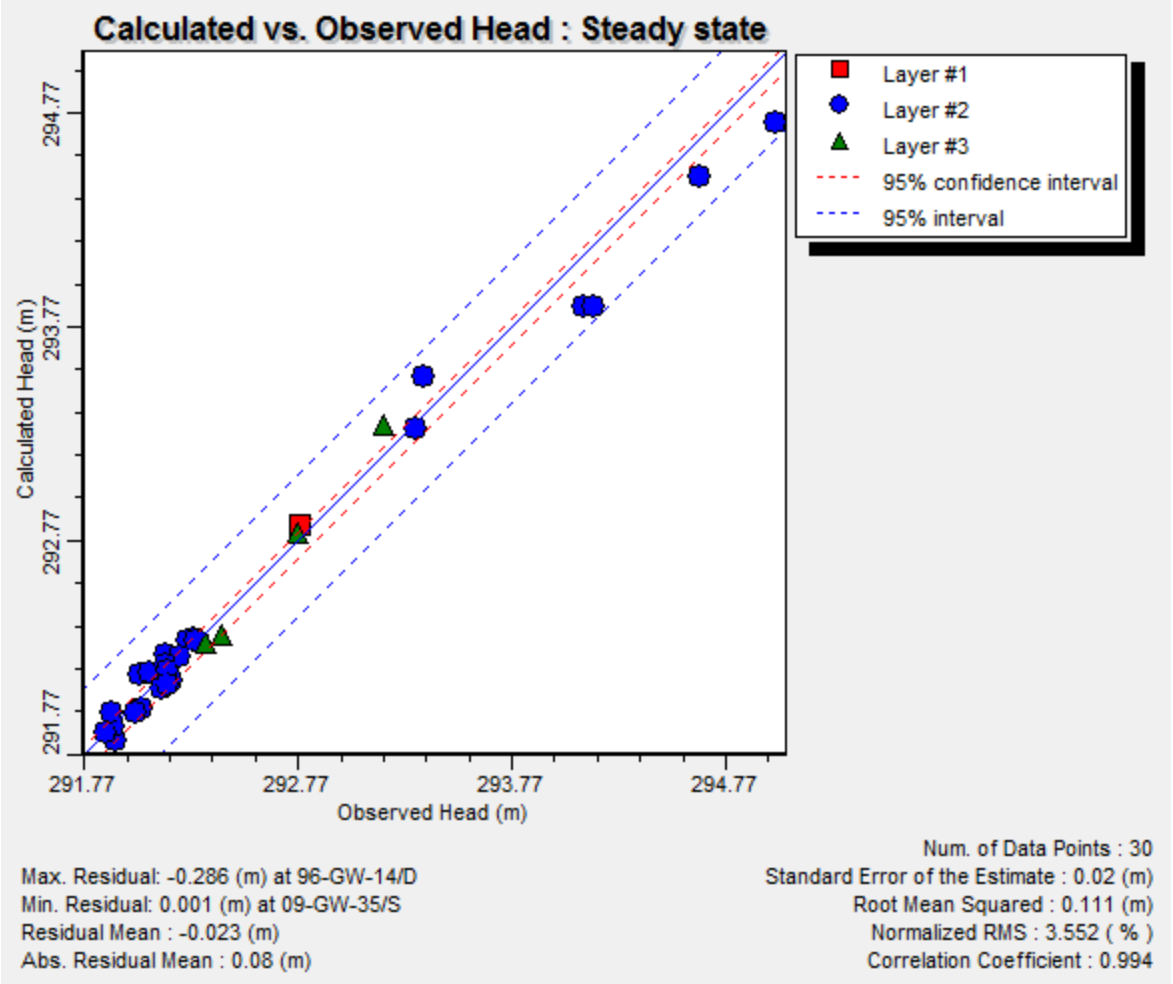

Figure 4.16 Final Model With Pumping Wells Calibration Plot

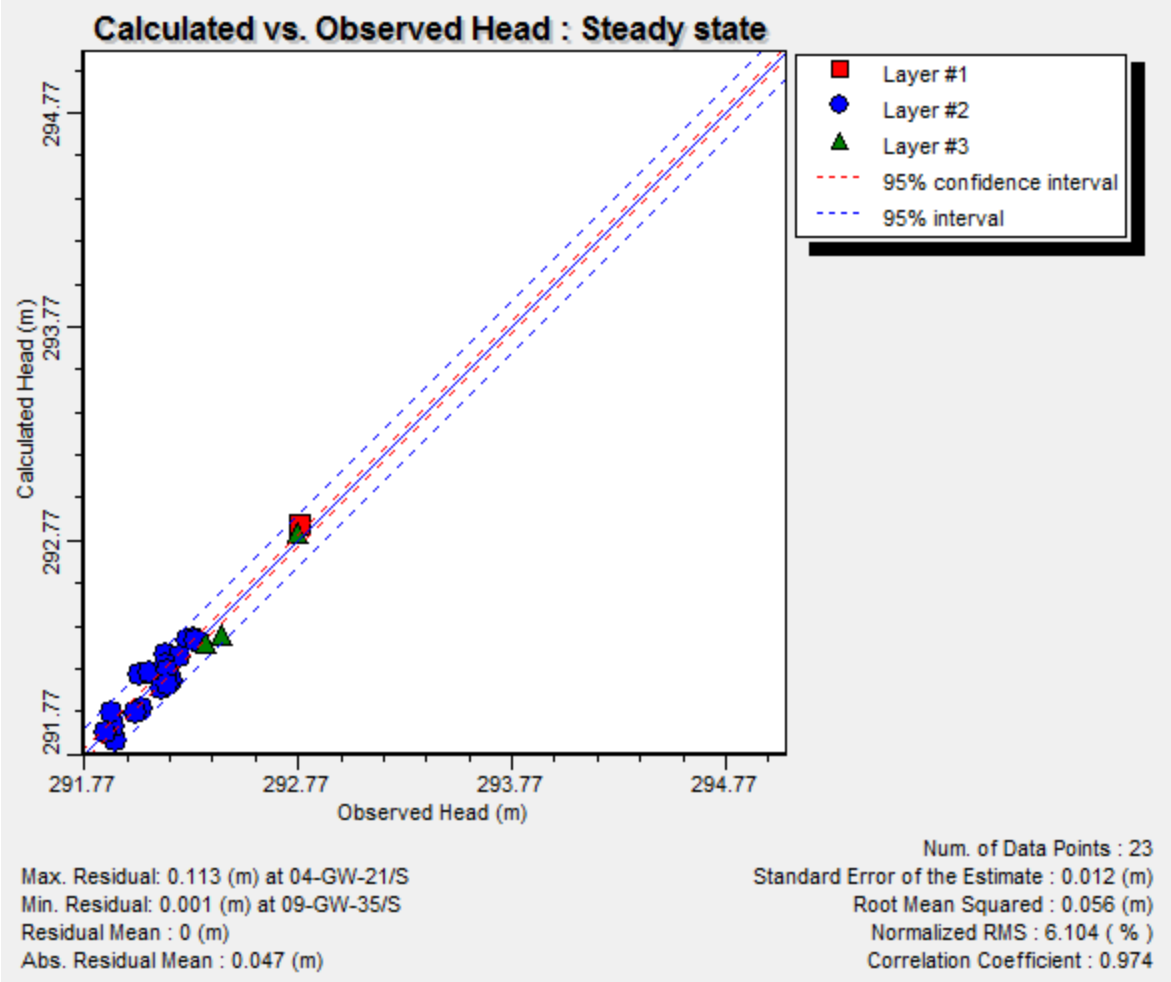

Figure 4.17 Validation Calibration Plot With High Head Data Points Removed

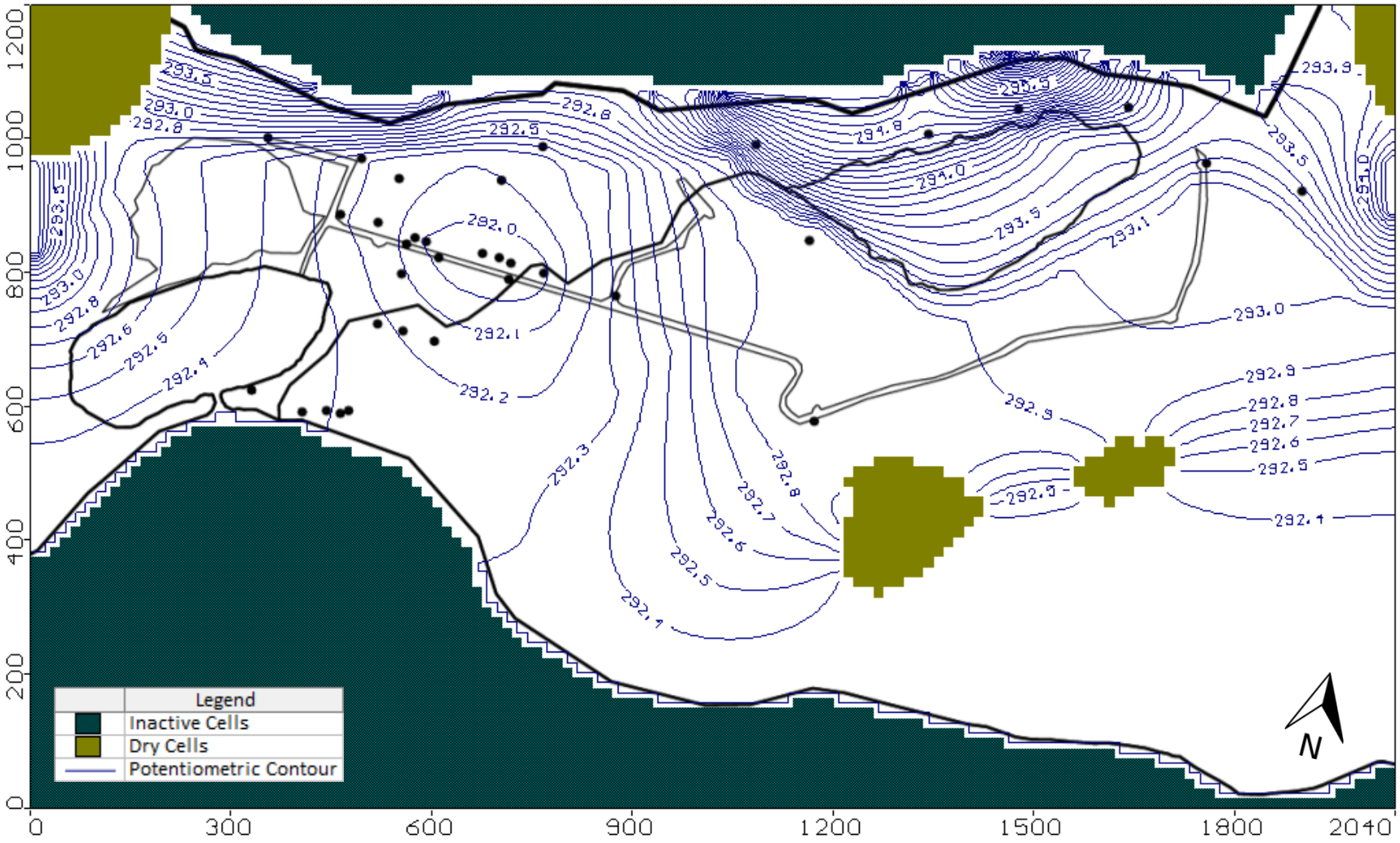

Figure 4.18 Final Validation Simulated Potentiometric Surface

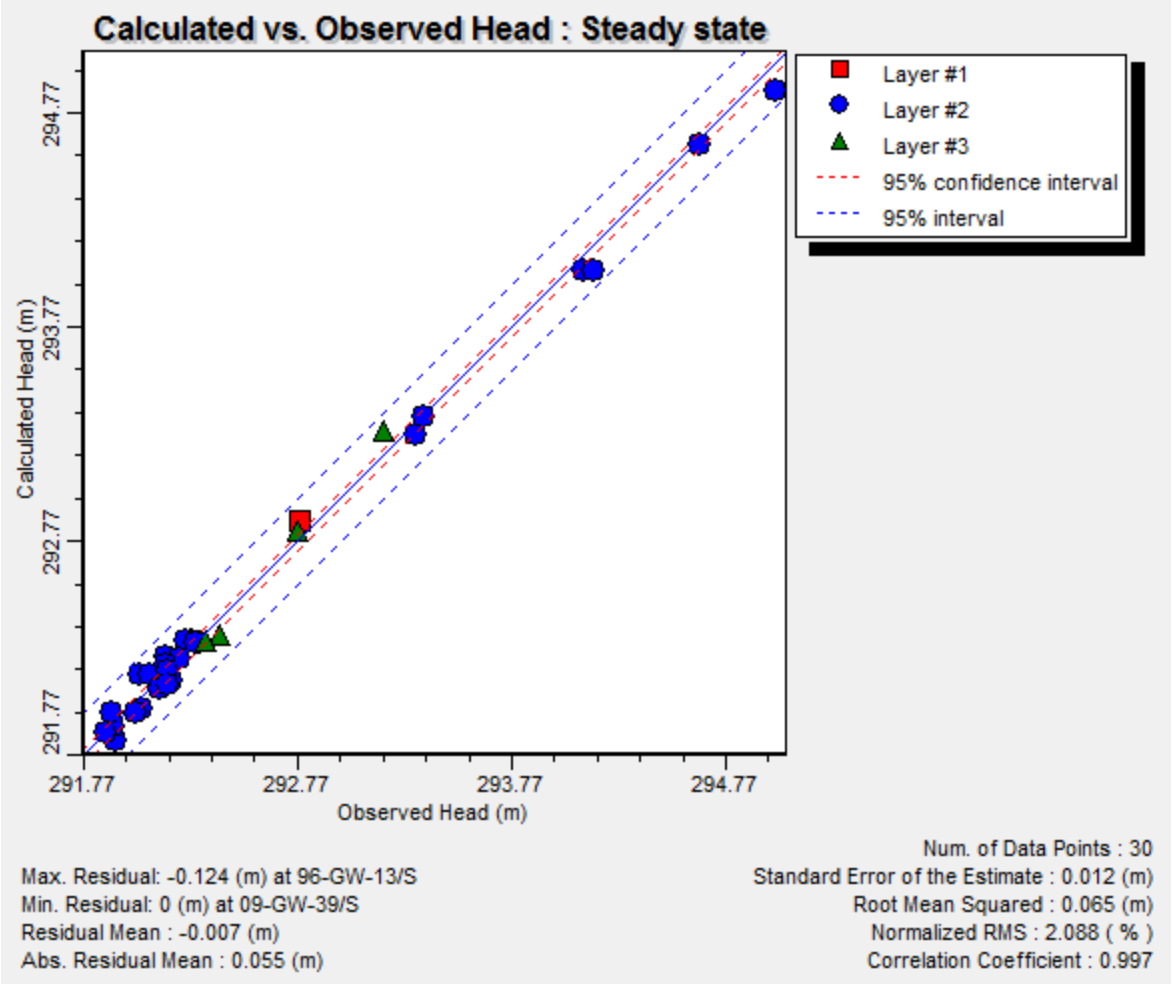

Figure 4.19 Final Validation Calibration Plot

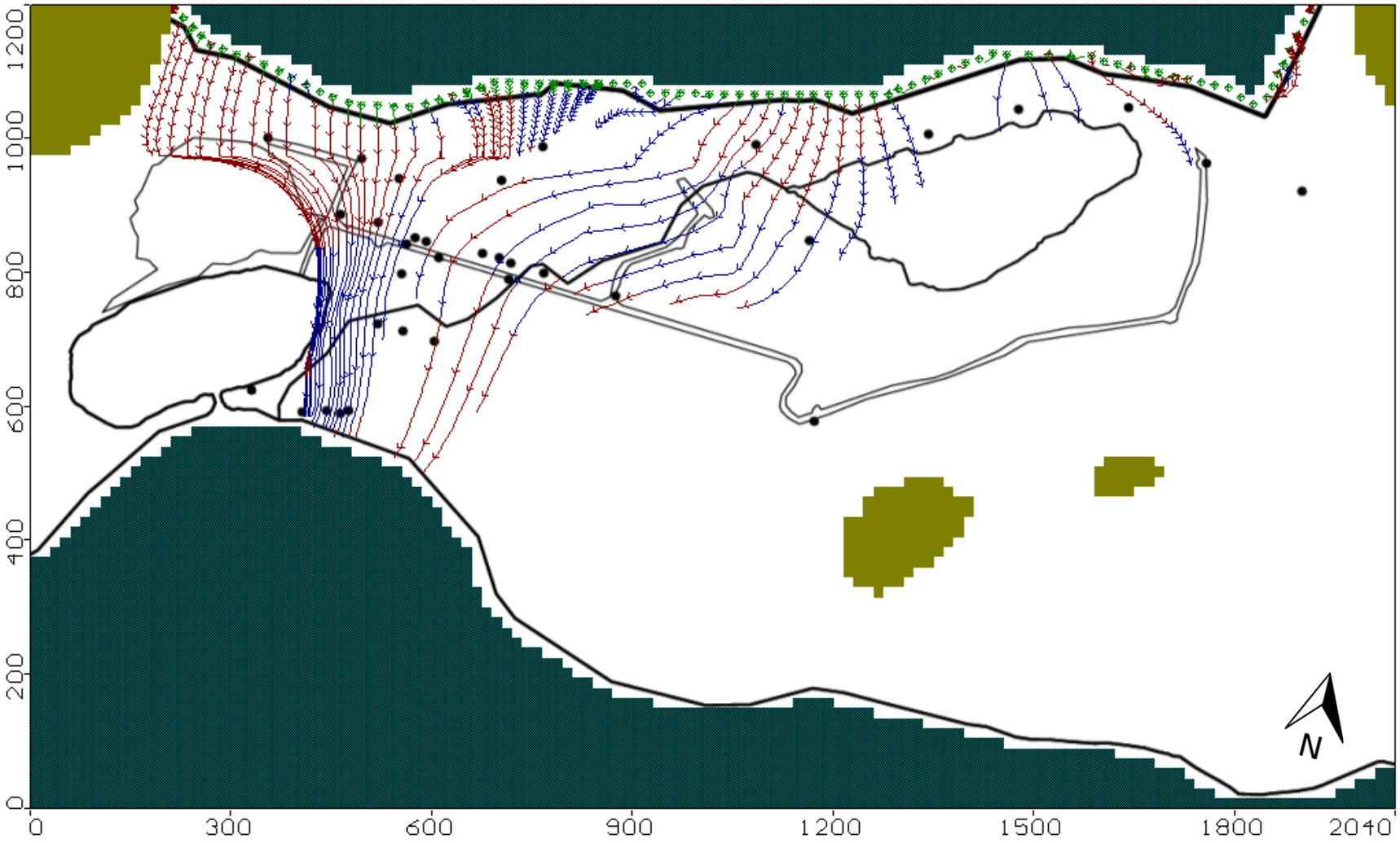

Figure 4.20 Particle Tracking Path Lines (12 Year Simulation)

5.0 CONTAMINANT TRANSPORT MODELLING

Contaminant transport modelling is performed as a secondary step to groundwater flow modelling. In order to simulate contaminant transport at a contaminated site, an accurate groundwater flow model must first be created and calibrated. If the groundwater flow model is incomplete, or does not accurately represent the site conditions, then the contaminant transport model will also be inaccurate. A contaminant transport model uses the output total head values from the groundwater flow model as well as the input fate and transport parameters to calculate the concentrations of the contaminants for each cell of the model. This is achieved by computing numerical solutions to the differential equation which governs contaminant transport (Equation 2.17) as described in section 2.9.3.

5.1 MODELLING METHODOLOGY

The methodology for modelling the fate and transport of contaminants through the subsurface of a site follows the modelling process shown in Figure 4.1. Once a groundwater flow model is constructed, calibrated, and validated, the various input conditions that are required for simulating the transport of contaminants through the model can then be input. Similar to the groundwater flow model inputs, these parameters are typically estimated from historical data or published literature values, and then adjusted during a calibration process.

Since two groundwater flow models were needed to represent the hydrogeologic conditions at the Northern Ontario gold mine site for before and after the start of pumping, two contaminant transport models are also required. The first 12 year time period of each simulation was

performed using the April 2009 final calibrated model, which does not include the effect of the pumping wells. This simulation period represents the evolution that the contaminant plumes would experience due to the natural hydrogeologic conditions of the site between 1997 and 2009. The output results of this simulation were then input into the April 2011 final validated groundwater flow model to determine the effects of the pumping wells on the contaminant plumes. The second part of the simulations represents the change in plume shapes due to the effects of the pumping between 2009 and present.

Initial contaminant transport simulations were performed using sulphate (SO_4^{2-}) as a tracer contaminant. Dissolved sulphate is a by-product of the oxidation of iron sulphide minerals found in the mine tailings, as described in section 2.4.2, and therefore, when detected downstream, indicates the presence of contaminated water which originated in the TMA. Additionally, because sulphate is an anion, it is not adsorbed to the surface of the negatively charged soil particles. For this reason, it is generally assumed that these highly soluble anions are not sorbed onto soil particles. Sulphate transport can therefore be simulated in a model which only considers the effects of advection and hydrodynamic dispersion. Simulating a contaminant which is unaffected by sorption allows an easier method of determining the influence of the model's source term and dispersion parameters. The pre-mining concentrations, as well as 2008 and 2010 concentration contours for dissolved sulphate were reported by Piteau Associates Engineering Ltd. (2011), and are displayed in Figure 5.1.

Calibration of the transport model was then performed systematically by conducting simulations in groups. First, those which considered only advection and dispersion, then those

which included the effects of sorption. This allowed the simulations to be performed on simple cases first before becoming more complex. Tables 5.1 and 5.2 summarize the simulations which were conducted on the transport of sulphate and cobalt, respectively during the calibration process and also indicate the changes that were made to each parameter. In order to assess the calibration of the cobalt transport simulations, the extents of several output concentration contours were compared to the observed concentrations measured in the monitoring wells during 2009, 2010, and 2012 (shown in Figure 3.19).

The calibrated contaminant transport model is then used to conduct a sensitivity analysis. This was performed by individually adjusting the dispersivity (α_x) and sorption (k_d) parameters by one order of magnitude, and monitoring their effect on the simulated plume extents. If the adjusted input parameter had a lager influence on the simulation results, it would indicate that the model has a high sensitivity to that parameter. Table 5.3 summarizes the simulations which were conducted as part of the sensitivity analysis, and the input parameters which were used for each simulation.

5.2 Model Construction, Inputs, and Boundary Conditions

5.2.1 Model Construction

For the construction of the contaminant transport model for the Northern Ontario gold mine site, all of the input parameters and dimensions of the groundwater flow model were used. The contaminant transport therefore uses the exact same extents, grid size, ground surface elevations, and layer thicknesses as the groundwater flow model described in section 4.2.1.

5.2.2 INPUT PARAMETERS

Input parameters for a contaminant transport model include both soil characteristics and contaminant species characteristics. Soil characteristics (transport parameters) required by the contaminant transport model include dry bulk density, effective diffusion coefficient, and dispersivity coefficient values. Species characteristics (fate parameters) required by the contaminant transport model include sorption and biodegradation coefficients. Since only inorganic contaminants are being modelled at the Northern Ontario Gold Mine site, it is assumed that biodegradation does not play a key role, and only sorption rates are considered. Additionally, sorption rates are assumed to be described using a linear isotherm, and are input into the model by a linear distribution coefficient (k_d). The initial estimates of the contaminant transport input parameters are summarized in Table 5.4, and described in further detail below.

DIFFUSION

The effects of diffusion were input into the contaminant transport model as estimated effective diffusion coefficients for each model layer and also for each contaminant being simulated. The effective diffusion coefficients were calculated using Equation 2.9 as the product of the molecular diffusion coefficient and the tortuosity coefficient, both of which were estimated from published literature values. Molecular diffusion coefficients are a contaminant specific parameter, and have been reported as 92.45×10^{-6} m^2/day for sulphate (Alvarez & Illman, 2006), and 93.83×10^{-6} m^2/day for cobalt (Ribeiro et al., 2002). Both of these reported values were determined at 25°C. The tortuosity coefficient is a property of the porous material, and was estimated to be 0.67 for sandy material (Batu, 2006), and approximately 0.35 for clayey

material (Rowe et al., 1988). Table 5.5 summarizes the values that were used to calculate the effective diffusion coefficients for the contaminant transport model.

DISPERSION

The effects of mechanical dispersion in the contaminant transport model are accounted for by inputting approximated values for the plume's dispersivity coefficients (α_L, α_h, α_v). The initial estimate for the magnitude of the longitudinal dispersivity coefficient (α_L) used in the Northern Ontario gold mine site model was obtained from Equation 2.8 using the approximate observed plume length. Since the observed sulphate and cobalt plumes at the Northern Ontario gold mine site travel into or below the adjacent lake, the overall length of the plume is not well known. For this reason, minimum and maximum plume lengths were estimated, and a range of dispersivity values was calculated. The maximum plume length was estimated based on the longest simulated flow path between the TMA and the lake for the particles shown in Figure 4.20. From this figure, an approximate plume length of 1000m was obtained, and a longitudinal dispersivity value of 11.77m was calculated from Equation 2.8. The minimum plume length was estimated based on the shortest distance between the TMA and the lake. This distance is approximately 500m, which equates to a longitudinal dispersivity value of 9.12m from Equation 2.8. Values for transverse dispersivity (α_y) and vertical dispersivity (α_z) were entered into the contaminant transport model as fractions of the estimated longitudinal dispersivity value. The ratios which were input for these values were those recommended by Alvarez & Illman (2006), as described in section 2.7.2.2, and the initial estimated values are displayed in Table 5.4. The same dispersivity values were input into all three layers of the model.

SORPTION

The linear sorption isotherm, as described in section 2.7.3.1 is assumed to accurately describe the partitioning of the dissolved contaminants between the solid and liquid phases in the subsurface of the site. In order to input this sorption process into the contaminant transport model, the linear distribution coefficient (k_d) of the contaminant must be estimated.

Initial adsorption estimates for dissolved cobalt for the Northern Ontario gold mine site model were obtained from Abakar (2015), who performed batch adsorption tests on a soil sample taken from the site. This soil sample contained 87.8% by mass of particles in the 2-75 μm range (Abakar, 2015), and is likely representative of the silty-clay material which overlies the majority of the site, as described in section 3.3. Although the results of these tests demonstrate that the Freundlich isotherm provided the best fit for the data, the reported results were used to estimate a linear partitioning coefficient which was approximately representative of the isotherm in the low concentration range (less than 15 mg/L). From these data, a distribution coefficient of 7.5 mL/g (7.5×10^{-9} L/μg) was determined to be representative of the silty-clay layer. This value also correlates reasonably with distribution coefficients for other metals on silt and clay soils reported by Rowe et al. (2004). This value was therefore used for the silty-clay of layer 1, and the till of layer 3 in the Northern Ontario gold mine site model (see Table 5.4). However, the sorption capacity of soil for dissolved cobalt has been shown to have a high correlation with the soil's surface area (Bradl, 2004). This is not surprising, since the adsorption of inorganic ions typically occurs through cation exchange onto the surfaces of clay minerals, as described in section 2.7.3.1. It is therefore very likely that the distribution coefficient value for the material in the sand layer is much lower than that of the clay layer material.

In order to obtain an approximate distribution coefficient value for the sand layer, a linear correlation between the soil's distribution coefficient and specific surface area was assumed. Table 5.6 lists effective diameter and specific surface area values which are approximately representative for different types of soil (Jury & Horton, 2004). Comparing the reported specific surface area for the Northern Ontario gold mine site silty-clay sample of $3.8x10^5 cm^2/g$ (Abakar, 2015) to Table 5.6, these sources tend to be in general agreement. Using a linear correlation between fine sand with a specific surface area of $444.4 cm^2/g$ and the values reported for the silty-clay sample, the fine sand would have an approximate distribution coefficient of $8.8\ x10^{-3} mL/g$ ($8.8\ x10^{-12} L/\mu g$). This value was used as the initial distribution coefficient for the sand aquifer in layer 2 of the contaminant transport model (see Table 5.4)

5.2.3 Boundary Conditions

The boundary conditions for a contaminant transport model are the means of providing the model with a location and term for the contaminant source. Boundary conditions which can be specified using the MT3DMS engine in Visual MODFLOW are lines of constant concentrations, point sources, evapotranspiration concentrations, and recharge concentrations.

For the Northern Ontario Gold Mine site contaminant transport model, constant concentration boundary conditions were used to represent the source of contamination and provide solute mass transport into the model domain. The constant concentration cells were assigned to the top layer of the model, in a row two cells deep along the edge of the TMA location as shown in Figure 5.2. The source could not be assigned to all the cells of the top layer which were inside the TMA because many of them are designated as inactive. The cells along the edge of the TMA

which remain active were therefore assigned the constant concentration boundary condition. These cells represent the dissolved concentrations in the tailings pore water which are slowly seeping through and beneath the moraine ridge and tailings dams. Source depletion was not considered in the contaminant transport model simulations because the Northern Ontario gold mine site is still in operation, and is continually depositing fresh tailings into the TMA.

In order for this constant concentration boundary condition to accurately represent the contaminant source on the site, the input concentration at which the contaminants are entering the model would have to be estimated. First, the maximum concentrations of each contaminant measured in the wells downstream of the source were noted. From Figure 3.16 and Figure 3.19, we can see that yearly average dissolved cobalt concentrations in well GW-96-14S exceed 35µg/L after 2011, with one test in 2011 exceeding 40µg/L (Appendix A). For Sulphate, the observed dissolved concentration contours shown in Figure 5.1 (Piteau Associates Engineering Ltd., 2011) indicate that concentrations exceeding 900mg/L have been measured in the groundwater monitoring wells adjacent to the TMA. If these observed concentrations of dissolved sulphate and cobalt measured in the groundwater were migrating from the TMA, then the source concentration would have to be the same magnitude, or greater. In addition to this rationale, Figure 5.3 displays the concentration time series of dissolved cobalt and sulphate measurements taken from the tailings decant pool and the seepage collection ditches adjacent to the tailings dams. This figure shows that maximum dissolved cobalt concentrations occur in TLG-2 (the tailings decant pool), where a maximum of 70µg/L and an approximate average between 30-40µg/L have been measured. The maximum dissolved sulphate concentrations occur in TLG-5 (the finger drains adjacent to tailings dam B), where maximum concentrations

exceeding 1300mg/L and an approximate average near 1100mg/L have been measured. These values for sulphate and cobalt exceed, but agree well with the maximum concentrations measured in the groundwater monitoring wells. Therefore a concentration of 1100mg/L and a concentration of 40µg/L were used as initial source concentrations for sulphate and cobalt, respectively.

5.3 MODELLING RESULTS

A contaminant transport model uses the input properties and boundary conditions, and calculates the concentration distribution of dissolved contaminants in every cell within the model domain. The results of the transport modelling are displayed through various sets of concentration contours, which each represent the simulated contaminant plume at a specific simulation time.

5.3.1 INITIAL SIMULATIONS

Initial contaminant transport simulations were conducted using sulphate because it is assumed to act as a tracer and be unaffected by sorption. The intent of simulating the transport of a tracer contaminant before attempting to simulate cobalt transport is to gain a better understanding of the contaminant source term and the effects of dispersion, without having to also consider the effects of sorption. The initial sulphate source was input into the model as a constant concentration of 1100 mg/L in the location shown in Figure 5.2 and in the top layer only. The diffusion and dispersion input parameters used in each sulphate simulation are displayed in Table 5.1. The output concentration contours of run #1 indicated that the resulting

sulphate contamination plume would be transported through the tailings dams and moraine ridge in the top layer of the model only 21m downstream of the specified constant concentration source cells over a 20 year simulation period. The lack of contaminant movement in this simulation is likely due to the very low hydraulic conductivity of the top layer, which causes advective transport to occur very slowly through the silty-clay. The simulated plume also remained only in the top layer, and no simulated sulphate concentration contours advanced downward into the sand aquifer layer. This is likely due to the fact that no vertical hydraulic gradient is simulated in the groundwater flow model. Since the simulated sulphate plume did not even reach the monitoring wells located closest to the contaminant source cells in a 20 year simulation period, the results of run #1 were not considered to be realistic. These results indicate that the source likely has much more direct contact with the sand aquifer layer than originally assumed, and placing the modelled source in the top layer only does not accurately represent the site conditions. Since there is no vertical gradient present in the model to transport the source concentrations downward from layer 1 into layer 2, it was necessary to edit the source location so that it was assigned to both layer 1 and layer 2 of the model.

Since the sand layer is believed to be the location in which the majority of contaminant transport is taking place at the northern Ontario gold mine site, it was made the main focus of the contaminant transport modelling. Additionally, since the majority of the groundwater monitoring wells have a screened interval within the sand aquifer layer (see Table 3.1), the output concentration contours from the sand layer provide the best comparison to the observed concentrations. For these reasons, the center of the sand layer is the location from

which the simulated concentrations of the contaminant transport model are taken when the model output concentration contours are presented.

With the source concentrations input into both layer 1 and 2 of the model, Figure 5.4 displays the results of run #2 in the form of dissolved sulphate concentration contours. This run was conducted for an 11.5 year simulation period, and therefore represents the plume shape in October 2008. The simulation period was chosen so the results could be compared to the observed concentration contours in Figure 5.1. The first important observation made from the contaminant transport simulation results shown in Figure 5.4 is the shape of the 600, 800, and 1000mg/L concentration contour lines. These contours seem to extend away from the TMA and toward the lake in two distinct locations. This seems to indicate that there are actually two main concentration fronts migrating away from the TMA instead of the single plume shown in Figure 5.1. In the simulation results of Figure 5.4, one of the concentration fronts appears to be originating from the western portion of the TMA, and travelling almost directly southward toward the lake. The second seems to be originating from the TMA near the western edge of the seepage collection pond, and travelling in a southwestern direction toward the lake. Examination of the simulated concentration contours in the eastern portion of the model, however, indicates that contaminant transport is occurring relatively slowly in that area. This is likely due to two main factors; first, the low hydraulic conductivity values assigned to the sand aquifer layer in this area would limit advective transport, and second, the seepage collection pond in the model is acting as a sink for the high concentrations of sulphate.

To examine the quality of the simulation results, Figure 5.4 is compared more thoroughly to Figure 5.1. One important observation is the location of the 1000mg/L concentration contour. In Figure 5.4 this contour extends southward away from the TMA past the location of 5 different monitoring wells, however, as seen in Figure 5.1, none of the measured concentrations in the monitoring wells have exceeded 1000mg/L, and this contour is not present. This would seem to indicate that the input sulphate concentrations at the model source are too high. However, when the 600mg/L contour is examined, its location relative to the lake is in general agreement in both Figures 5.1, and 5.4.

To investigate the possibility of the source concentration being too high, another simulation (run #3) was performed using a source concentration of 900mg/L. As seen in Figure 5.5, when the source concentration was lowered to 900mg/L, the simulated concentrations in the area above the seepage collection pond matched the measured concentrations much more closely, as seen by the location of the 800mg/L contour in Figure 5.1 and 5.5. However, when comparing the concentrations near the edge of the lake, it can be seen from Figure 5.5 that the simulated concentrations do not reach nearly as high as the observed concentrations. This can be seen by comparing the location of the 600mg/L concentration contour in Figures 5.1 and 5.5. In an attempt to get improved matching of the simulated and observed plumes, the dispersivity values were changed in run #4. Through a trial-and-error process, it was determined that in order for the simulated concentrations adjacent to the lake to exceed 600mg/L, the longitudinal dispersivity input value would need to be approximately 0.1m. However, a longitudinal dispersivity value of 0.1m is very low for a plume of approximately 1000m in length, and was considered to be unrealistic. When compared to the historically measured dispersivity values in

Figure 2.6, this point would fall well below the other data points for the same range in plume length.

For this reason, the longitudinal dispersivity input was reset to its original value of 11.77m, and instead the source was divided into an eastern and a western section, as shown in Figure 5.6. This allowed two different source concentrations to be used on either side of the TMA in the model. The source concentration in the eastern portion of the TMA was left at 900mg/L, and the western portion was raised back to 1100mg/L. The results of this simulation (run #5) are shown in Figure 5.7, which agrees well with the observed concentrations both in the wells located north of the seepage collection pond and the wells located adjacent to the lake.

The initially estimated dispersivity values were then revised to adjust the spread of the plume. In run #6 the longitudinal dispersivity was lowered from 11.77m to 9.12m, while the transverse horizontal and vertical dispersivities remained at 10% and 5% of the longitudinal dispersivity, respectively. In run #7 the transverse horizontal and vertical dispersivity ratios were reduced to 5% and 1% of the longitudinal dispersivity respectively. These changes in dispersivity values were intended to narrow the plume, and provided a more accurate match to the observed sulphate concentrations in wells adjacent to the lake. The results of the simulations with adjusted dispersivity values in run #7 are displayed in Figure 5.8.

In order to compare the simulated results to the observed 2010 sulphate contours displayed in Figure 5.2, the simulation time was extended. Figure 5.9 presents the simulated plume after a transport time of 13 years, which would represent its extents in April 2010 (run #8). This simulation was used to represent the maximum amount of transport that would have occurred

prior to the pumping wells being activated in June 2010. Figure 5.10 presents the simulation results 6 months after the activation of the pumping wells in the model (run #9). This simulation was used to represent the conditions of the sulphate plume in October 2010, approximately the same time that the observed measurements were actually taken from the monitoring wells. Comparing these figures, the 2010 observed contours of Figure 5.1 match much more closely to those in Figure 5.9 than they do to those in Figure 5.10. This seems to indicate that the sulphate plume in the model is much more responsive to the pumping wells than was actually observed by the measured concentrations. However, this lack of response of the sulphate concentrations to the pumping wells seems anomalous considering that both the observed dissolved cobalt and iron concentrations dropped in the groundwater monitoring wells between the pumping wells and the lake immediately upon activation of the pumping (as seen in Figures 3.19 and 3.21).

To ensure that the dissolved sulphate concentration contours in Figure 5.1 were not created in error or incorrectly labelled, the concentration-time series for the observed measurements from the groundwater monitoring wells between the pumping wells and the lake were examined (wells 95-GW-2, 06-GW-26, 06-GW-27, 06-GW-28, 09-GW-37, 09-GW-38, and 09-GW-39). The concentration time series of these wells (displayed in Appendix C) indicate that, in most cases, both dissolved cobalt and dissolved sulphate concentrations begin to drop immediately upon commencement of pumping in July 2010. However, wells 06-GW-26, 06-GW-27, and 06-GW-28 have sulphate concentrations which seem to remain constant temporarily, or even peak at the measurement taken in October 2010 before dropping. This delay is only seen in these wells, however, and is also not experienced by the dissolved cobalt

concentrations. Although the model does not experience this slight delay in sulphate concentrations in these three wells, the reduction in sulphate concentrations to levels below 100mg/L is simulated by the model to occur by April 2012, the same time this level is reached in the observed data. Since this delay was only observed in a small number of wells, and occurred for a short time period (6 months), the model was considered to sufficiently represent the observed sulphate plume evolution (in 2009 and 2012), and was used to proceed to the calibration process using dissolved cobalt concentration data.

5.3.2 CALIBRATION

Calibration of the contaminant transport model was performed using cobalt as a dissolved contaminant, and was performed systematically. Separate groups of transport simulations were carried out to evaluate the cumulative effect of dispersion and sorption on the evolution of the cobalt plume. The transport simulations conducted during the model calibration process for dissolved cobalt are listed in Table 5.2. The first cobalt transport simulation was performed using the same dispersivity values as the final sulphate simulations. The concentrations used to represent the constant cobalt source were determined as described in section 5.2.3, and were input into both layer 1 and 2 of the model. The distribution of these concentrations in the east and west portion of the source area was chosen to mimic the distribution used for the sulphate modelling; the eastern concentration was assigned a value approximately 25% lower than the western concentration.

Calibration of the cobalt transport model was performed by simulating a time period of 12 years. The output of these simulations would therefore represent the plumes extent during

April 2009, which can then be compared to the observed concentration contours displayed in Figure 3.19. The output plume extents and concentration contours that are presented and discussed in this section for all cobalt transport simulations summarized in Table 5.2, were taken from the center of layer 2 (the sand aquifer layer) of the model.

The first cobalt simulation was performed considering only the effects of advection and dispersion. The results of the advection-dispersion only simulation (Figure 5.11) indicate the development of a much larger plume of greater concentrations than what was actually observed in 2009 on the site (Figure 3.19). This indicates that the sorption of dissolved cobalt onto the subsurface soils plays a major role in its transport through the sand aquifer.

The effects of sorption onto the various subsurface soils was included in the model beginning with run #11 by inputting the initial estimated linear distribution coefficients for dissolved cobalt listed in Table 5.4. As expected, once sorption values were input, the simulated plume from run #11 (shown in Figure 5.12) was much smaller, and had lower concentrations than those which were simulated by the advection-dispersion only simulation of run #10. However, it should be noted that the simulated plume still produced concentrations adjacent to that lake that were higher than the observed measurements. It is likely that more attenuation by sorption is actually occurring than is being accounted for in the model. This was further investigated by more closely examining the effects of the distribution coefficient for layer 2 (the sand aquifer layer).

The effect of cobalt sorption onto the sandy aquifer material in layer 2 of the model was first examined in run #12 by setting the distribution coefficient of this layer to zero. This would

remove the effects of cobalt sorption onto the sand layer, and only allow sorption to occur on layers 1 and 3 of the model. The expected result of this change is the expansion of the simulated cobalt plume produced in run #11 (Figure 5.12). Although the results of run #12, as presented in Figure 5.13 display a larger plume than Figure 5.12, the difference is minimal. The initial distribution coefficient input into the model for the sand layer (8.8×10^{-12} L/µg), therefore has little effect on the advancement of the cobalt plume through the sand layer. This is likely due to the fact that it is so small in magnitude.

Therefore, although the cobalt source is located in layers 1 and 2 of the model, and cobalt transport occurs mainly through the sand layer (layer 2), the distribution coefficients of the top and bottom layers (layers 1 and 3) of the model have a noticeable impact on the cobalt transport through layer 2. Comparing the results of run #10 (Figure 5.11) with run #12 (Figure 5.13), a noticeable difference in the plume concentrations located in the center of the sand layer is observed. Since all other parameters were held constant between these two runs (see Table 5.2), this difference in simulated plume size can only be attributed to the sorption of dissolved cobalt onto the material in the top and bottom layers of the model.

To further analyze the effect of the sand layer distribution coefficient, this value was adjusted through several simulations on a trial-and-error basis. The results of this analysis are shown in Figure 5.14 and Table 5.2 for run #13. As seen in Figure 5.14, this simulation was able to produce cobalt concentrations adjacent to the lake which are in general agreement with the observed measurements presented in Figure 3.19. However, the simulated plume still tends to

produce values which are higher than observed next to the TMA north of the seepage collection pond.

As described in section 4.2.2, during the construction of the groundwater flow model, two zones of distinctly different hydraulic conductivity needed to be created in order to accurately represent the hydrogeologic conditions of the sand layer. If the difference in hydraulic conductivity values between these two zones is due to a change in grain size, or silt/clay content, then the specific surface area of the zones would also be affected. It would then be reasonable to assume that the distribution coefficients for these two zones could also be quite different from each other. For this reason, the sand layer was divided into two sorption zones, identical to those used in the initial hydraulic conductivity distribution, as displayed in Figure 4.5. For the first simulation which incorporated two sorption zones in layer 2 (run #14), the northern zone was assigned the distribution coefficient which was used for run #13, and the southern zone was assigned the originally estimated distribution coefficient value for the sand layer (see Table 5.2). The resulting plume of run #14 was very similar to that of run #13 in the northern portion of the site. In the southern portion of the site, however, the plume from run #14 was noticeably larger than the results of run #13. This plume expansion was caused by the reduced distribution coefficient value in the southern sorption zone of the model. The result of this plume expansion caused the simulated plume to produce concentrations adjacent to the lake which were higher than the observed concentrations in Figure 3.19.

The distribution coefficient of the northern zone was then increased through a trial-and-error process in run #15. This caused a reduction in the plume concentrations by contracting the

plume in the northern portion of the site near the TMA. The results of this simulation are presented in Figure 5.15, which agrees well with the observed 2009 concentrations presented in Figure 3.19.

In order to compare the simulated results to the observed cobalt plume's reaction to the pumping, the simulation was extended until April 2012 (run #16, Table 5.2). The results of this simulation demonstrate a sudden contraction of the cobalt plume between the pumping wells and the lake almost immediately upon the commencement of pumping (see Figure 5.16). This simulated reaction occurred very similarly to the sudden drop in observed 2012 cobalt concentrations presented in Figure 3.19. Both the 2010 and 2012 simulated contours matched the observed 2010 and 2012 contours shown in Figure 3.19 very closely.

5.3.3 Sensitivity Analyses

Sensitivity analyses for the Northern Ontario gold mine site model were performed on the dispersion and sorption parameters and, the cobalt source term, the grid size, and the effect of seasonal groundwater elevation changes. By adjusting each of these parameters individually, while keeping the others constant, that parameter's effect on the simulated cobalt plume was observed. The beginning values for all of the parameters used in the sensitivity analysis are the same as the final calibrated contaminant transport model used in run #15 (Table 5.2). A summary of the sensitivity analysis simulations and the parameters which were used for each run are found in Table 5.3.

Increasing the input dispersivity values of the model by one order of magnitude caused considerable change to both the size and shape of the cobalt plume. Comparing Figure 5.15 and

5.17, the increase in dispersivity values caused an expansion of the plume width, but a significant reduction to the plume length. The main changes in the plume shape can be seen by examining the 0.9 µg/L concentration contour line. In the eastern portion of the site, beneath the seepage collection pond, the plume has travelled further away from the TMA when the dispersivity values were increased. On the contrary, in the western portion of the site, the two main plumes have been significantly shortened, and the concentrations no longer reach the edge of the lake in Figure 5.17. This is likely due to the fact that dispersivity acts in all directions, including vertically. The increased vertical spreading of the plume has caused an increase in the amount of dissolved cobalt which has travelled into, and therefore been sorbed by, the top and bottom layers of the model. It was also observed that the size and concentration of the simulated cobalt plumes in the top and bottom layers of the model were significantly increased as a result of this sensitivity simulation.

Sensitivity analysis of the sorption values was performed separately for each zone. Neither increasing nor decreasing the distribution coefficient in the top or bottom layer of the model produced a noteworthy effect on the simulated cobalt plume in the sand layer (run#18-21). This is mainly due to the fact that these layers have both a much lower hydraulic conductivity (less advective transport), and a much higher sorption rate (more attenuation) than the sand layer. When the distribution coefficient of the southern sorption zone of the sand layer was decreased by one order of magnitude (run #22), a negligible impact on the cobalt plume was also observed. Since the distribution coefficient of this zone is very low, it has little effect on cobalt transport. When the southern zone's distribution coefficient was raised by one order of magnitude (run #23), a noticeable but not greatly significant shrinking of the simulated plume

was produced. Simulated cobalt concentrations in the wells adjacent to the lake were lowered by approximately 1µg/L. In the northern zone of layer 2, a high degree of sensitivity to changes in the distribution coefficient was displayed. Raising the distribution coefficient of this zone by one order of magnitude (run #24) effectively shrunk the plume to just 125m at its most elongated point. This is not surprising considering that this increased distribution coefficient value is in the same order of magnitude, and nearly as great as the value which is input for the clay layer. Alternatively, decreasing the distribution coefficient of the northern zone of layer 2 by one order of magnitude (run #25) had the opposite effect. As displayed in Figure 5.18, when the distribution coefficient of this zone was reduced, the plume expanded much more than it had in previous simulations. Simulated concentrations in wells adjacent to the lake were increased by as much as 5µg/L compared to the results of run #15 (shown in Figure 5.15).

Due to the variations in observed cobalt concentrations measured in the decant pool of the TMA (presented in Figure 5.3), a sensitivity analysis was performed to determine the effect of a time variable source concentration on the contaminant transport model results (run #26). A piecewise function was created which used five time steps to vary the model source concentration to represent the changes observed in the decant pool concentrations in Figure 5.3. The source function began with a concentration of 30µg/L for 1.5 years (April 1997-October 1998), and then increased to 40µg/L for another 1.5 years (October 1998-April 2000) before increasing again to 50µg/L for 4 years (April 2000-April 2004). The concentration then dropped to 25µg/L for 2.5 years (April 2004-October 2006) before increasing slightly to 30µg/L for the remaining 2.5 years (October 2006-April 2009). The concentrations were also held constant between the east and west portions of the source throughout the simulation. The results of this

simulation after a 12 year time period are presented in Figure 5.19, and compared to Figure 5.15. Comparing these two figures, it can be seen that the time varying source simulation produced a plume which had a slightly greater extent, but a lower maximum concentration.

The influence of the model's grid size on both the groundwater flow and contaminant transport results was also tested. To determine this effect, multiple simulations were performed in which the grid size of the final calibrated model was either coarsened or refined, and all other input parameters remained constant. Run #27 was performed using a grid size of 30m x 30m, which was coarsened by a factor of two from its original size of 15m x 15m. The result of the coarsening of the grid was a noticeable decrease in the degree of calibration of the groundwater flow model to the April 2009 observed data. The maximum residual of the model increased to 0.148m at well 96-GW-11 (originally -0.091m at well 95-GW-10D), the residual mean increased to 0.058m (originally 0.003m), and the absolute residual mean increased to 0.063m (originally 0.033m). These results indicate that the calculated head values across the majority of the model have increased on average, and decreased the overall fit of the data. An alternative simulation (run #28) was performed using a grid size of 7.5m x 7.5m, which was refined by a factor of two from the original grid size of 15m x 15m. The results of refining the grid had very little effect on the model's degree of calibration to the April 2009 observed groundwater data. The maximum residual increased slightly in magnitude to -0.094m at well 95-GW-10D, while the absolute residual mean increased by only 1mm, to 0.034m. This seems to indicate that increasing the grid size by a factor of two would decrease the accuracy of the model enough to affect the quality of the calibration. However, decreasing the grid size in order to increase the precision of the model has no effect on the model accuracy or degree of

calibration. From these results it is concluded that the 15m x 15m grid is sufficiently small as to not have an effect on the model calibration, and allows the calibration to be grid size independent.

A steady state groundwater flow model was used throughout this thesis project to represent the groundwater flow conditions at the site. This type of model was assumed to reasonably represent the site conditions because, as described in section 3.4, the groundwater flow patterns on the site do not change as the groundwater table raises and lowers seasonally. Since the groundwater flow model was both calibrated and validated using seasonal low groundwater elevation data, a sensitivity analysis was performed to investigate the impact of a change in the simulated groundwater table elevation on the model calibration. In run #29, all boundary conditions of the April 2009 final calibrated groundwater flow model were increased by 0.8m to represent the groundwater table elevation conditions during the August 2009 fall high event while all other inputs remained constant from the final calibrated model. The resulting simulated potentiometric surface (shown in Figure 5.20) was then compared to the observed fall high groundwater elevation data which was collected in August 2009. Using 31 observed data points, the maximum residual of the simulation was -0.22m at well 04-GW-21 and the absolute mean residual was 0.083m. These residuals represent approximately 9.9% and 3.7% of the observed total head drop across the site (2.23m between wells 96-GW-13 and 06-GW-27), respectively. With a maximum residual less than 10% of the observed total head drop, the fit of simulation to the observed data was determined to be acceptable. This indicates that the groundwater flow model can accurately simulate the observed site conditions regardless of the groundwater elevation being simulated. The main effect of raising the boundary conditions

in run #29 was a reduction in the number of dry cells in the sand layer of the model in the central and eastern portions of the site, south of the seepage collection pond. This can be seen by comparing Figure 5.20 to the potentiometric surface of the April 2009 final calibrated model shown in Figure 4.13. This may potentially affect the volume of groundwater which is allowed to flow southward in this area rather than westward during seasonal high events. This would likely not have an impact on the area of greatest concern of the site, but may influence the amount of cobalt transport which occurs in the eastern portion of the site over a long time period.

Additional investigation into the effect of increasing the simulated water table elevation on the calibration of the model was performed by simulating a seasonal high event which also included the effect of the pumping wells. This was performed in a manner similar to the groundwater flow model validation step, as described in section 4.4. In run #30, pumping wells were added to the model which was used in run #29, and the results were compared to the November 2011 collected groundwater data, which represent the 2011 seasonal high event. In this simulation, the pumping wells were assigned pumping rates which were recorded during the same time period as the observed groundwater elevations. Since the observed groundwater table in November 2011 was approximately 0.3m lower than the observed groundwater table in August 2009, the North and South constant head boundary conditions were lowered by 0.3m from those used in run #29. The eastern boundary condition was also lowered by 1.5m while all other input parameters remained constant. The resulting simulated potentiometric surface was compared to the seasonal high observed groundwater elevation data collected in November 2011. Using 34 observed data points, the maximum residual of the simulation was 0.206m at

well 96-GW-14D and the absolute mean residual was 0.078m. These residuals represent approximately 9.5% and 3.6% of the observed total head drop across the site (2.17m between wells 96-GW-13 and 06-GW-27), respectively. With a maximum residual less than 10% of the observed total head drop, the fit of simulation to the observed data was determined to be acceptable. These sensitivity analyses performed on the groundwater table elevation have shown that the calibrated and validated groundwater flow model can accurately simulate the observed groundwater flow conditions during the seasonal low and high events both before and after the pumping wells were installed.

5.4 Model Assumptions and Limitations

While the groundwater flow and contaminant transport modelling of the Northern Ontario Gold Mine site were conducted in a manner which would simulate the observed site conditions as accurately as possible, several assumptions were required during the modelling process which lead to limitations of the model. These assumptions were typically required either due to the complexity or uncertainty and/or sparseness of the observed data and typically resulted in either simplifications or approximations of site conditions. All assumptions which were made during the construction and calibration of the model are explained and justified in this section.

5.4.1 Groundwater Flow Model

Groundwater flow for the Northern Ontario gold mine site was simulated using steady-state conditions. This means that the model calculated the output potentiometric surface by determining the equilibrium water balance between the inflows and outflows of the various boundary conditions. Using this type of simulation assumes that the hydrogeologic conditions

of the site remained constant throughout the time period being simulated. The model therefore does not account for the time dependant changes of any of the groundwater flow input parameters. Additionally, since groundwater elevation monitoring in the nested wells indicated insignificant, or varying vertical gradient through the sand layer, the groundwater flow model was also created without consideration for vertical groundwater flow. As discussed in section 3.4, a thorough examination of the historical hydrogeologic conditions of the site was conducted to determine the seasonal changes in groundwater flow by comparing potentiometric surfaces of the site at different time periods. Through examination of the collected site data, it was found that the seasonal changes in groundwater elevations did not significantly affect either the horizontal or vertical hydraulic gradients that were measured, or the direction of groundwater flow in the subsurface of the site. Due to the consistency of the groundwater flow direction and gradient inferred from data measured at the site, it is considered reasonable to represent the groundwater flow using a steady state model, and this assumption is not likely to have a significant impact on the contaminant transport simulation results. A similar assumption was made by both Artimo et al. (2004) and Moldovan et al. (2008), who also determined that it was reasonable to create a steady state groundwater flow model and use it to investigate a contaminated site.

However, a steady state model also cannot account for the effects of temperature changes on the groundwater flow conditions. During the winter months, frost penetration can affect the hydraulic conductivity of the subsurface soils. If the frost penetration is sufficiently deep to cause freezing of the site's aquifer material, the groundwater flow could potentially be affected. The impact of this freezing effect was mitigated by comparing the groundwater flow

condition at the seasonal low period (prior to the spring thaw) and the seasonal high period (after the site is completely thawed). Since the observed groundwater flow patterns were determined to have the same direction, it was reasonable to assume that frost penetration had a negligible effect on the groundwater flow conditions at the site, and isothermal conditions were assumed in the model.

The recharge rates which were assigned to the groundwater flow model were approximations of the infiltration that would occur in different areas of the site based on the observed site conditions. Since groundwater flow was modelled using steady-state conditions, the recharge rates also remained constant throughout the simulation period. Therefore, this does not account for seasonal effects which will cause the infiltration rate at the site to vary throughout the year such as periods of high precipitation during the spring, or surface freezing during the winter months. The effect of a long winter season on the average infiltration experienced by the aquifer was part of the reason that a relatively low recharge rate was assigned to the model. In addition, when determining the input value which should be used as a recharge rate in this model, multiple simulations were performed, and a range of different values were used. From these simulations, it was determined that a change in the recharge rate had a negligible effect on the simulated potentiometric surface.

The boundary conditions used for the groundwater flow model were also inferred from collected site data. The distribution of total head values assigned along the northern boundary of the model was interpreted from the potentiometric surfaces which were created using collected site data. As discussed in section 4.4, although the distribution of these head values

across the northern boundary affected the calibration of the wells located closest to the TMA, it did not significantly affect the calibration of the wells in the western region of the model, which is the area of greatest concern to the contaminant transport model. The eastern and western boundary conditions were created to represent the western and eastern component, respectively, of the groundwater flow at these boundary locations. Due to the steep incline in surface topography in these areas, it was not reasonable to assume that groundwater flow would occur parallel to the model boundary. The value for the eastern boundary was estimated based on the observed groundwater elevations in the wells closest to this location (wells 95-GW-4 and 96-GW-11); however, this location is far from the area of greatest concern of the model. The eastern boundary condition did have an effect on both the groundwater flow model and the contaminant transport model in the area of concern. The estimation of the value for this boundary condition was made based on the elevation of the ground surface, and the estimated thickness of the aquifer layer in this area. This was necessary due to the lack of information about the groundwater conditions to the west of the overburden pile. During the model calibration process, calibration of the hydraulic conductivity zones was performed multiple times using various values for this boundary. This was done to minimize the impact of the uncertainty in this value.

The geological information used for the groundwater flow model was obtained from borehole logs, which were recorded during the installation of various monitoring wells across the site. These boreholes were adequate for identifying the presence of the site's main geological units, but provided sparse data in many areas of the site. When the groundwater flow model was constructed, the layer thicknesses were interpolated and extrapolated from the borehole data

in order to cover all areas of the model extents. This produced some unexpected layer thicknesses in areas of the site where there were very few monitoring wells, and where the data were being extrapolated to the model's edges. This included areas along the edge of the lake where no wells are located, and the sand layer was reduced to zero thickness as well as the area around the topographical high point in the center of the site where the silty-clay layer was projected to exceed 6m in thickness. By comparing the projected layer thicknesses of the model in these areas to borehole logs in other comparable areas of the site (for example comparing the edge of the lake in the model to borehole results taken from the lake's edge in a different area of the site), they were determined to not likely represent the actual subsurface conditions. Although these areas have sparse data simply because they are not in the area of focus for contaminant transport, and are not of greatest concern for subsurface characterization, extreme results such as zero thickness sections in the sand layer would affect the groundwater flow paths in the model. Therefore, in these areas, fictitious points needed to be input in order to provide more reasonable layer thicknesses across the entire model domain. The data for the fictitious points were estimated based on the borehole logs in similar areas and on the ground surface topography.

In addition to areas where sparse data existed, areas where many closely spaced wells are present can also cause an issue. While the majority of closely spaced borehole logs were in general agreement about the thickness of the various subsurface layers, a few wells indicated very different results. This would indicate the presence of a very sudden change in layer thickness. An example of this change is shown in cross section C-C' of Figure 3.2, which indicates a sudden change in the elevation of the bedrock surface between point W-25 and H-

25A. A sudden change in the bedrock surface and the pinching out of the sand layer, as indicated by these boreholes, can have a large impact on the flow of groundwater. In this location, it is believed that the change in bedrock surface is one factor that contributed to the groundwater flowing in a southwestern direction, rather than directly southward from the TMA (the flow follows the thickest portion of the aquifer). This was accounted for in the model during the creation of the hydraulic conductivity zones in the sand layer. The size, shape, and value assigned to each of the hydraulic conductivity zones were used to cause southwesterly flow in this area and calibrate the model to the observed groundwater elevations down gradient. Although various assumptions needed to be made in the creation of the groundwater flow model, they were mainly limited to areas of the model which were regarded to be of lesser importance. Since the groundwater flow model was validated by accurately simulating the response of the pumping wells in the aquifer, it is not believed that any of the aforementioned assumptions will have any significant impact on the objective of this work.

5.4.2 Contaminant Transport Model

Similar to the groundwater flow model, the contaminant transport model was also simulated under steady-state conditions. The input conditions for the contaminant source location, size, and concentration therefore all remained constant throughout the simulations. However, due to the nature of the TMA, which is the source of the contaminants at the Northern Ontario gold mine site, the source is likely time dependant. Throughout the years of mine operation, the volume of tailings in the TMA, and therefore the size of the contaminant source, has been steadily increasing. For the beginning of the simulation, which is intended to correspond to the

beginning of tailings deposition in the TMA, the modelled source concentration is likely too high for the first few years, as indicated in Figure 5.3.

Additionally, a steady state source term cannot account for natural fluctuations of the source concentrations in the TMA, as indicated in Figure 5.3. The concentrations of all dissolved constituents in the TMA would fluctuate over time due to a number of factors including precipitation, tailings deposition rate, mineral composition of the mined ore, and any other factor which could affect the rate of the iron sulphide oxidation reactions described in section 2.4.2. The oxidation of sulphide minerals and production of dissolved sulphate in the mine tailings would also not be an instantaneous process. In the beginning years of the sulphate transport simulations, the input source concentration may significantly overestimate the actual sulphate concentrations which were available for transport during that time in the TMA. These factors could all cause the simulated transport in the beginning years of the simulation to be much faster than actually occurred. The sensitivity analysis that was performed on the contaminant source term determined that lower cobalt concentrations would occur in the plume when a time varying source was simulated. This indicates that although the source used in the contaminant transport model is likely too high in the first few years of the simulation, it allows the cobalt transport to be estimated conservatively, since a larger mass of cobalt is entering into the model than that which is actually occurring at the site. Over estimating the contaminant source can therefore help to produce conservative results when future remediation scenarios are simulated.

Figure #	Run #	Simulation End Date	Source		Dispersivity (m)			Distribution Coefficient (kd) (L/µg)				Simulation Details
			West mg/L	East mg/L	(α_L)	(α_h)	(α_v)	Layer 1	Layer 2		Layer 3	
									North	South		
	1	Oct. 2008	1100	1100	11.77	1.177	0.589	-	-	-	-	Source in layer 1 only
5.4	2	Oct. 2008	1100	1100	11.77	1.177	0.589	-	-	-	-	Source in Layer 1 and 2.
5.5	3	Oct. 2008	900	900	11.77	1.177	0.589	-	-	-	-	Reduced source concentration from run #2
	4	Oct. 2008	900	900	0.1	0.01	0.005	-	-	-	-	Reduced dispersivity values from run #2 to match observed plume extension
5.7	5	Oct. 2008	1100	900	11.77	1.177	0.589	-	-	-	-	Increased source concentration from run #2 in eastern portion only
	6	Oct. 2008	1100	900	9.12	0.912	0.456	-	-	-	-	Reduced longitudinal dispersivity from run #5
5.8	7	Oct. 2008	1100	900	9.12	0.456	0.091	-	-	-	-	Reduced horizontal and vertical dispersivity ratios from run #6
5.9	8	Apr. 2010	1100	900	9.12	0.456	0.091	-	-	-	-	Represents the maximum extent of the sulphate plume
5.10	9	Oct. 2010	1100	900	9.12	0.456	0.091	-	-	-	-	0.5 years after pumping well commencement

Effective diffusion coefficient constant for all simulations (Layer 1,3: $D_e=32.36x10^{-6}$ m^2/day, Layer 2: $D_e=61.94x10^{-6}$ m^2/day) (see Table 5.4)

Table 5.1 Summary of the Sulphate Transport Simulations

Figure #	Run #	Simulation End Date	Source		Dispersivity (m)			Distribution Coefficient (kd) (L/µg)				Simulation Details
			West µg/L	East µg/L	(α_L)	(α_h)	(α_v)	Layer 1	Layer 2		Layer 3	
									North	South		
5.11	10	Apr. 2009	40	30	9.12	0.456	0.091	-	-	-	-	Extents of cobalt contamination if no sorption ocurred
5.12	11	Apr. 2009	40	30	9.12	0.456	0.091	$7.5x10^{-9}$	$8.8x10^{-12}$	-	$7.5x10^{-9}$	Input initial distribution coefficient estimates
5.13	12	Apr. 2009	40	30	9.12	0.456	0.091	$7.5x10^{-9}$	0	-	$7.5x10^{-9}$	Removed effect of sorption in layer 2 from run #11
5.14	13	Apr. 2009	40	30	9.12	0.456	0.091	$7.5x10^{-9}$	$1.8x10^{-10}$	-	$7.5x10^{-9}$	Increased effect of sorption in layer 2 from run #11
	14	Apr. 2009	40	30	9.12	0.456	0.091	$7.5x10^{-9}$	$1.8x10^{-10}$	$8.8x10^{-12}$	$7.5x10^{-9}$	Divided sand layer into north and south sorption zones
5.15	15	Apr. 2009	40	30	9.12	0.456	0.091	$7.5x10^{-9}$	$5.6x10^{-10}$	$8.8x10^{-12}$	$7.5x10^{-9}$	Adjusted north sorption zone of layer 2 from run #14
5.16	16	Apr. 2012	40	30	9.12	0.456	0.091	$7.5x10^{-9}$	$5.6x10^{-10}$	$8.8x10^{-12}$	$7.5x10^{-9}$	2 years after pumping well commencement

Effective diffusion coefficient constant for all simulations (Layer 1,3: $D_e=32.84x10^{-6}$ m^2/day, Layer 2: $D_e=62.87x10^{-6}$ m^2/day) (see Table 5.4)

Table 5.2 Summary of the Cobalt Transport Simulations

Figure #	Run #	Simulation End Date	Source		Dispersivity (m)			Distribution Coefficient (k_d) (L/µg)				Simulation Details
			West µg/L	East µg/L	(α_L)	(α_h)	(α_v)	Layer 1	Layer 2		Layer 3	
									North	South		
5.17	17	Apr. 2009	40	30	91.2	4.56	0.91	$7.5x10^{-9}$	$5.6x10^{-10}$	$8.8x10^{-12}$	$7.5x10^{-9}$	Increase dispersivity by one order of magnitude
	18	Apr. 2009	40	30	9.12	0.456	0.091	$7.5x10^{-8}$	$5.6x10^{-10}$	$8.8x10^{-12}$	$7.5x10^{-9}$	Increase distribution coefficient in layer 1
	19	Apr. 2009	40	30	9.12	0.456	0.091	$7.5x10^{-10}$	$5.6x10^{-10}$	$8.8x10^{-12}$	$7.5x10^{-9}$	Decrease distribution coefficient in layer 1
	20	Apr. 2009	40	30	9.12	0.456	0.091	$7.5x10^{-9}$	$5.6x10^{-10}$	$8.8x10^{-12}$	$7.5x10^{-8}$	Increase distribution coefficient in layer 3
	21	Apr. 2009	40	30	9.12	0.456	0.091	$7.5x10^{-9}$	$5.6x10^{-10}$	$8.8x10^{-12}$	$7.5x10^{-10}$	Decrease distribution coefficient in layer 3
	22	Apr. 2009	40	30	9.12	0.456	0.091	$7.5x10^{-9}$	$5.6x10^{-10}$	$8.8x10^{-13}$	$7.5x10^{-9}$	Decrease k_d in layer 2 south zone
	23	Apr. 2009	40	30	9.12	0.456	0.091	$7.5x10^{-9}$	$5.6x10^{-10}$	$8.8x10^{-11}$	$7.5x10^{-9}$	Increase k_d in layer 2 south zone
	24	Apr. 2009	40	30	9.12	0.456	0.091	$7.5x10^{-9}$	$5.6x10^{-9}$	$8.8x10^{-12}$	$7.5x10^{-9}$	Increase k_d in layer 2 north zone
5.18	25	Apr. 2012	40	30	9.12	0.456	0.091	$7.5x10^{-9}$	$5.6x10^{-11}$	$8.8x10^{-12}$	$7.5x10^{-9}$	Decrease k_d in layer 2 north zone
5.19	26	Apr. 2009	Time Variable		9.12	0.456	0.091	$7.5x10^{-9}$	$5.6x10^{-10}$	$8.8x10^{-12}$	$7.5x10^{-9}$	Source varies with time using piecewise function
	27	Apr. 2009	40	30	9.12	0.456	0.091	$7.5x10^{-9}$	$5.6x10^{-10}$	$8.8x10^{-12}$	$7.5x10^{-9}$	Increased grid size by factor of 2
	28	Apr. 2009	40	30	9.12	0.456	0.091	$7.5x10^{-9}$	$5.6x10^{-10}$	$8.8x10^{-12}$	$7.5x10^{-9}$	Decrease grid size by factor of 2
	29	Aug. 2009	40	30	9.12	0.456	0.091	$7.5x10^{-9}$	$5.6x10^{-10}$	$8.8x10^{-12}$	$7.5x10^{-9}$	August 2009 Boundary Conditions
5.20	30	Nov. 2011	40	30	9.12	0.456	0.091	$7.5x10^{-9}$	$5.6x10^{-10}$	$8.8x10^{-12}$	$7.5x10^{-9}$	November 2011 Boundary Conditions

Effective diffusion coefficient constant for all simulations (Layer 1,3: $D_e=32.84x10^{-6}$ m^2/day, Layer 2: $D_e=62.87x10^{-6}$ m^2/day) (see Table 5.4)

Table 5.3 Summary of Sensitivity Analysis Simulations

Parameter	Input
Sulphate Diffusion (D_e):	
Layer 1 - Silty Clay	32.36×10^{-6} m^2/day
Layer 2 - Sand Aquifer	61.94×10^{-6} m^2/day
Layer 3 - Till	32.36×10^{-6} m^2/day
Cobalt Diffusion (D_e):	
Layer 1 - Silty Clay	32.84×10^{-6} m^2/day
Layer 2 - Sand Aquifer	62.87×10^{-6} m^2/day
Layer 3 - Till	32.84×10^{-6} m^2/day
Dispersion:	
Longitudinal (α_x)	11.77 m
Horizontal (α_y)	1.177 m
Vertical (α_z)	0.589 m
Sulphate Sorption (kd):	
All Layers	0 L/mg
Cobalt Sorption (kd):	
Layer 1 - Silty Clay	7.5×10^{-9} L/µg
Layer 2 - Sand Aquifer	8.8×10^{-12} L/µg
Layer 3 - Till	7.5×10^{-9} L/µg

Table 5.4 Initial Contaminant Transport Model Input Parameters

Parameter	Value	Source
Molecular Diffusion Coefficient (D_0):		
Sulphate	92.45×10^{-6} m^2/day	Alvarez & Illman (2006)
Cobalt	93.83×10^{-6} m^2/day	Ribeiro et al. (2002)
Tortuosity Coefficient (τ):		
Layer 1 - Silty Clay	0.35	Rowe et al. (1988)
Layer 2 - Sand Aquifer	0.67	Batu (2006)
Layer 3 - Till	0.35	Rowe et al. (1988)

Table 5.5 Molecular Diffusion and Tortuosity Coefficients

Material	Effective Diameter (cm)	Specific Surface Area (cm^2/g)
Gravel	2×10^{-1}	11.1
Sand	5×10^{-3}	444.4
Silt	2×10^{-4}	1.11×10^{5}
Clay	2×10^{-4}	7.40×10^{6}

Table 5.6 Representative Effective Diameter and Specific Surface Area Values (Jury & Horton, 2004)

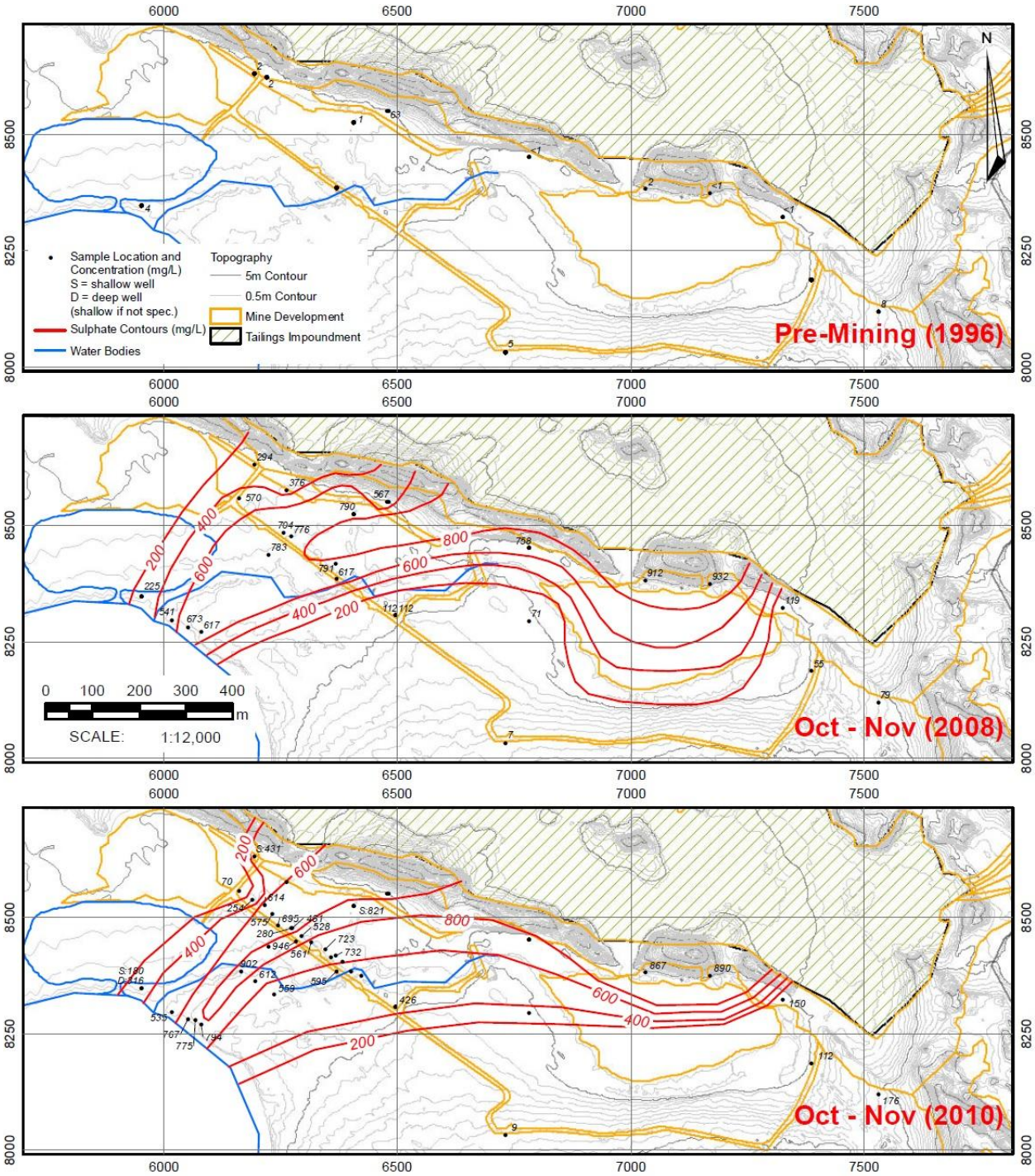

Figure 5.1 Observed Sulphate Concentration Contours (1996, 2008, 2010) (Piteau Associates Engineering Ltd., 2011)

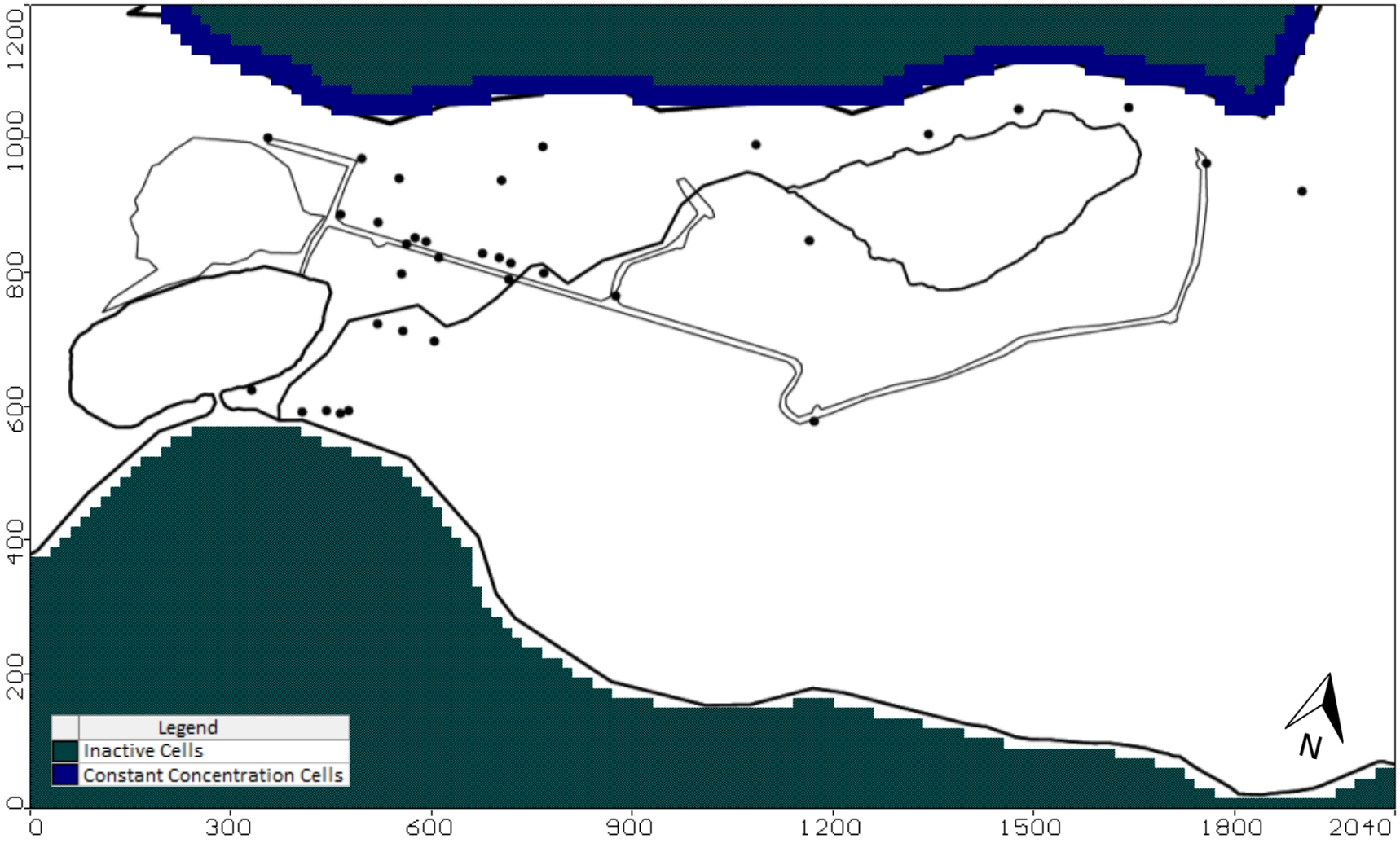

Figure 5.2 Contaminant Transport Model Source Location

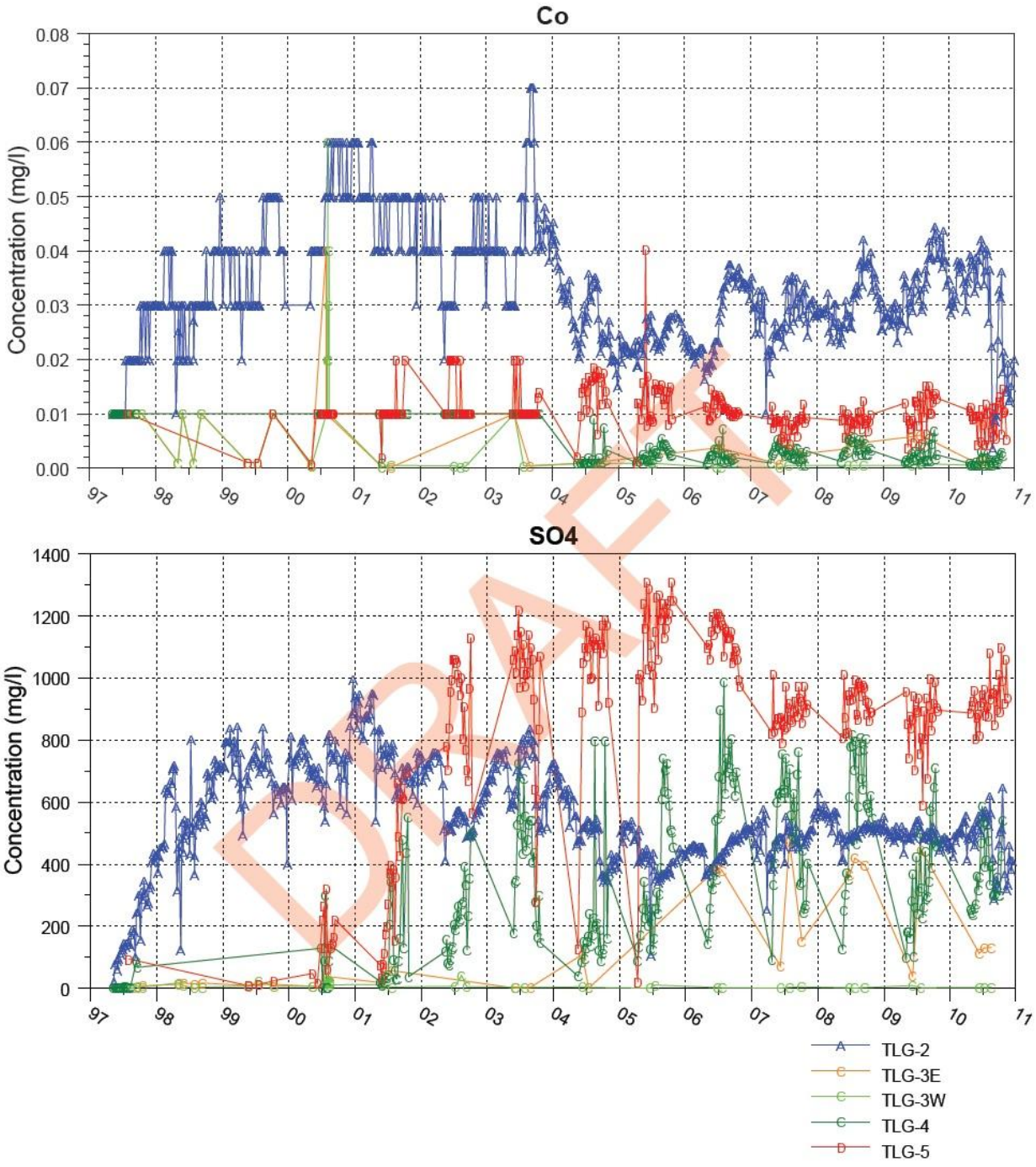

Figure 5.3 Dissolved Cobalt (Co) and Sulphate (SO4) Concentrations in Tailings Pond and Seepage Collection Ditches (Piteau Associates Engineering Ltd., 2011)

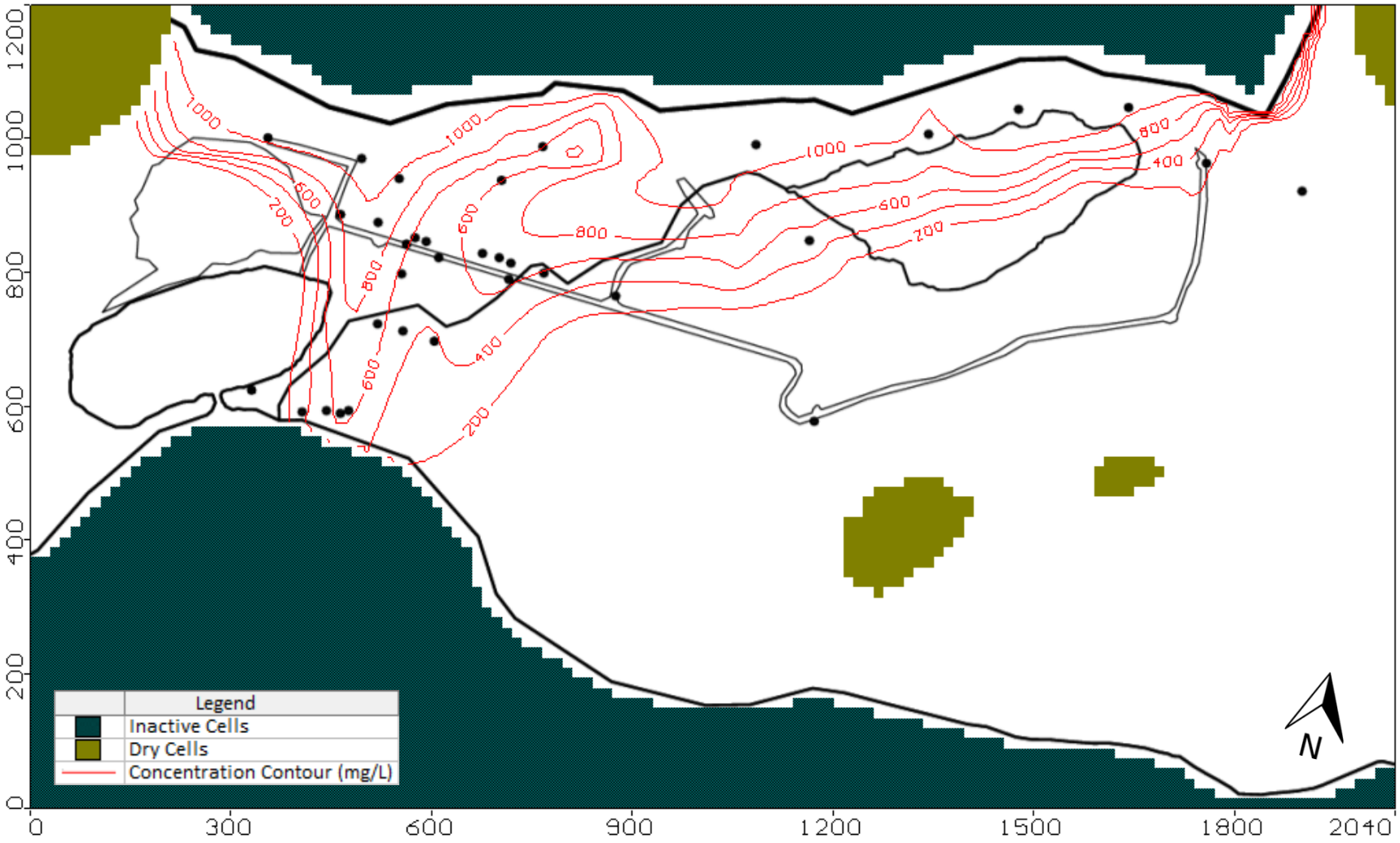

Figure 5.4 Sulphate Plume at 11.5 Years (October 2008) Using Run #2 Parameters (See Table 5.1)

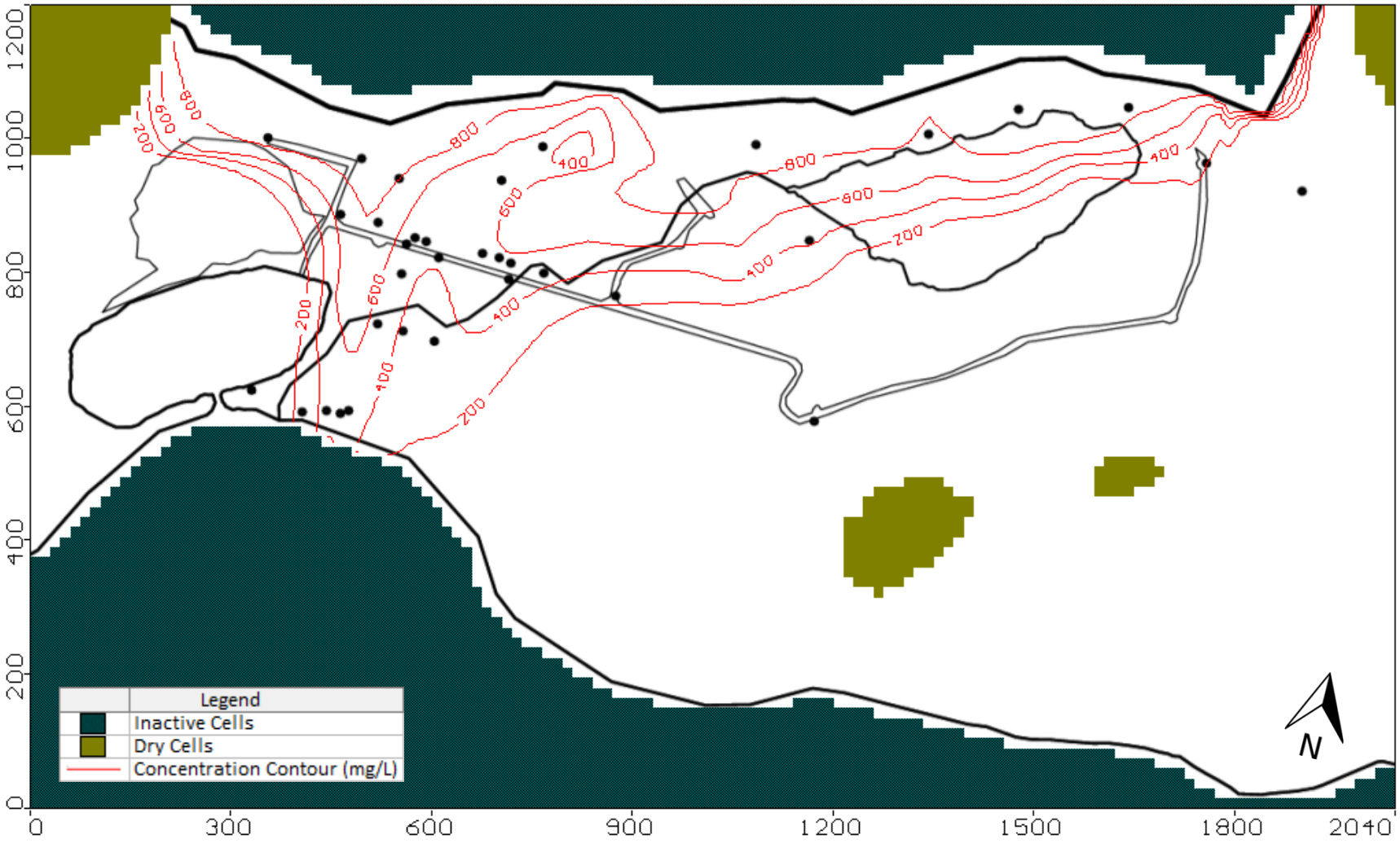

Figure 5.5 Sulphate Plume at 11.5 Years (October 2008) Using Run #3 Parameters (See Table 5.1)

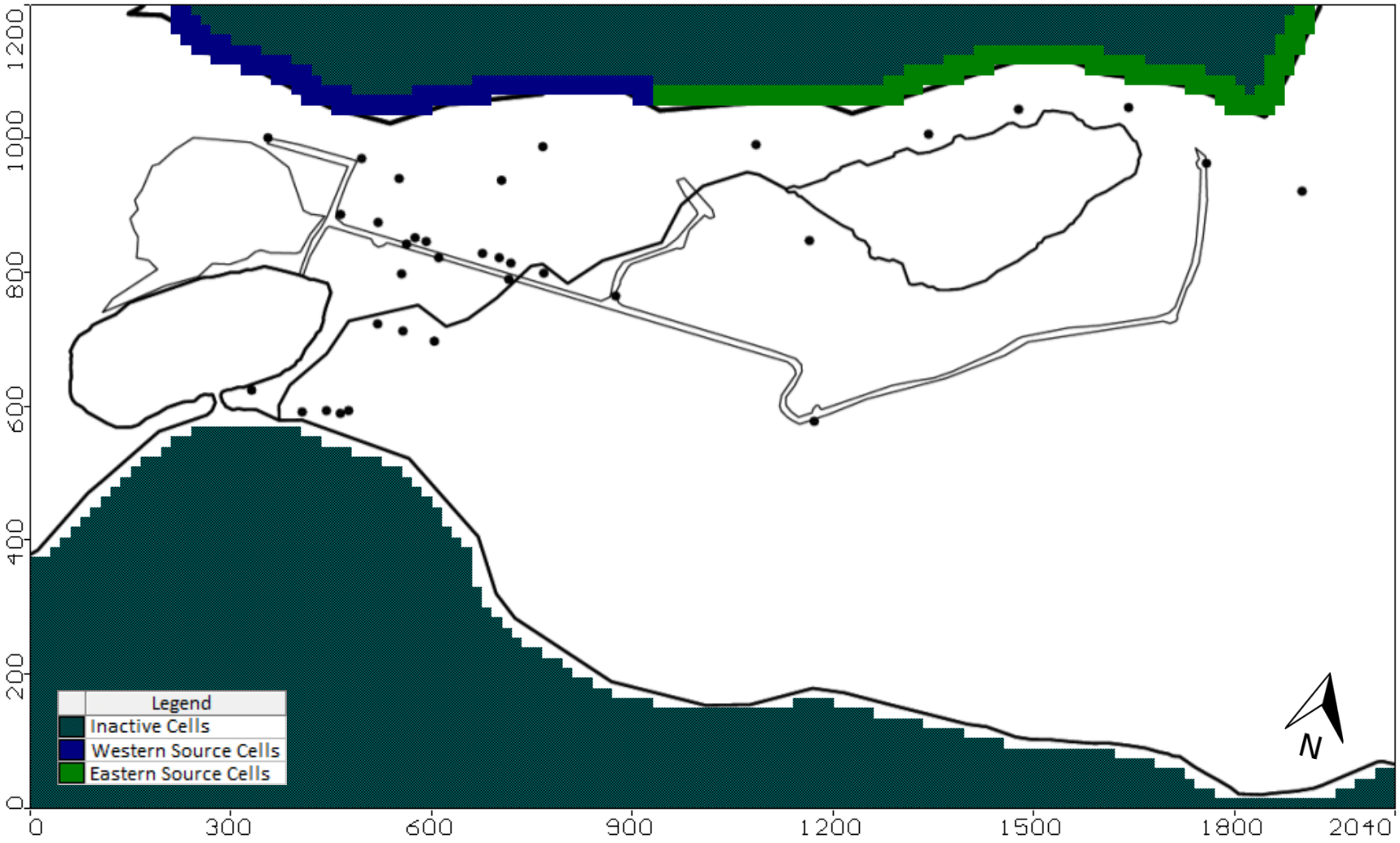

Figure 5.6 Revised Contaminant Source Location

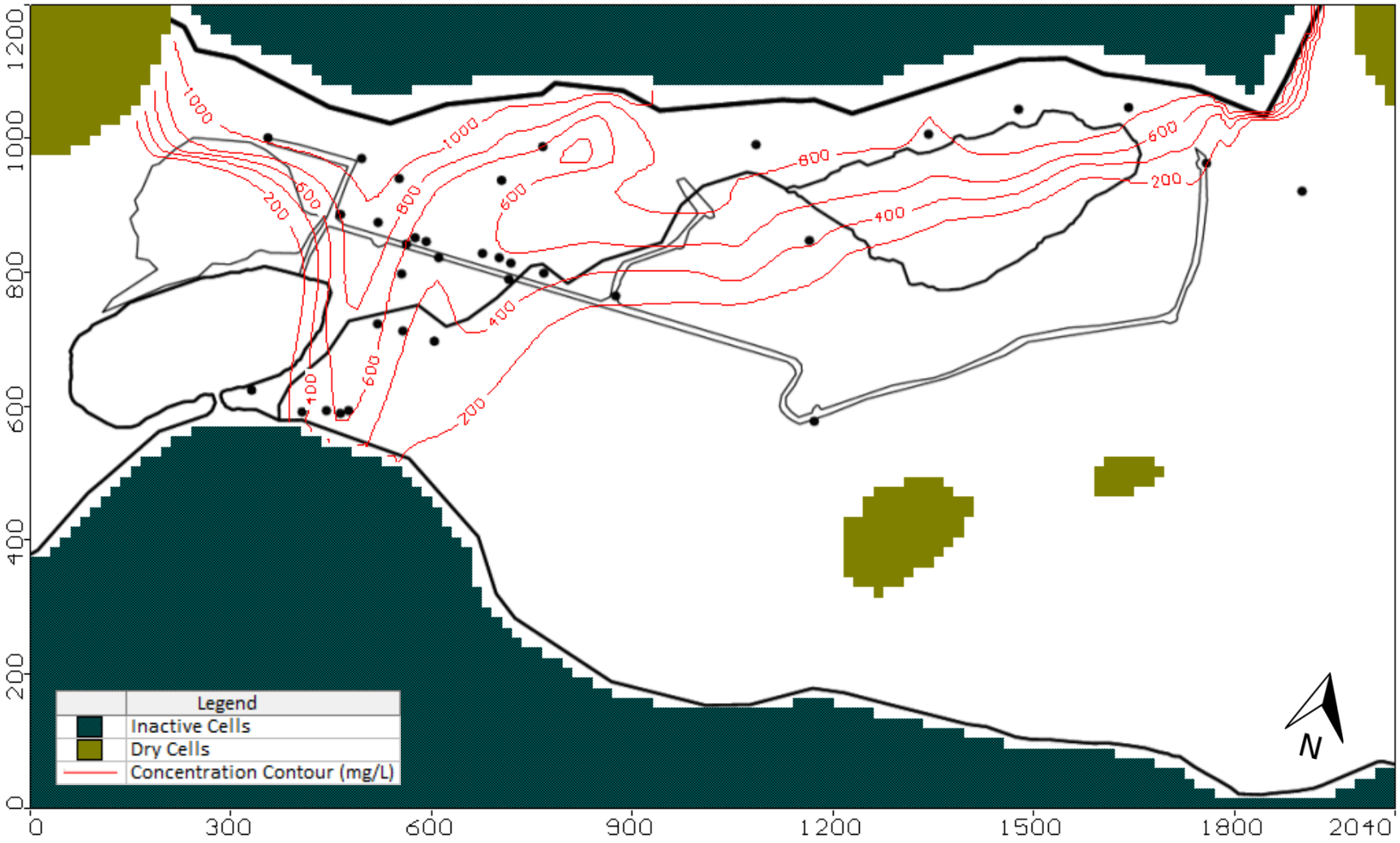

Figure 5.7 Sulphate Plume at 11.5 Years (October 2008) Using Run #5 Parameters (See Table 5.1)

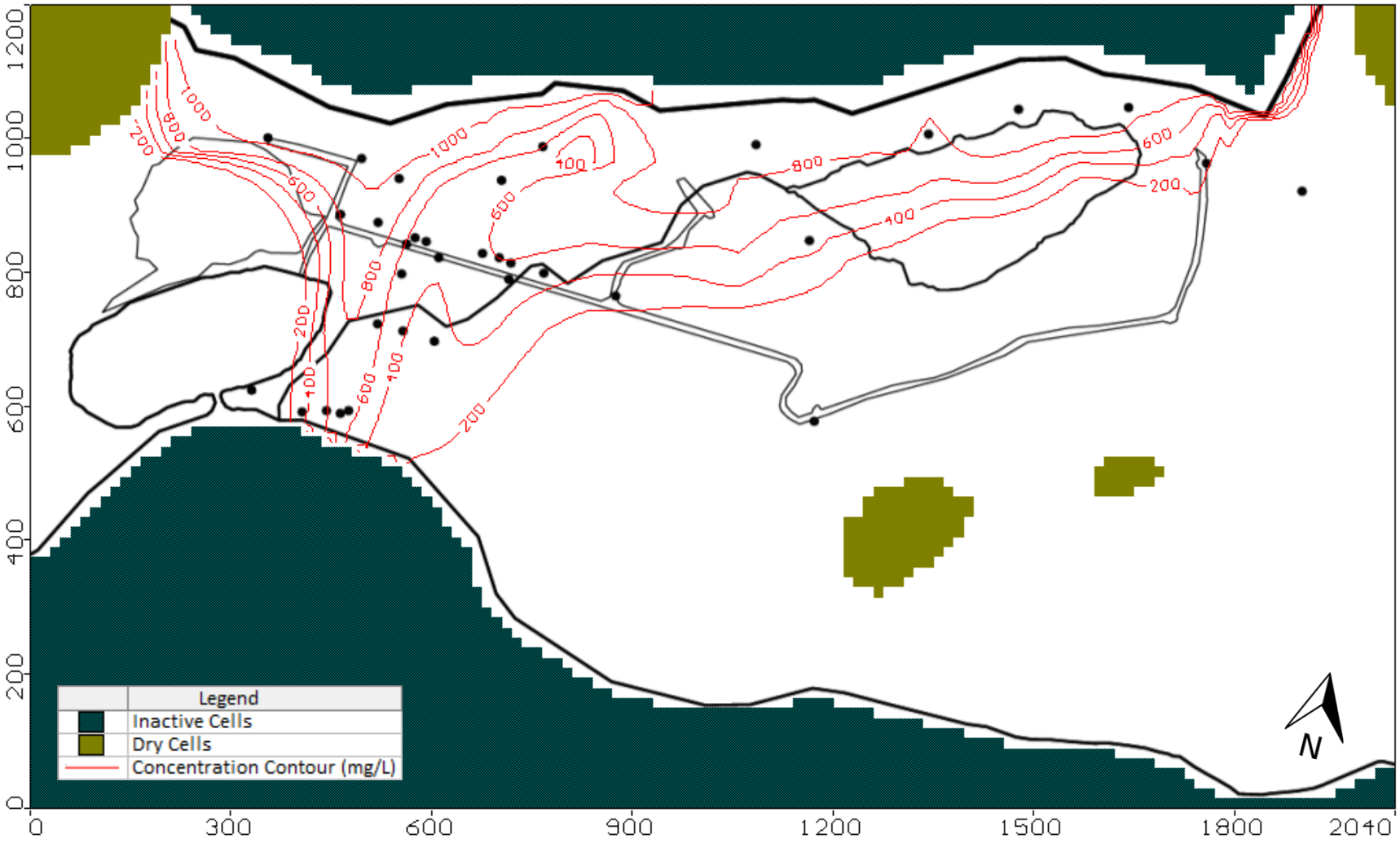

Figure 5.8 Sulphate Plume at 11.5 Years (October 2008) Using Run #7 Parameters (See Table 5.1)

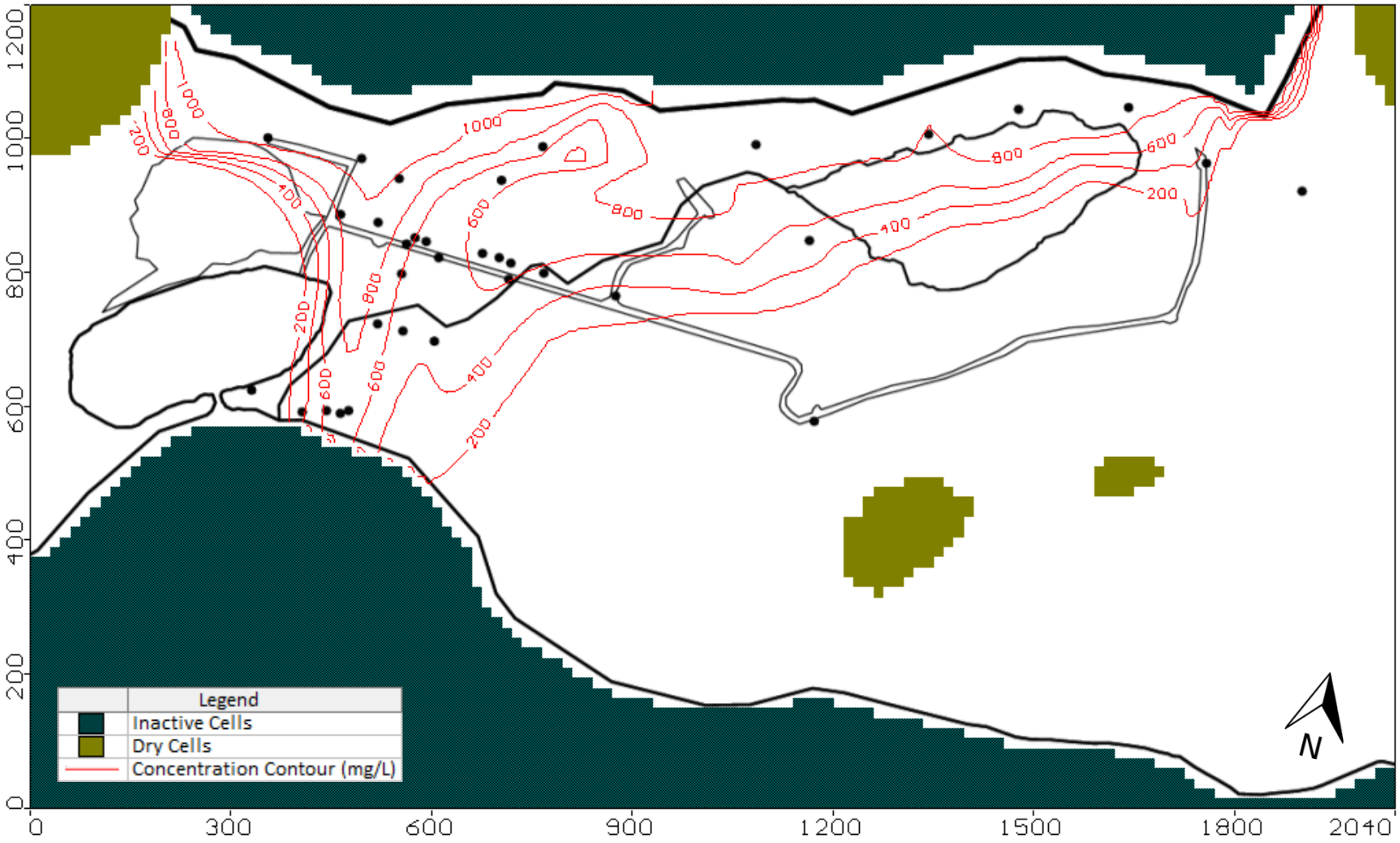

Figure 5.9 Sulphate Plume at 13 Years (April 2010) Using Run #8 Parameters (See Table 5.1)

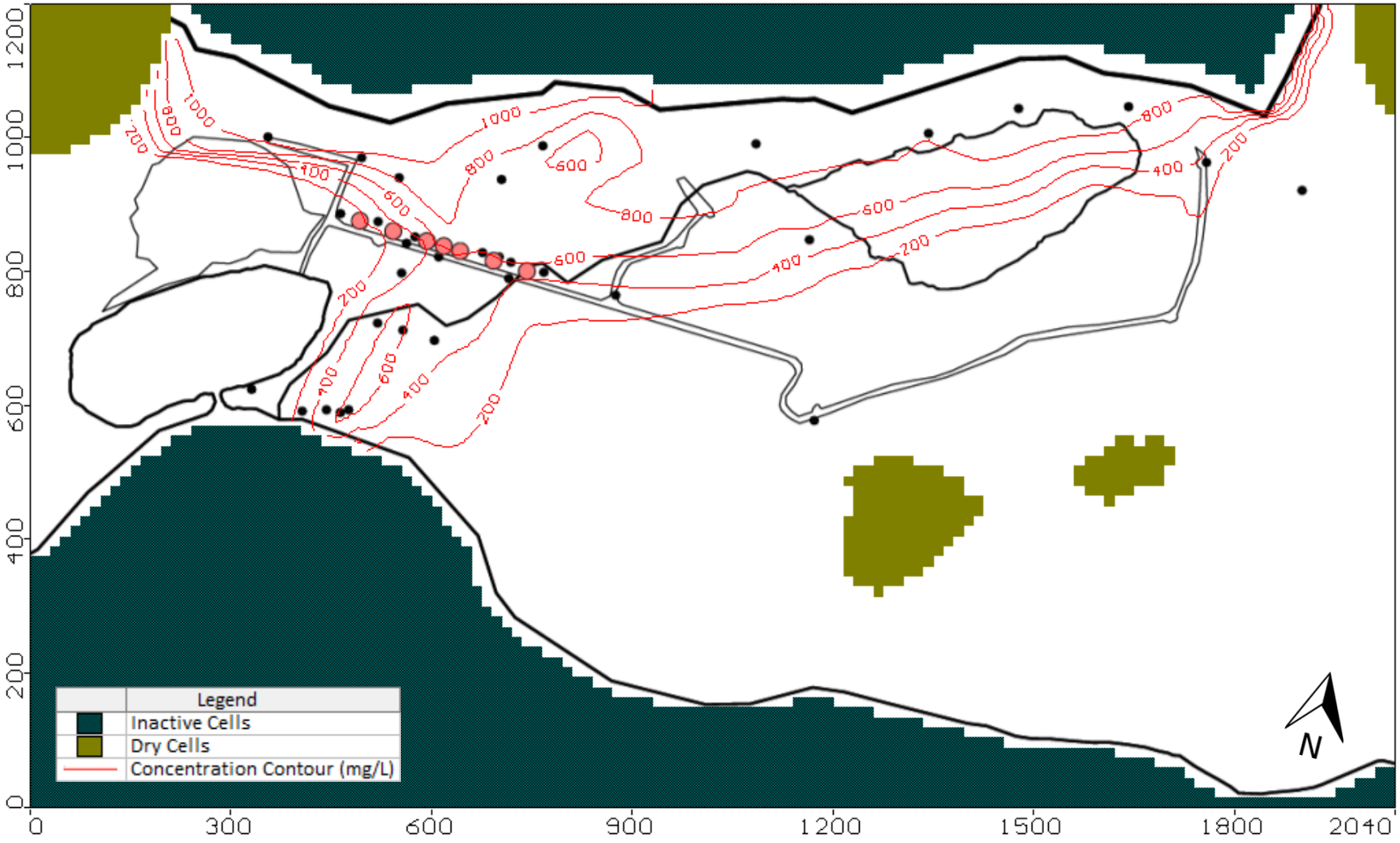

Figure 5.10 Sulphate Plume 0.5 Years After Pumping Well Commencement (October 2010) Using Run #9 Parameters (See Table 5.1)

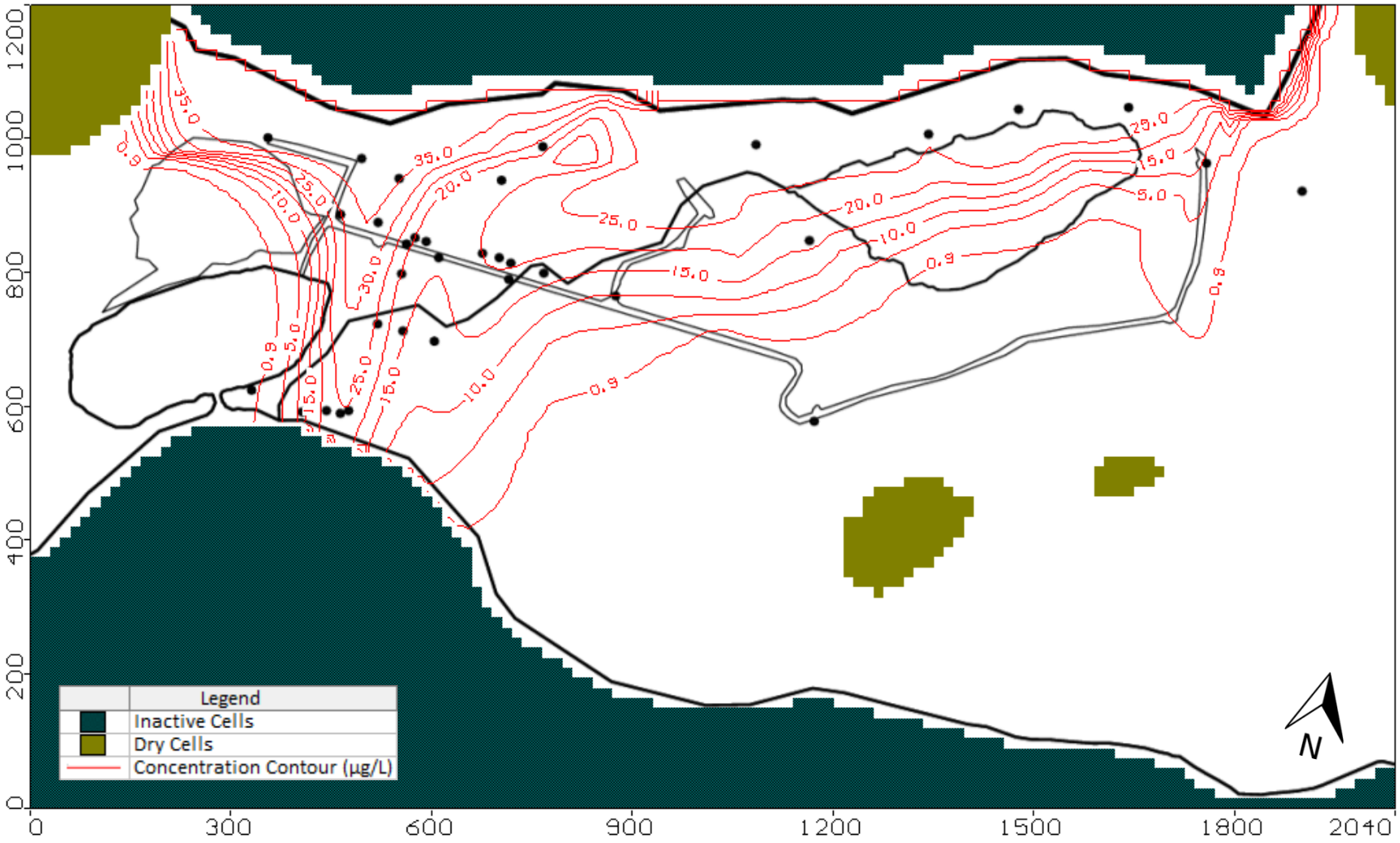

Figure 5.11 Cobalt Plume at 12 Years (April 2009) Using Run #10 Parameters (See Table 5.2)

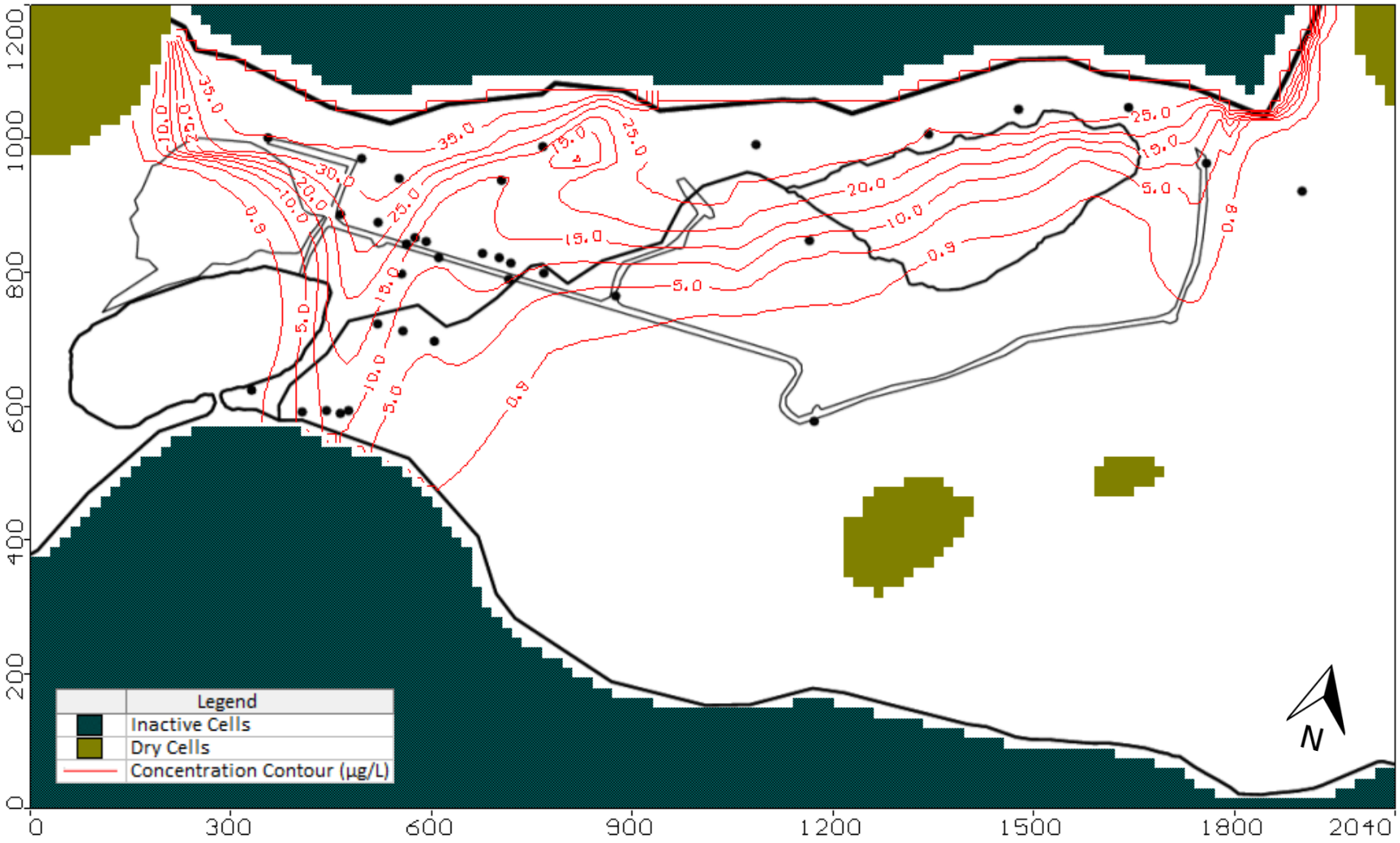

Figure 5.12 Cobalt Plume at 12 Years (April 2009) Using Run #11 Parameters (See Table 5.2)

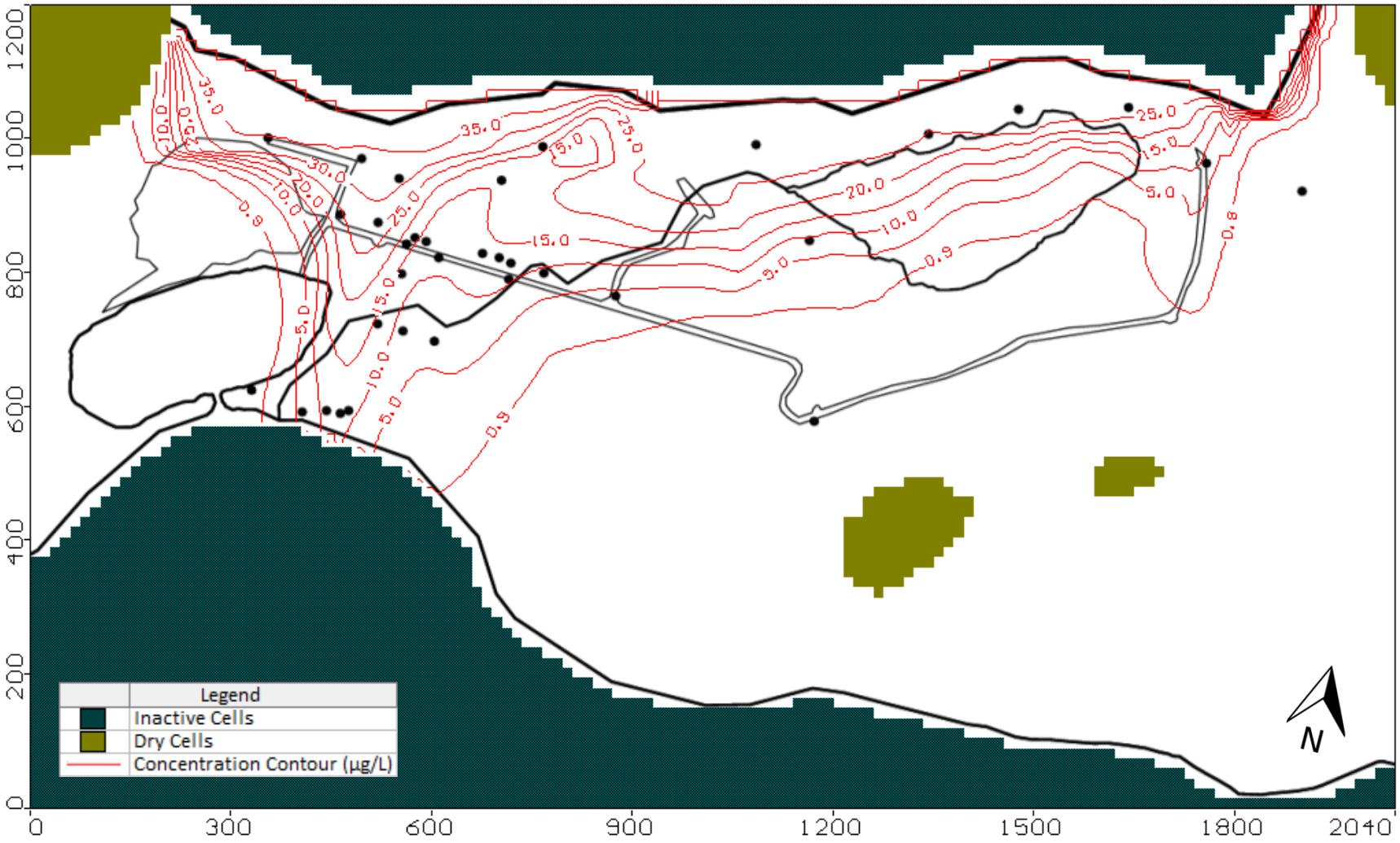

Figure 5.13 Cobalt Plume at 12 Years (April 2009) Using Run #12 Parameters (See Table 5.2)

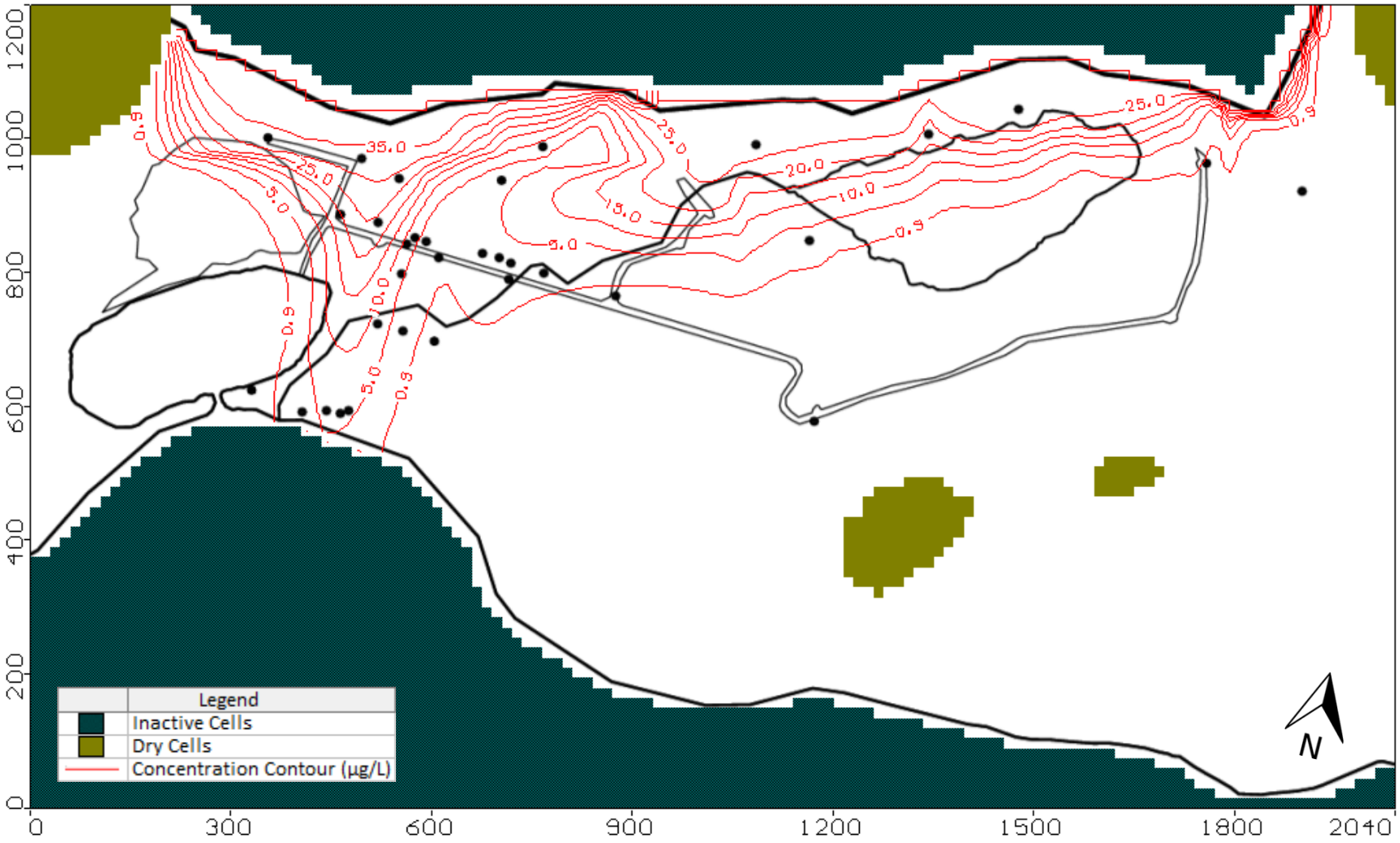

Figure 5.14 Cobalt Plume at 12 Years (April 2009) Using Run #13 Parameters (See Table 5.2)

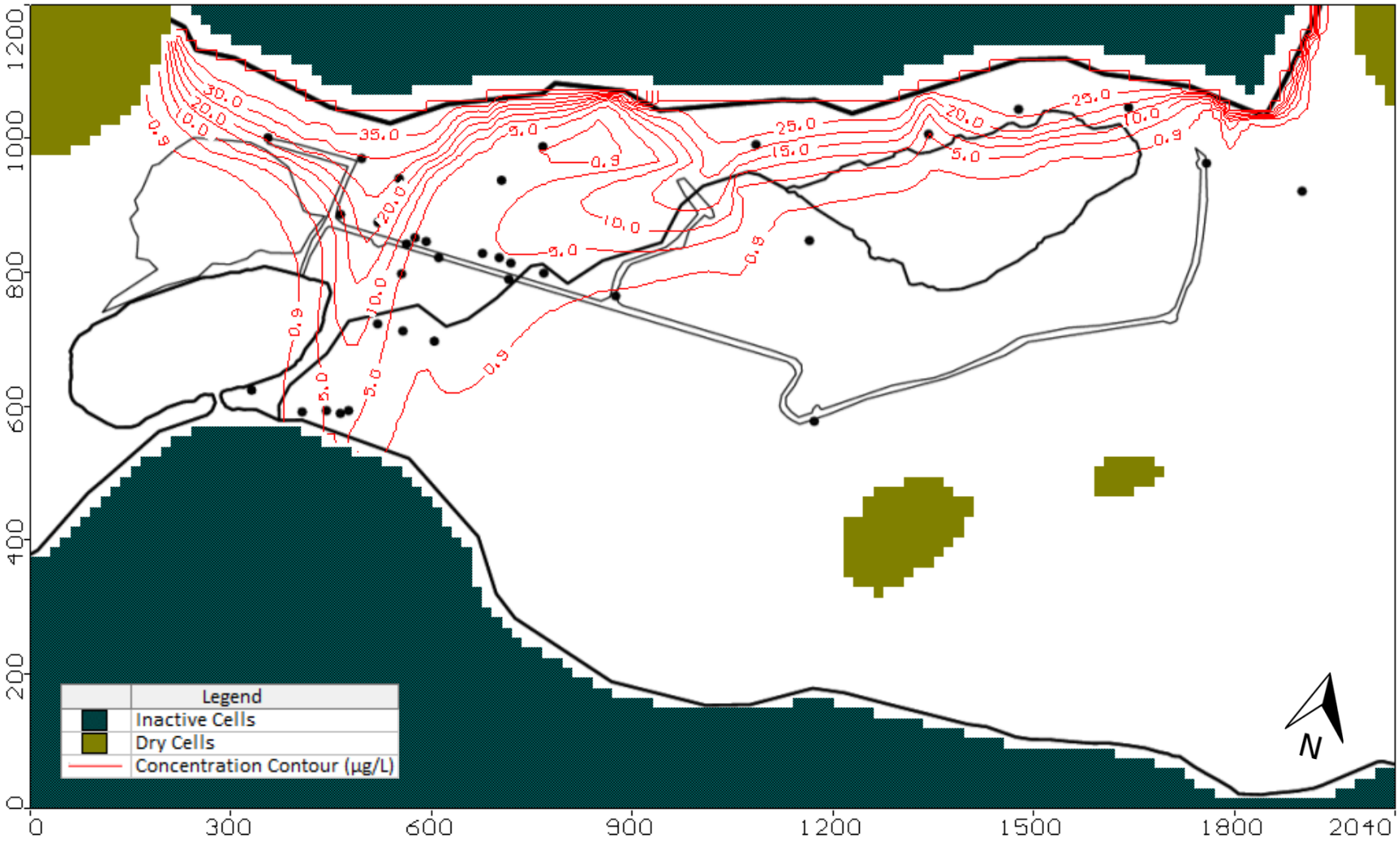

Figure 5.15 Cobalt Plume at 12 Years (April 2009) Using Run #15 Parameters (See Table 5.2)

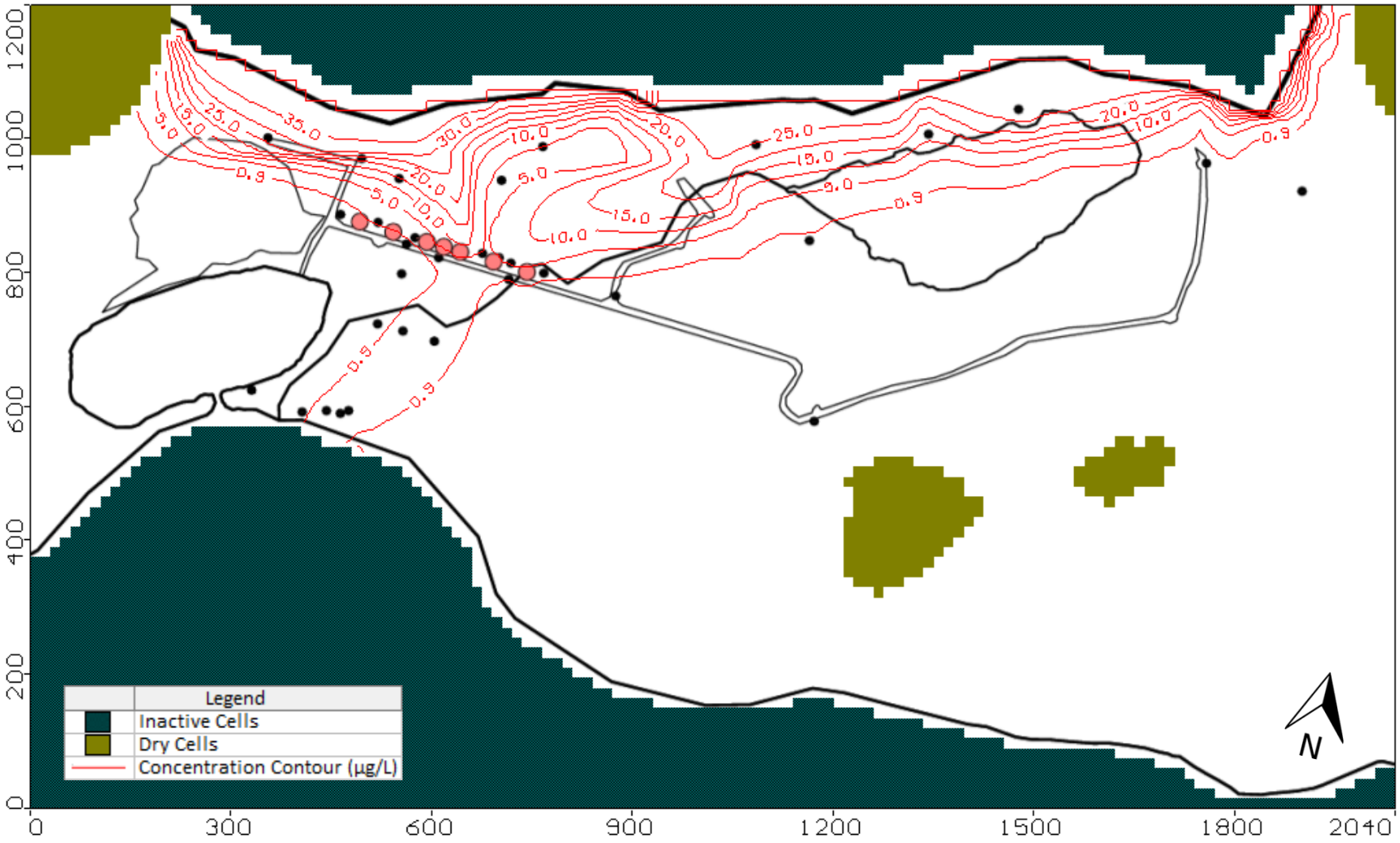

Figure 5.16 Cobalt Plume 2 Years After Pumping Well Commencement (April 2012) Using Run #16 Parameters (See Table 5.2)

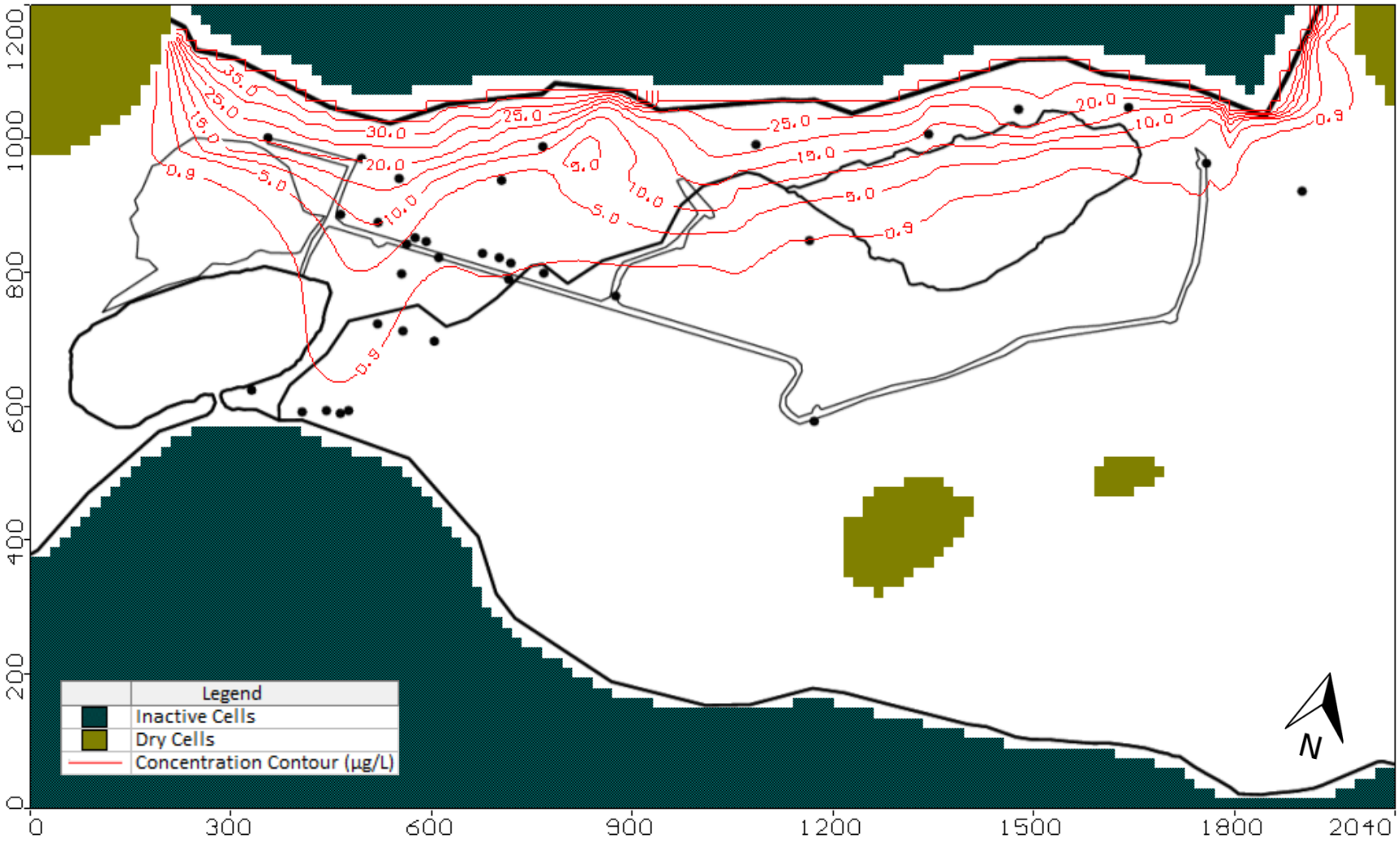

Figure 5.17 Cobalt Plume at 12 Years (April 2009) With Increased Dispervity Parameter From Run #15 By One Order of Magnitude (See Table 5.2 and 5.3)

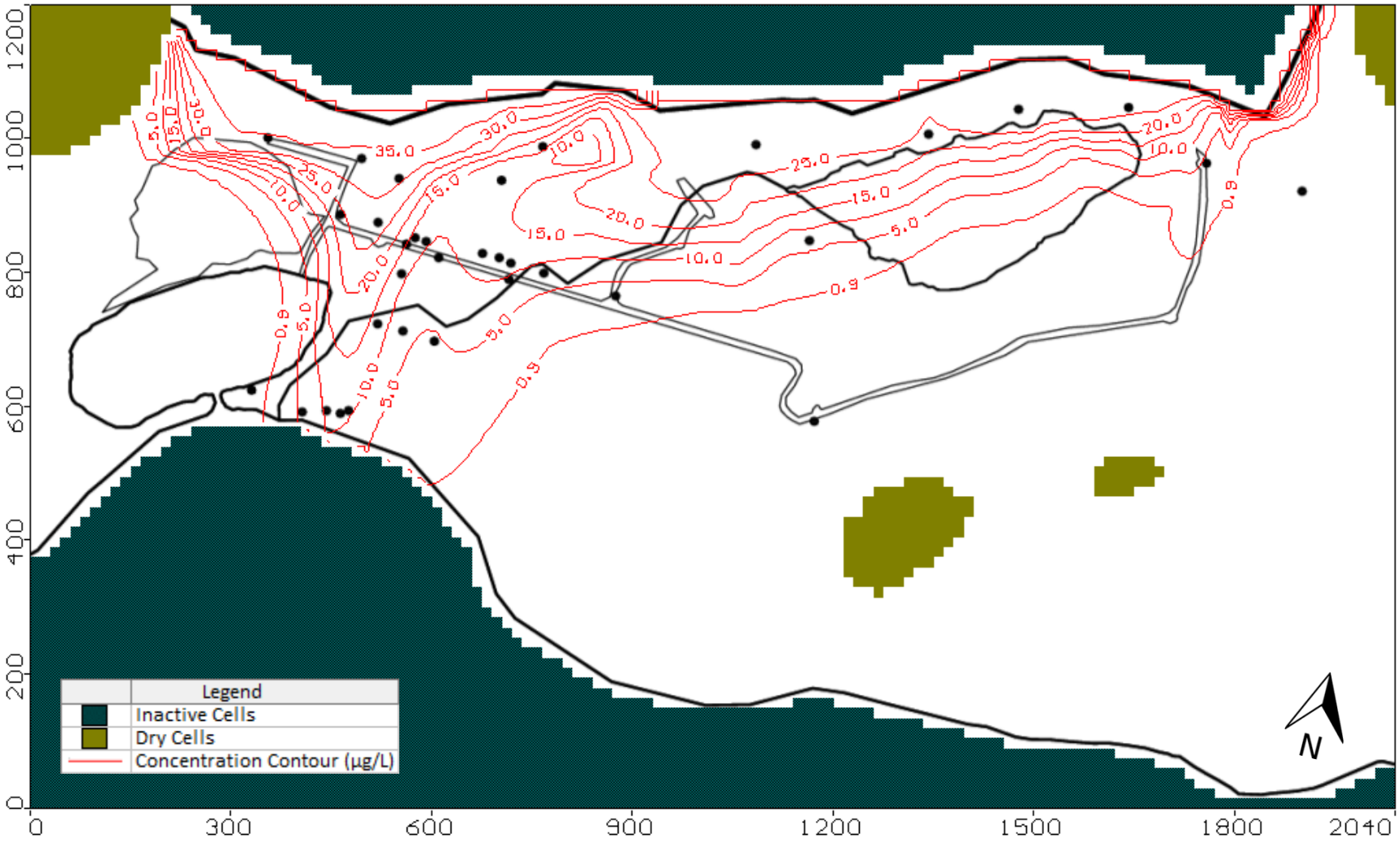

Figure 5.18 Cobalt Plume at 12 Years (April 2009) With Decreased Distribution Coefficient In Layer 2 North Zone From Run #15 By One Order of Magnitude (See Table 5.2 and 5.3)

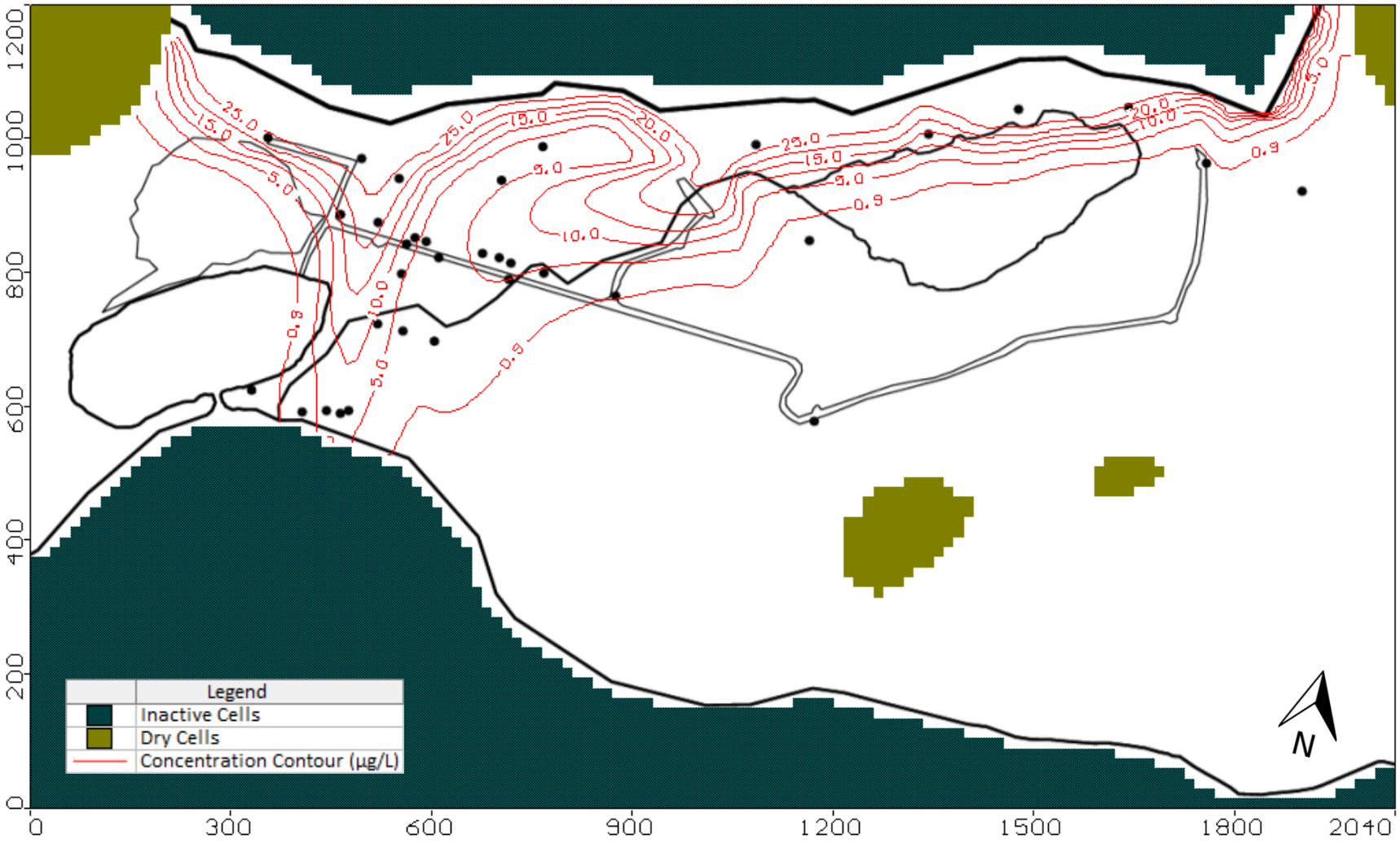

Figure 5.19 Cobalt Plume at 12 Years (April 2009) Using Run #15 Parameters and a Time Dependant Source (See Table 5.2 and 5.3)

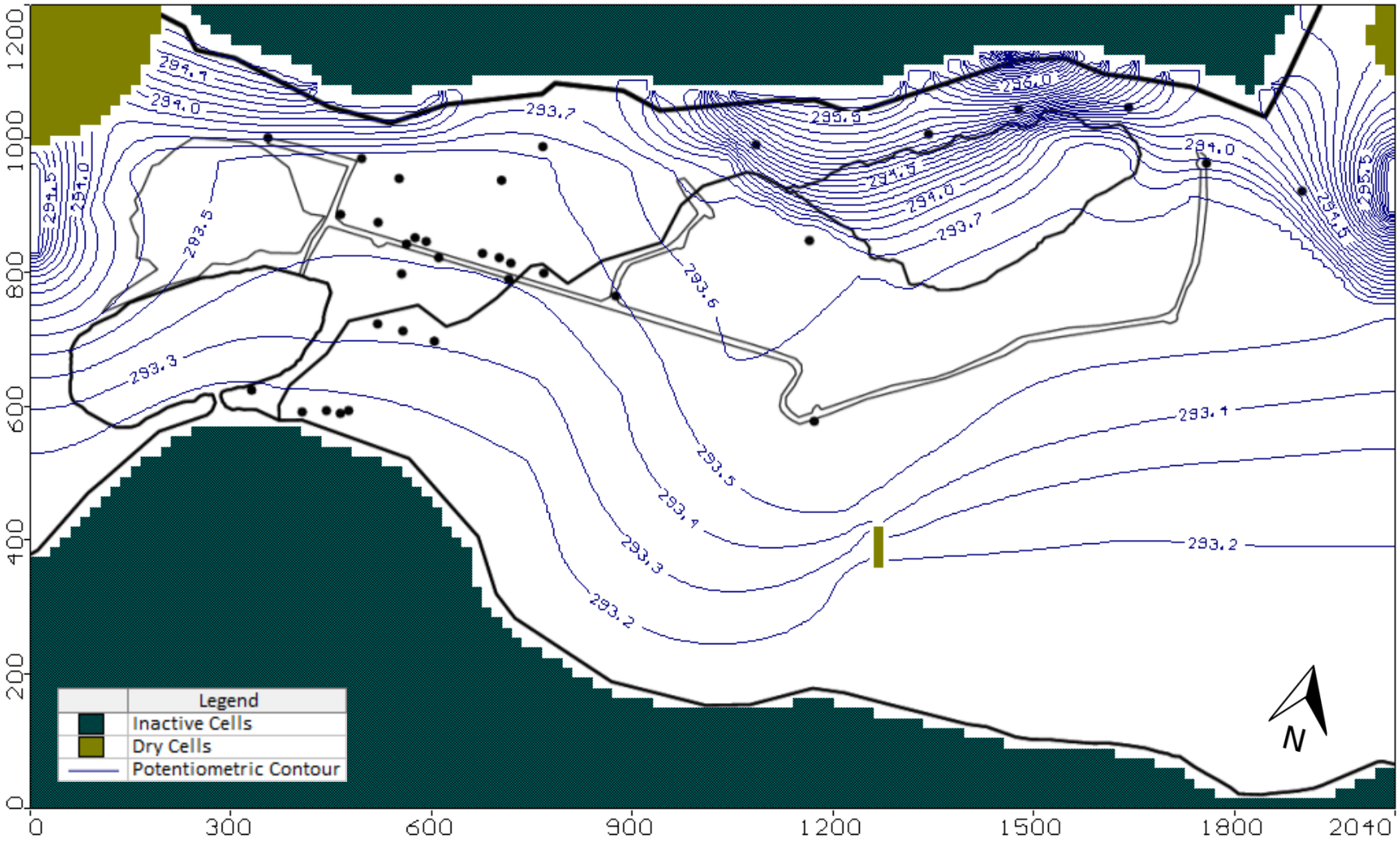

Figure 5.20 Simulated Potentiometric Surface Using 2009 Fall High Boundary Conditions (Run #29)

6.0 Assessment of Remedial Activities and Monitoring Well Network

Once groundwater flow and contaminant transport models have been sufficiently calibrated, analyzed, and tested using historical data, the model can then be used to simulate future contaminant scenarios. Since all of the previous modelling steps were conducted in order to build confidence in the capability of the model to perform realistic simulations, it is considered reliable for conducting simulations of future contaminant scenarios. These types of simulations, which can provide insight into how the contaminant plume will continue to evolve beyond the observed data, are of great value for management of a contaminated site. This is especially true for sites where remediation efforts are being planned, and the contaminant plume`s reaction to the remedial effort is largely uncertain.

To provide a basis for any future contaminant movement to be compared, the groundwater flow and contaminant transport model was used to first assess the extents of the plume at the present day. The present day cobalt plume at the Northern Ontario gold mine site was simulated using the input parameters of run #16 (see Table 5.2) with a simulation time extended by 3 years with pumping wells activated. These results correspond to the conditions of the simulated plume in April 2015, which is assumed to be representative of the present day. This plume is shown in Figure 6.1, and was used as the basis for all future scenarios. It is important to note that, throughout the 5 year simulation period since the pumping wells were commenced, the simulated plume steadily decreased in both size and concentration between the pumping wells and the lake. However, as seen in Figure 6.1, the concentrations in this area

no longer exceed the OPWQOs, and this figure is the first yearly time step in which the simulated concentrations between the lake and the pumping wells are negligible.

As indicated in section 1.2, two of the primary goals of this thesis work were to assess the effectiveness and optimize the performance of the current pumping well system, and to perform a preliminary investigation into the use of a permeable reactive barrier on the site. These two objectives were both accomplished using the groundwater flow and contaminant transport model to simulate the cobalt plume`s reaction to various future scenarios. The steps which were taken in order to accomplish these two objectives are presented and described below.

6.1 PUMPING WELL SYSTEM OPERATION

Investigation of the current pumping well system was intended to assess the efficiency of the current use of the pumping wells, and identify the optimum operation of the pumping wells in the future. Using the calibrated groundwater flow and contaminant transport model to perform this investigation allows numerous future pumping scenarios to be simulated, and their effect on the cobalt plume to be assessed. Numerous sets of simulations were therefore conducted to evaluate various pumping scenarios. Each simulation was conducted using the calibrated input parameters from run #16 (see Table 5.2).

The first scenario was continuing to run all of the pumping wells at the yearly average pumping rates which were originally input into the groundwater flow model, listed in Table 4.6. This scenario gives an indication as to what will happen to the cobalt plume if the pumps are allowed to continue running as they have been previously. This scenario is vital as it should be

used as basis to which any other scenario is compared. The second presented scenario is the complete removal of the pumping wells from the model after the simulation exceeds the present day (April 2015). This scenario would represent an alternative extreme where the pumping wells were all turned off, and the natural groundwater flow was allowed to take over once again. The third scenario proposes that the pumping wells could be run intermittently, allowing the natural groundwater flow to advance the plume for a period of time before reactivating the pumping wells to cause plume regression once again. Alternatively, a fourth scenario proposes to reduce the flow rate at which the pumps are run as an attempt to create equilibrium in which the plume would be neither advancing nor regressing.

6.1.1 Scenario 1: Continue with Current Pumping Rates

With the pumping rates unchanged from their original input values, the contaminant transport model was used to simulate any movement that the cobalt plume would experience over the next 15 years into the future. The results of this simulation are presented in Figure 6.2, which represents the conditions of the cobalt plume in year 2030. Comparing Figures 6.1 and 6.2 it is clear that no significant change in cobalt concentrations occurs between the pumping wells and the lake during this time period. This is due to the fact that there were no longer any significant concentrations of cobalt between the pumping wells and the lake after the 2015 time step. Therefore, continual pumping after 2015 would serve the purpose of preventing cobalt contaminated groundwater from migrating past the pumping well locations. However, the pumping wells being operated at the current pumping rates have proven to be capable of causing regression of the cobalt plume by drawing contaminated groundwater away from the

lake. It is therefore likely that the current pumping rates could effectively be reduced, and the wells could still be effective in preventing the advancement of the cobalt plume.

An increase in plume concentrations did, however, continue to occur between the pumping wells and the TMA, as well as plume expansion in the eastern portion of the model. Concentrations continued to rise between the pumping wells and the TMA, as indicated by the relatively large expansion of the 20µg/L and 25µg/L concentration contours in the central portion of the model between Figures 6.1 and 6.2. In the eastern portion of the site, an additional lobe has also developed in the 0.9µg/L cobalt contour to the east of the seepage collection pond.

6.1.2 Scenario 2: Cease Pumping

The output from the present day simulation (April 2015) in Figure 6.1 was input into the original calibrated groundwater flow model, which allowed the plume to advance under the natural hydrogeologic conditions of the site once again. Immediately upon removal of the pumping wells, the cobalt concentrations once again began migrating past the access road towards the lake. Within two years of the pumping wells being turned off, the 0.9µg/L cobalt concentration contour was once again intersecting the edge of the lake, and by the third year of the simulation the cobalt concentrations calculated at the well locations adjacent to the lake were almost 5µg/L (similar to their observed concentrations in 2009). The concentration contours of the cobalt plume three years after turning off the pumping wells are displayed in Figure 6.3. From this simulation it is concluded that if the pumping wells were to be completely deactivated in 2015, the cobalt plume would advance sufficiently to cause 5µg/L concentrations

to be detectable adjacent to the lake within three years (by 2018). By the fourth year after the pumping wells were deactivated (2019), the simulated concentrations adjacent to the lake exceeded the highest concentrations which have ever been observed in this area, as seen in Figure 6.4.

6.1.3 Scenario 3: Intermittent Pumping

Since it is not desirable to allow the dissolved cobalt concentrations adjacent to the lake to exceed the trigger level (5µg/L), the pumping wells would therefore have to be reactivated for a period of time to allow them to once again decrease the plume size. In order to determine the period of time in which the pumping wells would need to be reactivated to sufficiently shrink the cobalt plume, the simulation was expanded from scenario 2 (Figure 6.3), to include a pumping well reactivation period. As a result of extending the simulation with the pumping wells reactivated, the cobalt concentrations between the pumping wells and the lake receded in a manner very similar to how they receded on initial commencement of the pumping well system in 2010. After four years of pumping well reactivation (2022), the extent of the cobalt plume returned to approximately the same size as the April 2015 present day simulation displayed in Figure 6.1. These results indicate that a pumping time of four years would likely be required to reduce the plume advancement that would naturally occur during three years of the pumping wells being inactive.

This simulation was further advanced to include another cycle of pumping well inactivation by once again deactivating the pumping wells in the model until the simulated 5µg/L cobalt concentration contour advanced to the edge of the lake. This occurred once again over a 3 year

simulation period (2025), very similarly to the previous cycle. The pumping wells were then reactivated in the model once more, and the simulation was continued until insignificant concentrations of cobalt remained in the sand aquifer between the pumping wells and the lake. For the second cycle, a longer reactivation period of five years (2030) was required to sufficiently reduce the simulated cobalt plume to insignificant concentrations between the pumping wells and the lake. The reactivation period is likely increasing in length due to the fact that the dissolved cobalt plume which advanced during the second three year deactivation period had higher concentrations than the plume which advanced during the first three year deactivation period. Regardless if the pumping wells are active or not, the cobalt concentrations between the pumping wells and the TMA are continuing to increase over time. Therefore, each time the pumping wells are deactivated, the concentrations which begin to advance past the pumping well locations are higher than they were during the previous deactivation period. This trend will continue until the area between the pumping wells and the TMA reaches the source concentration, or the source term begins to be depleted upon closure of the mine.

The results of the simulated cobalt plume after the completion of two pumping well deactivation cycles is presented in Figure 6.5 and represents the extent of the cobalt plume in year 2030. Figure 6.5 therefore represents the exact same simulation period as Figure 6.2 of scenario 1, except the pumping wells were completely deactivated for six out of the fifteen years simulated (40% of the time). Even though these two plumes were simulated using very different pumping scenarios, output plumes displayed in Figure 6.2 and 6.5 are nearly identical.

Using the cyclical pumping schedule of scenario 3 can therefore produce the same results as scenario 1 with 40% less pumping required.

6.1.4 Scenario 4: Reduced Pumping Rates

Although the simulations of scenario 3 have produced promising results, it may not be desirable to have all of the pumping wells on the site deactivated and sitting idle for a three year period of time without being used. An alternative way to reduce the overall volume of groundwater being removed from the aquifer by the pumping wells while allowing the pumps to remain active would be to reduce the pumping rate. In this scenario, all wells remained continually active, but the pumping rate was reduced as an attempt to reach equilibrium in which the plume was neither advancing nor regressing.

This scenario was analyzed by performing a series of simulations which allowed the pumping wells to run steadily for a period of 15 years (2030) at various pumping rates. Beginning with the initial input pumping rates in Table 4.6, the first run of this scenario presents the exact same conditions as scenario 1. The input pumping rates were then lowered for the successive simulations to observe the impact on the cobalt plume after a 15 year simulation period (2030). Results of this simulation indicate that very little change in the cobalt plume will occur during this 15 year simulation period, even if the pumping rates are significantly reduced. Figure 6.6 displays the results of the simulation performed with each pumping well running at only 50% of the original pumping rate input value. Compared to the results in Figure 6.2, the extent of the plume in Figure 6.6 is slightly larger in the area of the pumping wells, as observed from the location of the 0.9µg/L concentration contour. However, the plume is not further expanding in

this area over time. Although the extent of the plume in this scenario is slightly larger than that of scenario 1, it is important to point out that the cobalt concentrations between the pumping wells and the TMA are noticeably lower. This is illustrated by the location of the 20µg/L cobalt concentration contour. These lowered concentrations are attributed to the lower pumping rate creating a smaller hydraulic gradient, and less flow away from the TMA, resulting in less advective transport of cobalt with time.

6.1.5 Scenario 5: Reduced Number of Active Pumping Wells

Another scenario which was simulated was simply reducing the number of active pumping wells at the site. Reducing the total pumping rate of each well by 50%, as proposed in scenario 4, has been shown to reduce the quantity of water pumped while continuing to capture the cobalt plume. However, operating pumping wells continually well below their capacity is likely not efficient or desirable. For this reason, scenario 5 proposes the option of deactivating a number of the pumping wells. If the plume can be captured using less pumping wells, the unused pumps could be permanently decommissioned to save operation and maintenance costs.

This scenario was investigated by performing a series of simulations in which one or more of the pumping wells were deactivated, while the others continued to operate at their original pumping rate. In order to match the reduction in pumping volume accomplished by scenario 4, the pumping well system would have to be reduced to just three wells. To allow the remaining wells the greatest chance to capture the contaminant plume over a wide area, it was decided to keep the well on each end active as well as one in the middle. Since the highest concentrations of cobalt being allowed to migrate past the pumping wells in Figure 6.2 is in the area of wells

09-PW-6, 09-PW-7, and 09-PW-8, well 09-PW-6 was decided to be the middle well which was left active. This simulated scenario therefore had pumping wells 09-PW-4, 09-PW-5, 09-PW-7, and 09-PW-9 deactivated, while 09-PW-3, 09-PW-6, and 09-PW-8 remained active. The results of this simulation after a 15 year transport time (2030) as shown in Figure 6.7 is nearly identical to the plume produced in scenario 4, as shown in Figure 6.6.

6.2 PERMEABLE REACTIVE BARRIER (PRB)

A preliminary investigation into the possible use of a permeable reactive barrier (PRB) on the Northern Ontario gold mine site was conducted. The goal of this investigation was to determine the location and size of barrier that would be required if a PRB system were to be considered for this site. A PRB may want to be considered for the Northern Ontario gold mine site to act as a replacement for the pumping wells. A more passive method of restricting cobalt transport may be of great economic benefits in the long run. For this reason, the approach to the PRB investigation is to have the PRB replace the pumping wells, rather than be used in combination with the pumping wells.

The location of the PRB would have to be such that the natural hydrogeological conditions of the site would cause the contaminated water to pass through it when the pumping wells are deactivated. Figure 6.3 represents the location in which the cobalt plume would advance to within three years of pumping well deactivation, and therefore gives a good indication of the appropriate location for a PRB. Two possible locations for the PRB are shown on Figure 6.8. The potential of a PRB installed in each of these two locations to restrict the movement of the dissolved cobalt plume was analyzed using contaminant transport simulations. In the

simulations, the reactive medium of the PRB was represented by assigning a line of highly sorptive cells into the model in the location of the proposed barrier. For the purpose of this investigation, a distribution coefficient of $2.5x10^{-6}$L/µg was used for the barrier material. This value was approximated from batch adsorption test results published by Abbas et al (2014) who investigated the ability of activated carbon to remove dissolved cobalt from solution. The hydraulic conductivity of the PRB material was assumed to be 0.1 cm/s, similar to that of the sand layer in the vicinity of the barrier. The PRB was assigned one cell thick, in layer 1 and 2 of the model. This assumes that the barrier material would be 15m thick, and would extend from the ground surface to the top of the till layer which underlies the aquifer.

One obvious choice for a PRB location would be parallel to, and south of, the gravel access road along which the pumping wells are located. This location is noted in Figure 6.8, and is ideal because it is downstream of the existing plume, it is perpendicular to the groundwater flow direction, and it is easily accessible for installation and maintenance purposes. The results of the simulated PRB in location 1 are shown in Figure 6.9 after a transport time of 15 years. Due to its location slightly downstream and covering nearly the entire width of the original plume, a PRB in this location would likely be effective in capturing the majority of the dissolved cobalt. Only small portions of the cobalt plume were able to avoid the barrier, and the concentrations did not exceed 5µg/L for the time period investigated. The 0.9 µg/L cobalt concentration contour intersects the edge of the lake, but this did not occur until year 13 of the simulation. Although this location for the barrier would likely be effective, the main issue concerning it would be its size. In order to cover the entire width of the plume at this location, the proposed PRB would need to be almost 380m long. In addition, the sand aquifer in this area of the site is

approximately 3.6-7.9m in thickness, and the bottom of the aquifer ranges from 6.8-13m deep. By creating a budget zone corresponding to the location of the PRB cells in the model, the ZoneBudget engine was utilized to determine the mass of cobalt sorbed onto the barrier material during each year of the simulation. The sorption of cobalt onto the barrier material in this simulation began almost immediately upon pumping well deactivation, likely due to the close proximity of the barrier to the restrained plume. In the first year 0.27kg of cobalt was sorbed onto the barrier material, succeeded by 0.62kg in the second year, and 0.75kg in the third year. This rate continued to increase, reaching almost 0.98kg in the final year of the simulation.

The second location noted in Figure 6.8 was chosen because it would allow a smaller barrier to intercept the plume in the location where the highest cobalt concentration contours would intercept the lake (see Figures 6.3 and 6.4). The results of the simulated PRB in location 2 are shown in Figure 6.10 after a transport time of 15 years. A small portion of the plume, with low cobalt concentrations, was once again able to avoid the barrier; however concentrations bypassing the barrier did not exceed 5µg/L for the time period investigated. Although only the 0.9µg/L concentration contour intersected the edge of the lake, this occurred only two years into the simulation and this contour remained in a constant location for the remainder of the transport time. The size of this barrier is approximately 195m in length, the aquifer in the area is approximately 4.9-7.7m in thickness, and the bottom of the aquifer ranges from 8.1-12m deep. Similarly to the previous simulation, the ZoneBudget engine was used to calculate the mass of cobalt sorbed onto the barrier material during each year of the simulation. The rate of cobalt sorption during this PRB simulation was slow at first, increasing by 0.26kg over the first

three years of the simulation, however, after the third year of the simulation, the rate of the sorbed cobalt mass increased significantly. During the fourth year of the simulation approximately 0.31kg of cobalt was sorbed onto the barrier material. This rate of sorption continued to rise steadily as the more concentrated portion of the cobalt plume began to reach the barrier. By the final year of the simulation (year 15) the rate of sorbed cobalt was over 0.48kg/yr, and continued to show an increasing trend.

By comparing the amount of cobalt which would be sorbed to the barrier over a given time period to the maximum sorption capacity of the reactive material, the longevity of the barrier material can be estimated. The maximum adsorption capacity of activated carbon for cobalt is reported to be 111.11 mg/g at pH 9 (Abbas et al., 2014). However, this value was determined at optimal conditions, and is considerably higher than values reported for other reactive media. It should therefore be regarded at the high end of the range for reasonable maximum sorption capacities of reactive media which could be used in a PRB. By dividing the maximum mass flow rate of cobalt entering the barrier material by the cross sectional area of the barrier material perpendicular to groundwater flow, the mass flux of cobalt can be obtained. In the final year of each of the PRB simulations, the average mass fluxes perpendicular to groundwater flow for cobalt entering the barriers were approximately 0.45g/m^2yr and 0.39g/m^2yr for PRB1 and PRB2, respectively.

Due to the vast size of the Northern Ontario gold mine site, the length of a PRB which could effectively capture the entire width of the cobalt plume would need to be extensive. This combined with the relatively low cobalt plume concentrations (in the order of micrograms per

litre), results in very low mass flux values for cobalt entering the barrier materials. In addition, existing site features such as the fish habitat restrict the areas in which a PRB can be located. Therefore, as an alternative to the extremely long PRB which would be required to capture the cobalt plume at this site, a funnel and gate type PRB system, as described in section 2.10.2, should be considered. Low permeability cut-off walls could be installed into the aquifer to direct the groundwater on the outer edges of the cobalt plume, toward a centrally located reactive gate. Additionally, since the simulated cobalt plume flows beneath the edge of the fish habitat, a cut-off wall could be used to direct this part of the plume eastward toward a location where a reactive gate could be installed. A funnel and gate system would therefore likely provide a more efficient way to capture the very wide cobalt plume at the Northern Ontario gold mine site.

6.3 Groundwater Monitoring Well Network

The groundwater monitoring well network at the Northern Ontario gold mine site includes 43 groundwater monitoring wells and 7 pumping wells through which groundwater elevation data, and groundwater samples for quality testing, are currently being collected. Groundwater elevation data from the wells are typically collected monthly, while groundwater samples are typically collected two to four times per year, depending on the well.

Throughout the course of this modelling work, a thorough investigation of both the collected groundwater elevation data and geochemical data of the collected samples has been performed. Although a certain number of anomalies and variation in the observed data is expected, a few wells have been noted for investigation due to consistently erratic or

anomalous results. Recent groundwater level measurements in wells 95-GW-6S and 95-GW-6D are very consistently reported with a one meter difference in elevation. However, prior to 2007, these wells indicated very little difference in elevation. The recent elevation difference between these two wells is likely an error in measurement, and it is recommended that the top of standpipe elevations of the wells be re-surveyed.

Well 95-GW-10S was often noted during groundwater level testing to be frozen or blocked at various depths, which prevented the elevation from being measured and recorded. This well has also produced a large number of anomalous results which vary drastically from the measurements taken from well 95-GW-10D. In addition, well 95-GW-10D was also noted to consistently have measured water level values approximately 0.1-0.15m higher than the other wells also located adjacent to the lake (wells 09-GW-26, 06-GW-27, 06-GW-28, and 10-GW-40).

As discussed in section 3.4, and shown in Figure 3.8, groundwater elevation data collected from well 96-GW-15S were consistently lower than those collected from wells 96-GW-15D and 95-GW-6S, which is located down-gradient. Further investigation into this well determined that each time the top of standpipe elevations of the monitoring wells have been re-surveyed, this well has increased in elevation. During the most recent survey, noted to have occurred in May 2013, the top of standpipe elevation for well 96-GW-15S was measured 0.365m higher than what it was first reported in November 1996. If the drastic increase in the top of standpipe elevation is not due to an error in measurement, it could impact the ability of the well to produce reliable data. Over the same time period, the top of standpipe elevation of well 96-GW-15D has only risen by 0.079m. As a general recommendation, to improve the certainty of

the collected groundwater elevation data, annually scheduled resurveys of standpipe elevations are suggested for all wells. It is also suggested that monitoring well installations mitigate the effects of frost heave by allowing the protective casing to extend down into the top surface of the bentonite grout seal, preventing the concrete surface pad from coming in contact with the standpipe (Striggow, 2013).

6.3.1 Future Groundwater Monitoring Well Recommendation

Although the groundwater monitoring network extends across most of the site, some areas which could use improvement have been identified. As mentioned earlier, no groundwater monitoring wells are present in the westernmost portion of the site to the west of the overburden storage pile. For this reason, the groundwater conditions and hydraulic gradient present in this area are unknown. This caused the western boundary condition to be estimated based on the surface topography, and by using a trial-and-error approach. A groundwater monitoring well installed in this area could determine the groundwater elevation conditions and the hydraulic gradient in the easterly direction toward the pumping wells. This would help to provide more certainty to the value of the western boundary condition assigned to the model. In addition, logging the subsurface stratigraphy during the installation of the well would confirm aquifer thickness, and slug testing could be performed to estimate the hydraulic conductivity of the sand layer in this area. Groundwater sample collection for water quality analysis from this location would also be able to confirm whether or not any dissolved cobalt is avoiding capture by the pumping wells and migrating towards the lake in this area.

Another recommended location for the installation of a groundwater monitoring well is in the eastern portion of the site along the gravel access road to the south of well 95-GW-4. As seen in Figures 6.2, 6.5, 6.6, and 6.7, when simulations are progressed into the future, a new lobe develops in the cobalt concentration contours to the east of the seepage collection pond. A groundwater monitoring well installed to the south of well 95-GW-4 would be able to detect this potential lobe further down gradient of the TMA and provide information about the extent and progression of the cobalt plume in the future.

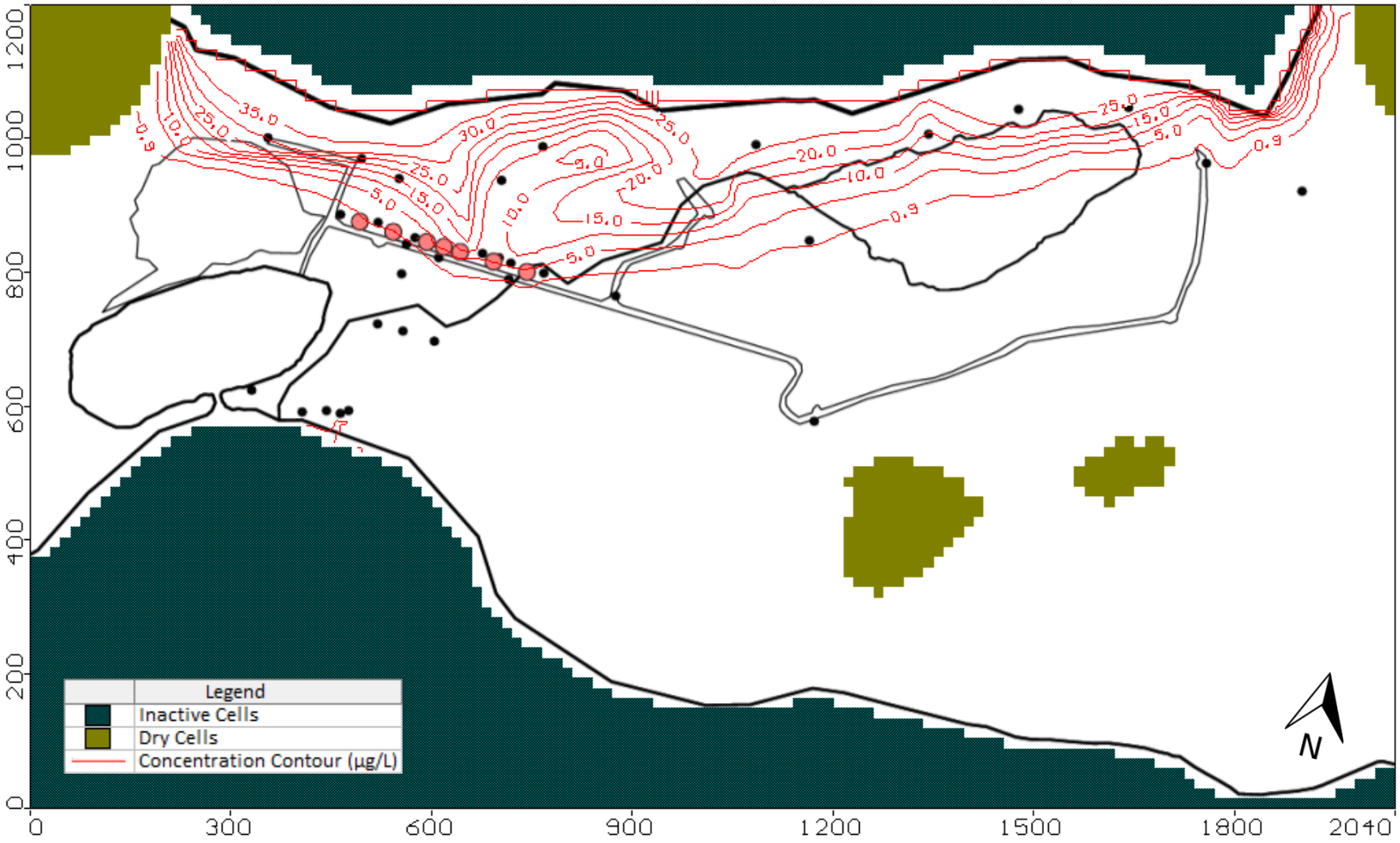

Figure 6.1 Cobalt Plume 5 Years After Pumping Well Commencement (April 2015) Representing Present Day Conditions

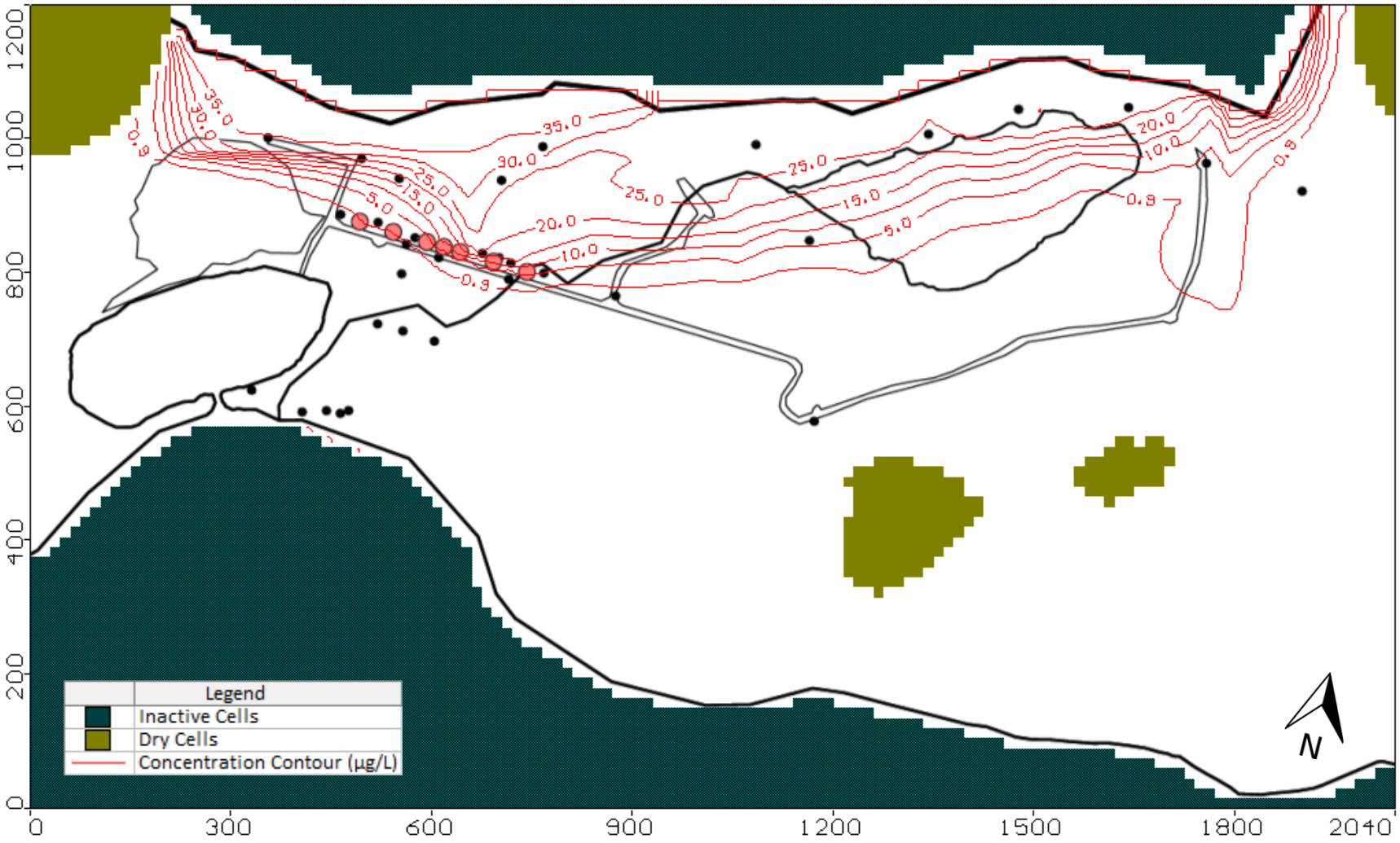

Figure 6.2 Cobalt Plume 20 Years After Pumping Well Commencement (April 2030)

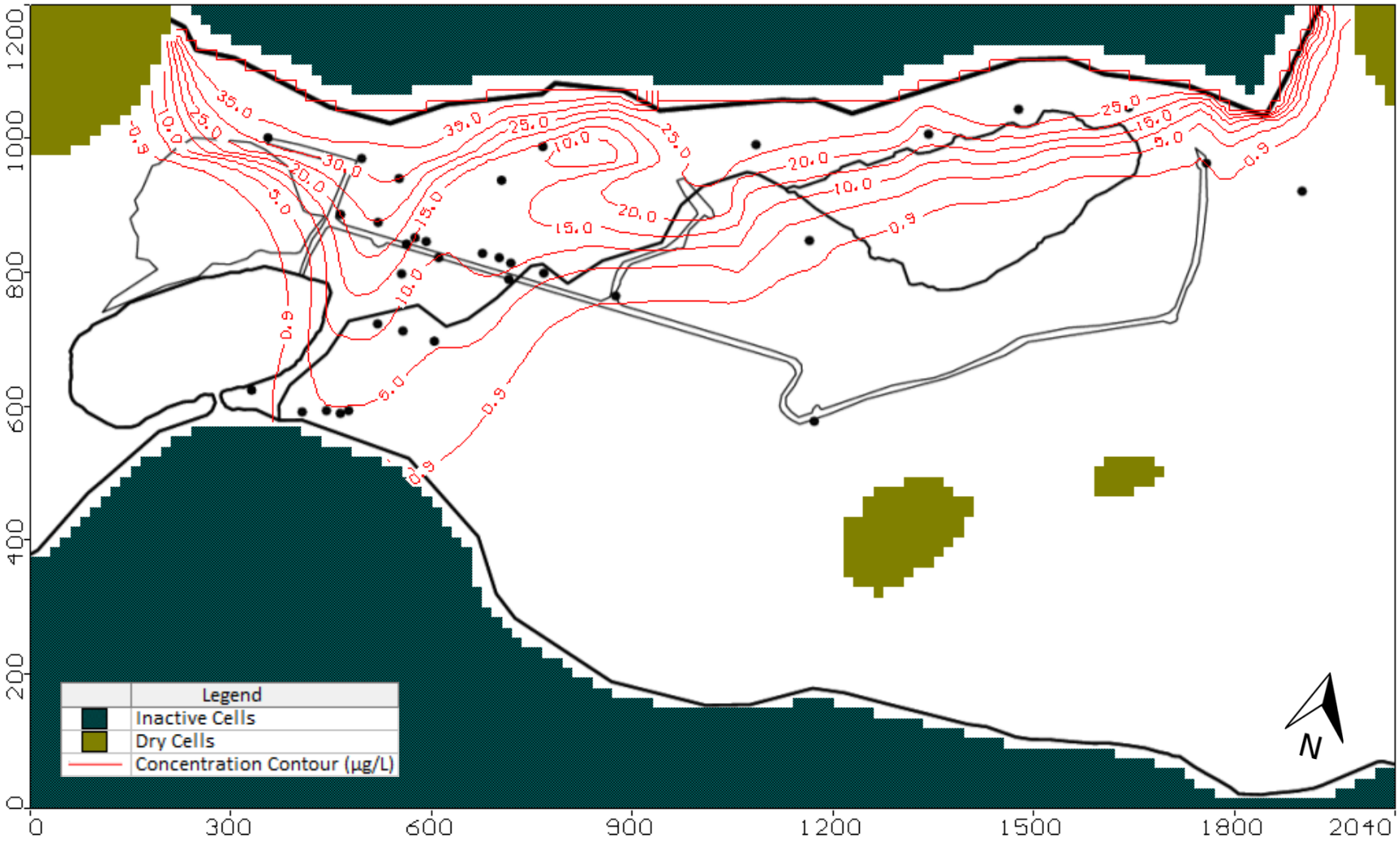

Figure 6.3 Cobalt Plume 3 Years After Pumping Wells Ceased (April 2018)

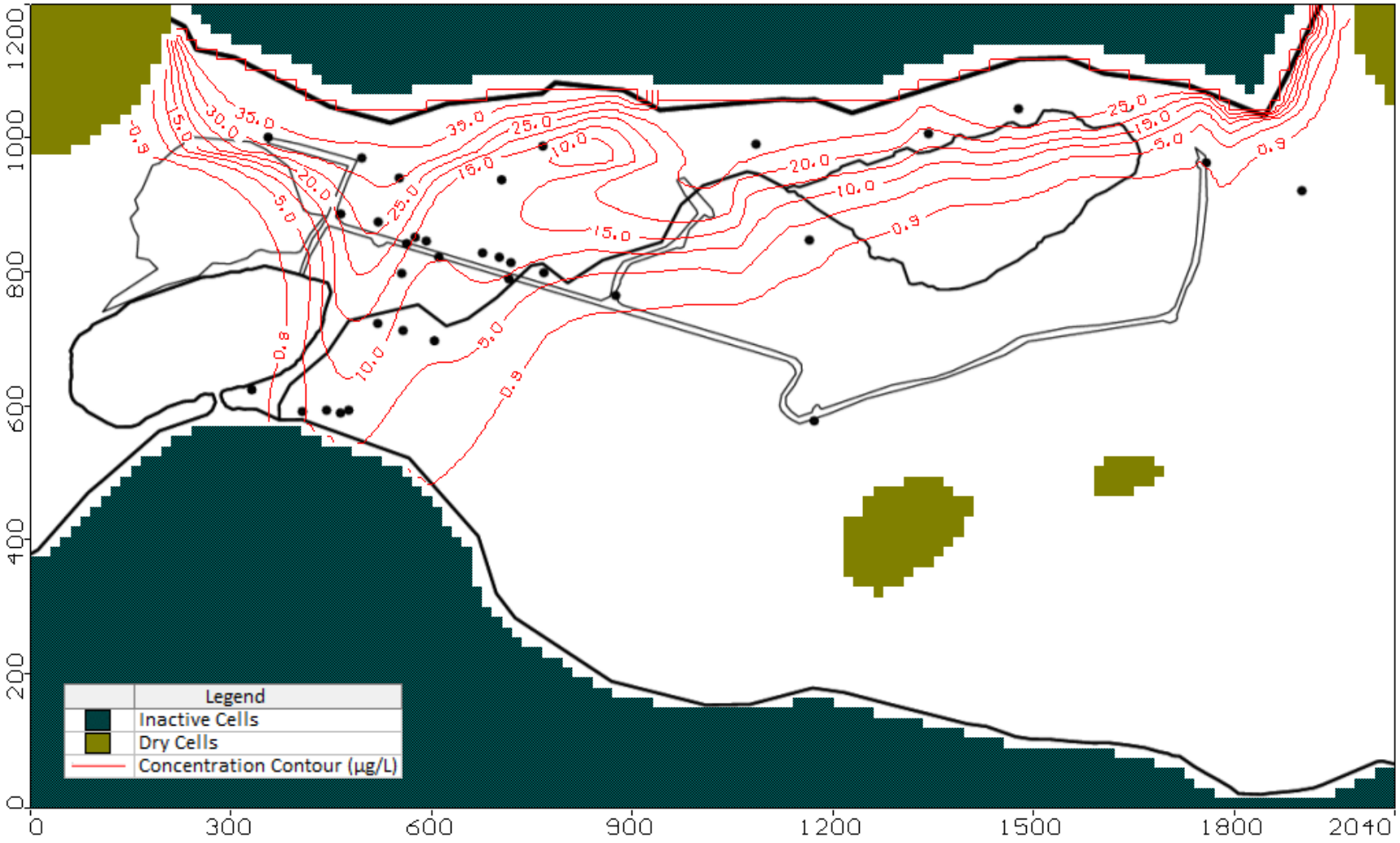

Figure 6.4 Cobalt Plume 4 Years After Pumping Wells Ceased (April 2019)

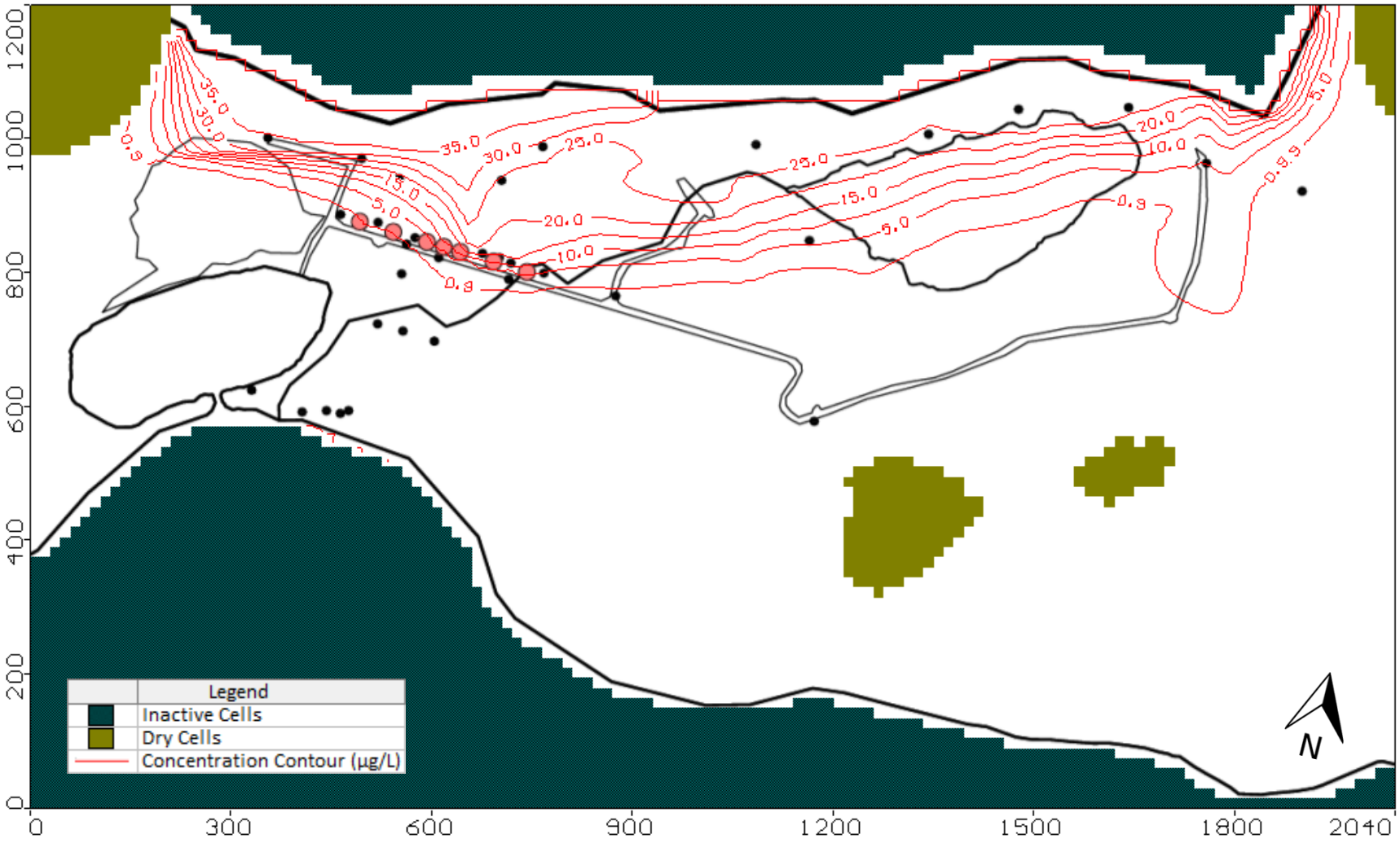

Figure 6.5 Cobalt Plume After Two Pumping Well Deactivation Cycles (April 2030)

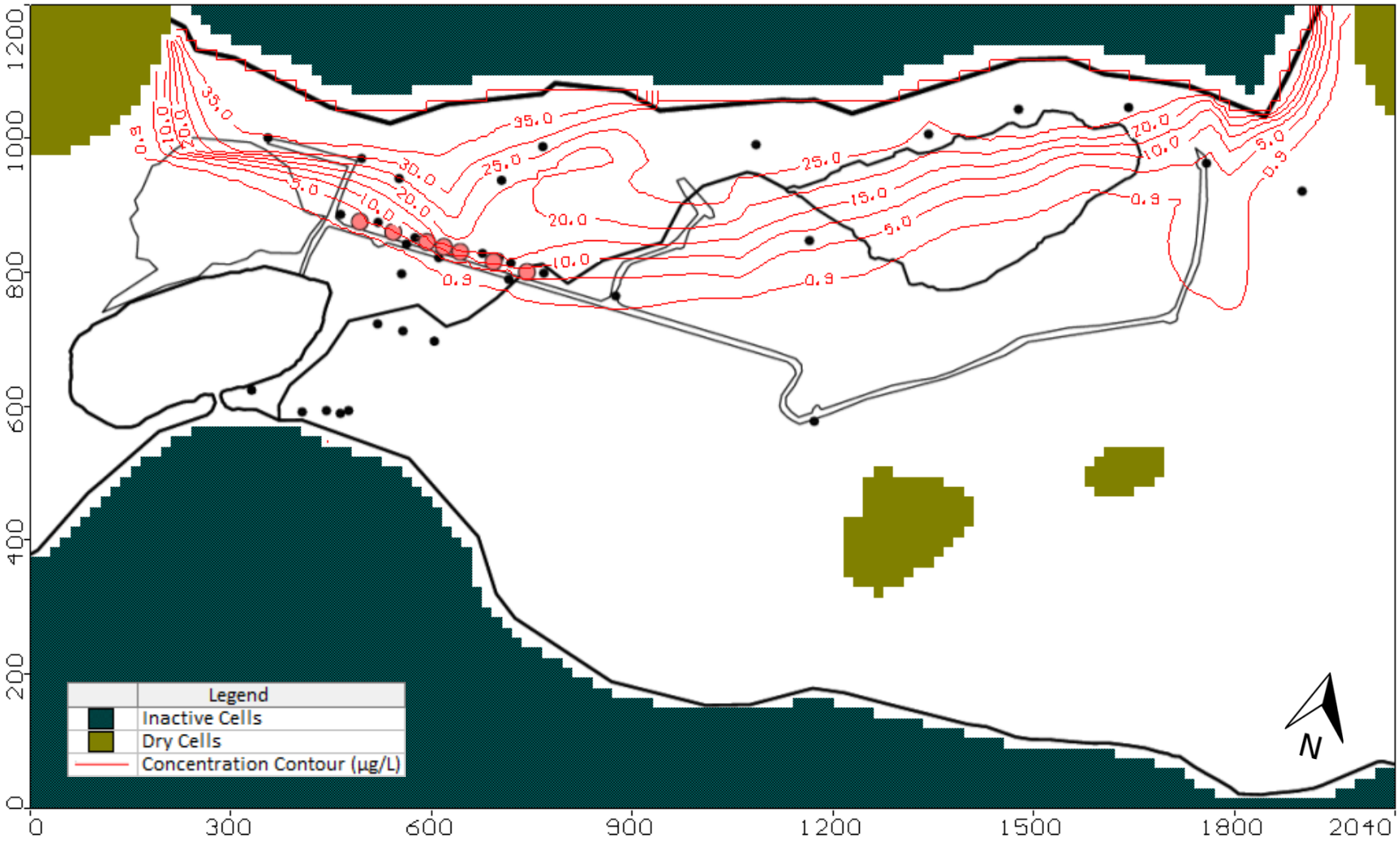

Figure 6.6 Cobalt Plume Using 50% Pumping Rates For 15 Years (April 2030)

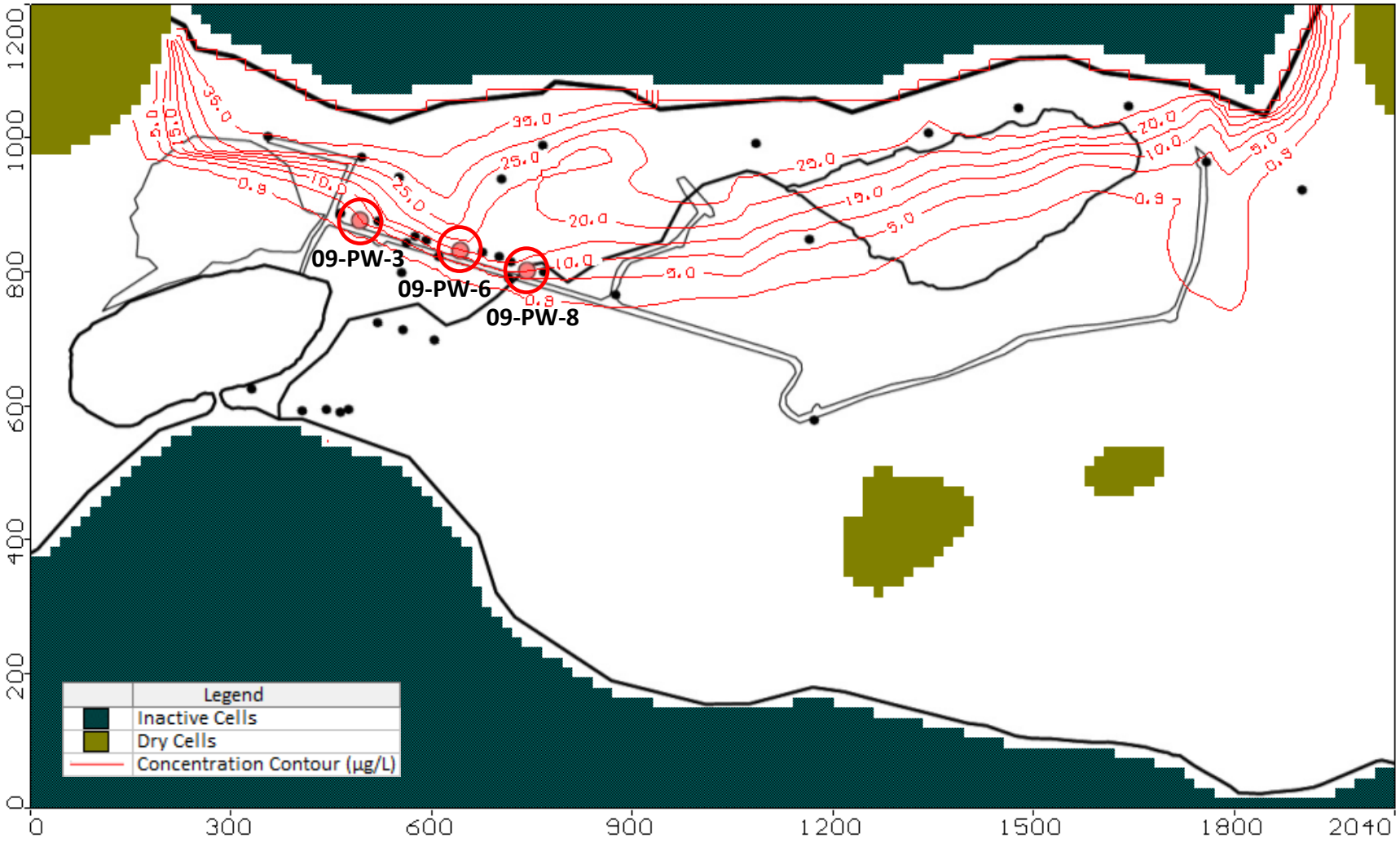

Figure 6.7 Cobalt Plume With Wells 09-PW-3, 09-PW-6, and 09-PW-8 Active For 15 Years (April 2030)

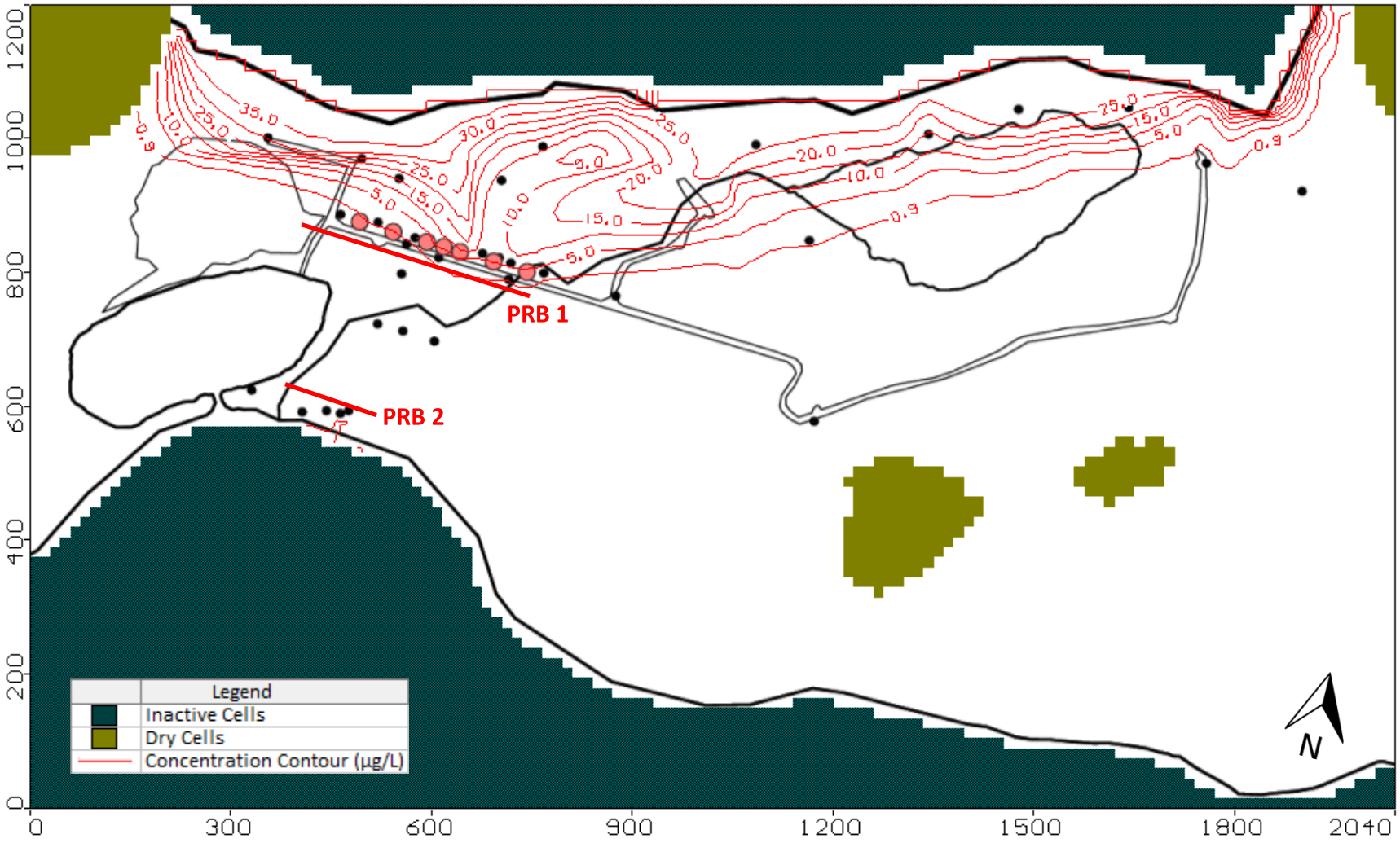

Figure 6.8 Two Analyzed PRB Locations With Cobalt Plume Representing Present Day Conditions (April 2015)

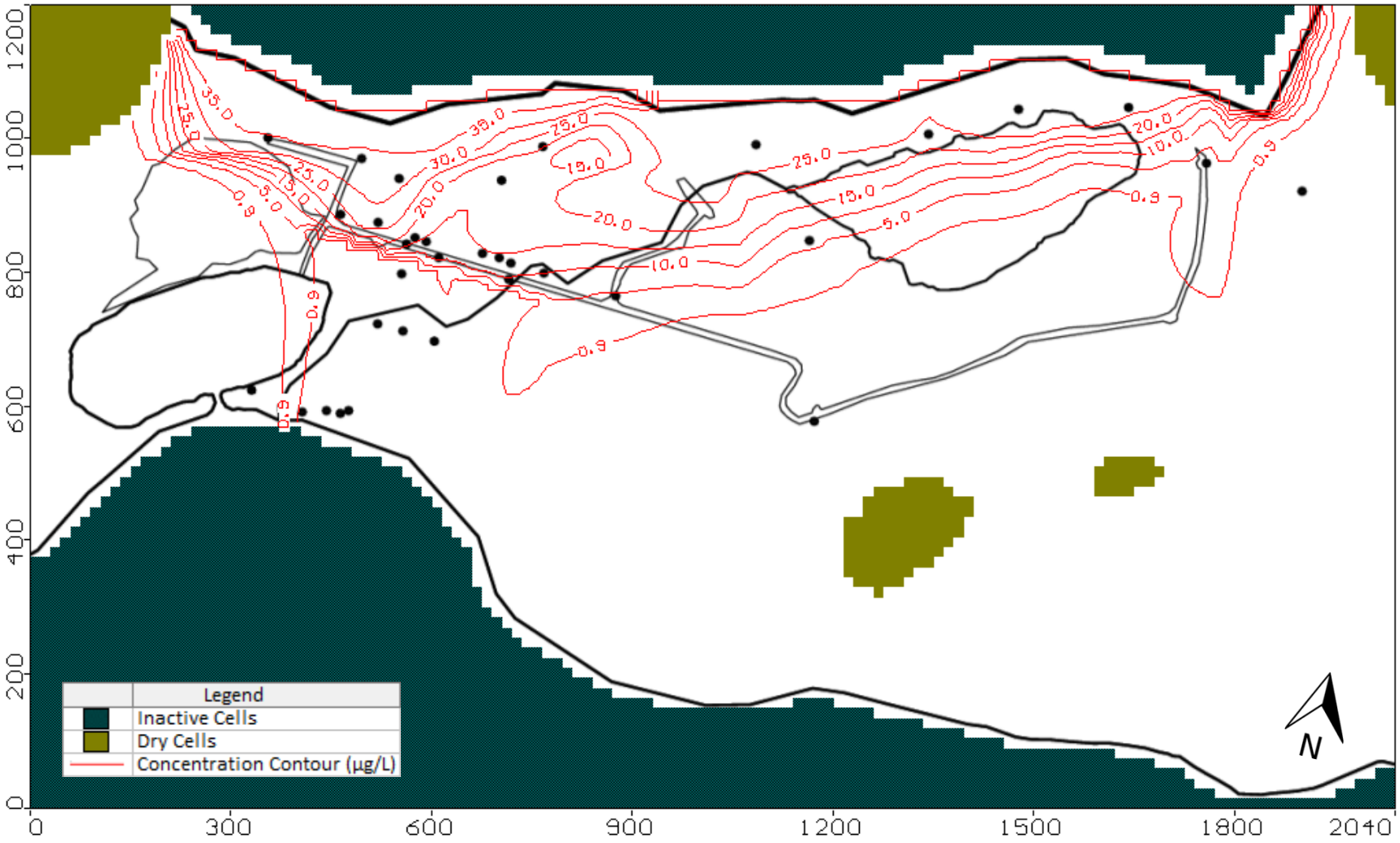

Figure 6.9 Permeable Reactive Barrier 1 After 15 year Simulation (April 2030)

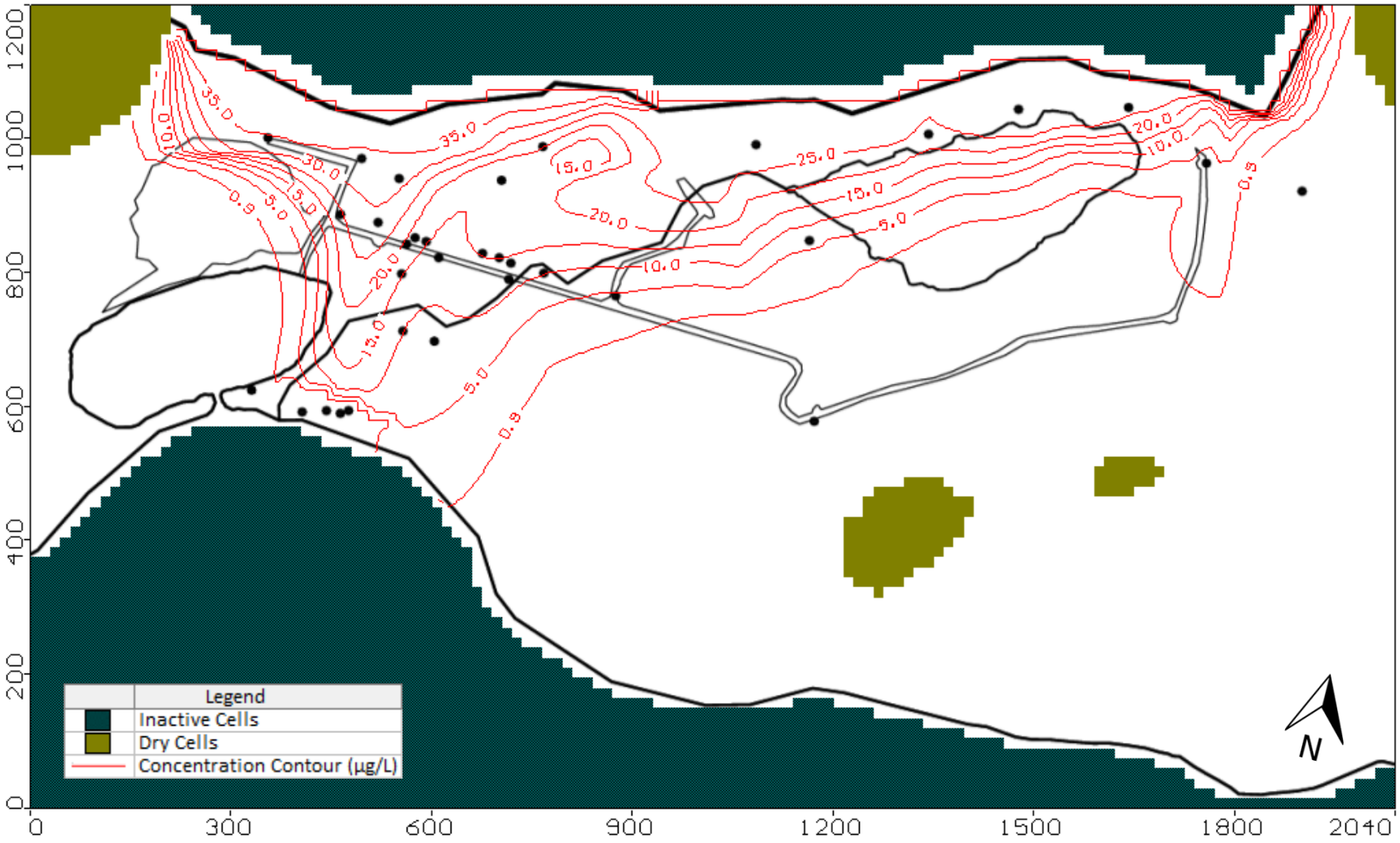

Figure 6.10 Permeable Reactive Barrier 2 After 15 Year Simulation (April 2030)

7.0 SUMMARY, CONCLUSIONS AND RECOMMENDATIONS

7.1 SUMMARY OF THE RESEARCH WORK

The objectives of this thesis project, as presented in section 1.2 have been achieved and the results are presented throughout the previous six chapters. The available site data was organized and analyzed to determine the site history and characteristics in Chapter 3. The geological data from borehole logs were used to determine the main stratigraphic units found beneath the site and construct geological cross sections of the site's subsurface conditions. Groundwater elevation data were then analyzed to examine the time dependant changes which were experienced at the site, and the groundwater flow patterns were determined. The groundwater elevation data were also used to create potentiometric surface contour plots which represent the groundwater flow conditions at significant points in time. The dissolved cobalt and iron concentration data determined from samples collected from the groundwater monitoring wells were then used to define the extents of the plumes, and display their evolution with time through a series of measured concentration contour plots.

A groundwater flow and contaminant transport model was then constructed using Visual MODFLOW Premium, version 2011.1 and the collected site data described above. The input parameters and boundary conditions for the model were then estimated through a combination of collected site data and literature values. The MODFLOW-2005 engine was used to simulate groundwater flow through the model, which was then calibrated to the observed groundwater data collected in April 2009 (before the pumping wells were activated). After

manual calibration of the boundary conditions, recharge rates, and hydraulic conductivity zones was performed, the WINPEST engine was used to perform a final calibration on the hydraulic conductivity values in the aquifer layer of the model. The calibrated groundwater flow model was then validated by simulating the aquifer's observed response to the activation of the pumping wells. The groundwater elevation data collected in April 2011 (after the pumping wells were activated) was used to represent the observed response of the aquifer to the pumping well activation.

The validated groundwater flow model was then used to perform contaminant transport simulations using the MT3DMS engine. Initial simulations were performed using sulphate as a contaminant to develop an understanding of the source term and estimated dispersivity values. The transport of dissolved cobalt was then simulated, and a calibration of the distribution coefficients was performed. The observed extent of the cobalt plume in 2009 was used as the target for calibration. The effects of a change in the dispersion and sorption parameters were then examined during the sensitivity analysis.

The final groundwater flow and contaminant transport model was then used to simulate the future movement of the cobalt plume. An assessment of the pumping well system was conducted through the creation of five pumping scenarios. The five scenarios were simulated to examine the effect that various changes to the pumping well system would have on the cobalt plume over a 15 year simulation time (2015-2030). A preliminary investigation into the use of a permeable reactive barrier (PRB) at the site was also conducted. Two locations were proposed,

and the effect of a PRB on the cobalt plume advancement, if the pumping wells were to be turned off, was examined for a 15 year simulation period (2015-2030).

7.2 CONCLUSIONS

The following are key observations and results of this research:

1. Using a piecewise distribution of hydraulic conductivity values in the sand layer of the groundwater flow model was able to achieve a good fit to the April 2009 observed groundwater elevation data. Using 19 observed data points, the maximum residual head value was -0.091m in well 95-GW-10D, and the absolute mean residual was 0.033m (Figure 4.14). When compared to the total head drop of 2.44m across the site, between wells 95-GW-13 and 07-GW-28, these errors represent a maximum and average of 3.7% and 1.4%, respectively.
2. The groundwater flow model, which was calibrated to April 2009 (prior to pumping well activation) data, can accurately simulate the change in the observed potentiometric surface due to the activation of the pumping wells, and is considered validated. In the area of greatest concern of the model, a good fit to the April 2011 (1 year after the pumping wells were activated) observed groundwater elevation data was achieved when pumps were added to the model while all other groundwater flow parameters and input conditions were held constant (Figure 4.17).
3. When the pumping wells are not active, the fastest flow path between the tailings management area (TMA) and the lake is in the sand layer travelling from the location of Dam A almost directly southward and slightly to the east of the fish habitat (Figure

4.20). A non-reactive particle travelling along this flow path would take almost 7 years to reach the edge of the lake without considering attenuation processes.

4. The pumping well system has been effective in causing a reduction of dissolved cobalt concentrations between the pumping wells and the lake. The same response of the cobalt plume can be seen in both the observed concentration contours (Figure 3.19) and the simulated concentration contours (Figures 5.15 and 5.16).
5. By April 2015 only negligible concentrations of dissolved cobalt will remain in the aquifer between the pumping wells and the lake (Figure 6.1).
6. If the pumping wells were left running under their current operating conditions they are capable of preventing the advancement of the dissolved cobalt plume toward the lake until at least 2030 (Figure 6.2).
7. If the pumping wells were turned off, it would take approximately 3 years for the dissolved cobalt concentrations to once again exceed the trigger level of 5µg/L in wells adjacent to the lake (Figure 6.3).
8. The pumping well system could be run intermittently, with the pumping wells being deactivated and reactivated for a number of years, and successfully restrain the cobalt plume advancement. The pumping wells would need to be active for approximately 4-5 years to reduce the plume advancement that would naturally occur during a 3 year period in which they were inactive.
9. With each pumping well's pumping rate reduced to 50% of its current value, the pumping well system would be able to prevent the advancement of the cobalt plume until at least 2030 (Figure 6.6). Using this scenario, the dissolved cobalt concentrations

between the TMA and the pumping wells would also be lower than those simulated through scenario 1 for the same time period.

10. If pumping wells 09-PW-4, 09-PW-5, 09-PW-7, and 09-PW-9 were deactivated, the pumping well system would be able to prevent the advancement of the cobalt plume with wells 09-PW-3, 09-PW-6, and 09-PW-8 remaining at their current pumping rates until at least 2030 (Figure 6.7). Using this scenario, the dissolved cobalt concentrations between the TMA and the pumping wells would also be lower than those simulated through scenario 1 for the same time period.

7.3 Recommendations for Future Work

Recommendations for future work to be conducted on the Northern Ontario gold mine site include both the refinement/improvement of the existing groundwater flow and contaminant transport models presented, and the expansion of the quantity and quality of the site remediation scenarios being simulated. The continual collection of groundwater elevation data and groundwater samples for water quality analysis are also recommended. Future groundwater elevation data could be used to detect any unexpected changes in the groundwater condition if they were to occur. Continual groundwater quality analysis would allow the continual evolution of the cobalt plume to be monitored, and the observed measurements could be used to confirm or refute the results of future contaminant transport simulations.

The quality of the results produced by the groundwater flow and contaminant transport model is dependent on the values of the measured and estimated input parameters. For this reason,

improvement of confidence in the model results can be achieved by improving the certainty of the various model input parameters. Further site characterization is therefore recommended to develop a better understanding of several of the hydrogeological parameters used in the model. Additional slug testing is recommended to be performed on all monitoring wells across the site to develop a better understanding of the distribution of hydraulic conductivity values throughout the sand aquifer layer. A subsurface characterization method such as seismic soundings could also be used to detect changes in the sand layer properties. This could also be used to better characterize the depth and thickness of the sand aquifer in areas of the site where no boreholes have been drilled or confirm the extent of the sudden increase in bedrock elevation and pinching of the sand layer seen between point W-25 and H-25A in cross section C-C' of Figure 3.2.

As mentioned in section 6.3, some improvements to the groundwater monitoring network are also suggested. A new groundwater monitoring well installed to the west of the overburden storage pile could provide information regarding the amount of easterly flow which is being caused by the pumping wells. Additionally, a new groundwater monitoring well to the south of well 95-GW-4 along the gravel access road could help to monitor the extent and concentration of the cobalt plume as a new lobe develops to the east of the seepage collection pond. It is recommended that any new monitoring well installations allow the protective casing to extend down into the top of the bentonite seal and prevent concrete padding from coming in contact with the well standpipe to minimize the potential for frost heaving. In addition it is recommended that the top of standpipe elevations of all wells be re-surveyed on an annual or bi-annual basis to improve the certainty of the collected groundwater elevation data.

As discussed in section 2.8, flux management principles could be used to quantify the relative importance of the various lobes which are predicted to exist based on the simulated cobalt plume. Monitoring well control planes could be set up at the site between the pumping wells and the TMA perpendicular to the locations of the simulated lobes. By setting up control planes across the plume at different locations, changes in the mass flux of cobalt or other contaminants can be measured, and attenuation rates can be estimated. Additionally, control planes could be used to quantify the increase or decrease in cobalt mass flux from the TMA with time. As noted in section 2.8.3 once a reliable groundwater flow and contaminant transport model can outline the plume centerline, the concentration data collected along this centerline could also be used to estimate the attenuation rates for the detected contaminants.

Due to the relatively high sensitivity of the contaminant transport model to the distribution coefficient in the northern portion of the sand layer, further investigation into this parameter is also recommended. Batch sorption tests performed on various samples of aquifer material would provide more certainty into how the sorption properties of the aquifer vary spatially across the site.

Further modelling simulations which are recommended would be to more closely investigate the use of a PRB at the site. The investigation which was performed in this thesis was intended for preliminary purposes and used simplified conditions and did not consider costs. A more detailed investigation into the use of a PRB is therefore recommended for the northern Ontario gold mine site. This investigation should include a more in depth consideration for the hydraulic conductivity and thickness of the barrier material. Additionally, simulations could be performed

which compare the use of various funnel and gate system layouts, and the effects that a funnel wall would have on the groundwater flow and contaminant transport models in various areas.

REFERENCES

Abakar, R. (2015). *Contamination Prevention Using an Electrokinetic Barrier - Cobalt Trapping.* M.Sc. Thesis, Lakehead University, Thunder Bay, ON.

Abbas, M., Kaddour, S., & Trari, M. (2014). Kinetic and Equilibrium Studies of Cobalt Adsorption on Apricot Stone Activated Carbon. *Journal of Industrial and Engineering Chemistry, 20*, 745-751.

Almas, A. R., & Manoko, M. L. (2012). Trace Element Concentrations in Soil, Sediments, and Waters in the Vicinity of Geita Gold Mines and North Mara Gold Mines in Northwest Tanzania. *Soil and Sediment Contamination, 21*, 135-159.

Alvarez, P. J., & Illman, W. A. (2006). *Bioremediation and Natural Attenuation* . New Jersey: John Willey & Sons, Inc.

Annable, M. D., Hatfield, K., Cho, J., Klammler, H., Parker, B. L., Cherry, J. A., & Rao, P. S. (2005). Field-Scale Evaluation of the Passive Flux Meter for Simultaneous Measurement of Groundwater and Contaminant Fluxes. *Environmental Science & Technology, 39*, 7194-7201.

Appelo, C. A., & Postma, D. (2005). *Geochemistry, Groundwater and Pollution* (2 ed.). Great Britain: A.A. Balkema Publishers.

Artimo, A., Salonen, V.-P., Pietila, S., & Sarapera, S. (2004). Three-dimensional geologic modeling and groundwater flow modeling of the Tollinpera aquifer in the Hitura nickel mine area, Finland - providing the framework for restoration and protection of the aquifer. *Bulletin of the Geological Society of Finland, 76*, 5-17.

Batu, V. (2006). *Applied Flow and Solute Transport Modelling in Aquifers; Fundamental Principles and Analytical and Numerical Methods.* Boca Raton, Florida: CRC Press.

Bedell, P. R., Firlotte, F. W., & Atherton, K. (2002). A Case Record of Tailings Dam Construction Using Residual Soils. *Canadian Geotechnical Journal, 39*, 409-416.

Blowes, D. W., Ptacek, C. J., & Jurjovec, J. (2003). Mill Tailings: Hydrogeology and Geochemistry. In J. L. Jambor, D. W. Blowes, & A. I. Ritchie (Eds.), *Environmental Aspects of Mine Wastes* (Vol. 31, pp. 95-116). Vancouver: Mineralogical Association of Canada.

Bockelmann, A., Zamfirescu, D., Ptak, T., Grathwohl, P., & Teutsch, G. (2003). Quantification of Mass Fluxes and Natural Attenuation Rates at an Industrial Site With a Limited Monitoring Network: A Case Study. *Journal of Contaminated Hydrology, 60*, 97-121.

Bradl, H. B. (2004). Adsorption of Heavy Metal Ions on Soils and Soils Constituents. *Journal of Colloid and Interface Science, 277*, 1-18.

Coduto, D. P. (1999). *Geotechnical Engineering Principles and Practices.* Upper Saddle River, New Jersey: Prentice Hall, Inc.

Dunnivant, F. M., & Anders, E. (2006). *A Basic Introduction to Pollutant Fate and Transport: An Integrated Approach with Chemistry. Modeling, Risk Assessment, and Environmental Legislation.* New Jersey: John Wiley & Sons, Inc.

Dyer, J. A., & Scrivner, N. C. (1998). A Practical Guide for Determining the Solubility of Metal Hydroxides and Oxides in Water. *Environmental Progress, 17*(1), 1-8.

Einarson, M. D., & Mackay, D. M. (2001). Prediction Impacts of Groundwater Contamination. *Environmental Science & Technology, 35*(3), 66-73.

Gelhar, L. W., Welty, C., & Rehfeldt, K. R. (1992). A Critical Review of Data on Field-Scale Dispersion in Aquifers. *Water Resources Research, 28*(7), 1955-1974.

Goltz, M. N., Close, M. E., Yoon, H., Huang, J., Flintoft, M. J., Kim, S., & Enfield, C. (2009). Validation of Two Innovative Methods to Measure Contaminant Mass Flux in Groundwater. *Journal of Contaminated Hydrology, 106*, 51-61.

Goltz, M. N., Kim, S., Yoon, H., & Park, J. (2007). Review of Groundwater Contaminant Mass Flux Measurement. *Environmental Engineering Research, 12*(4), 176-193.

Gould, W. D., & Kapoor, A. (2003). The Microbiology of Acid Mine Drainage. In J. L. Jambor, D. W. Blowes, & R. A. M (Eds.), *Environmental Aspects of Mine Wastes* (pp. 203-226). Vancouver: Mineralogical Assiciation of Canada.

Harbraugh, A. W. (2005). MODFLOW-2005, The U.S. Geological Survey Modular Ground-Water Model - the Ground-Water Flow Process. In *U.S. Geological Survey Techniques and Methods 6-A16.* Reston, Virginia: USGS.

HDR Engineering Inc. (2001). *Handbook of Public Water Systems* (2 ed.). New York: John Wiley & Sons, Inc.

Iribar, V., Izco, F., Tames, P., Antiguedad, I., & da Silva, A. (2000). Water Contamination and Remidial Measures at the Troya Abandoned Pb-Zn Mine (The Basque Country, Northern Spain). *Environmental Geology, 39*(7), 800-806.

Johanson, P. (2008). *Cobalt.* New York, NY: The Rosen Publishing Group, Inc.

Jury, W. A., & Horton, R. (2004). *Soil Physics* (6th ed.). New Jersey: John Wiley & Sons Inc.

Kam, S., Hmidi, N., & Mao, Y. (2014). Field Performance of Thickened Tailings Disposal at Musselwhite Mine. *Proceedings of the 17th International Seminar on Paste and Thickened Tailings* (pp. 627-641). Vancouver, BC: Paste 2014.

Kimball, B. A., Runkel, R. L., & Walton-Day, K. (2003). Use of Field-Scale Experiments and Reactive Solute-Transport Modelling to Evaluate Remediation Alternatives in Streams Affected by Acid Mine Drainage. In J. L. Jambour, D. W. Blowes, & A. I. Ritchie (Eds.), *Environmental Aspects of Mine Wastes* (Vol. 31, pp. 261-282). Vancouver: Mineralogical Association of Canada.

Kortatsi, B. K., & Akabzaa, T. M. (2009). Gold Mining in Ghana. In M. D. Corral, & J. L. Earle (Eds.), *Gold Mining: Formation and Resource Estimation, Economics and Environmental impact* (pp. 111-144). New York: Nova Science Publishers, Inc.

Lottermoser, B. (2007). *Mine Wastes: Characterization, Treatment and Environmental Impacts* (2 ed.). New York: Springer.

Marsden, J., & House, I. (1992). *The Chemistry of Gold Extraction.* Chichester: Ellis Horwood Limited.

Mays, L. W. (2012). *Ground and Surface Water Hydrology.* New Jersey: John Wiley & Sons, Inc.

McKay, L. D., Cherry, J. A., & Gillham, R. W. (1993). Field Experiments in a Fractured Clay Till 1. Hydraulic Conductivity and Fracture Aperture. *Water Resources Research, 29*(4), 1149-1162.

Mettler, S., Abdelmoula, M., Hoehn, E., Schroenenberger, R., Weidler, P., & von Gunten, U. (2001). Characterization of Iron and Manganese Precipitates from an In Situ Ground Water Treatment Plant. *Ground Water, 39*(6), 921-930.

Ministry of Environment and Energy. (1994). *Water Management: Policies, Guidelines, Provincial Water Quality Objectives of the Ministry of Environment and Energy.* Queen's Printer for Ontario.

Ministry of Northern Development and Mines. (2008). *Modernizing Ontario's Mining Act: Finding a Balance Discussion Paper.* Ontario.

Moldovan, B. J., Hendry, M. J., & Harrington, G. A. (2008). The arsenic source term for an in-pit uranium mine tailings facility and its long-term impact on the regional groundwater. *Applied Geochemistry, 23*, 1437-1450.

Morrison, S. J., Naftz, D. L., Davis, J. A., & Fuller, C. C. (2002). Introduction to Groundwater Remediation of Metals, Radionucleides, and Nutrients with Permeable Reactive Barriers. In D. L. Naftz, S. J. Morrison, J. A. Davis, & C. C. Fuller (Eds.), *Handbook of Groundwater Remediation Using Permeable Reactive Barriers* (pp. 1-15). New York: Academic Press.

Natural Resources Canada. (1996). *The Minerals and Metals Policy of the Government of Canada.* Ottawa: Minister of Public Works and Government Services Canada.

Neuman, S. P., & Zhang, Y.-K. (1990). A Quasi-Linear Theory of Non-Fickian Subsurface Dispersion, 1. Theoretical Analysis With Application to Isotropic Media. *Water Resources Research, 26*(5), 887-902.

Nielsen, D. M., Nielsen, G. L., & Preslo, L. M. (2006). Environmental Site Characterization. In D. M. Nielsen (Ed.), *Practical handbook of Environmental Site Characterization and Ground-Water Monitoring* (2 ed., pp. 35-205). New York: CRC Press.

Nielsen, D. N., & Schalla, R. (2006). Design and Installation of Ground-Water Monitoring Wells. In D. M. Nielsen (Ed.), *Practical Handbook of Environmental Site Characterization and Ground-Water Monitoring* (2 ed., pp. 639-805). New York: CRC Press.

Ohio EPA. (2007). Ground Water Flow and Fate and Transport Modeling. In *Technical Guidance Manual For Ground Water Investigations.* Columbus, Ohio: Ohio Environmental Protection Agency, Division of Drinking and Ground Waters.

Ontario. (1990). *Mining Act: R.S.O. 1990, Chapter M.14.* Service Ontario.

Ontario. (1994). Ontario Regulation 560/94 Effluent Monitoring and Effluent Limits - Metal Mining Sector. In *Environmental Protection Act.* Service Ontario.

Ontario. (2000). Ontario Regulation 240/00 Mine Development and Closure Under Part VII Of The Act. In *The Mining Act.* Service Ontario.

Pichtel, J. (2007). *Fundamentals of Site Remediation* (2 ed.). Maryland: Government Institutes.

Piteau Associates Engineering Ltd. (2011). *2010 Biennial Groundwater Monitoring Report.*

Powers, J. P., Corwin, A. B., Schmall, P. C., & Kaeck, W. E. (2007). *Construction Dewatering and Groundwater Control: New methods and Applications* (3 ed.). Hoboken, New Jersey: John Wiley & Sons, Inc.

Price, W. A. (2003). Challenges Posed By Metal Leaching and Acid Rock Drainage, and Approaches Used to Address Them. In J. L. Jambor, D. W. Blowes, & A. I. Ritchie (Eds.),

Environmental Aspects of Mining (Vol. 31, pp. 1-10). Vancouver: Mineralogical Association of Canada.

Price, W. A., & Errington, J. C. (1998). *Guidelines for Metal Leaching and Acid Rock Drainage at Minesites in British Columbia.* British Columbia Ministry of Energy and Mines.

Prietzel, J., Thieme, J., Eusterhues, K., & Eichert, D. (2007). Iron Speciation in Soils and Soil Aggregates by Synchrotron-Based X-ray Microspectroscopy (XANES, μ-XANES). *European Journal of Soil Science, 58*, 1027-1041.

Reichl, C., Schatz, M., & Zsak, G. (2013). *World Mining Data.* Vienna: International Organizing Committee for the World Mining Congresses.

Ribeiro, A. C., Lobo, V. M., & Natividade, J. J. (2002). Diffusion Coefficients in Aqueous Solutions of Cobalt Chloride at 298.15 K. *Journar of Chemical Engineering Data, 47*, 539-541.

Rowe, R. K., Caers, C. J., & Barone, F. (1988). laboratory Determination of Diffusion and Distribution Coefficients of Contaminants Using Undisturbed Clayey Soil. *Canadian Goetechnical Journal, 25*, 108-118.

Santos Jallath, J. E. (2009). Closure of Tailings Dams and Remediation of Soils Contaminated with Mining Wastes. In L. G. Torres, & E. R. Bandala (Eds.), *Remediation of Soils and Aquifers* (pp. 213-230). New York: Nova Science Publishers, Inc.

Sara, M. N. (2006). Ground-Water Monitoring System Design. In D. M. Nielsen (Ed.), *Practical Handbook of Environmental Site Characterization and Ground-Water Monitoring* (2 ed., pp. 517-572). New York: CRC Press.

Schlumberger Water Services. (2011). *Visual MODFLOW 2011.1 User's Manual: For Professional Applications in Three-Dimensional Groundwater Flow and Contaminant Transport Modeling.* Waterloo: Schlumberger Water Services.

Schwartz, F. W., & Zhang, H. (2003). *Fundamentals of Ground Water.* New York: John Wiley & Sons, Inc.

Sciences International, Inc. (2006). *Concise International Chemical Assessment Document 69: Cobalt and Inorganic Cobalt Compounds.* (J. H. Kim, H. J. Gibb, P. D. Howe, & M. Sheffer, Eds.) Germany: World Health Organization.

Seal, R. R., & Hammarstrom, J. M. (2003). Geoenvironmental Models of Mineral Deposits: Examples From Massive Sulfide and Gold Deposits. In J. L. Jambor, D. W. Blowes, & A. I. Ritchie (Eds.), *Environmental Aspects of Mine Wastes* (Vol. 31, pp. 11-50). Vancouver: Mineralogical Association of Canada.

Sharma, H. D., & Reddy, K. R. (2004). *Geoenvironmental Engineering: Site Remediation, Waste Containment, and Emerging Management Technologies.* New Jersey: John Wiley & Sons, Inc.

Spitz, K., & Trudinger, J. (2009). *Mining and the Environment: from Ore to Metal.* London: CRC Press.

Stenback, G. A., Ong, S. K., Rogers, S. W., & Kjartanson, B. H. (2004). Impact of Transverse and Longitudinal Dispersion on First-Order Degradation Rate Constant Estimation. *Journal of Contaminant Hydrology, 73*, 3-14.

Stevens, R. (2010). *Mineral Exploration and Mining Essentials.* Port Coquitlam: Pakawau Geomanagement Inc.

Stoica, A.-I., Florea, R.-M., & Baiulescu, G.-E. (2009). The Influence of Gold Mining Industry on the Pollution of Rosia Montana District. In M. D. Corral, J. L. Earle, M. D. Corral, & J. L. Earle (Eds.), *Gold Mining: Formation and Resource Estimation, Economics and Environmental Impact.* New York: Nova Science Publishers, Inc.

Striggow, B. (2013). Design and Installation of Monitoring Wells. In USEPA, *SESD Guidance.* Athens, Georgia: USEPA Science and Ecosystem Support Division.

Suthersan, S. S. (1997). *Remediation Engineering: Design Concepts.* New York: CRC Press, Inc.

Todd, D. K., & Mays, L. W. (2005). *Groundwater Hydrology* (3 ed.). New Jersey: John Wiley & Sons, Inc.

USEPA. (1998). *Permeable Reactive Barrier Technologies for Contaminant Remediation.* Washington: United States Environmental Protection Agency.

Verreydt, G., Van Keer, I., Bronders, J., Diels, L., & Vanderauwera, P. (2012). Flux-Based Risk Management Strategy of Groundwater Pollutions: The CMF Approach. *Environmental Geochemical Health, 34*, 725-736.

Water Management Consultants. (2005). *Preliminary Groundwater Model of the Tailings Basin.*

Water Management Consultants. (2007). *2006 Groundwater Monitoring Report.* Waterloo: Water Management Consultants.

Water Management Consultants. (2008). *2007 Groundwater Monitoring Report.*

Water Management Consultants. (2010). *Groundwater Interception System Installation.*

Xu, M., & Eckstein, Y. (1995). Use of Weighted Least-Squares Method in Evaluation of the Relationship Between Dispersivity and Field Scale. *Ground Water, 33*(6), 905-908.

Zheng, C., & Wang, P. P. (1998). *MT3DMS Reference Manual: Three Dimensional, Multi-Species Mass Transport Modeling.* Tuscaloosa, Alabama: Waterloo Hydrogeologic.

APPENDIX A: COBALT & IRON CONCENTRATION TIME SERIES IN WELLS 96-GW-6S, 95-GW-10D, 96-GW-14S, 96-GW-17, AND 06-GW-28

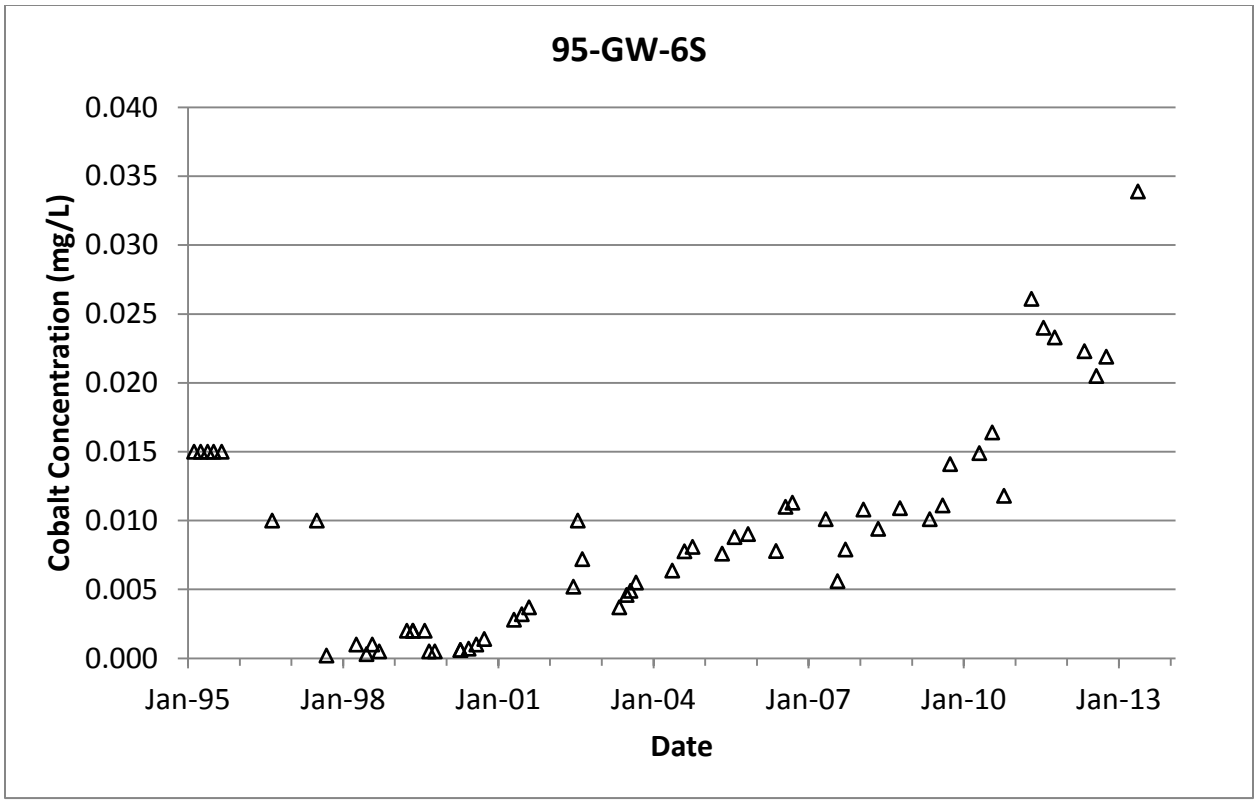
95-GW-6S
Cobalt Concentration (mg/L)
0.040
0.035
0.030
0.025
0.020
0.015
0.010
0.005
0.000
Jan-95
Jan-98
Jan-01
Jan-04
Jan-07
Jan-10
Jan-13
Date

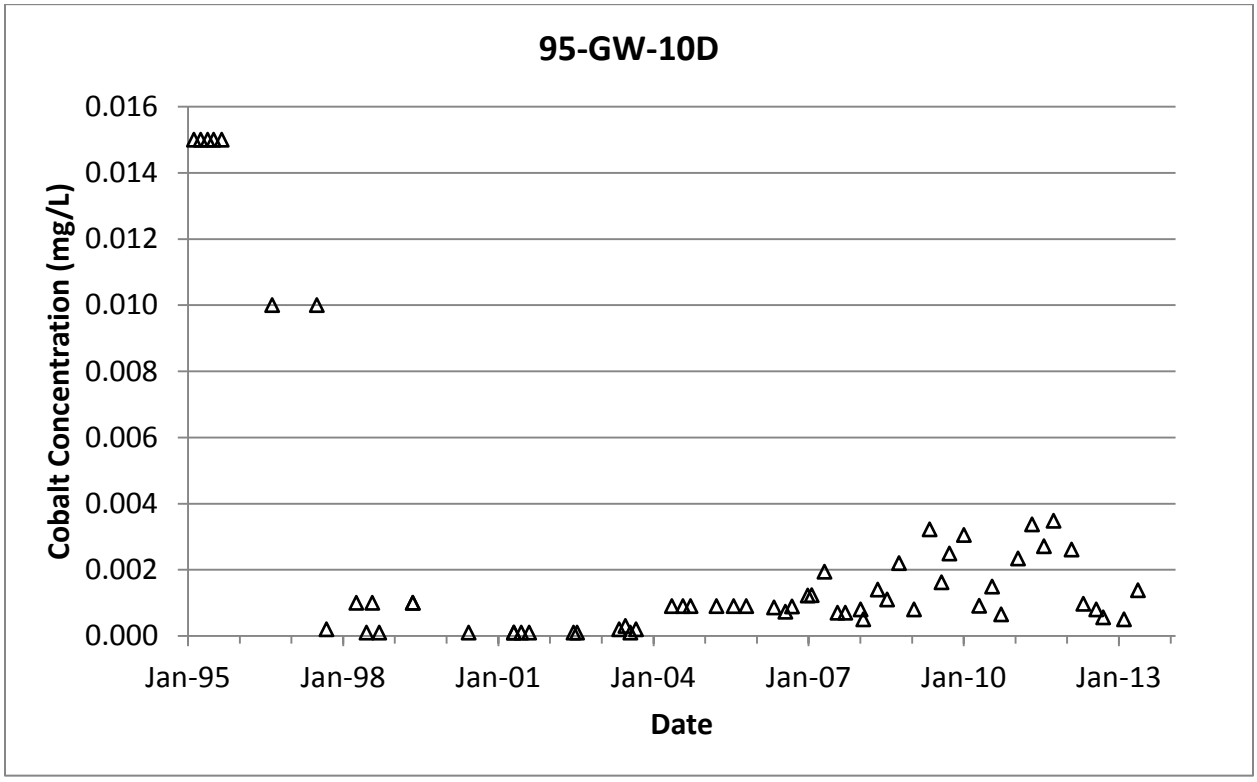
95-GW-10D
Cobalt Concentration (mg/L)
0.016
0.014
0.012
0.010
0.008
0.006
0.004
0.002
0.000
Jan-95
Jan-98
Jan-01
Jan-04
Jan-07
Jan-10
Jan-13
Date

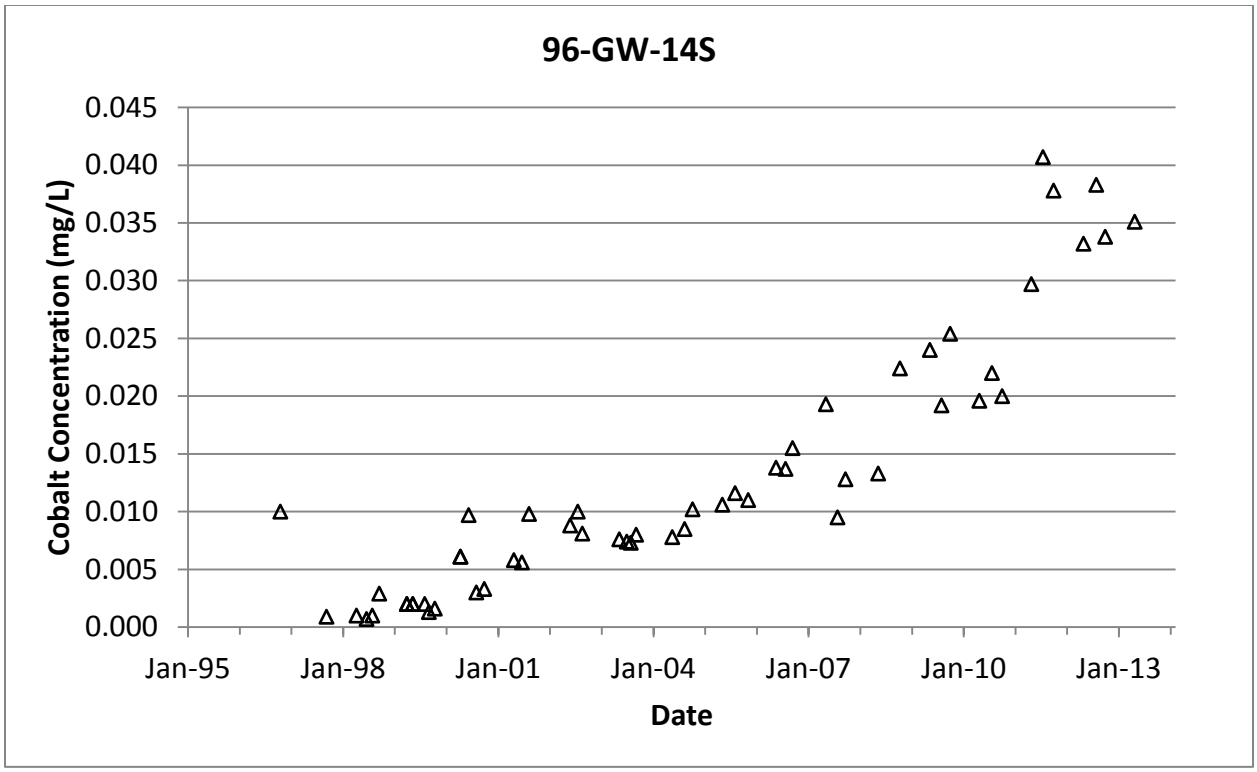
96-GW-14S
Cobalt Concentration (mg/L)
0.045
0.040
0.035
0.030
0.025
0.020
0.015
0.010
0.005
0.000
Jan-95
Jan-98
Jan-01
Jan-04
Jan-07
Jan-10
Jan-13
Date

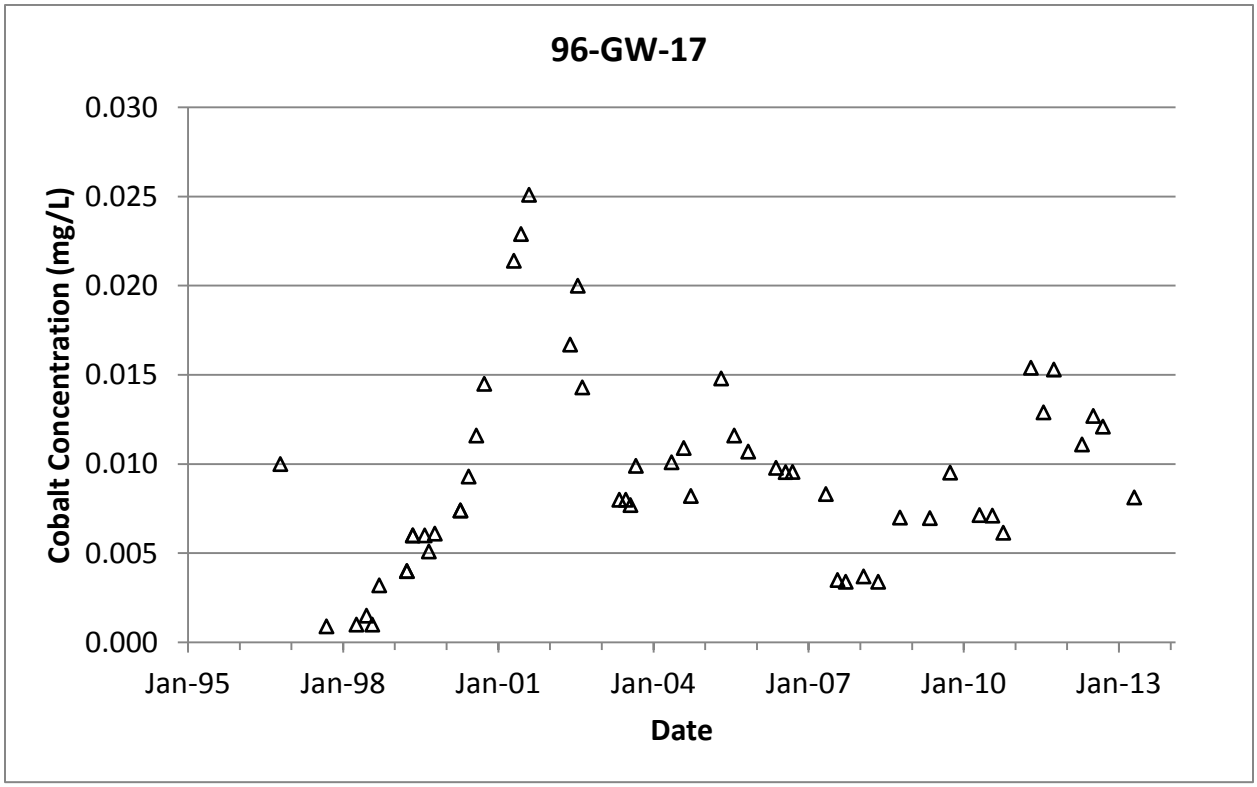
96-GW-17
Cobalt Concentration (mg/L)
0.030
0.025
0.020
0.015
0.010
0.005
0.000
Jan-95
Jan-98
Jan-01
Jan-04
Jan-07
Jan-10
Jan-13
Date

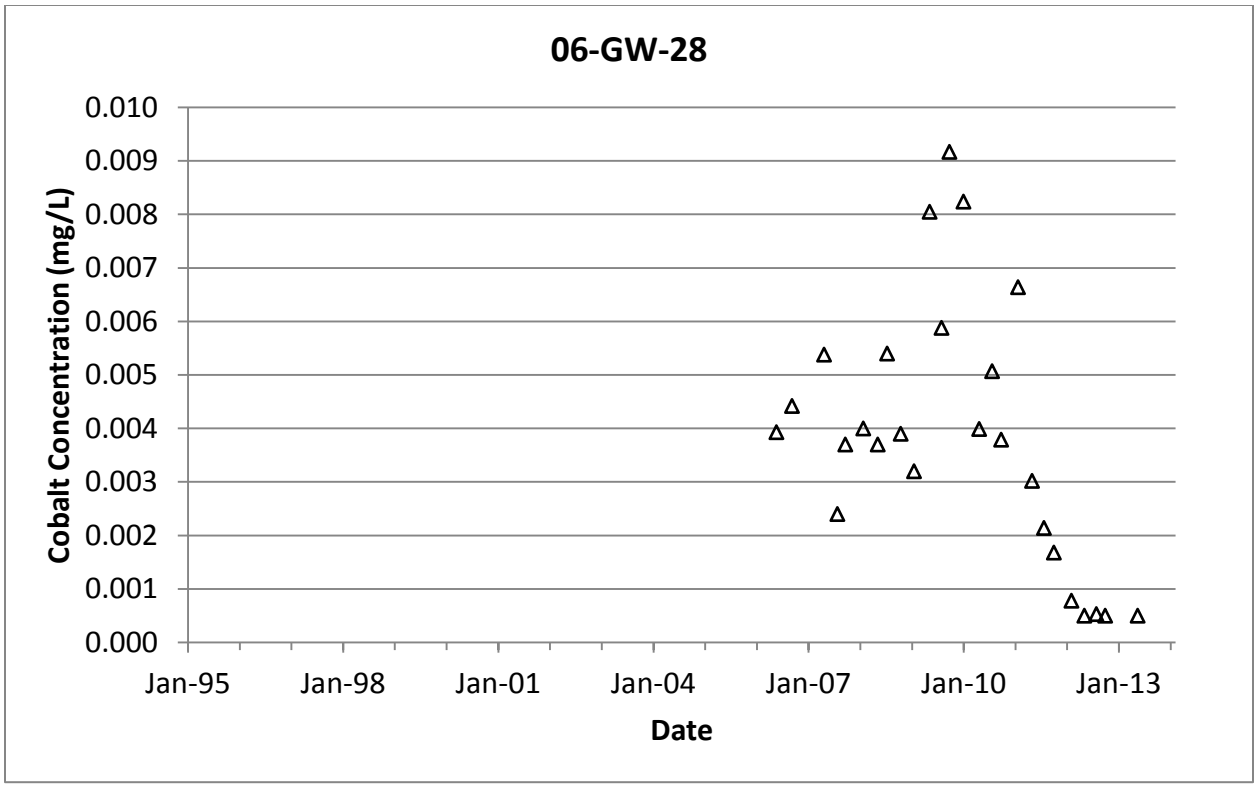
06-GW-28
Cobalt Concentration (mg/L)
0.010
0.009
0.008
0.007
0.006
0.005
0.004
0.003
0.002
0.001
0.000
Jan-95
Jan-98
Jan-01
Jan-04
Jan-07
Jan-10
Jan-13
Date

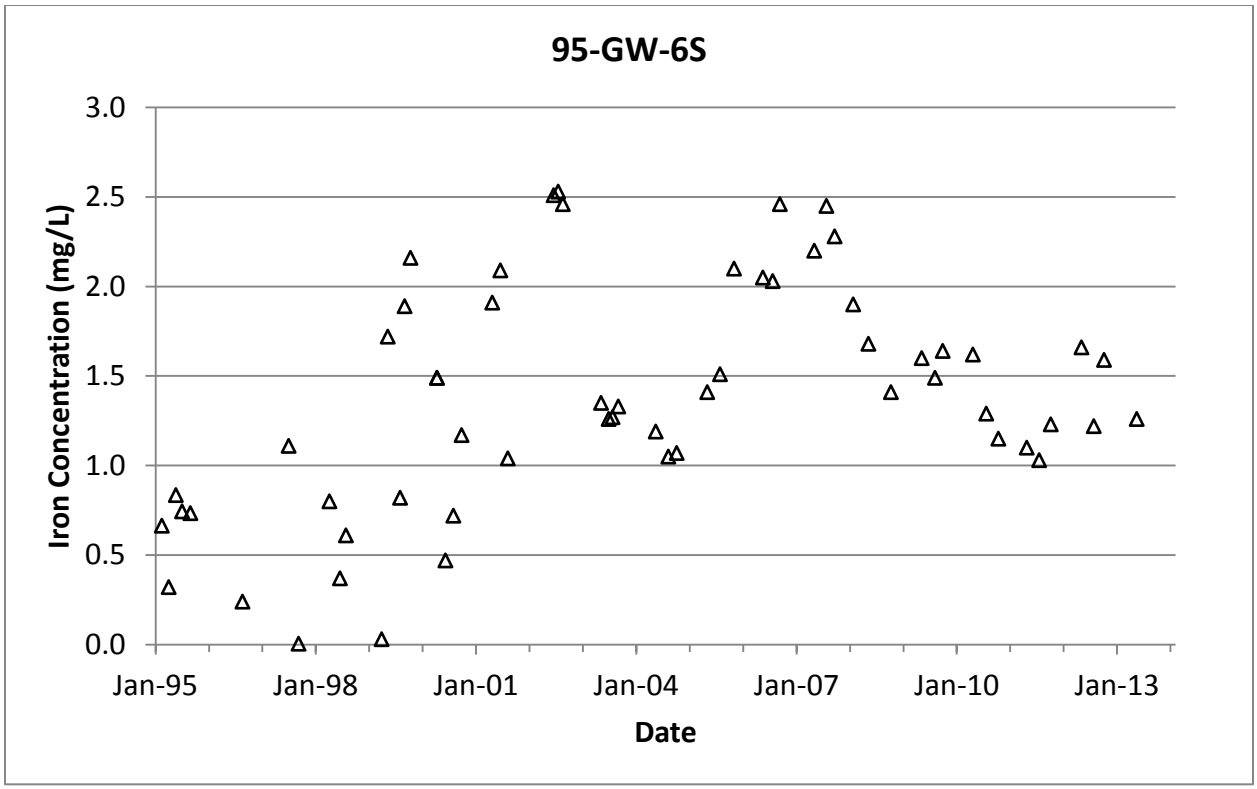
95-GW-6S
Iron Concentration (mg/L)
3.0
2.5
2.0
1.5
1.0
0.5
0.0
Jan-95
Jan-98
Jan-01
Jan-04
Jan-07
Jan-10
Jan-13
Date

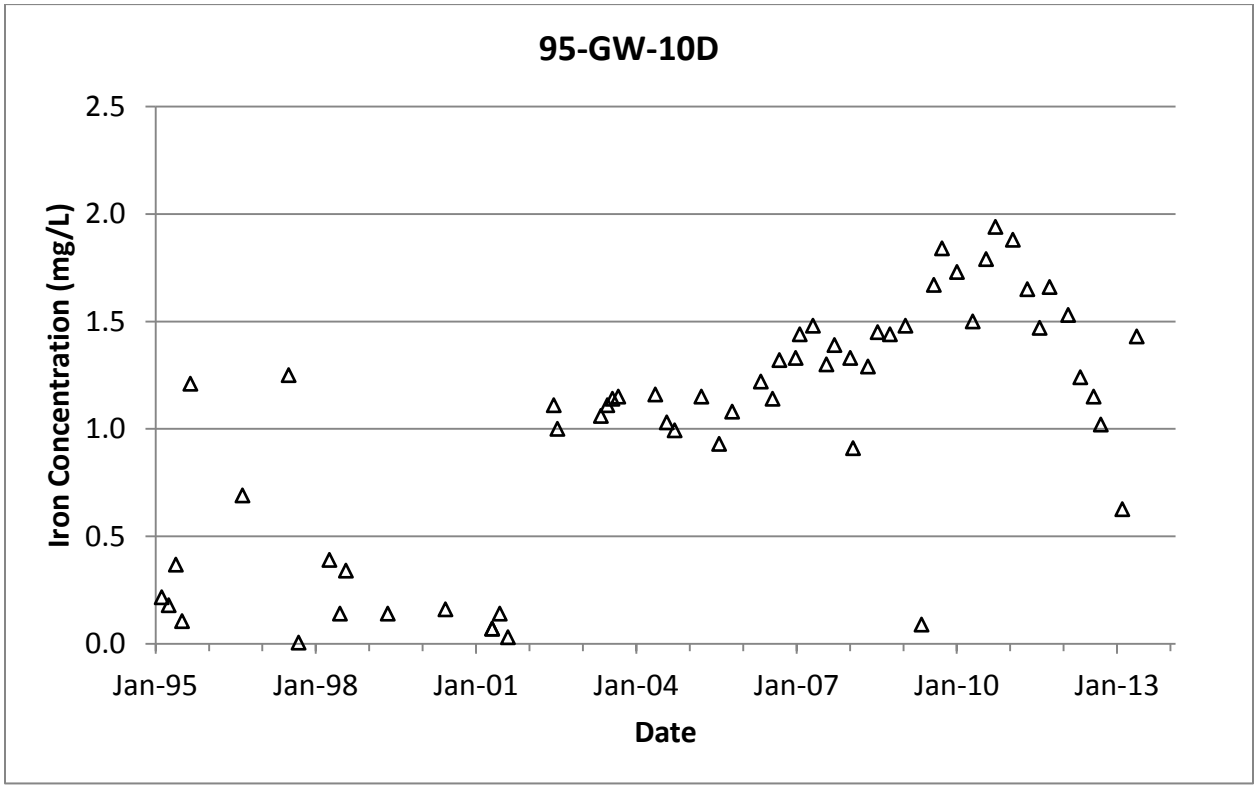
95-GW-10D
Iron Concentration (mg/L)
2.5
2.0
1.5
1.0
0.5
0.0
Jan-95
Jan-98
Jan-01
Jan-04
Jan-07
Jan-10
Jan-13
Date

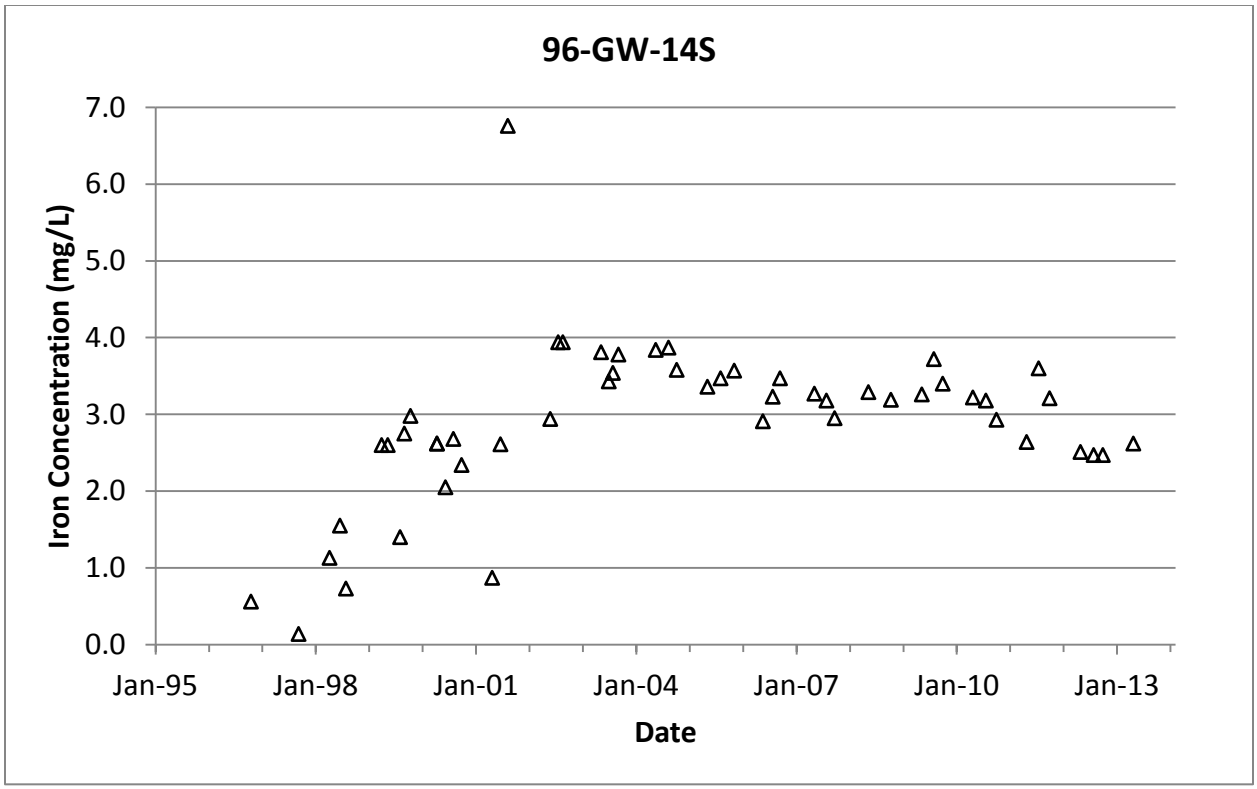
96-GW-14S
Iron Concentration (mg/L)
7.0
6.0
5.0
4.0
3.0
2.0
1.0
0.0
Jan-95
Jan-98
Jan-01
Jan-04
Jan-07
Jan-10
Jan-13
Date

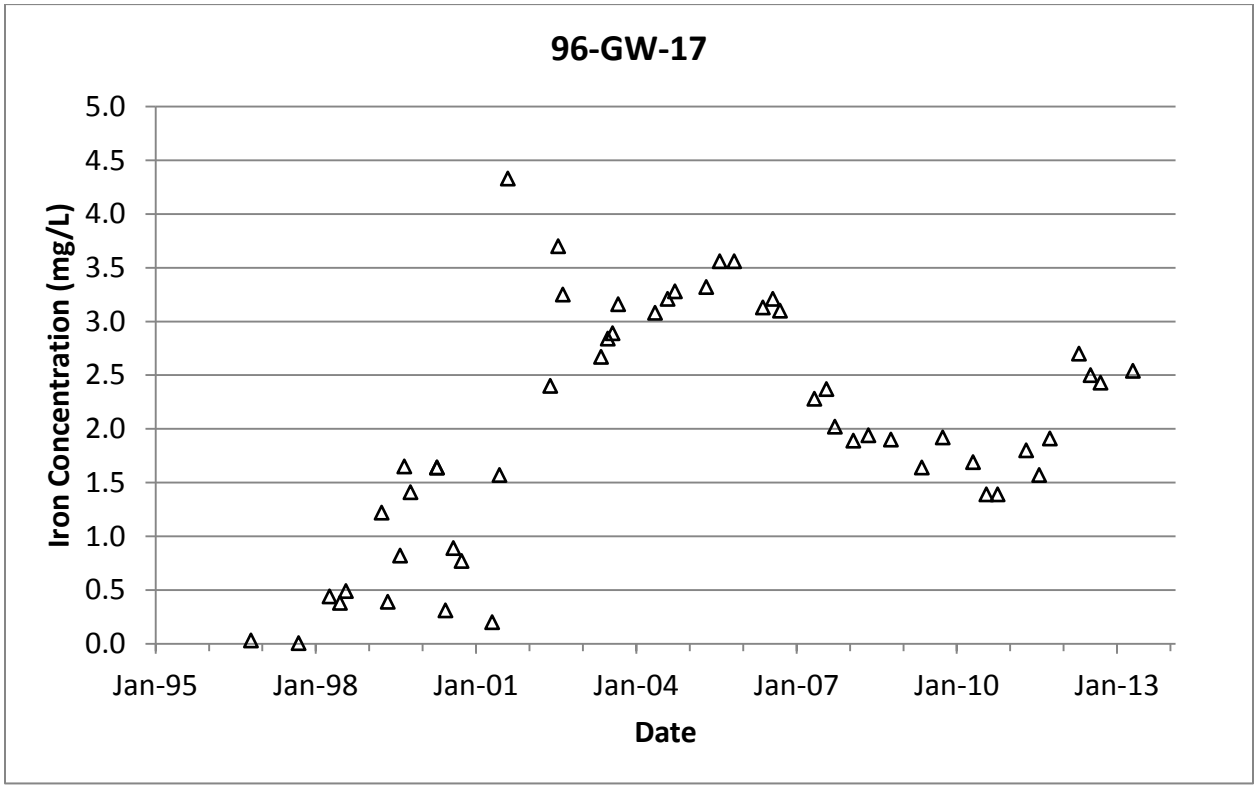
96-GW-17
Iron Concentration (mg/L)
5.0
4.5
4.0
3.5
3.0
2.5
2.0
1.5
1.0
0.5
0.0
Jan-95
Jan-98
Jan-01
Jan-04
Jan-07
Jan-10
Jan-13
Date

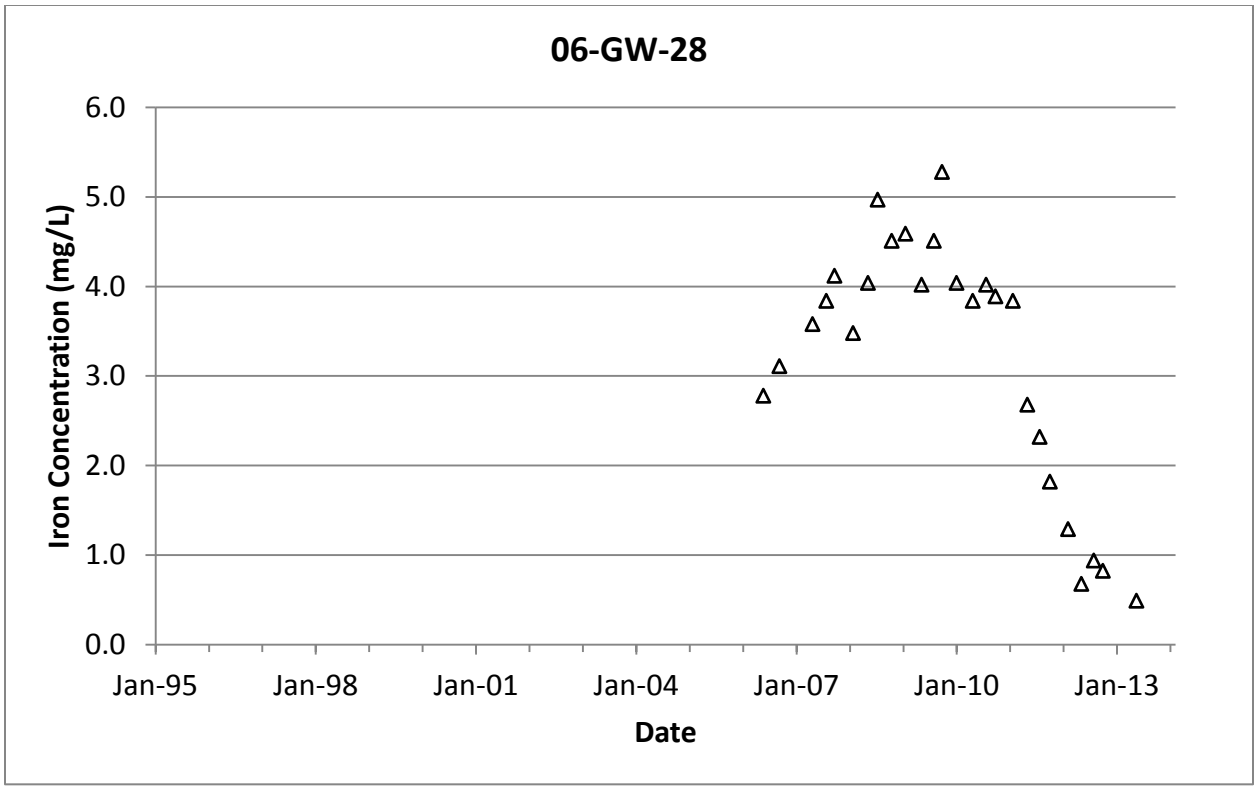
06-GW-28
Iron Concentration (mg/L)
6.0
5.0
4.0
3.0
2.0
1.0
0.0
Jan-95
Jan-98
Jan-01
Jan-04
Jan-07
Jan-10
Jan-13
Date

APPENDIX B: COBALT & IRON YEARLY AVERAGE CONCENTRATION DATA (2000, 2003, 2006, 2009, 2010, AND 2012)

Well Name	Yearly Average Dissolved Cobalt Concentrations (µg/L)					
	2000	2003	2006	2009	2010	2012
00-GW-19	-	0.70	6.44	12.80	3.94	0.50
04-GW-20	-	-	0.59	4.92	2.67	2.74
04-GW-21	-	-	5.95	7.93	9.82	32.87
04-GW-22	-	-	5.58	5.49	-	-
06-GW-24	-	-	5.48	7.46	2.76	3.62
06-GW-25	-	-	1.65	-	2.02	6.85
06-GW-26	-	-	3.75	3.41	1.50	0.50
06-GW-27	-	-	4.12	5.62	2.70	0.77
06-GW-28	-	-	4.18	6.58	5.27	0.58
07-GW-29	-	-	-	8.63	2.86	3.52
07-GW-30	-	-	-	9.33	4.18	7.81
07-PW-02	-	-	-	-	-	-
09-GW-31	-	-	-	-	5.56	20.70
09-GW-32	-	-	-	-	6.74	8.65
09-GW-33	-	-	-	-	10.67	8.51
09-GW-34	-	-	-	-	5.17	8.36
09-GW-35	-	-	-	-	3.14	2.70
09-GW-36	-	-	-	-	4.61	5.50
09-GW-37	-	-	-	-	5.37	-
09-GW-38	-	-	-	-	3.57	1.02
10-GW-40	-	-	-	-	5.07	2.35
95-GW-10D	0.10	0.20	0.83	2.03	1.53	1.24
95-GW-10S	0.10	0.13	0.37	1.05	0.87	0.28
95-GW-1D	0.10	0.10	0.10	0.50	0.50	0.50
95-GW-1S	0.20	0.10	0.10	0.50	0.50	0.50
95-GW-2D	0.60	0.80	0.69	1.48	0.50	1.91
95-GW-2S	0.10	0.20	6.22	6.95	4.04	1.16
95-GW-3D	0.26	0.40	0.36	0.50	0.50	0.50
95-GW-3S	0.62	0.63	6.35	5.78	1.97	10.82
95-GW-4D	0.10	0.10	0.12	1.44	0.90	4.52
95-GW-4M	0.10	0.20	0.10	1.32	0.50	1.10
95-GW-4S	0.90	0.78	1.05	4.48	2.31	10.77
95-GW-6D	0.18	0.10	0.10	0.65	0.54	0.50
95-GW-6S	0.86	4.68	10.03	11.77	14.37	21.57
96-GW-11	0.20	0.20	0.27	1.74	0.51	3.19
96-GW-12	0.10	0.13	1.93	8.40	7.44	17.85
96-GW-13	2.70	9.65	10.48	17.10	21.27	24.37
96-GW-14D	2.68	6.20	13.03	14.50	15.03	31.40
96-GW-14S	5.64	7.58	14.33	22.87	20.53	35.10
96-GW-15D	0.24	0.30	0.11	0.50	0.50	0.50
96-GW-15S	1.42	2.98	2.24	9.71	3.85	19.57
96-GW-17	10.04	8.40	9.63	8.25	6.80	11.97

- No Data Available

Well Name	Yearly Average Dissolved Iron Concentrations (mg/L)					
	2000	2003	2006	2009	2010	2012
00-GW-19	-	0.20	0.67	2.70	1.50	0.34
04-GW-20	-	-	0.88	1.94	1.95	1.60
04-GW-21	-	-	0.05	0.10	0.10	0.70
04-GW-22	-	-	2.02	1.79	-	-
06-GW-24	-	-	3.31	2.90	3.30	2.05
06-GW-25	-	-	0.04	-	1.86	1.35
06-GW-26	-	-	2.51	3.09	2.59	1.27
06-GW-27	-	-	2.94	3.46	3.00	1.52
06-GW-28	-	-	2.95	4.60	3.95	0.93
07-GW-29	-	-	-	2.57	1.75	1.09
07-GW-30	-	-	-	4.47	4.38	4.76
07-PW-02	-	-	-	-	-	-
09-GW-31	-	-	-	-	0.18	0.25
09-GW-32	-	-	-	-	3.79	3.22
09-GW-33	-	-	-	-	5.05	4.48
09-GW-34	-	-	-	-	4.92	5.39
09-GW-35	-	-	-	-	3.32	2.30
09-GW-36	-	-	-	-	3.39	3.14
09-GW-37	-	-	-	-	3.93	-
09-GW-38	-	-	-	-	3.20	1.47
10-GW-40	-	-	-	-	4.78	2.32
95-G10D	0.16	1.12	1.23	1.27	1.74	1.24
95-G10S	0.74	2.50	1.77	1.78	2.42	1.95
95-G1D	0.03	3.89	4.03	4.64	4.11	4.22
95-G1S	0.08	0.04	0.03	0.05	0.05	0.02
95-G2D	0.13	2.51	2.21	2.22	0.91	1.08
95-G2S	0.42	0.87	1.23	3.10	2.73	1.53
95-G3D	0.03	0.38	0.86	0.91	0.51	0.59
95-G3S	0.27	3.95	7.18	9.72	7.78	11.95
95-G4D	0.07	1.16	1.18	1.37	1.43	0.99
95-G4M	0.09	1.22	2.09	2.11	2.31	1.48
95-G4S	0.26	1.24	2.80	2.92	2.34	3.20
95-G6D	0.04	0.21	0.19	0.24	0.23	0.17
95-G6S	1.07	1.30	2.18	1.58	1.35	1.49
96-GW-11	0.03	0.04	0.03	0.26	0.05	0.35
96-GW-12	1.93	1.48	1.05	1.49	1.36	1.41
96-GW-13	0.68	1.54	1.22	2.26	2.28	3.57
96-GW-14D	1.03	6.95	4.86	3.73	2.95	3.08
96-GW-14S	2.46	3.64	3.20	3.46	3.11	2.48
96-GW-15D	0.04	0.07	0.83	0.99	0.82	1.19
96-GW-15S	0.03	0.03	0.03	0.05	0.05	0.02
96-GW-17	1.05	2.89	3.15	1.78	1.49	2.54

- No Data Available

APPENDIX C: SULPHATE & COBALT CONCENTRATION TIME SERIES IN WELLS 95-GW-2S, 06-GW-26, 06-GW-27, 06-GW-28, 09-GW-37, 09-GW-38 AND 09-GW-39

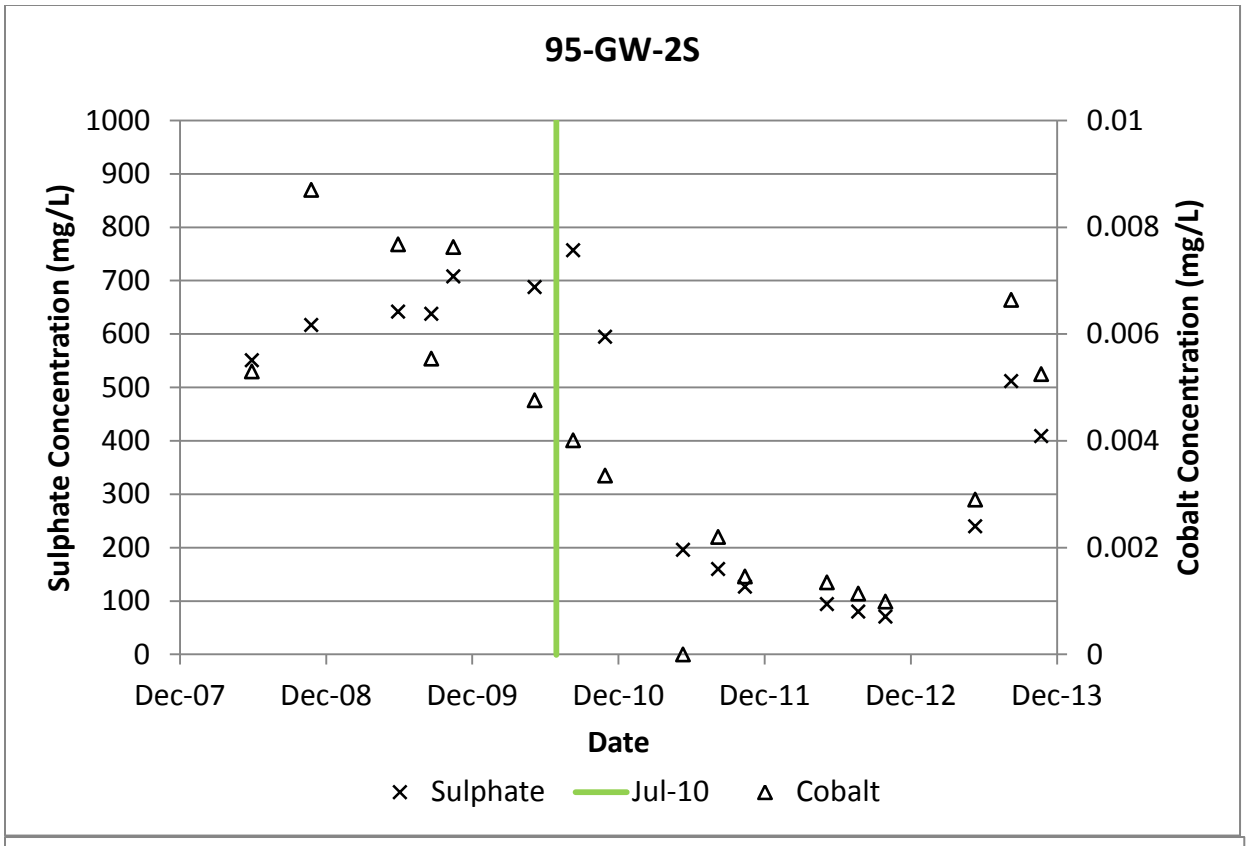
95-GW-2S
Sulphate Concentration (mg/L)
Cobalt Concentration (mg/L)
1000
900
800
700
600
500
400
300
200
100
0
0.01
0.008
0.006
0.004
0.002
0
Dec-07
Dec-08
Dec-09
Dec-10
Dec-11
Dec-12
Dec-13
Date
Sulphate
Jul-10
Cobalt

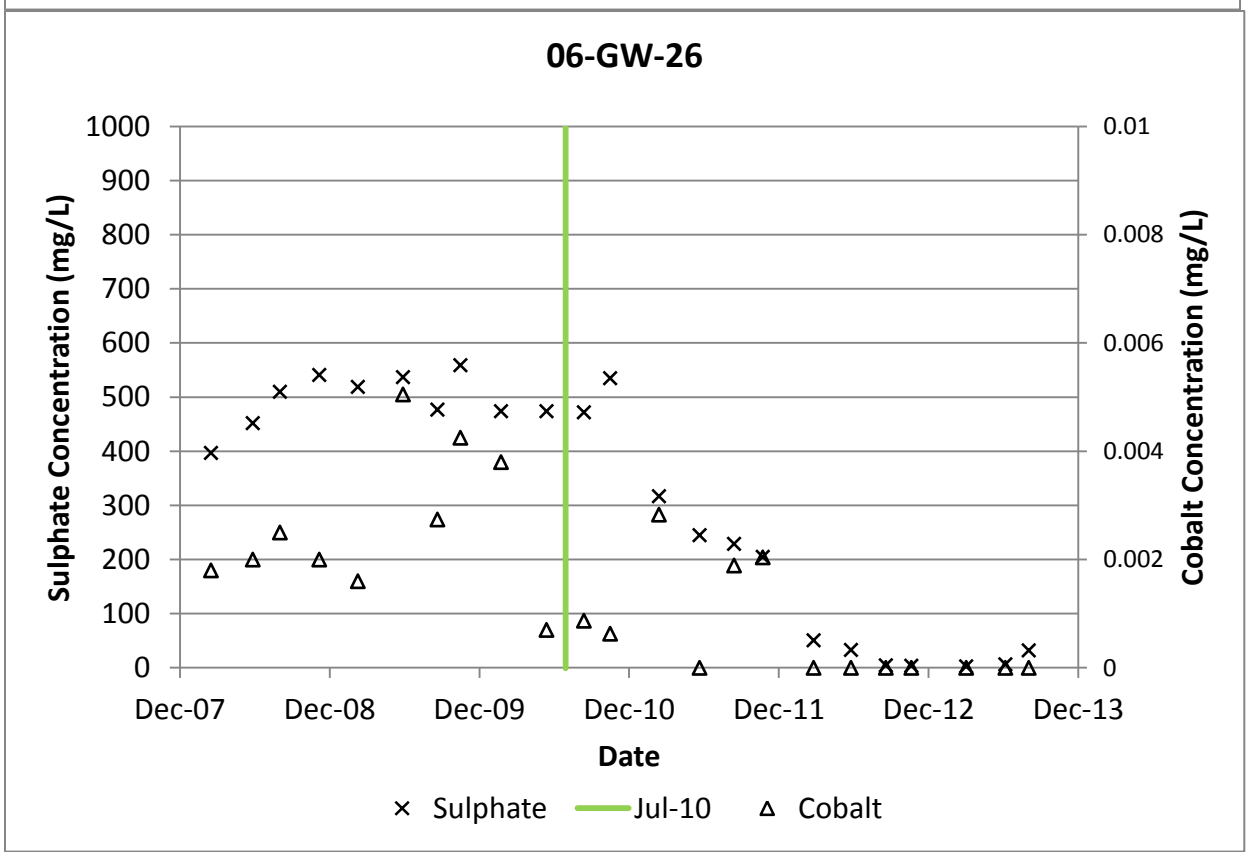
06-GW-26
Sulphate Concentration (mg/L)
Cobalt Concentration (mg/L)
1000
900
800
700
600
500
400
300
200
100
0
0.01
0.008
0.006
0.004
0.002
0
Dec-07
Dec-08
Dec-09
Dec-10
Dec-11
Dec-12
Dec-13
Date
Sulphate
Jul-10
Cobalt

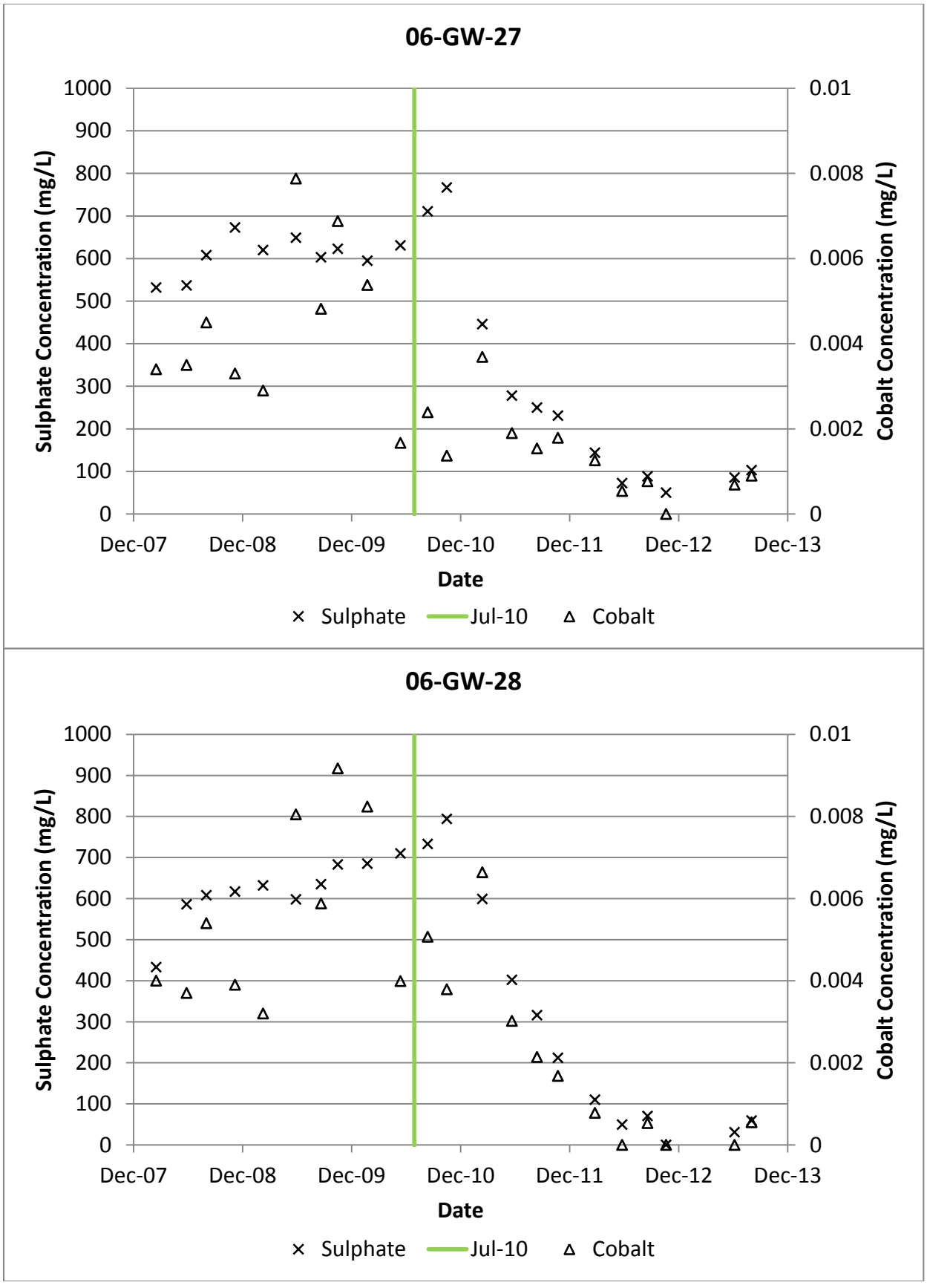
06-GW-27
Sulphate Concentration (mg/L)
Cobalt Concentration (mg/L)
1000
900
800
700
600
500
400
300
200
100
0
0.01
0.008
0.006
0.004
0.002
0
Dec-07
Dec-08
Dec-09
Dec-10
Dec-11
Dec-12
Dec-13
Date
Sulphate
Jul-10
Cobalt
06-GW-28
Sulphate Concentration (mg/L)
Cobalt Concentration (mg/L)
1000
900
800
700
600
500
400
300
200
100
0
0.01
0.008
0.006
0.004
0.002
0
Dec-07
Dec-08
Dec-09
Dec-10
Dec-11
Dec-12
Dec-13
Date
Sulphate
Jul-10
Cobalt

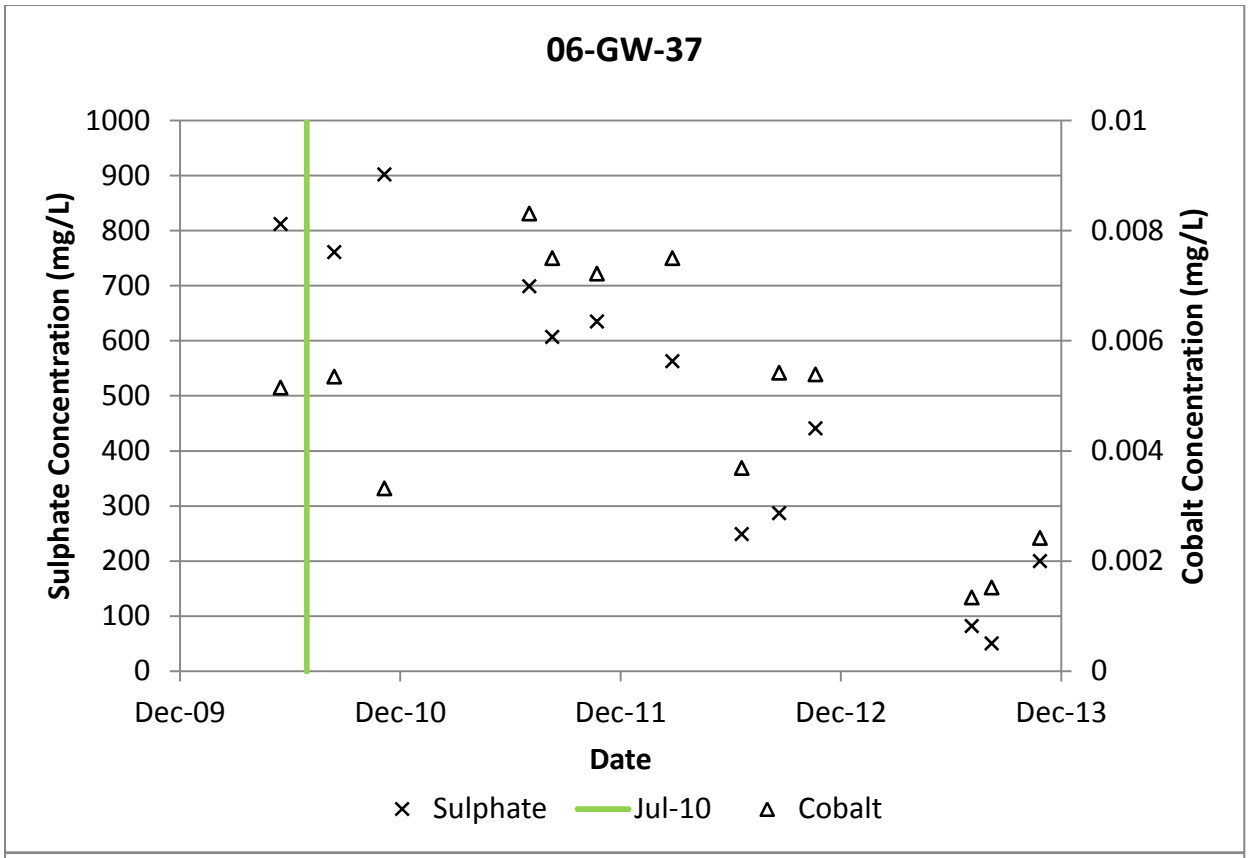
06-GW-37
Sulphate Concentration (mg/L)
Cobalt Concentration (mg/L)
1000
900
800
700
600
500
400
300
200
100
0
0.01
0.008
0.006
0.004
0.002
0
Dec-09
Dec-10
Dec-11
Dec-12
Dec-13
Date
Sulphate
Jul-10
Cobalt

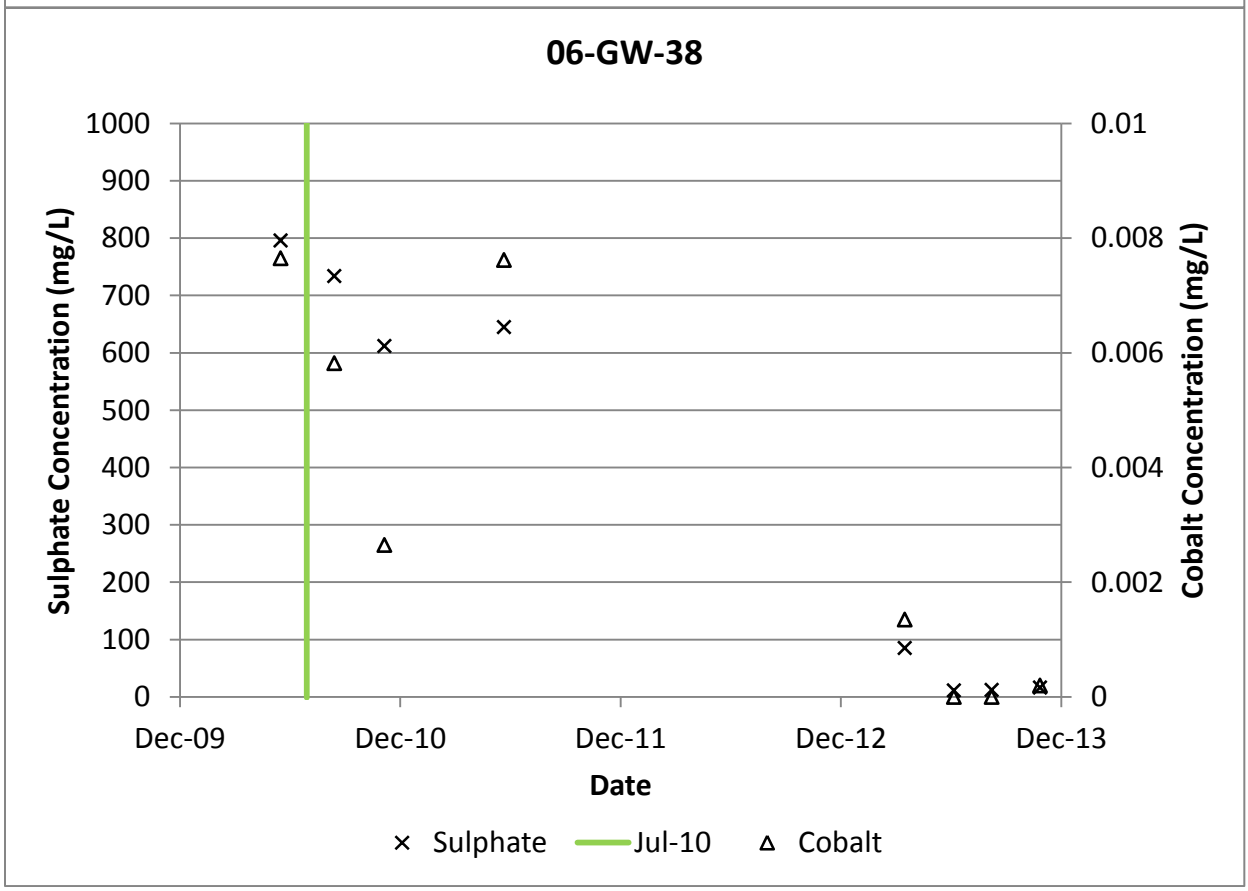
06-GW-38
Sulphate Concentration (mg/L)
Cobalt Concentration (mg/L)
1000
900
800
700
600
500
400
300
200
100
0
0.01
0.008
0.006
0.004
0.002
0
Dec-09
Dec-10
Dec-11
Dec-12
Dec-13
Date
Sulphate
Jul-10
Cobalt

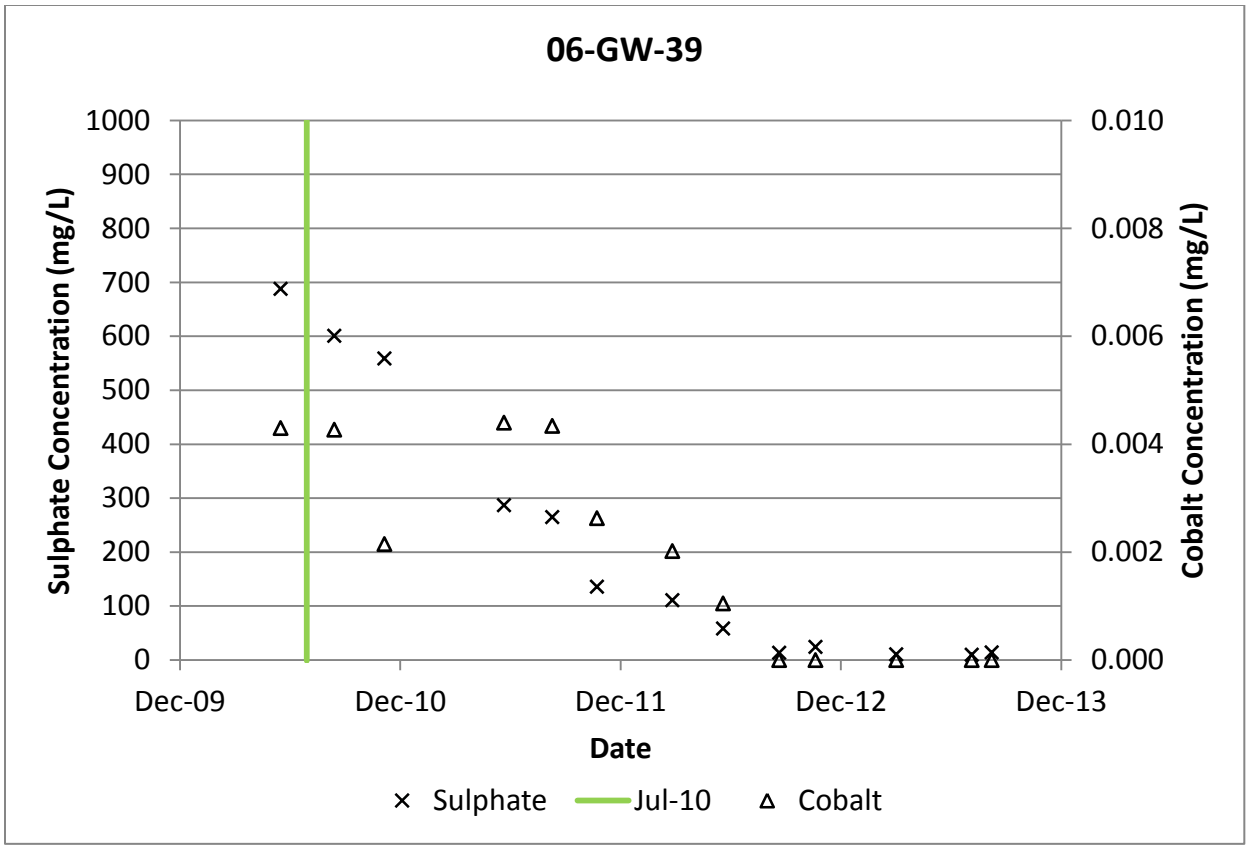
06-GW-39
Sulphate Concentration (mg/L)
Cobalt Concentration (mg/L)
1000
900
800
700
600
500
400
300
200
100
0
0.010
0.008
0.006
0.004
0.002
0.000
Dec-09
Dec-10
Dec-11
Dec-12
Dec-13
Date
Sulphate
Jul-10
Cobalt